Development of Dense Scintillating Radiation Hard Fluoride Glasses for the Electromagnetic Calorimeter of the Proposed Compact Muon Solenoid

A thesis presented for the degree
of
Doctor of Philosophy

November 1994

Timothy James Price
Department of Physics
Brunel University

Abstract

Hafnium based Heavy Metal Fluoride glasses have been produced and evaluated in a search for new dense scintillating materials. The principal motivation was the electromagnetic calorimeter of the Compact Muon Solenoid (CMS), a proposed detector for the Large Hadron Collider (LHC) at CERN, Geneva. Incorporating CeF_3 in these transparent glasses results in scintillators with fast time constants that are typical of crystalline CeF_3. Typical decay components of 9 ns (30%) and 25 ns (70%) have been measured.

To record the time distribution of scintillation light, an extension to the *single-photon* method, has been developed, it is optimised for materials with low light output. An alternative acquisition system which used a Multi-Channel Scaler has been critically evaluated for this application.

A low dose rate (1.2 $rads^{-1}$) ^{60}Co irradiation has been used to determine the radiation tolerance of the glasses. Radiation induced optical absorbance was predominantly located in the UV with tails extending into the visible region. These glasses show partial recovery of optical absorbance at room temperature. Compositional optimisation has shown that Indium and Cerium enhance radiation tolerance.

Table of Contents

Acknowledgements

I would firstly like to thank Peter Hobson who, for the entire duration of this programme, has fulfilled his role as a most competent supervisor. His insight and never-ending enthusiastic approach has helped to motivate me and maintain direction for the research.

My colleagues at the Rutherford Appleton Laboratory have played an important role in all aspects of the wider collaboration including, project management, complementary experimental work, Monte Carlo Studies, beam tests and the glass production. The collaboration involved R.M. Brown, D. Cockerill, P. Flower, M. Sproston, K. Bell, B. Kennedy, G. Grayer, L. Lintern and P. Jeffreys.

J. Parker has provided the kind use of his facilities at Sheffield University for fluoride glass production. His technical input has resulted in improvements to the production procedure.

It is a pleasure to acknowledge the contributions made by E. Devitsin, V. Kozlov, S. Potashov and V. Makhov from the Institute of General Physics, Moscow. They have provided several of the glass samples which have been evaluated in this work and performed Monte Carlo simulations for the beam tests.

I would like to thank Derek Imrie who has enabled me to complete my studies whilst working for the Physics Department. His generosity in lightening my departmental workload, allowing me to participate in the CERN beam tests, and also many progress meetings, has enabled me to play an important role within the collaboration.

Dedication

This thesis is dedicated to the memory of my Mother, Mavis Elizabeth Price who died on 30th December 1992, after a long illness.

CHAPTER ONE

Introduction

1.1. Introduction

The Large Hadron Collider (LHC) [1], an accelerator in which protons collide head-on with a centre of mass energy of 15.4 TeV, is planned to be built at CERN, Geneva by the year 2004. Protons will collide at two points around the ring, where large multipurpose detectors will be installed. The Compact Muon Solenoid (CMS) [2] is one of these experiments.

The aim of the work described in this thesis has been to develop scintillating glasses suitable for the active medium of the central Electromagnetic Calorimeter of CMS. In this chapter, the work is placed in context by describing very briefly the motivation for the LHC. The concepts of electromagnetic calorimetry are reviewed, introducing some key terms. The main detector sub-systems of CMS are described and then the various options which have been investigated for the active medium are discussed. The chapter concludes with separate sections which consider the relative merits of the homogeneous calorimeter materials such as CeF_3 or $PbWO_4$ crystals, compared to lead-scintillator sampling calorimeters, and summarises briefly the advantages of scintillating glasses.

1.2. Motivation

At low energy scales, there are four fundamental forces that mediate the interaction of fundamental fermions. These are the Strong, Weak, Electromagnetic and Gravitational forces. The Strong force binds quarks together to form hadrons (of which the proton and neutron are examples). Electromagnetism is responsible for the interactions of electrically charged particles, and gravity for interactions between particles having mass. The Weak interaction is responsible for the β-decay of nuclei and the fusion processes by which the Sun generates energy.

The last few decades have witnessed a remarkable growth in our knowledge of the nature of these forces and their inter-relationships. This has resulted in the 'Standard Model' of particles and fields. Higher energy accelerators provide an opportunity to access extended energy ranges allowing the study of new interactions and the possibility of producing new particles and force carriers. LEP at CERN, Geneva and SLC at SLAC California, are current accelerators which have both successfully produced huge numbers of Z gauge bosons and studied their decays in great detail. As a result, the Standard Model has been studied and confirmed with great precision. An upgrade to LEP (LEPII) is currently under construction and will probe CM energies above 160 GeV, the threshold for W^+W^- production.

The Large Hadron Collider is one of the next generation of high energy accelerators. In contrast to LEP and SLC, which collide electrons (e^+e^-), the LHC will collide hadrons (pp) at energies of 8 TeV on 8 TeV. The Standard Model postulates the existence of a 'Higgs' particle which is required to give mass to the physical $W^\pm$ and the Z gauge bosons. Discovery of the Higgs is the next milestone necessary to further understand the fundamental forces of nature.

1.3. The Large Hadron Collider (LHC)

The LHC is designed to study the interactions of quarks in the TeV energy range, where theory predicts significant deviations from the standard model. The LHC will collide protons at a beam energy of about 7.7 TeV and a luminosity of 10^{34} cm^2s^{-1}. This corresponds to a mean interaction rate $L\sigma$, of approximately 10^9s^{-1}.

The clearest signatures of Higgs particles involve their decay into charged leptons, or photons. For example, the Higgs is expected to decay into ZZ or WW final states; deviations from the SM would have cascade decays involving Ws and Zs. These gauge bosons will have to be detected through their charged leptonic decays as hadronic decays will be overwhelmed by QCD backgrounds. The purely leptonic or photonic branching fractions are often very small. A high luminosity is required because of the large constituent energies, low cross-sections and small branching ratios. This has a tremendous impact on detector design. A Standard Model Higgs which is in the mass range

$0.5M_Z < M_H < 2M_Z$ [3] will decay into a real and a virtual Z which, in turn, decay into pairs of electrons or muons.

As the Higgs will be detected by its decay via Intermediate Vector Bosons, it is relevant to require a dilepton mass resolution that matches the width of the Z. Equally, any narrow state decaying into charged lepton pairs will benefit from good momentum resolution, which will enhance its signal above non-resonant backgrounds. If the Higgs mass is between the probable discovery limit of LEP (90 GeV) and 130 GeV, the decay $H \rightarrow \gamma\gamma$ will provide a clear signature. In this region the width of the Higgs is expected to be extremely small ($\approx$ 10 MeV) [4] and will be entirely dominated by the instrumental resolution. It is this decay, and the requirement for excellent di-photon mass resolution, that imposes the strictest performance requirements on the electromagnetic calorimeter.

The LHC will be constructed in the existing LEP ring at CERN. LEP currently has four large experimental halls, each of which can accommodate one experiment. Initially, two large experiments will be installed at the LHC. One, ATLAS, uses a toroidal muon spectrometer magnet complemented by an inner superconducting solenoid. The second experiment, CMS (Compact Muon Solenoid) is, like ATLAS, a general purpose detector designed for studying proton-proton collisions, working at the highest luminosities of the LHC. The work undertaken for this thesis has been concerned specifically with detector development for the CMS electromagnetic calorimeter.

1.4. Electromagnetic Calorimetry

The large experiments designed to study High Energy Physics (HEP) identify individual outgoing particles by measuring their energy and momentum. For unstable particles, the lifetime is also an important parameter. Specialised sub-detectors each fulfil a specific role in particle identification. Inner tracking employing vertex reconstruction is used to measure the lifetime of short-lived states. The curvature of a track in a magnetic field is used to measure the momentum of charged particles. The total energy of a particle or a group of particles is measured using a calorimeter. There are two different varieties of calorimeters, hadronic and electromagnetic. In hadronic interactions, most of the energy is dissipated by ionisation loss of secondary pions. Nuclear reactions result in the multiplicative production of π^os. These decay into two photons and give an electromagnetic shower within a hadronic one. The longitudinal development of hadronic showers scales with the nuclear absorption (or interaction) length,

$$\lambda = \frac{\rho}{N\sigma_{abs}}$$ Equation 1.01

where N is the number of target atoms per cm^{-3}, ρ is the density (gcm^{-3}), and σ_{abs} is the absorption cross-section (cm^2). Hadronic calorimeters tend to be deeper than electromagnetic calorimeters because hadronic showers take longer to develop.

Electromagnetic calorimeters fall broadly into two groups, sampling and homogeneous. In both types, impinging high energy electrons and photons interact with the absorber producing spectacular showers in the dense medium. Showers result from the primary electron undergoing multiplicative Bremsstrahlung processes, producing high energy photons. The photons pair produce and further increase the number of particles in the shower. The precise theory of showers is very complicated and large fluctuations from the average behaviour are observed. A simple model which uses the electron radiation length, X_o is presented [5].

Above a critical energy E_c, given approximately by

$$E_c = \frac{800}{Z}$$ E_c (MeV) Equation 1.02

electrons lose energy predominantly by radiation and

$$-\frac{dE}{E} = \frac{dx}{X_o}$$ Equation 1.03

where X_o is known as the radiation length, it is given by,

$$\frac{1}{X_o} = \frac{4Z^2N}{137} r_o^2 \ln \frac{183}{Z^{1/3}}$$ Equation 1.04

where r_o is the classical electron radius, 2.82× 10^{-15} m, and Z is the Atomic number of the absorber. Integration of Equation 1.03 gives

$$\langle E \rangle = E_o \exp\left(-\frac{x}{X_o} \right)$$ Equation 1.05

where $\langle E \rangle$ is the electron energy remaining after traversing an absorber of thickness, x. Photons interact similarly to electrons, with a mean free path X_p, which is related to X_o by,

$$X_p = \left(\frac{9}{7} \right) X_o$$ Equation 1.06

The shower develops in the direction of the primary electron due to conservation of momentum. The number of particles in the shower initially grows exponentially with penetration depth. The lateral spread of the shower is much smaller than its longitudinal propagation. A parameter which describes the lateral spread is called the Molière radius, r_M. A popular definition is that, in a completely containing calorimeter, 99% of the shower energy is deposited in a cylinder of radius $3r_M$. r_M is related to X_o by,

$$r_M = \frac{21X_o}{E_c} \qquad E_c\ (\mathrm{MeV}) \qquad \text{Equation 1.07}$$

In an actual shower, electrons, positrons and photons are simultaneously present. The number of particles continues to grow until the mean energy decreases below E_c. At this point, ionisation mechanisms and the Compton effect begin to compete with radiation and pair production. The number of particles in the shower stops growing.

Ignoring energy loss to production of new particles, ionisation energies, and assuming that the average energy of the electrons positrons and photons is all the same, the shower stops growing when $E_o/3E_c$ particles are present in the shower. This happens at a distance, x_{max} from the origin,

$$x_{\max} = \frac{X_0}{0.78}\ln\frac{E_0}{3E_c} \qquad \text{Equation 1.08}$$

A calorimeter is segmented into many individual modules which make up an hermetic array. This enables precise location of the co-ordinates of the interaction. A finely segmented calorimeter maintains low occupancy and is also better able to distinguish two closely spaced, coincident showers. To measure accurately the energy of the primary, the shower has to be contained within the calorimeter. Lateral leakage into adjacent modules is easily corrected by summing the signal from all modules surrounding the one in which the primary particle (or photon) entered. Comparing the signal size in adjacent modules can also be used for precise position location if the granularity matches the r_M appropriately. Longitudinal leakage degrades the performance by causing a direct signal in the photodetector, and also due to fluctuations in the energy loss. These effects are minimised by ensuring that the calorimeter is sufficiently long ($\approx 25X_o$ for 50 GeV) to contain the majority of even the most energetic showers.

Energy from a high energy shower is dissipated to the lattice of the scintillating absorber causing electronic excitation and ionisation which result in the emission of light. Each module is optically isolated by wrapping with a reflective material. A photodetector on one end-face reads-out each calorimeter module. Under ideal circumstances, the detected signal varies in proportion to the energy of the primary particle. For a containing calorimeter the energy resolution is given by,

$$\frac{\Delta E}{E}=\frac{a}{\sqrt{E}}\oplus\frac{b}{E}\oplus c \qquad \text{Equation 1.09}$$

where $\oplus$ indicates taking the square root of the quadratic sum. The stochastic term involving 'a' arises from the statistical variation in the number of information carriers which represent the energy of the shower. The effect on energy resolution of electronic noise in the detector circuit involves the so-called noise term, 'b'. The constant term, c, results from the systematic effects for example day-to-day gain changes of the detector, lateral uniformity of light collection, shower leakage and the effect of dead material in front of the calorimeter.

1.5. The Compact Muon Solenoid

CMS has been designed with particular emphasis on the efficient identification and precise measurement of electrons, muons and photons over a large momentum range. The detector subsystems will be built around a high-field superconducting solenoid (≈4T) which provides an axial magnetic field for charged particle tracking. A cut-away view of the CMS detector is shown in Figure 1.01, the sub-detector systems are individually labelled. The overall diameter is 14 m, the length is 20 m, and the total weight is 12000 tons.

1.5.1. The Muon Spectrometer

A solenoid was chosen in preference to a toroid for the magnet configuration as it offers several advantages. A field parallel to the colliding beams constrains charged particles to bend in the transverse plane. The transverse position of the vertex is known accurately due to the small dimensions of the colliding beams (20 μm). In a solenoid, the momentum measurement starts at R= 0, whereas in a toroid, it starts after the absorber, at typically R= 3 m. The name CMS stems from this consideration as the solenoid allows the design to be compact. Experience has been gained in building large superconducting solenoidal magnets in other particle physics experiments e.g. ALEPH, DELPHI, etc.

The solenoid is expected to be 14 m long with an internal diameter of 5.8 m. The design provides a uniform magnetic field over the rapidity region $|\eta| < 2.5$. The calorimeters and trackers are accommodated within the inner coil radius; the magnetic flux is returned via an external 1.8 m thick saturated iron yoke which is instrumented with four layers of muon chambers.

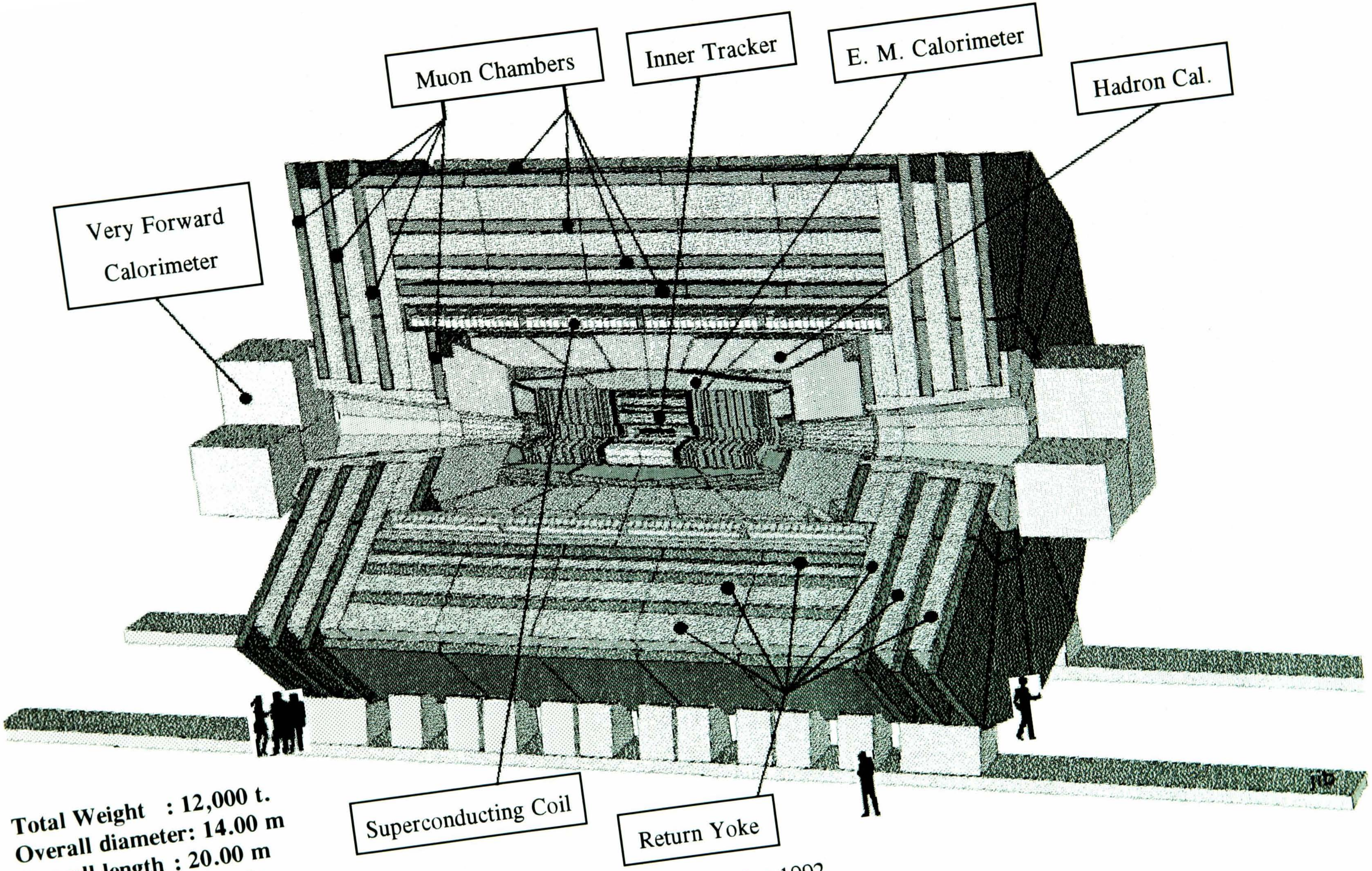

Total Weight : 12,000 t.
Overall diameter: 14.00 m
Overall length : 20.00 m
Magnetic field : 4 Tesla

Figure 1.01 A Three Dimensional view of the CMS Detector [2] Version 1992.

In the muon spectrometer, tracking information is collected from three detectors; the inner tracker, the calorimeters, and the four planes of muon chambers placed within the flux return yoke. Muons pass through the hadron calorimeters (9 interaction lengths, λ, at 90°), the magnet (1.2λ) and the tail catcher (2λ). The muon is constrained to pass through at least two of the four identical muon stations. Each contains planes of drift chambers which measure the muon's position to 100 μm and its direction to 1 mrad. Triggering planes are incorporated in each muon station to indicate the bunch crossing and also provide cuts on the muon momentum. The final muon tracking station is located after a total of 20λ of material. This ensures that only muons can reach it.

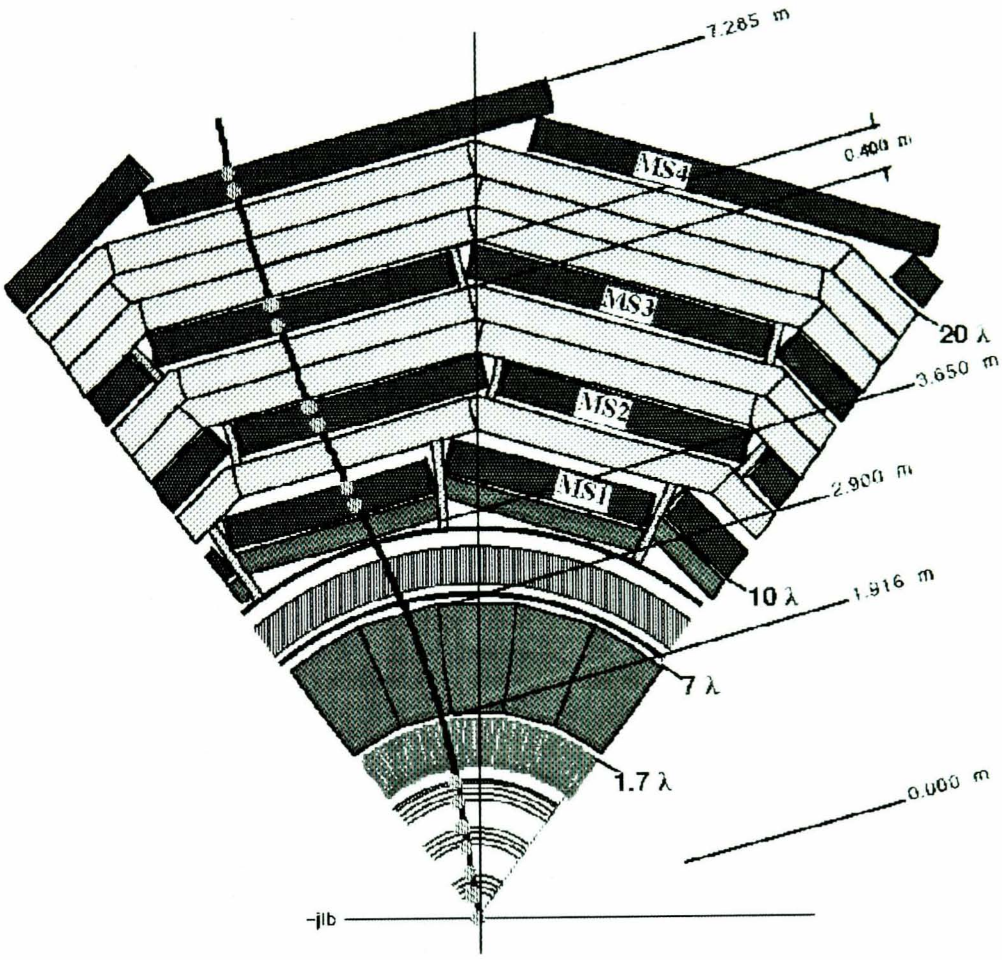

Figure 1.02 A 60° segment of a transverse section through the CMS detector at z=0 m. [6]

The magnetic field exerts the maximum bending force up to a rapidity of 1.5. In the range $1.5 < |\eta| < 2.5$, the field strength is still sufficient to maintain good resolution. Between $2.5 \leq |\eta| \leq 4.7$, muons are detected in the tracker and the four forward muon chambers. The combined momentum resolution is better than 3% at 0.4 TeV in the central rapidity region $|\eta| \leq 2.5$, degrading to 5% at 2 TeV. Low momentum ($p < 100$ GeV) muons are measured before the absorber with a precision of about 1% up to a rapidity of 2.5.

1.5.2. Tracking

The principal design aim of the inner tracker is to reconstruct all high p_t muons and isolated electrons produced in the central rapidity region with a momentum precision of $\Delta p/p = 0.1p_t$ (p_t in TeV). At a luminosity of $10^{34}cm^{-2}s^{-1}$, potentially interesting events will be superimposed on a background of approximately 500 soft charged tracks from ≥ 15 minimum bias events which occur during the same bunch crossing. To identify isolated leptons it is necessary to identify all high p_t tracks ($p_t > 2$ GeV), the defined goals are to fit isolated tracks with an efficiency of 95% and to fit 90% of high p_t tracks within jets. The 15 minimum bias events will be distributed along the beam direction with an r.m.s. of 5 cm, accurate back pointing will ensure all interesting tracks are consistent with a common vertex.

For accurate track fitting and to prevent problems associated with high occupancy, the detector cell size must be small. Solid-state and gas microstrip detectors can provide the required granularity and precision. Ideally their occupancy will not exceed 1%, this translates to $\approx 10^7$ channels. The tracker extends to a radius of 1.3 m and occupies the region $|Z| \leq 3.5$ m. The planes are distributed as shown in Figure 1.02 and Figure 1.03, straight tracks will intercept on average 12 planes of detectors in the barrel region and 20 planes in the forward region. To minimise secondary scattering, the material in the central region will correspond to 15% of a radiation length, X_o.

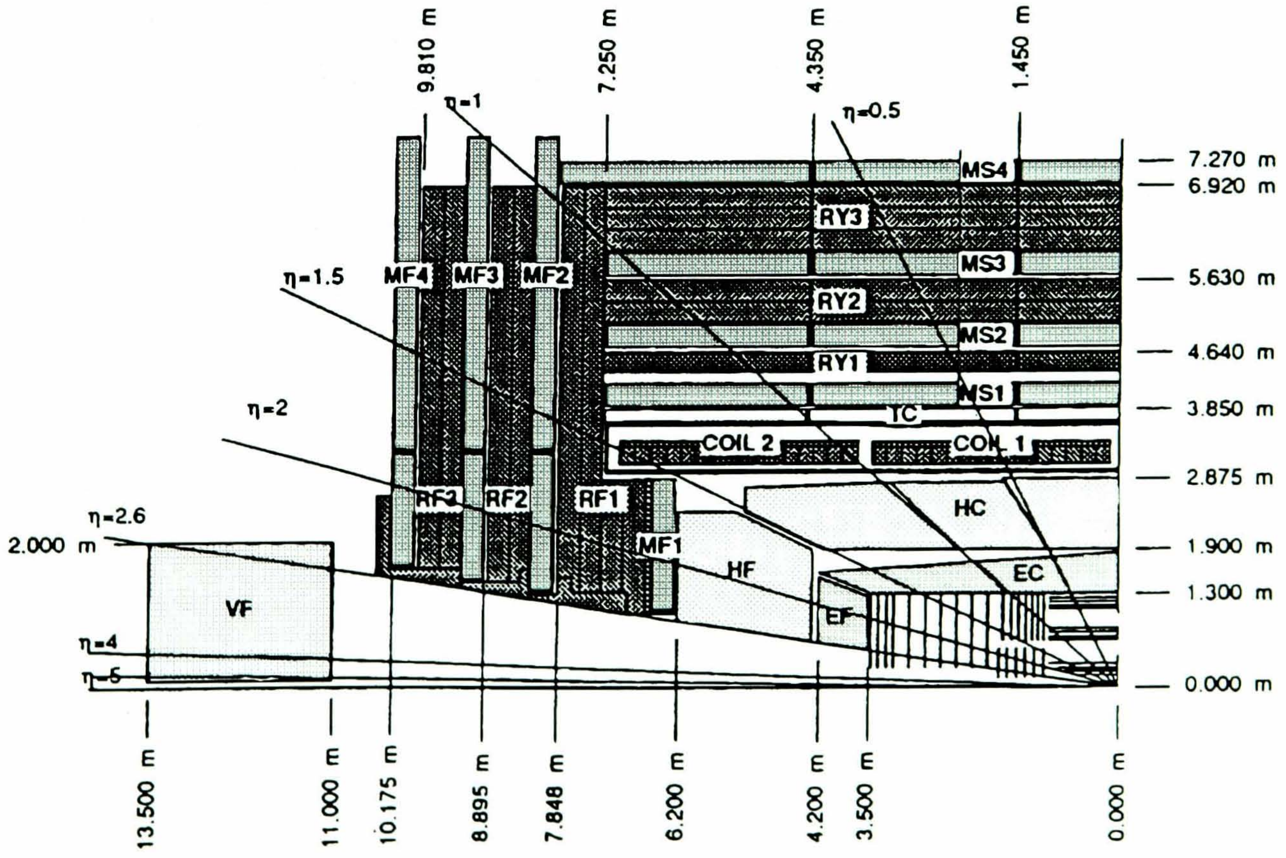

Figure 1.03 A section showing the sub-detectors of CMS [2].

1.5.3. Calorimetry

The barrel calorimetry is sandwiched between the inner tracking (R=1.3 m) and the inner radius of the magnet (R=2.9 m), the electromagnetic calorimeter extends from R=1.3 m to R=1.9 m, the hadron calorimeter occupies the radial region $1.9 < R \leq 2.9$ m. Forward hadron and electromagnetic calorimeters cover the rapidity region $1.5 \leq |\eta| \leq 2.6$. The layout of these sub-detectors is shown in Figure 1.03.

The Hadron and Very Forward calorimeters are described very briefly in the remainder of this section, the rest of the chapter is devoted to the central Electromagnetic calorimeter and ensuing discussion as this sub-detector is the principal motivation for the work of this thesis.

1.5.3.1. The Hadron Calorimeter

The technology chosen for the hadron calorimeter has been successfully employed in a number of earlier detectors; it was developed in the UA1 collaboration. Wavelength shifting fibres embedded in scintillating tiles are read out by clear fibres which transport scintillation light to remote photodevices [7]. The tile dimensions are dictated by the required segmentation, ($\Delta\eta \times \Delta\phi = 0.1 \times 0.1$ for $|\eta| \leq 2.0$), this has been chosen to match approximately the electromagnetic calorimeter. The design allows good hermeticity, good transverse granularity and moderate energy resolution, these properties are consistent with good mass resolution and two-jet separation. The detector planes are sufficiently compact to allow an adequate depth of absorbing material (9λ) to fit in the radial space available (97.5 cm at $\eta=0$). Copper has been chosen as the absorbing material for the HCAL because of its short interaction length ($\lambda = 1.2$ cm), in addition the intermediate Z minimises degradation of muon momentum resolution in the region dominated by multiple scattering.

If photodetectors which can operate in a high axial magnetic field can be identified, they will be placed inside the coil, the length of clear readout fibre will be ≈ 5 m. Otherwise ≈ 10 m of fibre will be required to reach detectors positioned externally. High field hybrid PMTs incorporating silicon detectors and also Silicon Avalanche Photodiodes (APDs) are currently being investigated. A possible design for the rapidity region $|\eta| \leq 1$ uses 37.5 mm thick copper plates allowing 8 mm gaps between adjacent layers for 4 mm thick scintillating tiles and associated mechanical support. At larger rapidities ($|\eta| > 1$), finer sampling is envisaged to achieve the required depth ($25X_o$) and energy resolution, $\sigma(E_t)/E_t \approx 20\%/\sqrt{E_t}$.

1.5.3.2. The Very Forward Calorimeter

The rapidity region $2.6 \leq |\eta| \leq 5$ is covered by the VFCAL. Extending coverage to this large rapidity significantly enhances the missing transverse energy resolution and also enables tagging of high energy forward jets. The high radiation environment in this forward region makes design of this detector challenging. Radiation tolerance and speed rather than the energy resolution are the major considerations. To this end, an exchangeable active medium (gas) is being considered in a design based on Parallel Plate Chambers (PPCs). Materials with low neutron activation cross-sections should be used. The VFCAL is a sampling calorimeter, the steel walls of the chambers could be used as the absorbing material.

A granularity of 10×10 cm^2 has been chosen for the VFCAL, to allow accurate determination of the centre of gravity of forward jets. These have a size $\sigma \approx 5$ cm at the front face of the VFCAL. which is at $|z| = 11$ m from the interaction vertex.

1.6. CMS Electromagnetic Calorimeter

The most demanding physics channel that the Electromagnetic calorimeter must detect is the decay of the intermediate mass Higgs to two photons. In this regime the energy resolution should not deteriorate the mass resolution significantly. The energy resolution given in Equation 1.09 is composed of three terms added in quadrature, the stochastic, constant and noise terms should all be small at an energy corresponding to half of the Higgs mass. Rejection of π^os carrying moderate transverse energy E_t (20-40 GeV) demands a good two shower separation capability, this implies good granularity. There are several options for the calorimeter material, CeF_3, $PbWO_4$, and glasses are the principal homogeneous contenders, an alternative solution constructed of alternate lead/ scintillator tiles read out longitudinally via WLS optical fibres is also proposed.

There is an extensive list of criteria to which the material that is ultimately chosen must conform, these include, high light yield (preferably at a wavelength > 300 nm), a short radiation length, a short decay constant (<30 ns with no slow component), a high radiation tolerance (>5 Mrad), small dependence of the light output on temperature, good mechanical properties, and acceptable cost. When the LOI was submitted, no single material had been identified which satisfied all of these criteria simultaneously.

The choice of a moderate granularity muon calorimeter which necessitates the use of a high magnetic field is put to best advantage if the muon detector starts immediately after the coil. 10λ of material are required to filter hadrons sufficiently for the muon calorimeter. It is advantageous to incorporate all of the calorimetry inside the coil as it is $> 1\lambda$ deep. Studies have shown that 1λ of material at a depth of 6-7λ into the hadron calorimeter (with a supplementary tail-catcher) does not significantly deteriorate the hadronic energy resolution or introduce significant tails into the energy distribution [8]. Using 7λ of Hadron calorimeter inside the coil pushes its inner radius to 1.90 m. In the overall design, the radial space $1.30 \leq R \leq 1.90$ is allocated for the ECAL. The choice of inner radius requires careful consideration, as it is governed by several conflicting issues. The wish to install all of the ECAL within the magnetic field, the material cost/cc, and the compactness of the overall detector all drive the inner radius to a small value. Energy pile-up (especially significant at high luminosities) and the ability to separate two showers are favoured in a design which uses a larger inner radius.

In order to prevent longitudinal shower leakage of high energy electromagnetic particles interacting in the calorimeter photodetectors, a depth of at least 25 X_o of active medium is required in the ECAL. In addition to cost/cc considerations, the space allocation constrains the choice of active medium to dense materials with short radiation lengths. For a CeF_3 calorimeter, the desired lateral granularity translates to a tapered block whose larger (back) ends have dimensions, $\approx 30\times 30$ mm^2. A longitudinal split in the calorimeter modules is required to achieve the required electron-jet identification, two-shower separation and photon direction measurements. In one scenario [2], a split at $8X_o$ is used, the lateral granularity in the first section is improved by subdividing the block into four smaller sub-units, each has an individual readout. Simulations have shown that a π^o rejection of 3, averaged over the relevant p_t range and an angular resolution of $\approx$ 40-65 mrad/$\sqrt{E}$ can be achieved [9]. Whilst reducing the length of individual calorimeter blocks is beneficial from the production perspective, the mechanical support becomes more complex.

A requirement for good energy resolution necessitates efficient light collection in this sub-detector, remote detectors read out using optical fibres (as are being considered for the HCAL) would compromise performance unacceptably. Detectors which operate in a (worse case) transverse 4T magnetic field must be employed, additionally they must be compact, inexpensive, have a stable response and a high quantum efficiency in the chosen spectral region. Silicon photodiodes are likely candidates as they are well matched to the CeF_3

scintillation emission [10]. Avalanche Photodiodes (APDs) are also being considered due to their thin sensitive region, although they are significantly more expensive.

The space allocation for the electromagnetic calorimeter also includes room to accommodate the supporting mechanics. This reduces the space available for the calorimeter modules. A cradle made from two sheets of a carbon fibre composite with an aluminium or Nomex honeycomb structure sandwiched in-between, holds an array of calorimeter towers. This cradle provides the required strength and structural rigidity whilst minimising the amount of material in front of the ECAL. Stainless steel supporting rings which are at a larger radius than the ECAL medium support the carbon fibre *super-modules* and individual calorimeter towers. Spacers are used to maintain a finite air gap between adjacent towers to allow for structural deformation during assembly, transport and installation. In the current design, the ECAL towers will start at $R \approx 1.40$ m.

If the specified energy resolution of the ECAL is to be maintained over a long period, a precise in-situ calibration of the response of individual calorimeter modules and the relative calibration (front/ back) is essential. A precise electronic pulser will be used to monitor and calibrate the readout electronics. Using a system of LED flashers and fibre optic cables fed into each individual calorimeter block, it should be possible to monitor day-to-day gain changes to $\approx 0.2\%$, this has been achieved in OPAL [11]. Using this validation and monitoring system, it should be possible to control the so called *constant term* to better than 0.5%.

1.7. Calorimeter performance requirements

The performance requirements of the individual sub-detectors are collected together in Table 1.01. The energy resolution is obtained from Equation 1.09. The radiation resistance is for an integrated luminosity of 10^{42} cm^{-2} corresponding to 10 years of running at the design luminosity.

1.8. ECAL active medium- the alternatives

1.8.1. Cerium Fluoride, CeF_3

A large amount of experience has been gained in previous experiments which have used crystalline electromagnetic calorimeters, these include Crystal Ball, Crystal Barrel, CLEO, CUSB and L3. Hermeticity and fine granularity are easily achieved, the engineering problems associated with production, monitoring and calibration have all been solved. To identify the most suitable alternative for the LHC application, a comprehensive appraisal of the properties of a number of crystals has been carried out by the Crystal Clear

Collaboration. Their work has identified CeF_3 as a promising material for CMS. Its properties are compared with the other potentially suitable materials in Table 1.02 at the end of this section.

Calorimeter Requirement	ECAL	HCAL	VFCAL
	e, γ	jet	jet
Energy Resolution			
stochastic a	≤ 0.03	≈ 0.8	≈ 1.0
noise b	0.15	≈ 1.0	≈ 3.0
constant c	≈ 0.005	≤ 0.03	≤ 0.05
Angular Resolution $\Delta\theta\gamma$ (mrad)	$\approx 40/\sqrt{E}$	-	-
Two shower separation $\Delta\theta\gamma\gamma$	≈ 5 mrad	-	-
Lateral granularity $\Delta\eta\times\Delta\phi$	0.025×0.025	0.1×0.1	(10×10 cm^2)
Longitudinal segmentation	2-fold	2-3-fold	3-fold
Depth	$\geq 25X_o$	$\geq 10\lambda$	$\approx 12\lambda$
Rapidity coverage	≤ 2.5	≤ 2.5	$2.5 \leq \lvert\eta\rvert \leq 5$
Timing	≤ 5 ns	≤ 5 ns	≤ 5 ns
Dynamic range (bits)	16	15	14-15
Radiation resistance			
dose (Mrad)	≈ 6 at $\eta = 2.6$	≈ 1.5 at $\eta = 2.6$	≈ 100
neutron fluence (n/cm^2)	1.3 10^{14}	6 10^{13}	$10^{16\text{-}18}$

Table 1.01 Performance requirements for the Calorimeters of CMS [2].

The radiation length of CeF_3 is 1.7 cm, this value translates to a tower height of 42.5 cm ($25X_o$), the total volume required in CMS is 26.4 m^3. At the quoted price ($2/cc), the cost of finished crystals would be ≈110 MCHF which is unacceptably high. This is the main factor which opposes the choice of CeF_3. The light yield of CeF_3 is a factor of ×10 higher than any of the competitors, this results in an energy resolution which is better than any of the other options,

$$\frac{\sigma}{E} = \frac{2.0\%}{\sqrt{E}} \oplus \frac{0.08}{E} \oplus 0.5\% \qquad (10 \leq E \leq 150 \text{ GeV}) \qquad \text{Equation 1.10}$$

Although pure CeF_3 is intrinsically very radiation hard (≥ 10 Mrad), impurities can lead to significant optical absorbance bands. Large single crystals are produced by the Bridgeman-Stockbarger technique which involves a seed crystal being withdrawn from a bath of molten high-purity CeF_3 at a rate of ≈ 1 mm per hour. As the crystal is withdrawn, CeF_3 is built onto the seed crystal, impurities predominantly remain in the melt. The impurity concentration in the melt increases as it becomes exhausted, eventually a significant proportion of impurities are included in the crystal. The impurity concentration in the crystal and hence the radiation tolerance can vary as a function of position along the crystal. To obtain single crystals radiation tolerant along their entire length, the *dirty* end has to be removed. Production of ultra-pure, long ($\geq$ 42.5 cm), single crystals is currently not possible. It is significantly easier to make crystals for a front/ back segmented calorimeter as the maximum single crystal length is reduced to only $\approx$ 25 cm, although growing 25 cm long single crystals is still technically difficult and expensive.

1.8.2. Lead Tungstate, $PbWO_4$

Although the cost per unit volume of $PbWO_4$ is expected to be only slightly cheaper than CeF_3, its radiation length (0.9 cm) is much smaller and consequently the volume required in a $25X_o$ calorimeter is reduced by $\approx$ 50%. Detector electronic noise has to be minimised for a calorimeter that uses this material as it has a marginal light yield (100γ/MeV). The energy resolution would be significantly deteriorated by punch-through of charged particles in the readout photodiode. This problem can be overcome by using $30X_o$ crystals or employing APDs as their sensitive thickness is small.

The light yield has been measured using small samples, test beam measurements of long single crystals obtained a yield more consistent with 50- 70γ/MeV. It is thought that the observed yield will increase as the purity and quality of the large single crystals improves. Complete recovery of radiation induced absorbance has been observed after irradiating small samples to 100 krad. The scintillation mechanism is highly quenched and displays a strong temperature dependence ($\approx$-1.9%/°C) at room temperature. The low yield necessitates the use of APDs, these are sensitive to the bias voltage and also temperature. Gain stability of 0.3% requires that the temperature is known to ±0.1°C, and the APD bias voltage is known to ±0.1V.

1.8.3. Pb/ Scintillator Electromagnetic Calorimeter

In an inhomogeneous design that has been proposed, the calorimeter modules are constructed from 2 mm thick lead tiles stacked alternately with 4 mm thick tiles of plastic scintillator. The scintillation light is read out via a number of WLS fibres which run along the entire length of the stack as shown in Figure 1.04. Tests have been performed using 4.7×4.7 cm^2 tiles in a 26 X_o configuration ($\leq$ 45 cm) read out with twenty-five, 1.2 mm diameter fibres doped with K27. A light yield of 10700 photons/GeV has been measured for a 3×3 matrix read out with silicon photodiodes, the energy resolution was,

$$\frac{\sigma}{E} = \frac{8.4\%}{\sqrt{E}} \oplus \frac{0.08}{E} \oplus 0.9\% \qquad (10 \leq E \leq 150\ \mathrm{GeV}) \qquad \text{Equation 1.11}$$

Shower particles passing down a WLS fibre detract from the lateral uniformity of this design, scans across the end face show clear dips in deposited energy corresponding to the fibre periodicity. The large number of components require accurate machining if the WLS fibres are to pass down the stack of >100 tiles, and if the hermeticity is not to be compromised. The process of light coupling into the WLS fibres and the intrinsic inefficiency of the WLS process deteriorate the light yield for this design. Consequently the energy resolution is inferior to the homogeneous options and the performance with respect to the Higgs→$\gamma\gamma$ is less good.

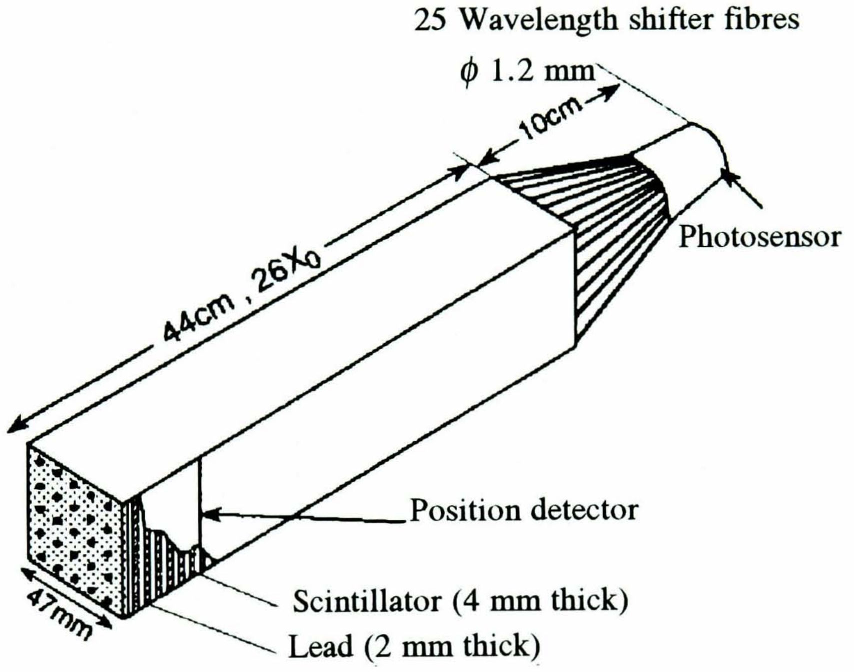

Figure 1.04 Schematic drawing of the CMS Pb/scintillator prototype module [2].

From the outset, the Pb/scintillator option offered several significant advantages, the most outstanding feature was the overall cost, especially if a non-projective design could be tolerated. The materials are readily available and relatively inexpensive. Although a large number of components are required to produce each module, the individual machining operations are simple. A non-projective geometry would require many thousands of identical modules (and hence $\approx 5\times10^6$ identical tiles), partially projective solutions would require some variations in the module geometry. The production cost of a fully projective ECAL involving significant variations on the machining of $\approx 5\times10^6$ tiles would counteract the benefit in material costs for the Pb/scintillator option.

Scintillators able to withstand doses of ≥ 5 Mrad suffering only 10% loss in light yield are available [12]. Further development of radiation tolerance of the WLS fibres have identified systems which suffer only 10% net reduction in light yield after doses of several Mrad [13]. Radiation tolerance in this design is intrinsically good, with no additional development, the rapidity range $|\eta| \geq 2.2$ could be covered. End plugs covering $2.2 < |\eta| \leq 2.6$ which were changed after 3-5 years would have to be used in the absence of further progress in radiation tolerance.

A Pb/scintillator calorimeter would work in an LHC environment with minimal further development although, the physics performance of a WLS option would never rival a viable homogeneous calorimeter due to the poor light yield. The value quoted above, 10700 photons/GeV, is down by a factor of ×150 compared to crystalline CeF_3 in a similar configuration.

Property		CeF_3	$PbWO_4$	HfF_4 Glass	Pb/scint
Radiation length	cm	1.7	0.9	1.6	1.7
Molière radius	cm	2.6	2.0	2.8	3.4
Density	g/cm^3	6.2	8.3	6.0	4.5
Photon Yield	γ/MeV	1500	100	165	13
τ (short)	ns	9	≤10	8	≤10
(long)	ns	32	36	25	-
% Light in 25 ns		50	85	70	≈ 100
Peak wavelength	nm	325	480	325	500
Temp.dependence of light yield	%/°C	0.15	-1.9	-0.39	-
Index of refraction		1.6	2.2	1.5	-
Radiation Hardness	Mrad	≈10	?	?	1
Vol. for 25 X_o, $|\eta| \leq 2.5$	m^3	26.3	12.5	24.5	26.3

Table 1.02 A comparison of the properties of crystals, glasses and the Pb/scintillator calorimeter options [14].

1.9. Glasses

1.9.1. Advantages of glasses over crystals

Production of a significant volume of large single crystals requires a substantial initial investment, it is slow, and has high running costs. It has been estimated that to purchase the furnaces and crystal drawing equipment to produce 26 m^3 of CeF_3 will require an initial investment of 25 MCHF, the production time scale is five years. In contrast a suitable glass calorimeter could be produced at a fraction of the cost, and on a shorter time-scale as much of the production infrastructure already exists. The blocks could be cast rapidly in fractionally oversized moulds and would require only minimal machining. The spending profile would be more favourable as the Bridgeman-Stockbarger crystal drawing equipment would not be required. A shorter production time scale would allow more time for R&D.

Glasses are cast in a single operation from one batch of molten material. Large single blocks are potentially less susceptible to variation in radiation tolerance along their length as they are more homogeneous than crystals. There is large scope for compositional optimisation in glasses whereas in crystals, in the main, it appears that radiation tolerance (for example) can only be improved by increasing the purity of the crystal.

1.9.2. Candidate glasses-current state of the art

Radiation damage studies have been performed on silicate glasses over a period of many years [15]. The majority of this work has concentrated on identifying the defect structures in silicate glasses. A *tool* which identifies if a particular defect is associated with electrons or holes is to dope with Ce^{3+}, a hole acceptor. If the radiation induced absorbance improves in the Ce doped glass, the implication is that, the defects are of the hole variety. This analytical *trick* has also been utilised in developing glasses suitable for use in severe radiation environments. In the silicate matrix Ce causes the UV edge to occur around 400 nm hence, radiation hard silicate glasses tend to be yellow in colour. Experimental techniques have been well developed for these types of investigations.

A general feature of the silicate matrix is that the density does not generally exceed 4 gcm^{-3}, doping with Pb can surpass this value but Pb generally detracts from the radiation tolerance in these glasses. Although a great deal of careful and convincing work has been performed using the silicate matrix [15], the materials identified have insufficient densities (see Table 6.01).

Over the last 10- 15 years, the demand for low loss optical fibres has stimulated new research into glasses based on the fluoride glass matrix. These have a transmission window that extends from the IR to a wavelength of 200 nm. The glass has other optical applications as it acts as an excellent host for rare-earth and transition metal ions. For ultra low intrinsic IR absorbance, the investigations have focused on a ZBLAN composition, in addition to its wide optical window, it is relatively resistant to chemical attack, has a suitable refractive index, and can be drawn into fibres. Some work has been carried out into the radiation resistance of this material as part of the general characterisation for optical fibre applications. The density of zirconates is $\approx$ 4 gcm^{-3}, which is too low for the LHC.

Replacement of Zirconium (Zr) with Hafnium (Hf) improves the density of fluoride glasses to $\approx$ 6 gcm^{-3} without adversely affecting any of the other physical properties. The transmission window in non-cerium doped glasses extends to 200 nm, Ce doping shifts the UV edge to ≈ 300 nm.

1.10. Statement of the aims:

At the beginning if this program of work, a specific aim was to assess the suitability of Heavy Metal Fluoride (HMF) glasses as candidate scintillators for the ECAL of CMS. There is an exacting list of standards which a successful material must satisfy. These requirements have been stated in the previous discussion of potential candidates. Studies were required to determine how closely HMF glasses conformed, and to develop new compositions which satisfied the criteria more exactly. As the composition of glasses can be varied widely, there is a large *variable-space* to be investigated. Specific aims were:

- **Radiation tolerance:** To evaluate the development of optical absorbance in these glasses when subjected to a realistic LHC radiation environment. To study the effects of compositional variation on radiation susceptibility, and devise strategies for minimising damage.
- **Scintillation Emission:** To determine the light yield for representative configurations (large blocks) using a realistic excitation source (test beam). Also to measure the time structure, the temperature dependence of light output, and the scintillation emission spectra of these glasses.
- **Other Physical Properties:** Knowledge of the radiation length, Molière radius, density, refractive index, susceptibility to chemical attack and mechanical properties are all important when assessing the suitability of HMF glasses for the CMS application.
- **Production:** Research and development into the technology required to produce large single blocks of this generic family of glasses.
- **Costing:** It is necessary to obtain a realistic estimate for the Western costing of large quantities (24.5 m^3) of this material. This involves determining the factors which dictate the cost, and devising strategies for minimising the overall expense. To compete effectively with CeF_3, a target price of $1/cc has to be realised.

---

[1] Design Study of the Large Hadron Collider, CERN 91-03.

[2] The Compact Muon Solenoid Letter of Intent, CERN/LHCC 92-3, LHCC/I 1, 1992.

[3] J.F. Gunion et al., *The Higgs Hunters Guide*, Addison Wesley Publishing Company, p162.

[4] P. Lecoq, CERN-PPE / 91-231.

[5] E. Segre, *Nuclei and Particles*, The Benjamin/ Cummings Publishing Company.

[6] WWW, "http://cmsinfo.cern.ch/cmsinfo/Welcome.html"

[7] M.G. Albrow et al., *Nucl.Instr. Methods*, **A256** (1987) 23.

[8] I. Kudla et al., *Nucl. Instr. Methods*, **A300** (1991) 480.

[9] E. Clayton et al., CMS TN / 92-50.

[10] J. Streibig, CMS TN / 92-41, 1992.

[11] K. Ahmet et al., *Nucl. Instr. Methods*, **A305** (1991) 275.

[12] V.V. Brekhovskikh et al., IHEP 91-164, 1991, Protvino, Russia.

[13] Solenoidal Detector Collaboration, Technical Design Report, SDC-92-201, 1992.

[14] T.S. Virdee, CMS TN / 94-31.

[15] A. Bishay, *J.Non-Cryst.Solids*, **3** (1970) 54.

CHAPTER TWO

Radiation Damage Studies in Heavy Metal Fluoride Glass

2.1. Introduction

Since the discovery of Heavy Metal Fluoride (HMF) glasses, radiation damage studies have been performed on a wide variety of principally Zirconium based glasses. In contrast to similar studies on alkali halide crystals in the 1950s, where the principal motivation was to gain a fundamental understanding of the underlying processes which were occurring, the present investigations are more strongly motivated by the potential applications of this exciting class of material. Of course, to identify the most promising compositions, a thorough understanding of the radiation induced defects is still required.

There are two mechanisms responsible for the formation of stable defects in HMF glasses; atoms are displaced from their initial positions by direct collisional impact (knock-on) and also by the non-radiative decay of an exciton (radiolysis). The majority of damage is thought to be caused by the latter process [1]. Radiolysis results in the formation of Frenkel pairs, these are composed of an interstitial atom and a vacancy. Much of the theoretical work which has postulated radiation damage in glasses by radiolysis has come from earlier studies on alkali halide crystals.

Frenkel pairs introduce new energy levels into the glass. These are located in the forbidden energy gap. Transitions from the valence band to empty trap levels or from populated trap levels to the conduction band can be achieved by absorption of optical radiation. This leads to degradation in the macroscopic absorbance of the glass. Radiation induced optically active sites are known as *colour centres* as their presence alters the absorbance spectrum and hence the colour of the glass.

After irradiation has ceased, improvements in optical transparency with time are observed as the induced damage recovers. This *annealing* at room temperature is attributed to recombination of Frenkel pairs. Thermal annealing of defects is explained by Frenkel pairs becoming mobile above a specific energy threshold and then recombining.

Over the last decade, Electron Spin Resonance (ESR) and optical studies have been used extensively to definitively identify many defect species which are produced by irradiation.

2.2. Nature of Radiation

2.2.1. Radiation Type

There are sources of radiation to which all materials are exposed, including natural radioactivity and Cosmic rays. The additional exposure which HMF glasses experience, depends upon the environment in which they are deployed. The barrel region of the electromagnetic calorimeter in the CMS detector of the Large Hadron Collider is one potential application of HMF glasses. This is an extremely severe radiation environment [2]. The high energy secondary particles and showers result in a dose profile shown in Figure 2.01. The neutron flux is expected to reach 10^{14} n cm^{-2} over the 10 year operational lifetime of the detector, assuming a design luminosity of 10^{34} cm^{-2} s^{-1}.

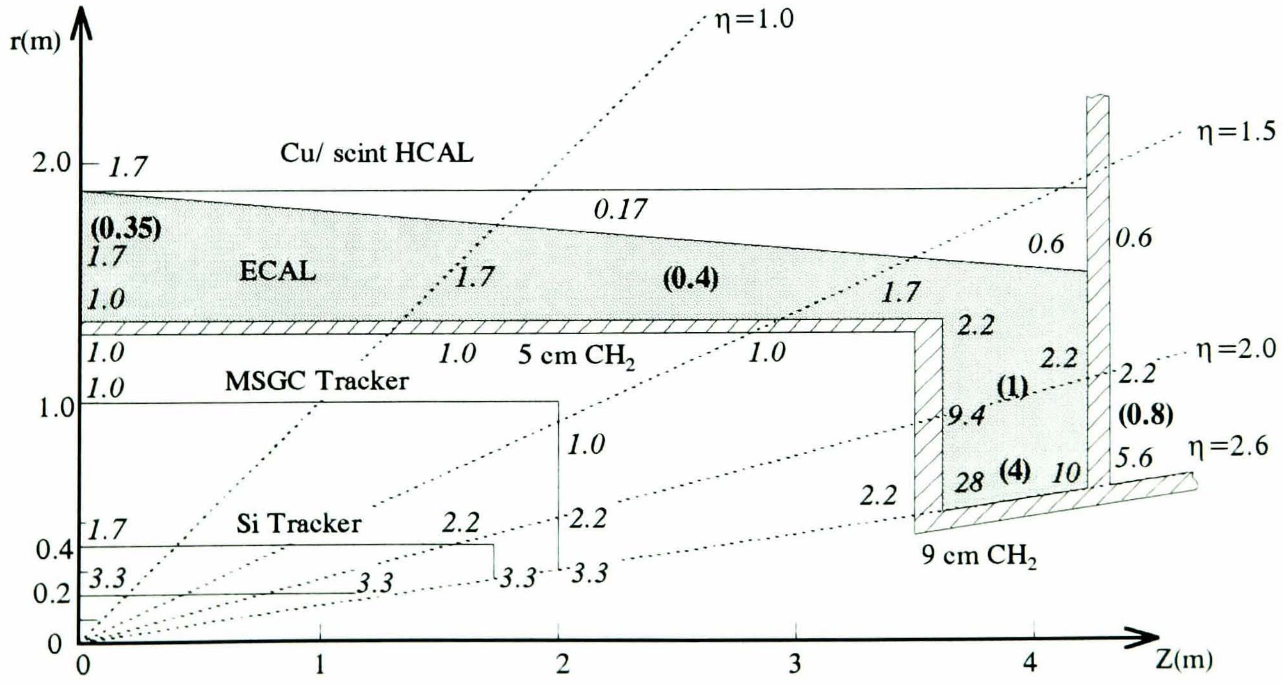

Figure 2.01 Neutron fluence and dose in CMS. The italicised numbers in the figure are the fluence in units of 10^{13} n/ cm^{2}. Numbers in brackets are the dose in Mrads. These numbers are given for an integrated luminosity of $L=10^{42}cm^{-2}$, corresponding to 10 years of running at design the luminosity [2].

In order to understand the creation of radiation induced damage in the HMF glass matrix, it is essential to be familiar with the underlying mechanisms by which the various sources of radiation interact. The fundamental interactions which result in the deposition of energy in materials are discussed below. They are subdivided into charged and uncharged interactions. Charged radiations are further separated into heavy charged particles and high energy electrons. Uncharged radiations are divided into photons and neutrons. Comprehensive reviews of the interaction of radiation with materials are found in many text books [3 , 4].

2.2.2. High Energy Charged Particles

In this discussion heavy charged particles include protons, alpha particles and larger fragments of atoms. Their primary interaction is through Coulomb forces between their positive charge and the negative charge of orbital electrons of the absorber atoms. As a result of Coulomb interactions, orbital electrons may be excited to higher energy levels within the atom or escape completely resulting in ionisation of the atom. In any one interaction, the energy lost to an orbital electron is a small fraction of the incident kinetic energy.

In passing through an absorbing medium, the heavy charged particle interacts simultaneously with many electrons, which reduce its velocity continuously. In very close encounters, the ejected electron may have sufficient energy to cause further ionisation. These electrons are known as delta rays and represent a secondary mechanism by which energy is transferred to the absorber.

The specific energy loss due to ionisation is given by the classical expression known as the Bethe formula,

$$-\frac{dE}{dx} = \frac{4\pi e^4 z^2}{m_o v^2} NB \qquad \text{Equation 2.01}$$

where,

$$B \equiv Z\left[\ln\frac{2m_o v^2}{I} - \ln\left(1-\beta^2\right) - \beta^2\right] \qquad \text{Equation 2.02}$$

In this equation v and ze are the velocity and charge of the primary particle, N and Z are the density and atomic number of the absorber atoms, m_o is the electron rest mass and e the electronic charge. I represents the average ionisation potential of the absorber and is determined experimentally. $\beta \equiv v/c$.

Direct collisional impact with the absorber nuclei is a second mechanism by which heavy charged particles interact. Due to the similarity in mass between light nuclei and the incident particle, it is possible to transfer a significant fraction of the incident kinetic energy to the recoil nuclei. This results in the incident particle scattering through an angle, θ. The differential cross-section is described for non-relativistic protons by classical Rutherford scattering.

$$\frac{d\sigma}{d\Omega} = \frac{1}{4}\left(\frac{Ze^2}{mv^2}\right)^2 \frac{1}{\sin^4(\theta/2)} \qquad \text{Equation 2.03}$$

In the equation above, m and v refer to the mass and velocity of the incident proton. Rutherford scattering can result in a drastic change in the path of the incident particle. Energy transfer to the recoil nuclei can result in displacement damage in the absorber.

2.2.3. Fast Electrons

When fast electrons pass through absorbing materials they interact with orbital electrons of the absorber. It is possible to transfer a large fraction of the incident electrons energy to individual target electrons as they have the same mass. This results in the incident electron following an erratic path. In addition, elastic scattering with target nuclei occurs. Bethe derived an equation for the specific energy loss of fast electrons due to collisional processes, this is similar to the Bethe formula for heavy charged particles.

$$-\left(\frac{dE}{dx}\right)_c = \frac{2\pi e^4 NZ}{m_o v^2}\left(\ln\frac{m_o v^2 E}{2I^2\left(1-\beta^2\right)} - (\ln 2)\left(2\sqrt{1-\beta^2}-1+\beta^2\right) + \left(1-\beta^2\right) + \frac{1}{8}\left(1-\sqrt{1-\beta^2}\right)^2\right)$$

Equation 2.04

The symbols have the same meaning as in the Bethe formula.

From classical theory, when a charge accelerates, which an electron does in the violent interactions along its path, it radiates Bremsstrahlung (braking) electromagnetic radiation. The linear specific energy loss for radiative processes is given by the equation,

$$-\left(\frac{dE}{dx}\right)_r = \frac{NEZ(Z+1)e^4}{137m_o^2c^4}\left(4\ln\frac{2E}{m_oc^2} - \frac{4}{3}\right) \qquad \text{Equation 2.05}$$

E and Z^2 in the numerator mean that the radiative loss is more significant at high energies, in materials with a high atomic number. The total linear stopping power is the sum of the collisional and radiative components,

$$\frac{dE}{dx} = \left(\frac{dE}{dx}\right)_c + \left(\frac{dE}{dx}\right)_r \qquad \text{Equation 2.06}$$

The interactions of fast electrons with orbital electrons of the absorbing material cause electronic excitation and ionisation. In addition, the collision of a fast electron with a lattice atom can result in a displacement. However, to transfer sufficient displacement energy ($>$10 eV), the electron must be highly energetic (100 keV). Collisions which result in displacements involve relativistic electrons scattering elastically in the Coulomb field of the atom.

From relativistic kinematic calculations, assuming pseudo-elastic collisions, it is possible to calculate, for an electron of mass m_o, the maximum kinetic energy which can be transferred to a stationary atom of mass, M by direct impact. The incoming particle has an initial kinetic energy E, the energy transferred to the atomic nucleus is denoted, T.

$$T = 2\frac{m_o}{M}\frac{\left(E + 2m_o c^2\right)E}{m_o c^2} \qquad \text{Equation 2.07}$$

Head-on collisions transfer the maximum energy to the atom. For glancing collisions, the energy transferred is reduced from its maximum value by a factor of,

$$\sin^2\left(\frac{\theta}{2}\right) \qquad \text{Equation 2.08}$$

The vast majority of collisions will be glancing. The differential cross-section was originally derived by Rutherford. This analysis considered non-relativistic particles. Darwin [5] reworked the analysis to obtain the relativistic expression suitable for scattering of classical electrons.

$$d\sigma_{DR} = \pi\left(\frac{Ze^2}{mc^2}\right)^2\left(\frac{1}{\beta^4\gamma^2}\right)\cos\frac{\theta}{2}\csc^3\frac{\theta}{2}d\theta \qquad \text{Equation 2.09}$$

For classical (relativistic) mechanics to apply, the condition, $\alpha > 1$, has to be satisfied where,

$$\alpha \cong \frac{Z}{137} \qquad \text{Equation 2.10}$$

This condition is not satisfied for most stable atoms. Consequently, it is necessary to treat relativistic electron scattering quantum mechanically. The de Broglie wavelength of relativistic electrons is small compared to the distance of closest approach in an interaction. Mott [6] derived the formula which is the sum of two convergent series. This can be incorporated as a correction factor, R in the Darwin Rutherford differential cross-section.

$$d\sigma_m = R d\sigma_{DR} \qquad \text{Equation 2.11}$$

R is a function of the atomic number (Z), β and θ. McKinley and Feshbach [7] derived an approximation for R which is valid for low Z elements

$$R_{McF} = \left(1-\beta^2 \sin^2\frac{\Theta}{2} + \alpha\beta\pi \sin\frac{\Theta}{2}\left(1-\sin\frac{\Theta}{2}\right)\right) \qquad \text{Equation 2.12}$$

Θ is the electron scattering angle in the centre-of-mass frame. $\theta \approx \Theta$, when the velocity of the centre of mass for the collision is very much smaller than the incident electron velocity,

$$d\sigma_{McF} = R_{McF} d\sigma_{DR} \qquad \text{Equation 2.13}$$

The McKinley Feshback correction to the Darwin Rutherford differential cross-section is used in Section 2.3.2, where knock-on damage specific to HMF glasses is discussed.

2.2.4. Cerenkov Radiation

If a charged particle moves through a material whose refractive index is n, its electric vector propagates with a velocity c/n. If the particle moves faster than the velocity of the electric field, the equivalent of a *bow wave* is emitted as shown in Figure 2.02

$$\beta c > \frac{c}{n} \qquad \text{Equation 2.14}$$

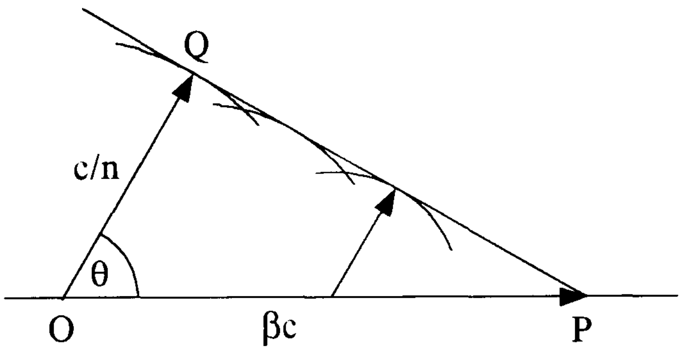

Figure 2.02 This shows the Hugens' construction for electromagnetic waves emitted by a moving charged particle. This is the source of Cerenkov radiation.

In the time that it takes for the charged particle to move from O to P, the electromagnetic wave emitted at O reaches a point Q on the bow wave. The direction of propagation of the electric vector means that the corresponding light makes an angle φ= $\cos^{-1}(1/n\beta)$ with the trajectory of the particle. The amount of light emitted per unit length in the frequency interval dv is,

$$dN = \frac{2\pi e^2}{\hbar c}\left(1-\frac{1}{n^2\beta^2}\right)\frac{dv}{c} = \frac{2\pi e^2}{\hbar c}\sin^2\theta\frac{dv}{c} \qquad \text{Equation 2.15}$$

Cerenkov radiation is emitted in the spectral range from the UV cut-off of the material to 600 nm. The intensity of Cerenkov radiation when a charged particle passes through a typical scintillator is significantly smaller than the amount of scintillation light produced.

2.2.5. Photons

Photons interact in all materials by three processes, *photoelectric absorption, Compton scattering* and *pair production*. These transfer a significant fraction or all of the photon energy to electron energy. The incident photon either disappears completely or scatters through a significant angle. The predominant interaction mechanism depends on the photon energy and also the Atomic number, Z of the absorbing material.

Photoelectric Absorption. The incident photon interacts with an atom and disappears. Its energy is transferred to a bound orbital electron which is ejected from the atom with an energy, E_{e^-}.

$$E_{e^-} = h\nu - E_b \qquad \text{Equation 2.16}$$

E_b represents the binding energy of the ejected photoelectron in its original shell. For gamma rays of sufficient energy, the interaction occurs with the most tightly bound (K shell) electron. The ionised absorber atom is rapidly filled by capture of a free electron or by filling from outer shells of the atom. For high energy photons, the majority of the photon energy is transferred to the photoelectron. Photoelectric absorption is the predominant interaction mode for relatively low energy gamma-rays. The effect is enhanced in high Z absorbers.

Compton Scattering. When an incident gamma photon interacts with an electron it is deflected through an angle, θ. The recoil electron can potentially carry off a significant fraction of the gamma-ray energy. Equations involving energy and momentum conservation give the scattered photon energy as a function of the scattering angle, θ.

$$h\nu' = \frac{h\nu}{1 + \frac{h\nu}{m_0c^2}(1-\cos\theta)} \qquad \text{Equation 2.17}$$

When the scattering angle is zero, the photon loses least energy. Even for the extreme case of θ = 180°, the photon still retains a fraction of its incident energy. The angular distribution of scattered gamma rays is predicted by the Klein-Nishina formula [3], the differential cross-section scales linearly with Z.

$$\frac{d\sigma}{d\Omega} = Zr_o^2\left(\frac{1}{1+\alpha(1-\cos\theta)}\right)^2\left(\frac{1+\cos^2\theta}{2}\right)\left(1+\frac{\alpha^2(1-\cos\theta)^2}{(1+\cos^2\theta)(1+\alpha(1-\cos\theta))}\right)$$

Equation 2.18

where $\alpha \equiv h\nu / m_0 c^2$ and r_o is the classical electron radius. There is a high probability of forward scattering at high gamma-ray energies.

Pair production. This interaction is dominant at high gamma-ray energies. It takes place in the Coulomb field of a nucleus and results in the production of an electron-positron pair. This process has an energy threshold of twice the rest mass of an electron (1.02 MeV), but is improbable until the gamma-ray energy reaches several MeV. In the interaction, the incident gamma-ray disappears, excess energy above 1.02 MeV is carried off as kinetic energy of the charged pair. Two 511 keV photons are subsequently produced when the positron annihilates. The probability of interaction via pair production scales approximately as the square of the Atomic number, Z.

The relative importance of each interaction mechanism is illustrated in Figure 2.03 [3], as a function of Z and gamma-ray energy. The left and right curves represent the energy at which the photoelectric and Compton cross-sections are equal and the energy at which the Compton and pair-production cross-sections are equal, respectively. The three areas in the graph represent where photoelectric absorption, Compton scattering and pair production are each the predominant interaction mechanism.

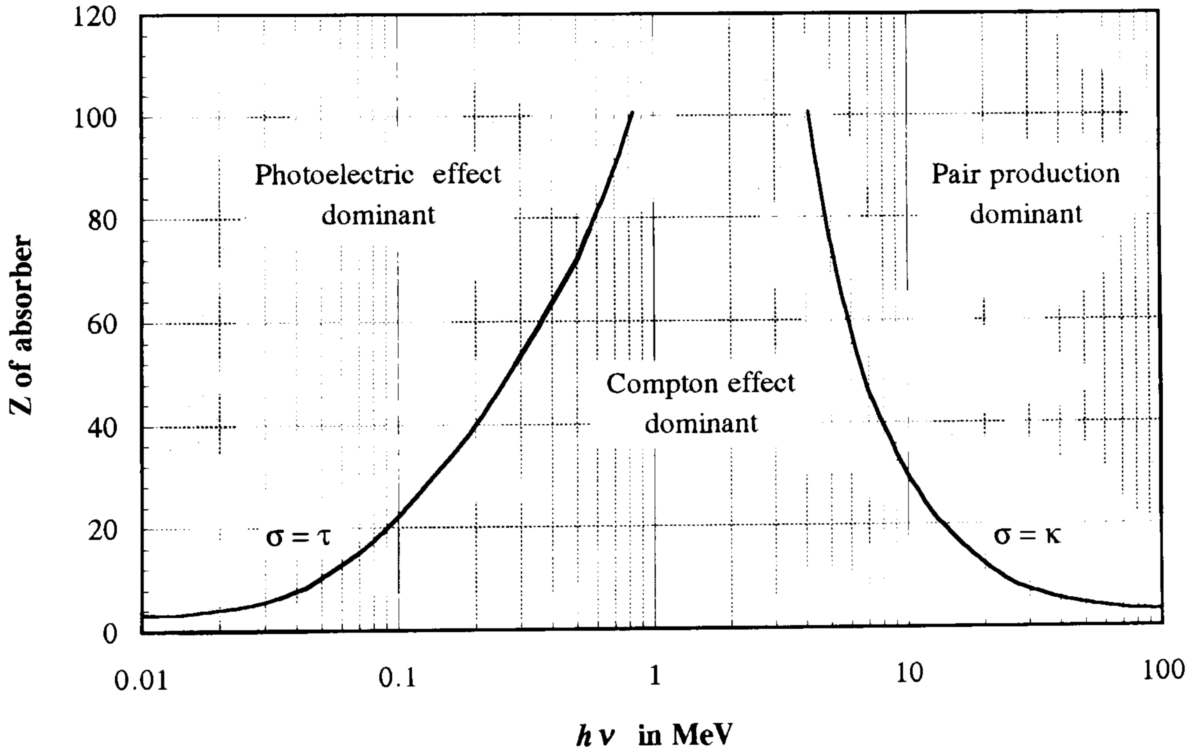

Figure 2.03 The relative importance of the three major types of gamma ray interactions. The lines show the values of Z and $h\nu$ for which the two neighboring effects are just equal [3].

2.2.6. Neutron

Neutrons are uncharged and hence do not interact in the Coulombic fields of atoms. They suffer collisions with nuclei of the absorber material. Elastic collisions can result in the neutron transferring a significant fraction of its energy to a charged recoil nuclei. Inelastic scattering results in the nucleus being excited to a higher energy state. Subsequent de-excitation is accompanied by the emission of a high energy gamma photon. Neutron-induced nuclear reactions are also possible.

The discussion concerning the relatively efficient transfer of energy between high energy charged particles and absorber nuclei (Section 2.2.2) is also pertinent to neutron irradiations due to the similarity between the absorber nuclei mass and that of a neutron.

For neutrons of a fixed energy, the probability of interaction per unit path length via the processes mentioned above, is constant. It is customary to define a cross-section per nuclei for each process. Multiplication by the number of target nuclei per unit volume gives the macroscopic cross-section,

$$\Sigma = N\sigma \qquad \text{Equation 2.19}$$

The total cross-section is the sum of the cross-sections for each process,

$$\Sigma_{tot} = \Sigma_{scatter} + \Sigma_{rad.capture} + \ldots \qquad \text{Equation 2.20}$$

Σ_{tot} is the probability per unit path length that any interaction will occur. It is equivalent to the linear absorption coefficient for gamma rays. Most of the damage caused by neutron irradiation results from the subsequent interactions of charged primary knock-on atoms displaced by incident neutrons [8].

2.3. Radiation Damage in Glasses

2.3.1. Radiation Interaction

Section 2.2 has shown that protons, neutrons and even high energy electrons can transfer significant energy to individual nuclei in addition to causing electronic excitation in the target material. The resulting displacement damage and subsequent interactions of the displaced atoms, can result in permanent changes in atomic structure. Induced damage in HMF glasses occurs as a consequence of two processes. Direct transfer of momentum from the impinging particle to a lattice atom can displace the stationary atom from its site, (knock-on). Also excitation of atomic electrons by ionising radiation can result in the formation of displacements. This latter process is known as *radiolysis*.

2.3.2. Knock-on Displacement

In this section the feasibility of atom displacement by knock-on processes resulting from ^{60}Co irradiation is considered. The 1.332 MeV and 1.173 MeV photons interact predominantly via the Compton process as shown in Figure 2.03. The energy spectrum of primary recoil photons has a Compton edge at ≈ 960 keV, but most have energies significantly below this. They principally interact photoelectrically. To understand the variation of displacement cross-section with electron energy, consider initially a mono-energetic electron irradiation, the scope of the discussion will later be extended to include a range of electron energies as observed in the ^{60}Co recoil electron spectrum.

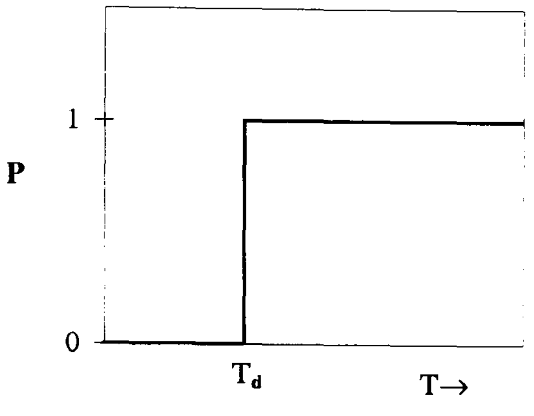

Figure 2.04 Displacement probability function, P for an isotropic square well potential of depth T_d, the threshold recoil energy.

Consider initially a simple displacement model, in which the material contains only one atomic species and each atom is in an identical environment. To displace a lattice atom from its site, requires a transfer of kinetic energy, T above some threshold value T_d. The probability distribution is shown in Figure 2.04. For energy transfers below T_d, the struck atom is never displaced, above T_d, the atom is always displaced. In non-metals, displacement energies depend on the bond strength, the local environment of the interstitial, and the electronic configuration which the interstitial adopts. For charged interstitials, there may be a contribution from electrostatic repulsion.

In highly ionic crystals, the bonding energy is given by the lattice Coulomb energy.

$$E_l = \frac{\alpha(r)(ze)^2}{4\pi\varepsilon r} \approx 8z^2(\mathrm{eV}) \qquad \text{Equation 2.21}$$

$\alpha(r)$ is the Madelung constant, (ze) the lowest common ion charge, ε the permittivity, and r the characteristic nearest-neighbour separation. The z^2 term means that singly ionised atoms have the lowest activation energies. In non-metals, the displaced atom may alter its charge state as it departs thus altering the Coulomb interaction term in the displacement energy equation.

The cross-section for atom displacement resulting from electron irradiation is the integral of the product of the atom displacement probability and the differential cross-section. Due to the dependence of the energy transfer with scattering angle, the differential cross-section is integrated from a minimum up to 180°. The form of cross-section verses energy is shown in Figure 2.05.

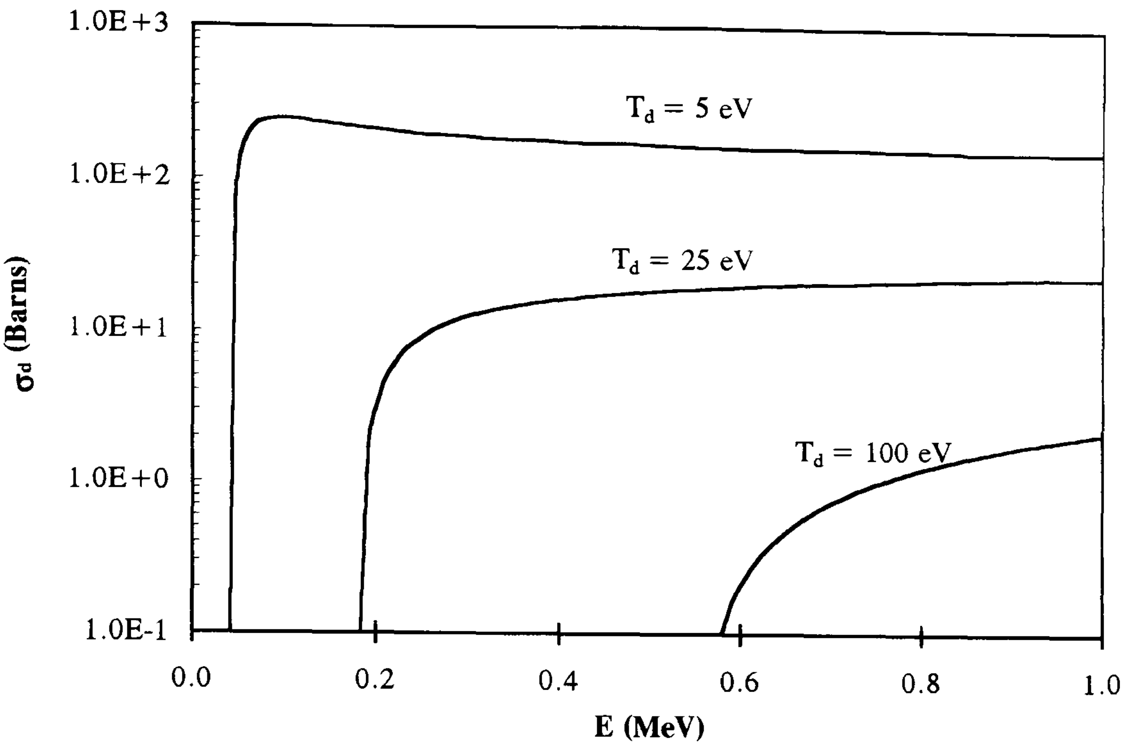

Figure 2.05 Cross-section for atom displacement, σ_d for Fluorine vs. electron kinetic energy, E for various step fnction energies, T_d.

The data has been calculated using the McKinley and Feshbach differential cross-section,

$$\sigma_{McF} = \pi\left(\frac{Ze^2}{mc^2}\right)^2\left(\frac{1}{\beta^4\gamma^2}\right)\left[\left(\frac{T_m}{T_d}-1\right)-\beta^2\ln\frac{T_m}{T_d}+\pi\alpha\beta\left\{2\left[\left(\frac{T_m}{T_d}\right)^{\frac{1}{2}}-1\right]-\ln\frac{T_m}{T_d}\right\}\right]$$

Equation 4.22

T_m is the maximum kinetic energy which an incident electron can transfer to an atom in a single collision. The absolute cross-section depends strongly on the value of T_d. Below threshold, it is not possible to displace the atom due to kinematic constraints. At threshold, the cross-section is relatively small as only head-on collisions can cause displacements. As the electron energy is increased the interaction cross-section increases as collisions of a more glancing nature are able to displace atoms. The different curves represent different step-function threshold energies, T_d.

In reality, the model incorporating a single displacement energy, T_d is over simplistic. Even for a sample which contains only one species, the displacement energy depends on the recoil direction of the displaced atom and also the type of defect configuration which results. Recombination of close Frenkel pairs, tends to round-off the T_d edge. This effect is accentuated in non-metal solids due to the long range Coulomb interaction. The probability of separated Frenkel pairs recombining is higher than in metals, for instance. In reality, a range of T_d values will be observed, more complicated probability profiles have been modelled [9 ,10].

In simple (ZBLAN) fluoride glasses, the singly charged Fluorine atom has the lowest binding energy as it is the smallest ion and is singly charged. Although it has not been possible to obtain the displacement energy for a Fluorine ion in the HMF glass matrix, the values for carbon in graphite (20 eV), and diamond (80 eV) are informative [11]. If the displacement energy for a Fluorine ion is 40 eV, impinging electrons with energy in excess of 275 keV are able to cause atomic displacements.

The Compton energy spectrum for ^{60}Co contains a significant fraction of recoil electrons whose kinetic energy exceeds 275 keV. Displacement damage involving the Fluorine ion is possible in HMF glasses as a consequence of ^{60}Co irradiation. However, it is worth emphasising a point made in Section 2.2.3; the energy transfer of fast electrons is predominantly to orbital electrons in the form of electronic excitation and ionisation. Only a small fraction of energy is dissipated in direct knock-on processes.

2.3.3. Radiolysis

Irradiation causes significant excitation and ionisation of the absorbing medium. The vast majority of electrons promoted to the conduction band rapidly thermalise, bind to hole states and recombine. Their energy is emitted as photons or dissipated to the lattice as phonons. A small fraction become separated and trapped at either electron or hole trapping sites, such as diamagnetic imperfections, or multi-valent impurity atoms. Electrons or holes can also become trapped by the spontaneous relaxation of a normal lattice site. This process is known as *self-trapping*.

An exciton is an excited bound combination of an electron with a hole, these move rapidly through the glass matrix interacting weakly. When self-trapping occurs, the exciton is localised and recombination can liberate, in a single interaction, energy packets in excess of the band gap of the absorber [11]. In certain materials, this energy can be transferred very efficiently to individual nuclei. Atomic displacements result if the energy transferred is above some threshold value characteristic of the material. *Radiolytic* damage describes the process where atomic displacements are created during irradiation by the non-radiative recombination of electron/ hole pairs.

Radiolysis can lead to permanent atomic displacements in a range of inorganic scintillators (halides, hydrides, azides, many silicates, ice, carbonates, chlorates and bromates). In many materials, radiolysis is the dominant mechanism of defect creation. Transfer of energy to electronic excitation can be more efficient than knock-on displacement. Hence more energy is available to cause displacements via radiolytic processes.

There are four criteria which facilitate the efficient transfer of electronic excitation energy to the displacement of lattice atoms. Firstly, the electronic excitation must be localised to one atomic site in the lattice. Secondly, the excitation must be associated with the target site for a period comparable to the phonon period in order to couple energy to the lattice. The energy criterion $T \geq T_d$ must be satisfied. Lastly, the energy transfer must be kinematically feasible and compete favourably with other excitation decay modes. e.g. luminescent recombination.

Radiolysis is not favoured in metals as the conduction band delocalises the excitation energy in times ≈ 1 fs. In semiconductors, the forbidden gap is relatively narrow (≈ 4 eV); electronic excitations are usually not able to form radiolytic defects due to the energy criterion. In contrast, insulators which have a wide band gap are ideal candidates for radiolysis. Optical de-excitation is usually in the form of slow phosphorescence. Ionisation of deeper-lying electrons leaves relatively immobile holes in the valence band. With no alternative electron trapping sites, the excited electrons must eventually recombine with trapped holes. The de-excitation of these localised exciton states can potentially transfer a substantial fraction of the energy to radiolytic processes.

As has already been mentioned in the section discussing knock-on processes, the displacement energy scales with the square of the common ion charge. Radiolysis is likely only for univalent anions as these have the lowest Coulomb binding energies. In HMF glasses, there is a large body of evidence [1, and references cited within] to support the theory of defect formation by the radiolytic process, as found in alkali halides. This is in contrast to damage in alkaline earth halides which occurs as a result of electron and hole trapping at the site of substitutionally trivalent cations [12].

2.3.4. Annealing

Irradiation can create copious defects in materials. The nature and spatial distribution of defects depends on the irradiation conditions. At a low enough temperature, the defects are immobile. As the temperature is raised, a point is reached where the interstitials and vacancies become mobile. There is evidence from studies in metals and semiconductors that interstitials become mobile at lower temperatures than vacancies.

There are several different processes which may occur when interstitials become mobile.

1) The interstitial may recombine with a vacancy.
2) An impurity atom may trap the interstitial atom.
3) The interstitial may become trapped at a physical defect. e.g. a surface.

4) The interstitial may interact with another interstitial leading to the aggregation of interstitials.

As the temperature is raised further, vacancies also become mobile, they are able to participate in vacancy versions of processes 1- 4. Differences in the local environment of trapped vacancies and interstitials lead to a range of thermal stabilities for defects. It is clear that the processes which result in annealing of Frenkel pairs are extremely complex. Irradiation of chemical compounds can result in a variety of different interstitial and vacancy species. The complexity of annealing outlined above means that a fully theoretical understanding is not currently possible.

The annealing behaviour of defects can be modelled. Consider the example of a homogeneous sample irradiated at low temperature using ^{60}Co photons. This results in Frenkel pairs randomly distributed through the sample. For the irradiation considered, the interstitial and vacancy of each Frenkel pair will be relatively close to each other. In addition, the density of defects will be sufficiently low that the mean distance between Frenkel defects is large compared to the mean distance between Frenkel pairs.

As defects become mobile, if there is sufficient interaction, the interstitial may move towards the vacancy and recombine. Otherwise, the interstitial will move in a random direction which may result in the pair becoming further separated. The former category are known as *close pairs,* the latter are *free*. Close pairs anneal independently of each other, the number which recombine obeys a simple differential equation. The rate constant consists of a Boltzmann term whose numerator is an energy threshold for migration.

Integration yields a decreasing exponential which describes the fall from an initial number of close pairs with time. After all of the close pairs have annealed, only free pairs are left. The radial distribution of interstitials from their vacancies will be indicative of the irradiation details. The common feature is the absence of interstitials within a certain capture radius of the vacancy due to close-pair annealing.

2.4. Review of Radiation Damage Studies in Fluoride Glasses

2.4.1. Introduction

There are many applications for optical components in radiation environments. Communications optical fibres are required to operate under a continual, low-rate irradiation from natural sources. Military systems should continue working after receiving doses associated with a nuclear explosion. Bulk optical components must continue to function in, for example, nuclear reactor instrumentation and 'hot-cell' windows. HEP particle detectors are required to maintain their transparency for years of high luminosity data acquisition.

It is essential to assess the feasibility of deploying these materials in hostile environments by studying the effects of radiation on glasses. A variety of analytical techniques are available to assist in definitively understanding the underlying processes which lead to radiation induced defects in fluoride glasses.

For over 50 years point defects have been studied in insulating crystals. Alkali halides have been used extensively in this work as their simple lattice structure and highly ionic nature are relatively simple to model for the *colour-centre* physicist [13]. This base of knowledge on crystals provides useful guidance on the processes occurring in glasses; the differences between damage processes in crystals and glasses will be elucidated later in the text.

The underlying change in atomic arrangements that cause radiation induced optical absorbance can not be identified from one simple measurement. Definitive identification of the defects created is only possible using a combination of complementary analytical techniques. Electron Spin Resonance (ESR) and optical studies are the two main areas of work. These are further enhanced by thermal studies and optical bleaching using polarised light which can be used to correlate ESR and optical observations. A description of these methods is given below.

2.4.2. Electron Spin Resonance (ESR)

ESR is an analytical technique used for identifying paramagnetic defects in materials [14]. In a system which has two energy levels, the population of the lower, N_1 and higher levels N_2 is given by the Maxwell-Boltzmann expression,

$$\frac{N_1}{N_2} = \exp\left(-\frac{\Delta E}{kT}\right) \qquad \text{Equation 2.23}$$

ΔE represents the energy difference between the two levels, k is the Boltzmann constant and T is the absolute temperature. In a magnetic field Zeeman splitting of the electron energy levels is observed due to the interaction of their spin angular momentum with the applied magnetic field. In the most simple case where the spin quantum number, S= $+\frac{1}{2}$, the two spin values are $+\frac{1}{2}$ and $-\frac{1}{2}$. The Pauli exclusion principal allows transitions between the two states because the spin quantum number changes by ±1. Interaction between the spin of the orbital electron and the magnetic moment of its nucleus leads to further *hyperfine* splitting of the energy levels.

Consider the electron orbiting a nucleus in a steady magnetic field. The electron spin experiences a torque with tends to align the electron spin with the magnetic field. However alignment is not possible as the electron spin has orbital momentum about the nucleus. The spinning electron precesses around the magnetic field axis as shown in Figure 2.06.

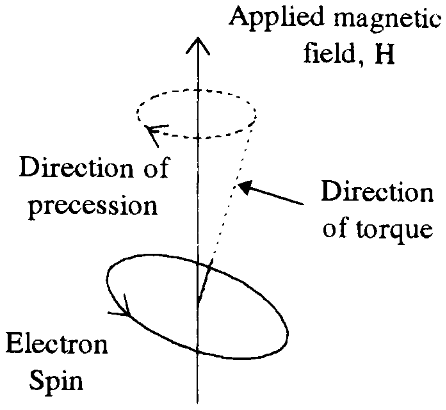

Figure 2.06 Precession of an electron in an applied magnetic field.

The energy difference between the two split levels is given by,

$$h\nu = g\beta H \qquad \text{Equation 2.24}$$

g is the spectroscopic splitting factor and is often equal to 2. β is the Bohr magneton and H the applied magnetic field. The discussions so far have considered a single electron. In a closed shell, the electrons pair up and the orbital and spin angular momenta of individual electrons cancel out. There is no net interaction with the magnetic field and ESR analysis is not possible. Shells which are incompletely filled may have an unpaired electron spin which results in a magnetic moment giving a paramagnetic substance.

The experimental implementation usually uses a fixed frequency excitation source and the magnetic field, H is varied. Resonance in the absorbance of the excitation source indicates electron transitions from lower to higher levels. The structure of the measured spectrum is indicative of the paramagnetic species as it includes details of hyperfine splitting of the parent nuclei. This is used to give a *finger-print* for the species which contains the unpaired electron. An ESR spectrum of a sample is composed of a combination of the individual signatures from each defect species present.

Most radiation induced defects are paramagnetic, involving an electron with unpaired spin. Transition metal ions and radiation induced defects are the only classes of paramagnetic defects in fluoride glasses and are therefore the only species which interact. The ESR signatures of all transition metal ions are well known, hence ESR provides an excellent probe for identifying defects induced by high energy radiation. In most cases, the individual types of paramagnetic defects which contribute to the composite ESR spectrum are easy to distinguish as they are relatively narrow and usually, their characteristic signatures do not overlap.

It is possible to calculate the ESR signature of a given material under favourable circumstances if there is some knowledge of the local environment of the specific paramagnetic defect present [15]. Close agreement between the predicted and measured ESR spectra indicates that initial speculation concerning the local atomic arrangement was correct. ESR is used in this way to identify the configuration which the defect species adopts in the host lattice.

Although ESR is ideal for determining the occurrence of stable defects which arise from unpaired electrons and holes, the method gives no information about the macroscopic optical absorbance which results from creation and population of these defects.

2.4.3. Optical Absorbance Measurements

The increase in optical absorbance of a sample as it is irradiated is one of the macroscopic effects which results from the creation of defects in the glass. A darkening of the initially transparent glass is observed. Absorbance measurements are made as a function of wavelength, with increasing dose. Optical absorbance usually occurs across a broad spectral range. The bands are predominantly located in the UV or visible, having tails which extend to longer wavelengths.

In exceptional circumstances, the induced absorbance can be separated into individual Gaussian bands, but it is more usual to see overlapping bands or spectra with no particular structure. To obtain quantitative information about the growth of individual absorbance bands and to correlate them with specific defect species identified from ESR measurements, it is necessary to separate and deal with each band individually.

There are three main avenues which enable the composite optical spectra to be separated into individual absorbance bands. Isochronal annealing is the most widely used. This exploits the difference in thermal stability of each defect species. Irradiations performed at liq.N_2 temperatures *freeze-in* defect species which may not be stable at room temperature. The sample is then warmed in typically 10K increments toward room temperature and then cooled to liq.N_2 where the absorbance is re-measured. The least stable defects anneal as some characteristic temperature is reached, and their optical absorbance bands disappear. Measurements can continue above room temperature to separate defects which are particularly stable. It is found that in a wide variety of fluoride glasses, all radiation induced defects disappear if the samples are heated to 450 K [16].

In some cases it is possible to fit a number of Gaussian profiles to optical absorbance data summing each to build up the observed composite spectra [17]. There is a high degree of uncertainty in the amplitudes, positions and widths of the individual absorbance features as they are so broad and usually, several overlap. This approach is primarily used in conjunction with other information. For example, if the centre positions of bands are known beforehand they can be set constant. This simplifies the mathematical fit.

The third tool for separating optical absorbance spectra into individual absorbance bands is *photodichoism*. This is a familiar phenomenon in halide crystals [18]. It arises as a result of certain defect species having anisotropic absorbance properties. Whereas in crystals, the initial orientation of defects is governed by the crystal symmetry, in glasses this is not the case and all defect orientations are equally probable. Polarised light bleaching with an intense, linearly polarised beam will result in those anisotropically absorbing defects aligned appropriately, not to absorb the bleaching light. These defects will survive annealing. All isotropically absorbing centres will anneal. Subsequent optical measurements using a less intense probe beam polarised 90° to the bleaching beam will only be sensitive to the surviving anisotropic defects.

Characterisation of radiation damage by optical absorbance studies is an analytical technique which is application oriented. The results of a representative irradiation establish directly the suitability or otherwise of a particular optical material. Absorption measurements give an accurate prediction of, to what extent the material will damage in the anticipated environment. Unfortunately, in isolation, this technique usually gives little information on the underlying causes of radiation induced damage.

Initial ^{60}Co irradiations of fluorozirconate glasses at room temperature showed significant damage in the UV and visible regions. However the ZBT [19] and ZBLALi [20] glasses tested were remarkably radiation hard in the wavelength region from 2.5 to 5 μm. This behaviour is typical of heavy metal fluoride glasses. Similarly, neutron exposures of 2.5×10^{11} n cm^{-2} caused no radiation induced damage in this window [21]. Mitra [21] observed a shift in the cut-off wavelength resulting from a neutron irradiation of 3×10^{11} - 3×10^{12} n cm^{-2}. A slight recovery was noted in the position of the UV edge over a two week period.

These early results were very well received by workers keen to exploit the extended IR transmission window of HMF glass fibres. However, the optical fibre industry could not afford to be complacent with regard to the threat of radiation induced absorbance as the tails of UV bands still caused some induced absorbance in the IR when the phenomenal path lengths ($> 10^4$ m) found in optical fibre applications are considered.

2.4.4. Correlation of ESR and Optical Measurements

To understand the radiation tolerance of HMF glasses, it is necessary to correlate features in the optical spectra with specific defects identified from ESR measurements. It may then be possible to tailor the glass composition so that the defect ion is excluded, or modify the composition so that population of the optically absorbing defect is not favoured. This systematic approach using both complementary experimental techniques has been the key to identifying many of the defect species which limit the radiation tolerance of HMF glasses.

The principal technique used for correlating optical and ESR data uses isochronal annealing to modify the radiation damage in a controlled way whilst recording both optical and ESR data. Common trends in the results as a function of annealing temperature are indicative of the features having a common origin. Thermal annealing of ESR signatures can also give important information about the kinetics of charge transfer between different defects. As one defect species anneals, the charge released may be captured by a different species. This is reflected in the growth of one ESR feature during annealing as another diminishes.

Identification of the defect species can be determined by producing a series of glasses which all have similar compositions. The test samples differ from the control by having a small molar fraction of the candidate defect compound in each. The set of glasses are evaluated using the methods described above. Any difference in the ESR and optical absorbance spectra is attributed to defect creation associated with the defect candidate.

It is also possible to identify defects associated with the intrinsic glass matrix by observing how the intensity of the ESR signature of that defect varies with the molar composition of the glass [17].

2.4.5. Identification of specific defect species

One of the first published works concerning irradiation of HMF glass was reported by Fisanich [22] in 1985. This work involved ESR and optical measurements following room temperature electron irradiations of ZBLA and HBL glasses. An optical absorbance band at 290 nm was observed for ZBLA and bands at 240 and 310 nm occurred in HBL, his experimental results are shown in Figure 2.07. The damage in HBL was twice as severe as that in ZBLA. Thermal annealing measurements of HBL correlated the 310 nm band with the two different defects identified from ESR measurements. A trapped hole and separate trapped electron were tentatively identified as the cause of the ESR centres in these materials. In ZBLA, a third defect centre was also present. From ESR data, this was assigned to a hole trapped at an impurity or defect site. Trapped holes released by 'Centre 3' during thermal annealing were re-trapped causing an increase in the 'Centre 2' intensity. It was pointed out that this additional centre is not present in HBL.

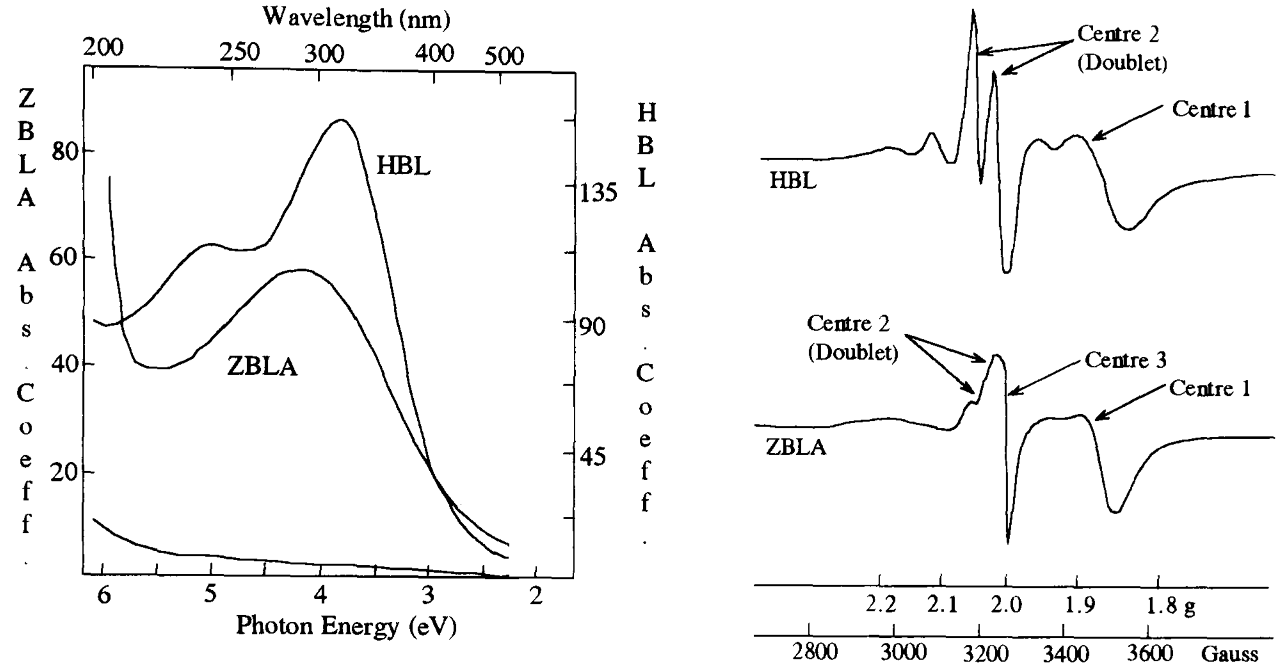

Figure 2.07 The room temperature optical absorbance (cm^{-1}) and ESR spectra measured at 77 K for HBL and ZBLA glasses. Microwave frequency 9.125 GHz, power 3 mW and the modulation amplitude was 10 G. Spectrometer gain was ×2 lower for the HBL sample. Picture taken from Fisanich *et al* [22].

In alkali halide crystals, radiation damage studies have shown that the predominant damage mechanism is radiolysis. This mechanism produces copious defects, Fluorine ions are displaced and squeezed onto adjacent lattice sites. The vacancy is known as an *F-centre* and the interstitial which has a dianion structure, X_2^-, is an *H-centre*. On warming to room temperature, these defects recombine. Alkaline Earth fluorides exhibit similar damage characteristics although defect creation is initiated by two Fluorine ions relaxing symmetrically towards each other, this provides a potential well which is able to confine a hole. The structure is identical to the H-centre, X_2^- although it is created by a different mechanism. Both types of defect are known as V_k centres for historical reasons.

Perturbed forms of the V_k centre are found, one important type is the X_3^{2-} which is found in heavily neutron irradiated LiF_3. Mixed X_2^- defects e.g., (FCl^-) are found in crystals which contain more than one type of halide. Many of the perturbed defects are stable up to 200 K.

Cases [23] irradiated samples of HB, ZB, and others at 100 K using a 100 keV X-ray set operating at 20 mA. He observed a resonance similar to 'Centre 1' of Figure 2.07 and concluded that these were associated with Hf^{4+} and Zr^{4+} ions.

Cases performed a computer line-shape simulation to explain the observed ESR spectra. The displacement model of an interstitial fluoride atom, F^{o}, in the glass matrix with a corresponding Zr^{3+} (or Hf^{3+}) defect could not explain the observed ESR spectra. To describe the recorded spectra it was necessary to include the ESR signature of an F_2^- defect. This is a displaced Fluorine atom sharing an electron with a Fluorine ion and was identified as a V_k-type defect.

Despite the inclusion of an F_2^- defect, Cases pointed out that there was not complete agreement between the ESR data and his simulation. He suggested that his model was too simplistic. However, Cases' description of damage in terms of just F^{o} and F_2^- centres was largely accepted until 1989, when a superior computer line shape simulation addressed the discrepancies between his experimental results and simulations [24]. A more accurate fit to the experimental data was obtained by considering three types of defects. Griscom [24], in addition to the F^{o} defect, used a linear combination of the F_2^- and F_3^{2-} defects. The latter corresponds to a trapped hole associated with three ^{19}F nuclei, as mentioned earlier, this defect has been observed in the disordered structure of heavily neutron irradiated LiF_3. Adjusting the ratio (F_2^-: F_3^{2-}) to 1:4, resulted in satisfactory agreement.

Simulations [24] have also shown that the Zr^{3+} defect originally described as an electron trapped on a Zr^{4+} (or Hf^{4+}) is in fact an F-centre. The electron is highly attracted to the neighbouring Zr^{4+}, effectively making it a Zr^{3+}. This is an important distinction, the radiation damage in HMF glasses is radiolytic as in alkali halides rather than by a process of electron and hole trapping at substitutional trivalent cations as in alkaline earth halides.

Friebele and Tran [17,25] observed the optical absorbance spectra of ZBLALi glass during isochronal annealing. They observed a band which could be resolved into four overlapping Gaussian components. During annealing the Gaussian component at 4.27 eV shifted in position by 0.25 eV. This shift was consistent with the Gaussian being composed of a linear combination of two defects with slightly different positions. The difference in thermal stability of each, caused the centre position of the overall feature to shift during isochronal annealing. By comparing the band intensities with ESR information it has been determined that the 4.27 eV band was composed of 4.21 eV (F_2^-) and 4.62 eV (F_3^{2-}) contributions.

2.4.5.1 *Oxygen Related Defects*

The so called *Central-line* feature at g=2.030 in the ESR spectra of these glasses was enhanced in water treated samples [26]. Griscom [27] also found that the *Central line* was enhanced in O_2 melted glasses and suppressed in glasses which were heated above 400 K in an Ar atmosphere. This defect is due to oxygen which is present as O_2^- molecular ions.

2.4.5.2. *Chlorine Related Defects*

Chlorine was identified as a defect species in HMF glasses due to the different production processes used by two independent groups. Cases *et al* [23] produced their glass samples under an inert Ar atmosphere. In contrast, Fisanich *et al* [22] used a Reactive Atmosphere Process, RAP involving CCl_4. After irradiation, the glasses prepared by Fisanich contained additional ESR components compared to the glasses made by Cases.

To establish whether Cl^- was responsible for the additional defect signature, Griscom and Tran [28] produced a series of glasses containing 0.0, 1.0 and 2.2 wt.% $BaCl_2$ under an Ar atmosphere. ESR measurements after X-ray irradiation at 77K showed F_3^{2-} and F_2^- defects. Isochronal annealing caused the thermally unstable F_3^{2-} and F_2^- defects to relax. Charge released by these defects is trapped by chloride ions to give FCl^-. Above 300 K, some holes are released by FCl^- and become trapped on the highly stable Cl_2^-. This defect corresponds to an absorbance band centred at 310 nm. Tanimura [29] showed that up to 5% Cl^- is incorporated into the matrix of a glass produced by RAP. Tanimura [30] also claimed that the stability of the Cl_2^- defect depends on the heavy metal. In ZBL and HBL, the 50% anneal temperatures of the 310 nm band are 350 and 450K respectively. Apparently, annealing of the Cl_2^- defect is controlled by release of the complementary trapped electron. The Hf^{3+} trap is deeper than Zr^{3+}.

The optical absorbance spectra of glasses studied by Fisanich [22] were dominated by features associated with Chlorine related defects. These had centre positions of 310 nm [Cl_2^-] and 260 nm [FCl^-].

2.4.5.3. *Bromine Related Defects*

Griscom [31] irradiated samples of ZBLAN glass doped with small quantities of NaBr. ^{60}Co irradiations at room temperature and 100 keV electron irradiations at 77 K were performed. The ESR spectra obtained from the doped glass were similar in structure to chloride doped glasses. Features corresponding to Br_2^- and FBr^- were quantitatively identified.

2.4.5.4. *Multi-valent Impurities*

Transition metal ions which are capable of adopting several different electronic configurations (e.g. Pb^{+}, Pb^{2+} and Pb^{3+}) are known as *aliovalent* impurities. The incorporation of aliovalent dopants into the matrix of a glass has been shown to improve radiation resistance as these sites act as electron or hole traps. They compete for charge and hence reduce the amount available to be trapped at other defect sites. Cerium acts as competitive hole trap in the fluoride matrix. This mirrors its well documented behaviour in silicate glasses [32]. Cases [23] observed a suppression in F_2^-, F_3^{2-} and the *Central line* defects which are all associated with hole trapping, whilst the Zr^{3+} electron type defect remained unchanged in glasses containing 5% CeF_3.

$Ce^{3+} \rightarrow Ce^{4+} + e^-$ traps holes

In addition to providing alternative traps sites for excited charge, there is evidence that aliovalent atoms may also act as recombination centres for electron / hole pairs.

Cases [33] tested fluorozirconate glasses based on ZBLALi with approximately 1 mol% of CrF_3, $MnCl_2$, and $FeCl_2$. The control sample showed F_2^- and F^o defects which corresponded to absorbance bands in the optical spectra, centred at 305 and 265 nm respectively. Zr^{3+} was also observed in the control sample, this gave rise to UV absorbance whose centre position could not be identified as it was too weak. The 3d-doped glasses showed ESR signatures characteristic of transition elements prior to irradiation. Corresponding optical absorbance bands centred at 290, 445, 650 and 678 nm were seen for the Cr doped sample. The Fe doped glass has a weak IR absorbance but more importantly, the UV edge in this material was shifted to a longer wavelength, this is characteristic of Fe^{3+} [33].

The Cr and Mn glasses developed absorbance bands centred at 260 nm, the Fe doped glass damaged at 340 nm. Significantly, after irradiation at 77K, the 3d-doped glasses displayed no signals from F_2^- ,F^o or Zr^{3+} type defects. It was concluded that 3d-ions strongly suppressed the damage produced by low temperature irradiation of fluorozirconate glasses.

Griscom [27] has shown that, after irradiation, the number of trapped holes $[F_3^{2-}] + [F_2^-] +$ [*central line*] in a fluorozirconate glass is equal to the number of trapped electrons $[Zr^{3+}]$. In Fe doped glass, this charge conservation equation was modified to include a term for the number of Fe^{3+} ions which are lost during irradiation. The Fe^{3+} ions act as additional electron traps converting to non-paramagnetic Fe^{2+}.

When fluorozirconate glasses were doped with Lead, and irradiated at low temperatures. ESR signatures observed corresponded to Zr^{3+}. In contrast to glasses containing no Lead, the Zr^{3+} signal diminished when this glass was annealed at 220K. Electrons are transferred from the Zr^{3+} to Pb^{2+} forming Pb^{+}. This explanation was proved correct by Friebele [17] who observed the growth of the Pb^{+} optical bands at 404 nm and 306 nm, during annealing measurements.

---

[1] D.L. Griscom, *J. Non-Cryst. Solids* **161** (1993) 221.

[2] The Compact Muon Solenoid Letter of Intent, CERN/LHCC 92-3, LHCC/I 1, (1992).

[3] G.F. Knoll, *Radiation Detection and Measurement*, John Wiley & Sons.

[4] E. Segre, *Nuclei and Particles*, The Benjamin/ Cummings Publishing Company.

[5] C.G. Darwin, *Phil. Mag.* **25** (1913) 201.

[6] N.F. Mott, *Proc. Roy. Soc.* (London) **A124** (1929) 425.

[7] W.A. McKinley and H. Feshbach, *Phys. Rev.* **74** (1948) 1759.

[8] J. Gittus, *Irradiation Effects in Crystalline Solids*, Applied Science Publishers Ltd., (1978) p5.

[9] J.B. Sampson, et al, *Phys. Rev.* **99** (1955) 1657.

[10] J.W. Corbett, et al, *Phys. Rev.* **108** (1957) 954.

[11] Ch.B. Lushchik, *Physics of Radiation Effects in Crystals,* North-Holland Physics Publishing, (1986) p507, general editors R.A. Johnson and A.N. Orlov.

[12] J.H. Beaumont, et al, *Proc. Roy. Soc. London* **A315** (1970) 69.

[13] W.B. Fowler, *Physics of Color Centers*, Academic Press, New York, (1968) p53.

[14] D.L. Griscom, *Glass Science and Technology* **4B**, Academic Press, Boston, (1990) p68.

[15] J.E. Wertz, and J.R. Bolton, *Electron Spin Resonance Elementary Theory and Practical Applications*, McGraw Hill, New York.

[16] I. Aggerwal and G. Lu, *Fluoride Glass Fibre Optics*, Academic Press Inc, ISBN 0-12-044505-0 p341 and cited references.

[17] E.J. Friebele, and D.C. Tran, *J. Non-Cryst. Solids* **72** (1985) 221.

[18] C.J. Delbecq, et al, *Phys. Rev.* **111** (1958) 1235.

[19] A. Rosiewicz, and J.R. Gannon, *Elect. Lett.* **17** (1981) 184.

[20] H.K. Levin, et al, *Glass Tech.* **24** (1983) 143.

[21] S.S. Mitra, et al, *Appl. Opt.* **26** (1987) 4443.

[22] P.E. Fisanish, et al, *J. Non-Cryst. Solids* **70** (1985) 37.

[23] R. Cases, et al, *J. Non-Cryst. Solids* **72** (1985) 51.

[24] D.L. Griscom, and E.J. Friebele, *Phys. Rev. B.* **43** (1991) 7427.

[25] E.J. Friebele, and D.C. Tran, *J. Am. Ceram. Soc.* **68** (1985) C-279.

[26] R.N. Schwartz, et al, *Radiat. Phy. Chem.* **32** (1988) 439.

[27] D.L. Griscom, and R.J. Ginther, *J. Non-Cryst. Solids* **113** (1989) 146.

[28] D.L. Griscom, and D.C. Tran, *J. Non-Cryst. Solids* **72** (1985) 159.

[29] K. Tanimura, et al, *J. Appl. Phys.* **58** (1985) 4544.

[30] K. Tanimura, et al, *J. Non-Cryst. Solids* **70** (1985) 397.

[31] D.L. Griscom, and R.J. Ginther, *J. Non-Cryst. Solids* **110** (1989) 273.

[32] J.S. Stroud, *J.Chem. Phys.* **37** (1962) 836.

[33] R. Cases, et al, *J. Non-Cryst. Solids* **87** (1986) 93.

CHAPTER THREE

Radiation Damage Studies: Experimental Details and Analytical Models

3.1. Introduction

This chapter describes the irradiation and annealing measurements which have been used for the evaluation of over one hundred different samples of HMF glass in the present work. To establish trends which correlate radiation tolerance with composition, it is necessary to characterise the development of radiation induced damage. Various methods for analysing the experimental data are considered.

Radiation tolerant glasses have been identified by investigating the effects of adding small amounts of various dopants to the basic composition. Most of the glasses have been produced by groups from UK Universities. The ability to specify, produce, and evaluate all glasses *in-house* has minimised the turn-around time from testing one batch to producing and testing new glasses. It has been possible to feedback information from one set of irradiation measurements in to the production of the next batch in as little as one month.

3.2. ^{60}Co Irradiation Studies at Brunel University

3.2.1. Irradiation

Discussions in Chapter 2 have demonstrated that ^{60}Co irradiation can lead to radiation damage in HMF glasses by both knock-on processes and radiolysis. A 3.3 Ci (06/94) ^{60}Co source at Brunel University was used for all γ irradiations. It is housed underground in the Physics Department radiation facility. The source is deployed by rotating a handle from outside the cell, this translates it along a flexible hose to one end which is inside the radiation cell. In the exposed position, the source is surrounded by a brass encapsulation at the end of the hose. Its dimensions are shown in Figure 3.01, it approximates a point source. The brass housing is 2 mm thick.

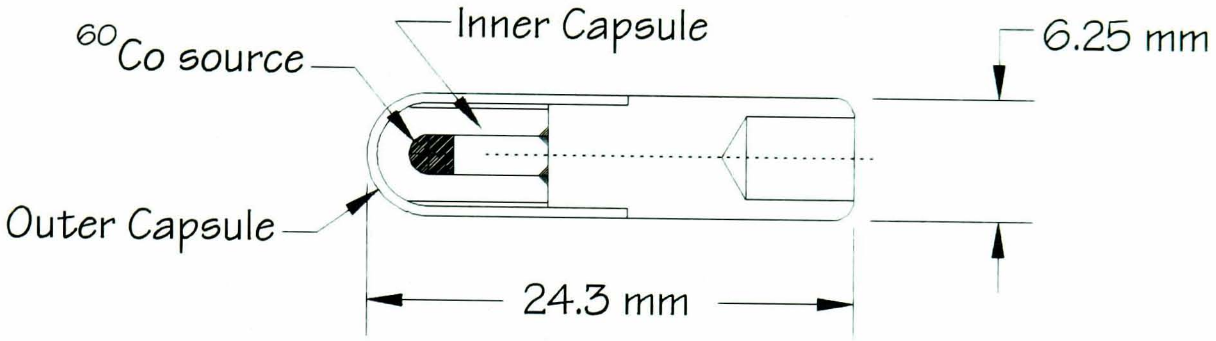

Figure 3.01 ^{60}Co mounting capsule model 60011, the source #2056 has a diameter of 1.78 mm and is 1.75 mm long.

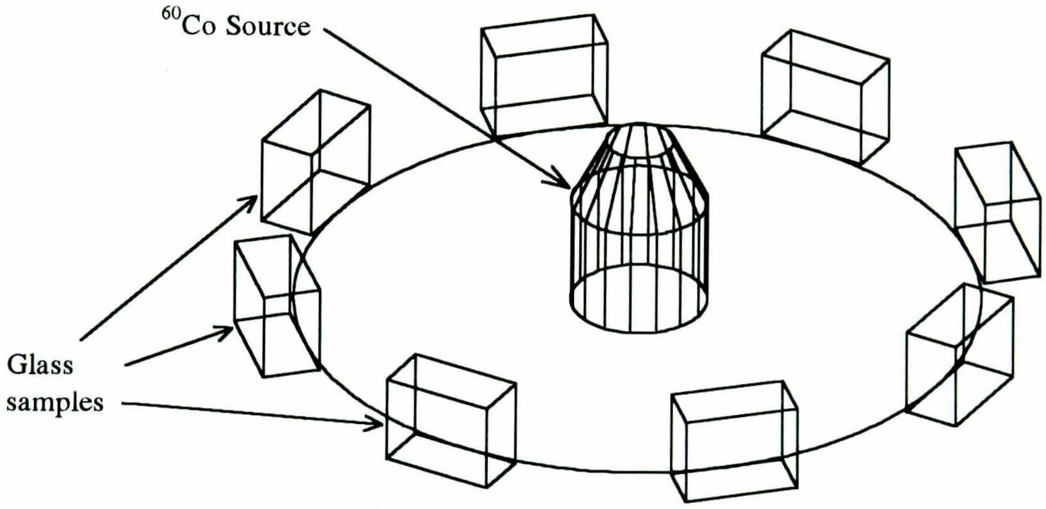

Figure 3.02 Glass samples surround the ^{60}Co source which protrudes through a hole in the oak platform. The separation of 3 cm ensures dose uniformity across the irradiated face of the samples.

An oak platform was constructed for irradiation of small glass samples. The brass ferrule protruded through a hole in the centre of the platform. It was positioned in the centre of the room to minimise radiation scattered from the concrete walls of the building. Glass samples were arranged radially around the source at a fixed distance as shown in Figure 3.02. The radial distance was never smaller than 30 mm for dose uniformity across the sample. Its value dictates the dose rate. Typically samples had dimensions, 20× 10× 5 mm^3. It was possible to irradiate up to eight or ten samples simultaneously.

3.2.2. Dosimetery

Characterisation of radiation induced damage relies on accurate estimates of the dose received during irradiation as well as measurement of radiation induced absorbance. The activity of the source has been calculated from the initial activity when it was purchased and the half life of ^{60}Co (5.271 years). This is shown in Figure 3.03 for the period 93/94. The activity was also verified using a ion chamber [1].

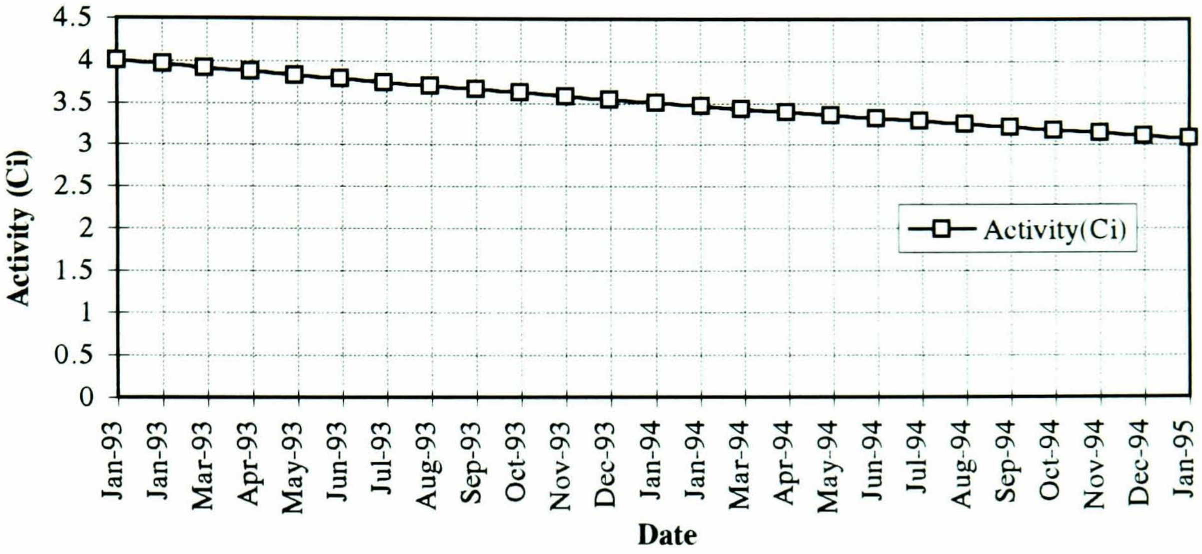

Figure 3.03 Activity of ^{60}Co source #2056 versus time.

The source is assumed to emit isotropically in to 4π sr. The absorbed energy per second, E (MeV s^{-1}) is,

$$E = Activity \times \frac{d\Omega}{4\pi} \times \left(1 - \exp(-\mu t)\right) \times E_{abs} \qquad \text{Equation 3.01}$$

$d\Omega$ is the solid angle subtended by the glass sample. μ is the linear attenuation coefficient (cm^{-1}) and t (cm) is the thickness of the glass. E_{abs} is the energy absorbed per interacting photon. The source activity (Bq) is multiplied by two because each decay produces two photons. Dose (MeV kg^{-1} s^{-1}) is defined as the energy absorbed per unit mass. Writing mass in terms of thickness, t, area, A, and density, ρ,

$$E = \frac{Activity}{4\pi D^2} \times \left(1 - \exp(-\mu t)\right) \times \frac{E_{abs}}{\rho t} \qquad \text{Equation 3.02}$$

GEANT 3.14 Monte Carlo has been used to calculate E_{abs}. The source is approximated by a collimated beam of gamma rays which were incident normally on the centre of a glass tile of square cross-section. The gamma ray energy was chosen randomly from the two characteristic photon energies with equal probability. Gamma rays were tracked through the material and all secondary electrons (and positrons) and photons were tracked down to a cut-off energy of 10 keV.

The deposition profile has been estimated using *GEANT*, and also *Photcoef* [2] which runs on a PC. This is similar to *GEANT* but runs in a lower specification computer environment by making some simplifying assumptions. It is claimed that agreement between the two systems is good at the few percent level [2].

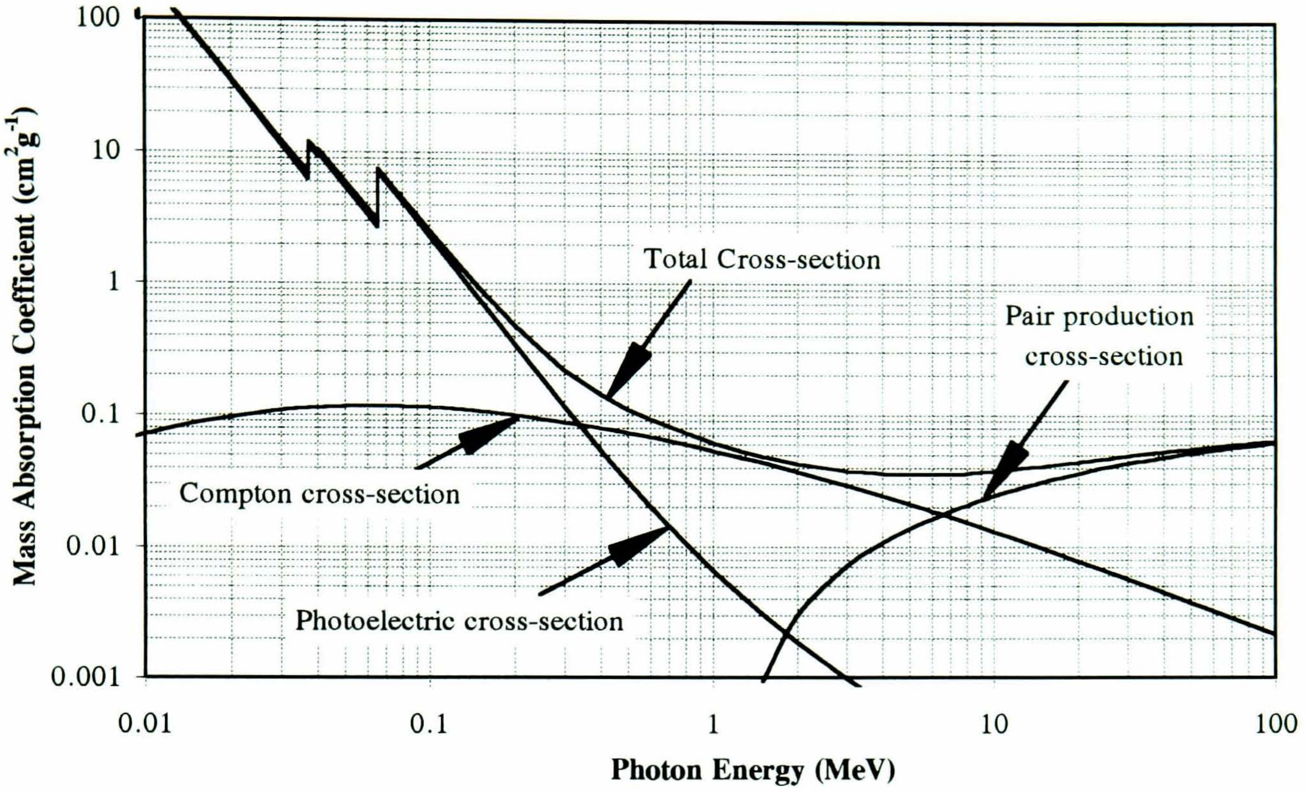

Figure 3.04 Energy dependence of the various gamma-ray interaction processes in HBCeA fluoride glass. This data was calculated using *Photcoef* [2].

Dose deposition profiles have been calculated for silicate and fluoride glasses irradiated directly with ^{60}Co γs. In low density (low *Z*) materials, the *build-up* layer extends a few millimetres in to the irradiated specimen, there is also a *fall off* at the rear face. In fluoride glasses (high Z), the build up and fall off layers do not intrude by more than 0.2 mm. The effect of the 2 mm brass encapsulation in which the source is housed has also been included in the electron transport calculation. The dose profile for a typical HMF glass composition (HBCeA) is shown in Figure 3.05. This corresponds to irradiation of a 5 mm thick sample at a distance of 30 mm and includes the dose enhancement caused by the brass layer. The high *Z* constituents in HMF glasses make the non-uniform dose deposition region at the rear face extremely thin. It was not necessary to use additional build-up layers to enhance electron transport at the rear surface.

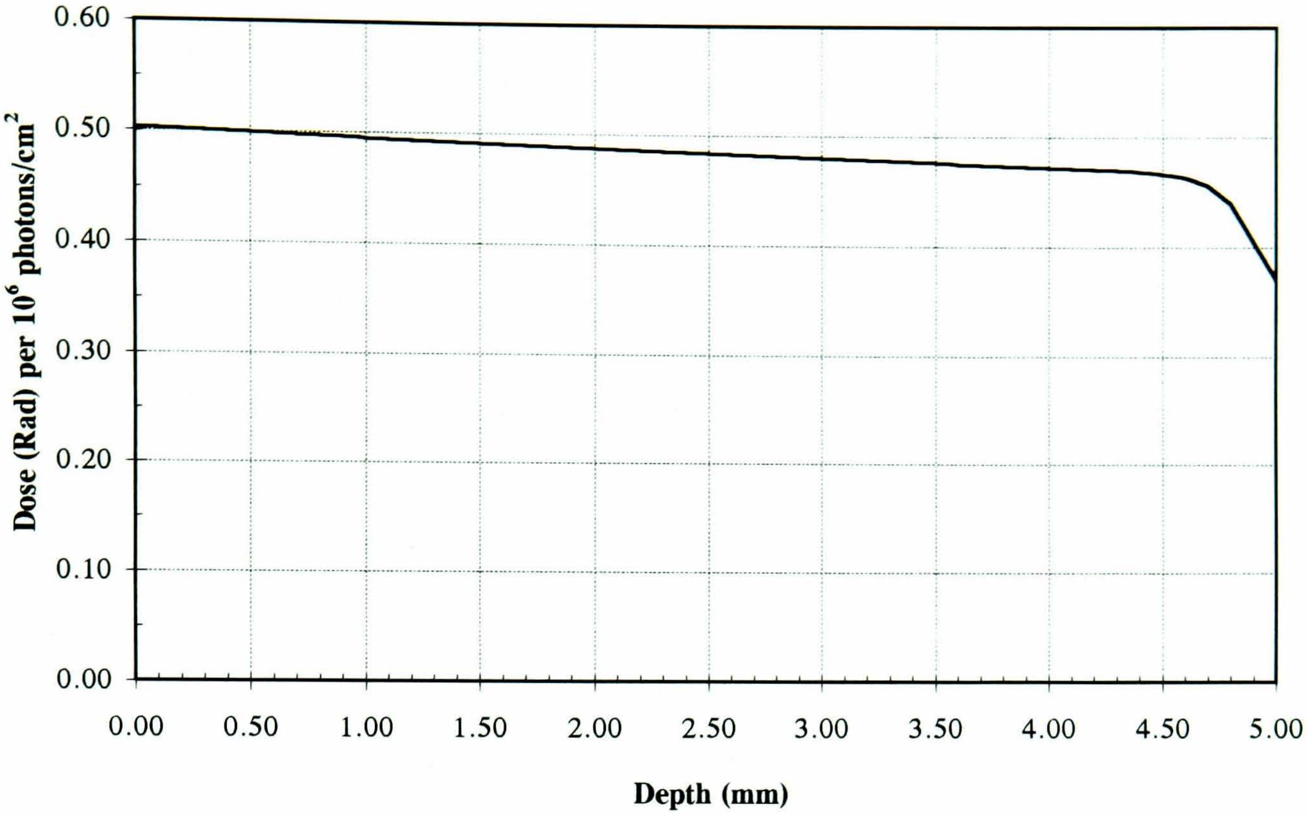

Figure 3.05 The dose profile for a 5 mm thick HMF glass, see the text for details. The combination of high Z materials and the overall high density is reflected in the thin build-up layer.

Assuming irradiation from a point source, the dose falls off with the inverse square of the separation. This separation, in addition to the source activity and the dose deposition considerations, was used to calculate the dose rate. At 30 mm, fluorohafnate glasses accumulated a dose at 1.2 rad s^{-1}, at 300 mm this value fell to 0.012 rad s^{-1}. The 30 mm rate corresponds to approximately 100× the expected rate for the Electromagnetic Calorimeter of CMS at the LHC.

3.2.3. Optical Studies

Optical absorbance measurements were recorded using a Perkin-Elmer UV/Vis/NIR Lambda 9 Spectrophotometer. The dual beam machine was designed for measurements of absorbance and transmission of liquid samples over the wavelength range from 160 nm to 8 μm. The lower wavelength limit, below 200 nm, is attainable using nitrogen purging of the sample chamber. The optical layout of the machine is shown in Figure 3.06. Liquid samples are contained in quartz phials whose optical path length is 10 mm. The phials are held in precision mounts, one intercepts the *object* and a second intercepts the *reference* beam as shown. Differential measurements are possible using a control sample in the reference path.

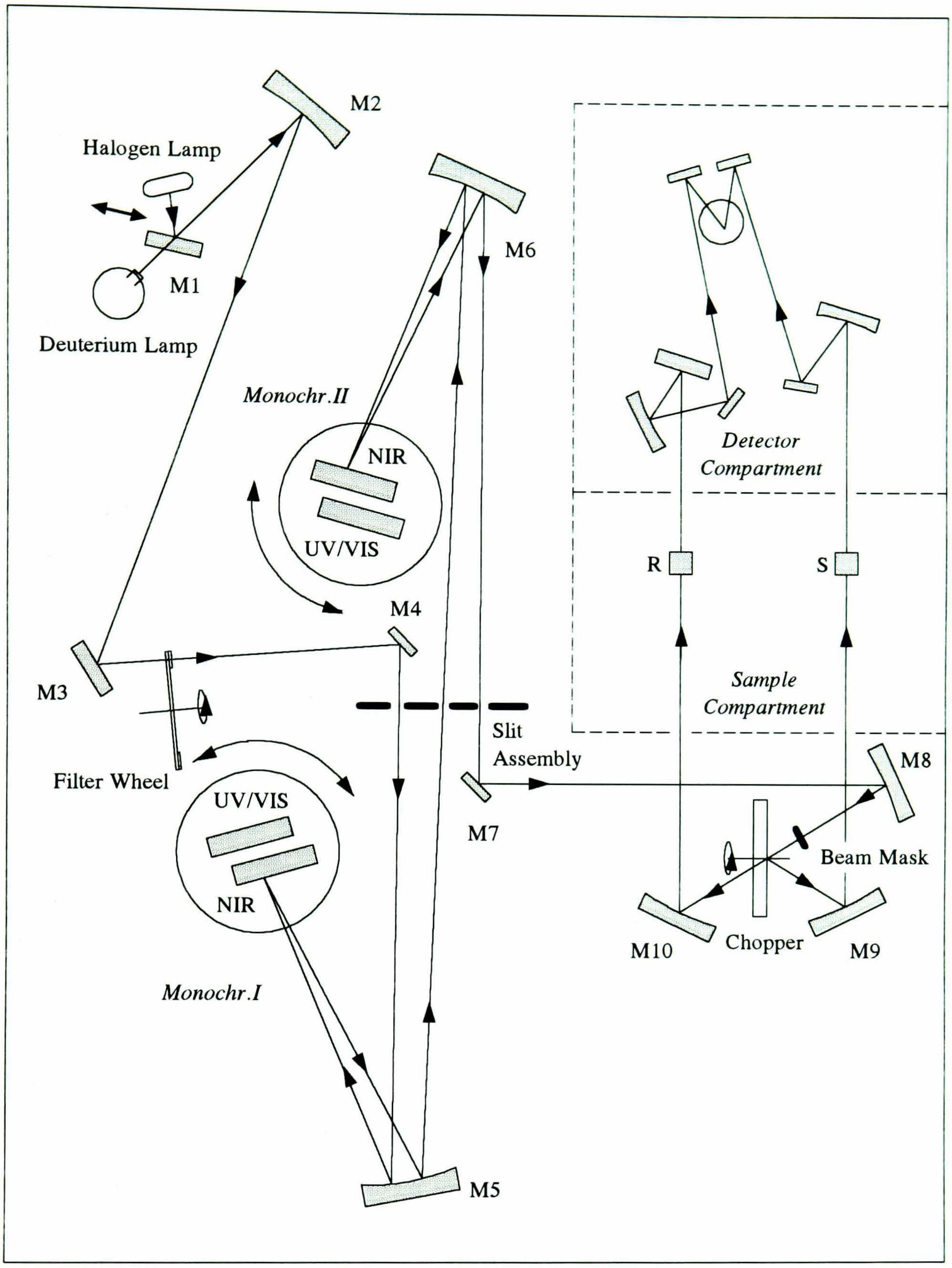

Figure 3.06 The optical layout of the Perkin Elmer Lambda 9 UV/ Vis./ NIR Spectrophotometer [3].

The spectrophotometer has a double monochromator to select the wavelength of the probe beam, but the transmitted light is detected directly. Any UV excited fluorescence scattered towards the detector can result in the absorbance being underestimated. This will cause negligible problems for HMF glasses because of the low light output of these glasses and also due to the small solid angle of the detector.

The system is controlled by a PC which automatically stores absorbance data to an output file. All of the data recorded over the entire research program used identical system settings. This allowed the use of purpose written routines to export the data from the parent application and import it into a separate application for storage, data correction, display and printing. The system settings are given in Table 3.01.

Start wavelength	650 nm	Changeover wavelength	319 nm
Stop wavelength	185 nm	Scan speed	240 nm/min
Interval	1 nm	Detector integration time	0.2 s

Table 3.01 Perkin Elmer system settings

3.2.4. Redesign of the Sample Holders

The UV spectrophotometer incorporates high quality quartz sample holders for absorbance measurements of liquid samples. These provide near identical optical paths for the *reference* and *object* beams. The collimated beams are undeviated in passing through the sample holders as the phials have good quality, parallel surfaces. Loss at each optical interface is common to both beams and hence results in no differential optical absorbance. Any differential measurements are due to variation in optical absorbance of the reference and object liquids.

The discussion concerning optical absorbance measurements of specifically Hafnate glasses is quite different and requires additional consideration. Glasses used in this programme of work were each unique. It was not possible to cut each sample in two to obtain a control for use in the reference path due to the small sample size (20×10 mm^2). Hafnate glasses are highly ionic and due to their toxic constituents, require specialist machining when cutting, grinding or polishing.

As produced, the fluoride glasses have opposite surfaces which are practically parallel and flat due to the construction of the mould in which they are cast. However, some distortion results from shrinkage during cooling. Visually the majority of glasses are optically isotropic. Some samples contain striations which result from the casting process. Additionally, crystallites, vacuum bubbles and particulate impurities are occasionally present. Accurate *reference* and *object* holders were designed and constructed for optical measurements of solid samples whose dimensions are given above. These allowed precise location of samples in the holders. The optical aperture had a diameter of 5 mm. One of the holders is shown in Figure 3.07.

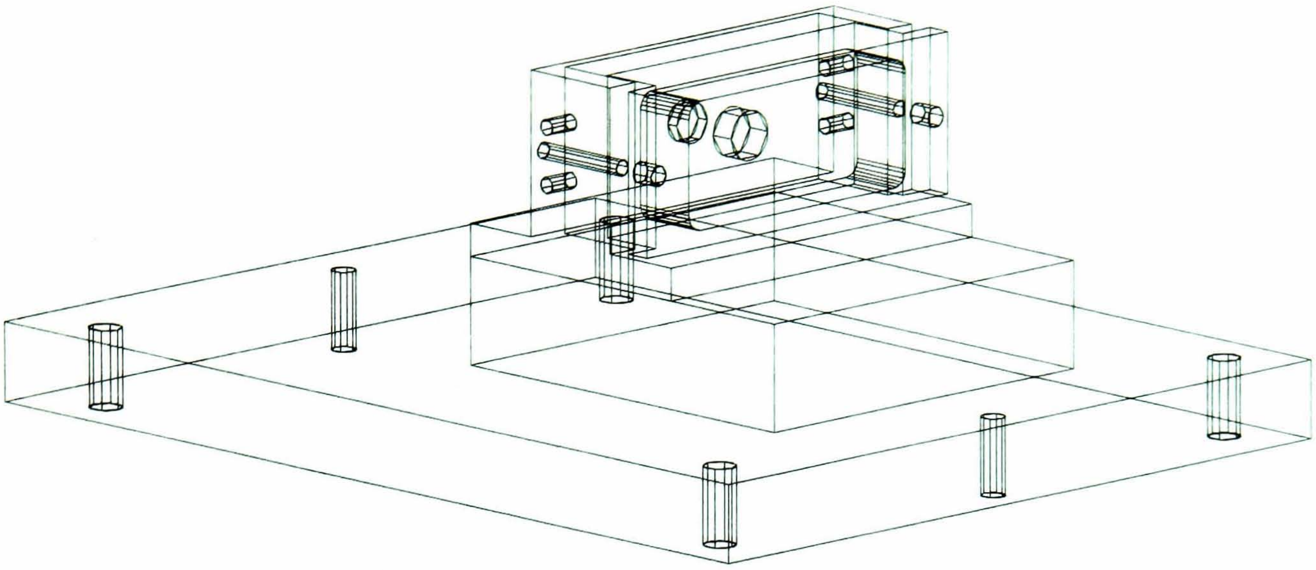

Figure 3.07 One of the sample holders designed for measuring the Absorbance of small glass samples. They are constructed of black *Tufnell* to minimise stray reflected light.

Due to the unavailability of control samples for use in the reference path, it was decided to leave the reference holder empty and obtain differential measurements by recording absorbance data before and after irradiation. Differential data could be calculated from the parent data. There is a hazard associated with multiple measurements of non-perfect samples which have to be removed from the holder in between measurements. It is essential to replace the glass sample in the holder in a consistent and repeatable way for each successive absorbance scan. This is specially important when the optical quality of the sample is poor.

The holders designed for this work allowed the samples to be held in a consistent fashion. Alignment arrows ensured that the glass samples were not rotated between successive measurements.

3.2.5. Preliminary Verification Testing

Various studies were carried out to establish the effects of sample repositioning and variation in sample quality on measured absorbance data. This work had several aims:

3.2.5.1. To verify that the system worked satisfactorily

The system was tested by measuring the absorbance spectra of a set of neutral density filters. ND1, ND2 and ND3 filters were used. Their measured transmission spectra agreed with the specification which accompanied them when purchased. The filters were optically isotropic and had flat, parallel surfaces.

The system was then tested with typical glass samples, some of these were not optically perfect. When the surface is not flat, non-parallel or irregular, the sample destroys the collimation of the probe beam resulting in a reduction of the light intensity falling on the entrance aperture of the detector. The measured absorbance is systematically higher as a result, because it includes the defocusing optical loss at the surfaces, in addition to the bulk loss in the optical medium.

The absorbance spectra of poor quality samples show a discontinuity at 319 nm. This corresponds to the wavelength at which the optical source is changed between the deuterium (UV) lamp and the tungsten halogen (Vis./NIR) lamp. This is probably due to the difference in the profile or degree of collimation between the two optical sources.

3.2.5.2. *To quantify the effects of sample mis-alignment in the beam.*

In normal operation, the sample holder is removed from the spectrophotometer to enable the glass sample to be loaded. The holder is then replaced and an absorbance spectrum recorded. For differential measurements, it is necessary to compare two spectra of the same piece of glass which correspond to the sample being loaded into the holder on two separate occasions. It is not possible to replace the sample exactly as before hence the recorded spectrum will be marginally different each time the glass is reloaded into the holder. To determine the level of discrepancy introduced by the reloading procedure, a typical sample of Hafnate glass was measured six times, removing and reloading it between each scan. Care was taken to locate the sample consistently each time.

Using a sample whose optical properties are representative of a typical hafnate glass has demonstrated that, if sufficient care is taken, it is possible to obtain a repeatability of ±0.002 OD. The Optical Density (OD) is defined by the equation $\mathrm{Log}_{10}(I_o/ I_x)$. If a poor quality sample is used, the repeatability is deteriorated and the need for extremely accurate repositioning in the sample holder is increased. Particular care is required to ensure that the sample is loaded properly, it is always necessary to ensure that the sample has not been reversed, rotated, or translated across the aperture of the sample holder.

3.2.5.3. *To estimate beam loss due to optical wedges*

Light passing through a non-normal interface suffers an angular displacement according to Snells law. If glass samples are used which have a wedge angle, α between their opposite faces, the collimated probe beam will be displaced, through an angle *θ*.

$$\left(\frac{n_2}{n_1}-1\right)\alpha=\theta \qquad \alpha\leq 10^\circ \qquad \text{Equation 3.03}$$

To quantify the loss as a function of wedge angle, a number of optical wedges were tested in the spectrophotometer. Perspex is easy to machine and polish. Its refractive index (1.495) is similar to that of Hafnate Glasses (1.505) although its transmission window does not extend so far into the UV. For these reasons, Perspex was used for the evaluation.

There was no significant dependence of absorbance with wavelength. The correlation between wedge angle and absorbance is shown in Table 3.02. Extrapolation to small angles indicates that the loss is 0.02 OD per degree of angular wedge. This is a constant loss and does not affect differential measurements involving just one sample. The loss due to displacement of the beam dominates over the loss due to variation of reflectance with angle of incidence for the range $0 < \alpha < 10°$.

Wedge angle α (°)	Absorbance	Transmission (%)
0	0.1051	78.50
2	0.1370	72.94
4	0.2011	62.93
6	0.3181	48.07

Table 3.02 Samples with non-parallel surfaces suffer a loss in transmission as indicated. This data was recorded at 500 nm for Perspex.

3.2.5.4. *Investigation of surface finish*

The Hafnate glass samples available initially did not have highly polished transmission surfaces. To determine the effects of imperfect transmission surfaces and the level of finish required to restore good transmission, Perspex was again used. Four tiles of the appropriate size were machined. Initially the transmission surfaces were of extremely high quality. One of these was 'polished' with 6 μm diamond paste. The second and third tiles were polished under water with Grit 1200 and Grit 1000 carborundum paper respectively. All samples were polished on one side only. The quality of surface finish decreases in the following order: 'as delivered' > 6 μm > Grit 1200 > Grit 1000. Figure 3.08 shows the transmission spectra of the three samples and the unpolished control, denoted *flat*. As expected, poor optical surfaces lead to scattering of the probe beam and a decrease in the transmitted intensity. Polishing with 6 μm diamond paste reduced the scattering loss to a certain extent although the transmission was still 10% lower than for the 'flat' sample. It was concluded that any improvement in optical flatness achieved by polishing would be more than offset by the loss due to an imperfect surface finish. Moreover, multi-stage polishing of these very hard, potentially hazardous HMF glasses should be avoided if possible. Surface scratches at the interface cause a scattering loss which is larger at shorter wavelengths. This is shown in Figure 3.08.

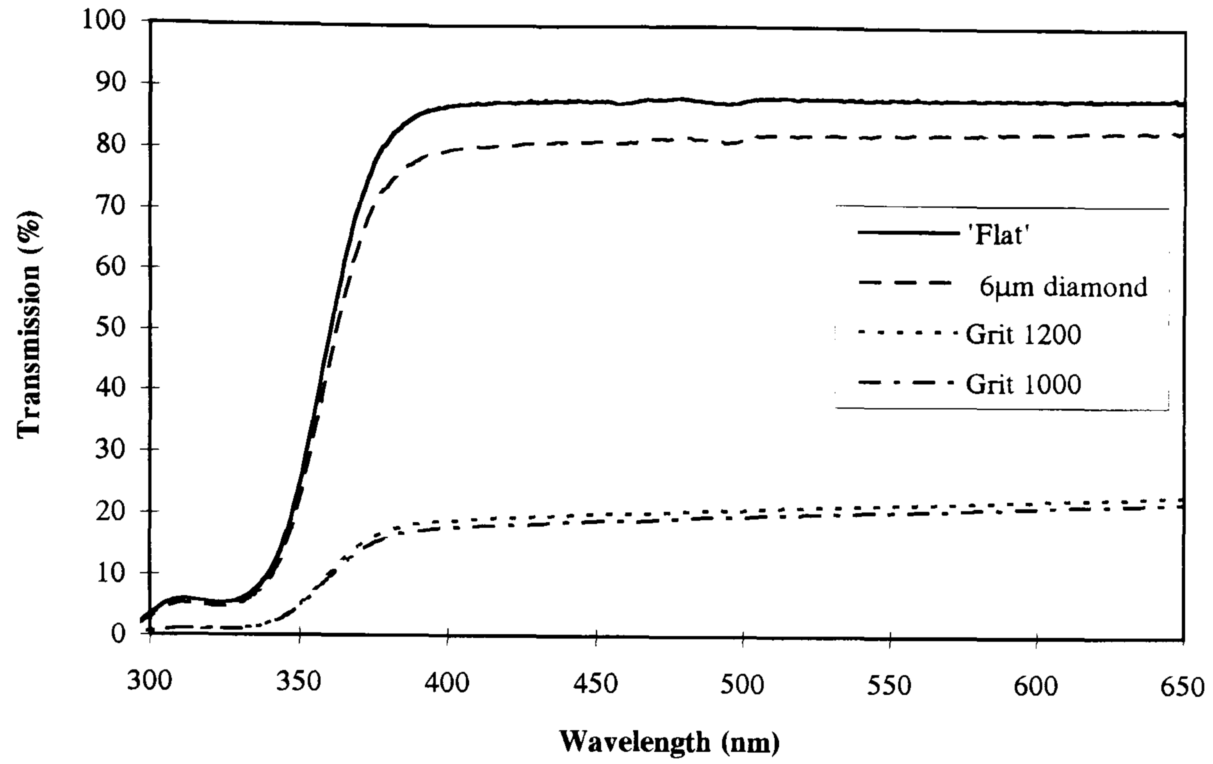

Figure 3.08 Transmission versus wavelength for samples of Perspex. These results indicate that even minor surface scratches (6 μm) severely degrade the transmitted intensity.

3.2.6. Transmission and Absorbance

Great care has to be exercised when discussing the reduction in the amount of light, measured using the spectrophotometer, when passing through a glass sample. There are several potential sources of light loss, some of which have been discussed in the previous sections:

1) Reflection loss at interfaces due to mismatch of refractive index.
2) Other sources of loss associated with the interface. (wedge angles, scattering, lensing)
3) Intrinsic absorbance of the material (absorbance bands, scattering centres).
4) Radiation induced optical absorbance of the material (colour centres).

Under ideal experimental conditions using a control sample in the reference beam, items 1) to 3) are common. Absorbance is a fundamental quantity linearly related to the number of scattering centres in the sample. In this case, radiation induced colour centres. Conversion to transmission gives the reduction in transmitted intensity due solely to radiation induced colour centres.

$$Transmission = 10^{-Absorbance} \times 100\% \qquad \text{Equation 3.04}$$

As defined in Equation 3.04, Absorbance is dimensionless. In the graphs appearing in this thesis, the absorbance is corrected to that which would be observed in a 1 cm thickness of material; the normalised absorbance is written, Absorbance (cm^{-1}). Absorbance is a logarithmic quantity. Transmission data plotted in terms of absorbance is visually 'compressed' in the range from 70 to 100% transmission and 'expanded' from 0 to 10% transmission. Our research into radiation damage in glasses concentrates on the deterioration of the *optical window*. The interest focuses on changes in the range from 70 to 100% transmission, precisely where the absorbance scale is compressed.

Absorbance data recorded using no reference sample is not related to the fundamental number of scattering centres as it includes contributions from items 1) to 4) in the list above. The correct way to handle this data is to subtract the pre-irradiation absorbance data, this being equivalent to performing the scan using a control sample. The resulting absorbance data is only due to *radiation induced absorbance*.

Radiation induced absorbance gives no indication of either the reflection loss or the fundamental intrinsic absorbance bands in the material. Both of these parameters are important when attempting to develop radiation hard glasses. For example, a glass which suffers no radiation induced absorbance is of no use as a potential calorimeter material if its unirradiated transmission is only 70% for a 10 mm path length.

The more tangible property from the application point of view is optical transmission. From external or internal transmission data, it is instantly possible to gauge to merit of the glass from the radiation tolerance standpoint. The transmission cut-off wavelength and intrinsic absorbance centres are immediately apparent. To compare radiation induced damage in one glass with another, the same optical path length has to be used. Optical absorbance scales linearly with the path length, transmission is relatively simple to calculate but is not linear.

Both presentation options have their advantages and disadvantages. For completeness, the radiation damage graphs in the results chapter of this thesis are presented in both forms.

3.2.7. Irradiation Schedules

In the preliminary investigations it was decided to use a logarithmic increase in dose starting at 1 rad and increasing to 100 rad by two factors of 10. The approximate dose rate for this regime was 0.012 rad s^{-1} for Hafnate glasses. From 100 rad to 1 Mrad, a dose rate of 1.2 rad s^{-1} was used, again absorbance measurements were made at logarithmic increments. All of the glasses were reasonably radiation hard up to 1 krad, so later irradiations tended to start at this value.

For analysis of radiation induced damage, it is more sensible to use a linear increase in dose as the damage changes steadily throughout the region from a few krad up to 500 krad or 1 Mrad. Measurements at nominally 0, 100, 200, 300, and 600 krads were used in the majority of cases. Some glasses have been irradiated to doses in excess of 1 Mrad. The 1 Mrad dose takes approximately nine days. Due to certain external constraints it was not always possible to maintain the schedule exactly.

3.2.8. Irradiation Conditions

In many materials, including HMF glasses, the radiation induced absorbance can be reversed, to a certain extent, by exposure to light. This has been demonstrated in BaF_2 [4], and CeF_3 [5]. Long term exposure to daylight or fluorescent strip lighting can induce optical 'annealing'. To ensure a consistent approach to all irradiations, the samples were irradiated in the dark and where possible, handled in subdued lighting. After irradiations had ceased, the glasses were stored in complete darkness at room temperature. Silica gel in the enclosure ensured that the atmosphere was dry.

The UV spectrophotometer scans downwards starting at the longest wavelength (650 nm) and finishing at 185 nm. By comparing successive scans of an irradiated glass it has been ascertained that the intensity of the probe beam is insufficient to initiate optical annealing in a single scan. Exposure to the dim lighting levels required to load and unload the sample in the spectrophotometer, and place and recover the sample on the irradiation platform, do not cause any measurable optically induced annealing.

The optical absorbance of each glass sample was measured within 30 minutes after the irradiation had halted. This minimised any error due to annealing of the glass samples with time. This work is not sensitive to any recovery which occurs on a time scale shorter than 30 minutes.

3.2.9. Room Temperature Annealing

After irradiation to a level of typically 600 krad or higher, irradiations were suspended and optical absorbance measurements recorded. These corresponded to the radiation induced damage with no room temperature annealing. Subsequent absorbance measurements were recorded to monitor the recovery of radiation induced absorbance as a function of time.

The absorbance spectra eventually attain a stable level. At this point, room temperature observations stop and the sample is stored, as described earlier. A program of work investigating the recovery of radiation induced damage by optical annealing has been started by Peter Hobson and Edward Maas at Brunel University. Their work uses the glass samples which have stopped annealing at room temperature.

3.2.10. Irradiation Block Diagram

The various stages of an irradiation for a set of glasses are summarised in the diagram of Figure 3.09. The irradiation measurements consist of usually six or more sets of readings, four or five additional observations are usually made to assess recovery at room temperature. For each individual glass, two data files are created, one concerning room temperature annealing, the other holds irradiation data as indicated by the faint lines in Figure 3.09. There is some duplication of data.

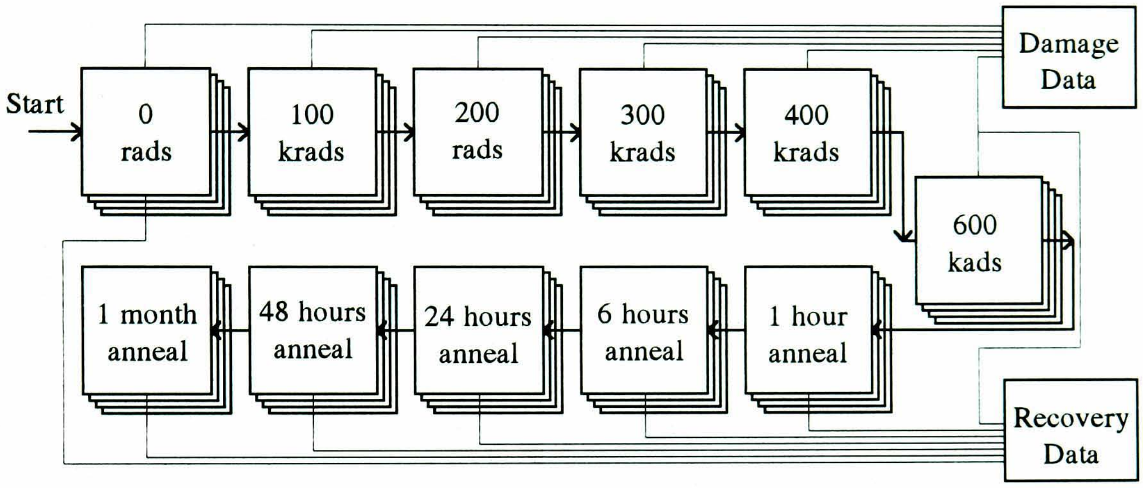

Figure 3.09 This flow chart shows the irradiation and annealing procedures schematically. The faint lines indicate the contents of damage and recovery data files.

3.3. Analysis of Radiation Damage and Annealing data

3.3.1. Introduction

The radiation damage studies involve room temperature measurements of optical absorbance in the wavelength range, $185 < \lambda < 650$ nm as a function of dose. Colour centres created in the glass cause macroscopic optical absorbance bands. These are predominantly located in the UV. The spectrum of radiation induced damage is related to the types of defects created, this is dictated by the composition of the glass.

Analysis of the radiation induced damage has been performed using three different approaches. The first gives a simple damage figure at a characteristic wavelength and dose; the second considers various models for the development of radiation induced damage as a function of wavelength. The third method models radiation induced absorbance in terms of Gaussian absorbance bands which correspond to radiation induced colour centres. The growth in amplitude of these bands is measured with increasing dose. The centre positions and widths of the bands are also fitted, these are not expected to vary.

3.3.2. Damage at 325 nm

The emission spectra (Appendix 1), light output (Appendix 2), and the time structure of scintillation light have been measured for fluoride glasses in the present work. Observations correlate the scintillation emission with Cerium [5, 6]. Incorporation of CeF_3 at the few % level can result in stable homogeneous samples, the UV cut-off in these glasses is moved from ≈ 200 nm to ≈ 295 nm by the addition of CeF_3 (see Chapter 6). The emission spectrum of Ce doped glasses is peaked at 320 nm and extends from 300 to ≈350 nm [7].

A relatively simple rating of the radiation tolerance of CeF_3 doped glasses which has been used by the collaboration involves measuring the radiation induced absorbance at 325 nm, this gives a Figure of Merit, *FOM*. The values are then normalised to a given radiation dose and a given thickness of absorbing material.

$$FOM_{norm} = FOM_{D,x,\lambda=325nm} \times \frac{10}{x} \times \frac{600}{D} \qquad \text{Equation 3.05}$$

The *FOM* is normalised to a sample thickness of 10 mm and a dose of 600 krad. The glass thickness, x is in millimetres and the absorbance measurement is recorded at a dose, D krad. The FOM_{norm} is primarily intended as a single figure rating for the radiation hardness of these glasses. This number can be used for estimating the effect of radiation induced damage on the measured light yield of Ce scintillation in HMF glasses. There are simplifying assumptions which this single figure of merit does not address. Radiation induced damage is a dynamic process. In most materials, the optical absorbance does not grow linearly with the absorbed dose over many orders of magnitude. In these materials, normalising to 600 krad using Equation 3.05 is not accurate. All of our glasses are normalised using an absorbance measurement which corresponds to a dose numerically close to 600 krad. This minimises the extrapolation error in FOM_{norm}.

Non-linear growth in absorbance with dose dictates that the figure of merit cannot be used to predict the induced damage at value which is significantly different from a measured dose. This figure is only useful when the measured dose is representative of the anticipated value in the final application.

3.3.3. Dynamic models of radiation induced damage

3.3.3.1. *Model 1*

During irradiation defects are created, these colour centres cause optical absorbance bands in the glass. Relaxation of defects by recombination also occurs. A dynamic equilibrium is established between centres populated as a function of dose and those centres which anneal as a function of time. A simple model for the change in the number of populated defect centres assumes a creation of defect centres at a rate which is proportional to the received dose. The model also assumes a constant probability of each populated defect relaxing as a function of time. The change in the population is given by the Ordinary Differential Equation (ODE),

$$dN = \alpha dD - \beta N dt \qquad \text{Equation 3.06}$$

The constant α (krad^{-1}) characterises the creation of colour centres, the constant β (s^{-1}) is an annealing time constant. Assuming a constant irradiation rate, $dD/dt = C$,

$$dN = \left(\alpha - \frac{\beta}{C} N\right) dD \qquad \text{Equation 3.07}$$

If $b \equiv \beta/C$ and initially $N = 0$ at $t = 0$.

$$N = \frac{\alpha}{b}\left(1 - \exp(-bD)\right) \qquad \text{Equation 3.08}$$

Solution of this ODE describes radiation induced absorbance growing as a saturating exponential and then recovering following a decaying exponential as a function of time after irradiation has finished. The equation below which describes annealing, assumes that the irradiation stops at $t=0$, at which time N_{max} radiation induced defects are present in the sample,

$$N = N_{\max} \exp(-\beta t) \qquad \text{Equation 3.09}$$

The number of absorbing centres is proportional to the macroscopic absorbance. This first level model has no absorbance wavelength dependence and assumes identical defects are created.

3.3.3.2. *Model 2*

Tanimura [8] has studied the development of radiation induced optical damage in HMF glasses. Samples of ZBL, ZBLA and HBL showed absorbance bands which could be described by slowly saturating exponentials. He compared his results with radiation damage studies on crystalline $RbCaF_3$ [9] and concluded that the slow development of bands in his HMF glasses was due to the creation of new defects. In contrast, radiation induced valence change phenomena are characterised by rapidly saturating behaviour [8].

Ohishi [10] irradiated ZBGA and ZBGAP fibres at room temperature and observed a linear increase in optical absorbance at 2.55 μm and 3.65 μm for the ZBGA and ZBGAP fibres. At higher doses, the absorbance saturated exponentially. Lead (denoted by 'P') in the ZBGAP glass has the effect of extending the linear growth region to 1 Mrad. The 2.4 μm band in ZBLA showed no linear region, damage followed a saturating exponential.

3.3.3.3. *Model 3*

Appourchaux [11] has irradiated a number of silicate based filter glasses and characterised their induced damage in terms of a saturating exponential term plus a linear term. He assumes that the ionising radiation creates colour centres from existing defects in the material, destroys colour centres and also makes new defects. The exponential term corresponds to the conversion of defects in to colour centres and the destruction of these defects. The linear term is related to the creation of new defects by irradiation.

$$\tau_{\lambda,D} = a_\lambda D + \sum_{i=1}^{n} t_{i,\lambda}\left(1 - \exp\left(\frac{-D}{d_{i,\lambda}}\right)\right) \qquad \text{Equation 3.10}$$

His definition of $\tau_{\lambda,D}$ given below is related to optical absorbance,

$$\tau_{\lambda,D} = \frac{-1}{e}\log\left(\frac{T_{D,\lambda}}{T_{0,\lambda}}\right) \qquad \text{Equation 3.11}$$

where $T_{D,\lambda}$ is the transmission. a_λ is the slope of the linear term (krad^{-1}cm^{-1}), t_λ is the saturation absorption coefficient (cm^{-1}), d_λ is the saturation dose constant in krad. The subscript, i represents the sum over the different types of colour centres.

3.3.3.4. *Observed behaviour in HMF glasses*

The induced damage which has been observed in the HMF glasses evaluated in this work does not show any fast saturation typical of valence change phenomena. Also, no linear growth of radiation induced absorbance with increasing dose has been observed. At a given wavelength, the radiation induced absorbance is adequately described by a saturating exponential in agreement with the ZBLA irradiation carried out by Ohishi [10]. Modelling the experimental data with an additional linear term as suggested by Appourchaux [11] does not produce a significantly better fit than a single exponential.

All of our radiation damage data has been fitted at 10 nm intervals to a single growing exponential. t_λ is the saturation absorption coefficient (cm^{-1}) for the current irradiation rate, $dD/dt =$ 1.2 rads^{-1}. The parameter, d_λ is the saturation constant in krad.

$$A_{D,\lambda} = t_\lambda\left(1-\exp\left(-\frac{D}{d_\lambda}\right)\right) \qquad \text{Equation 3.12}$$

The results from this analysis fall broadly in to two separate categories. The majority of glasses show a uniform growth rate of the radiation induced absorbance as a function of wavelength. This is indicated by a saturation constant, d_λ which does not vary significantly across the absorbance spectrum and relatively flat absorbance features. The flat nature of d_λ implies that all induced absorbance arises from one type of colour centre. If two centres cause the damage in a particular glass, their growth rates must be very similar.

The other category of glasses saturates more rapidly in the vicinity of UV edge. The dose constant falls off with increasing wavelength and maintains a reasonably constant value between $450 < \lambda < 650$ nm.

Our annealing studies contradict the simple recovery model (Model 1), the data is not described a single exponential. A large decrease in absorbance is initially observed but this slows for longer annealing times. This has been described elsewhere as a stretched-exponential behaviour [12],

$$A_t = A_{600krad} \times \exp\left(-\left((\beta t)^\alpha\right)\right) \qquad 0 \le \alpha \le 1 \qquad \text{Equation 3.13}$$

Complete recovery of radiation induced damage is never observed, a fraction of the populated defects are completely stable at room temperature. These observations indicate a range of defect stability. The amount of recovery as a fraction of the induced damage varies from glass-to-glass at room temperature.

The following two pages show an example of radiation induced absorbance and the subsequent recovery in a Samarium doped glass (P51). Figure 3.10 shows the optical absorbance as a function of wavelength at various different dose levels, it also shows the spontaneous recovery as a function of wavelength corresponding to various annealing times. The bottom graph shows the development of radiation induced absorbance at 350 nm, it is plotted as a function of dose with the fitted single exponential overlaid.

Figure 3.11 (top) shows the recovery as a function of time which is described by Equation 3.13, the fitted parameters are included in the graph . The fitted irradiation growth constant shown in the middle graph, it is reasonably constant as a function of wavelength. The final graph of Figure 3.11 shows the absorbance curve which corresponds to the damage saturating, this curve has been predicted from the data analysis.

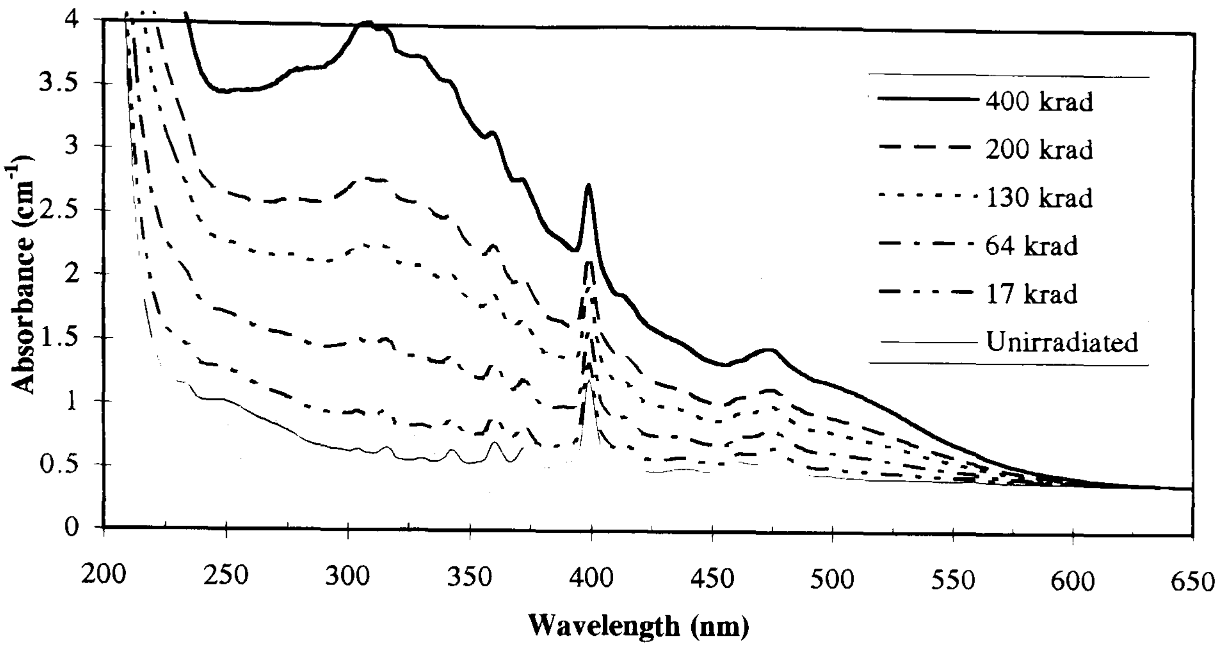

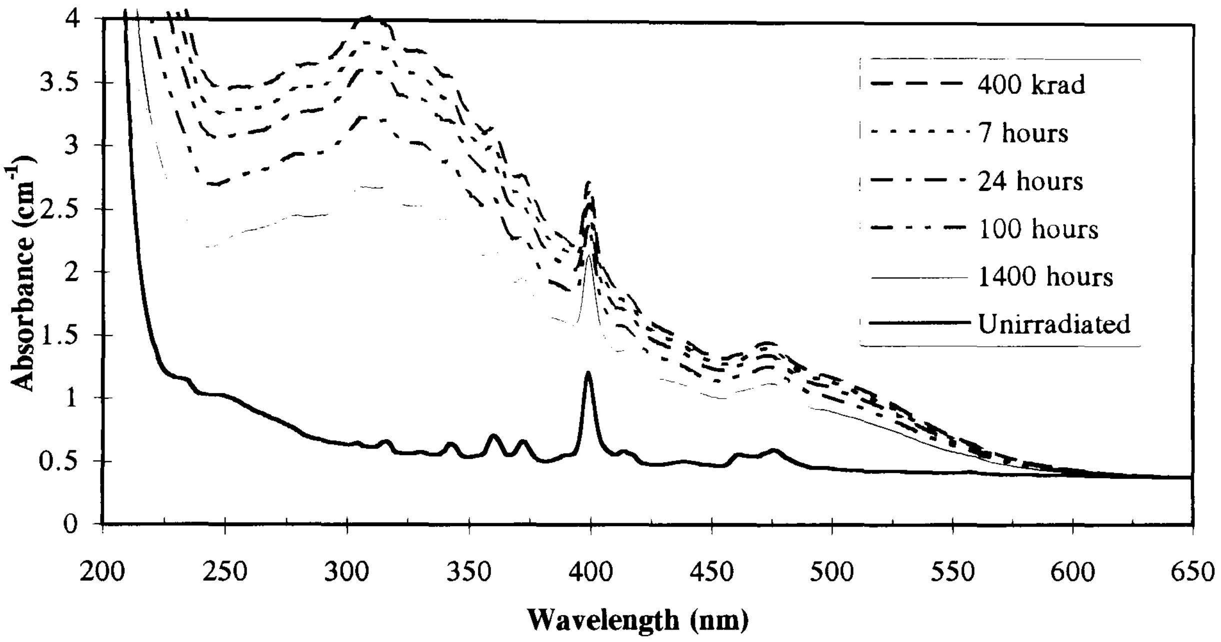

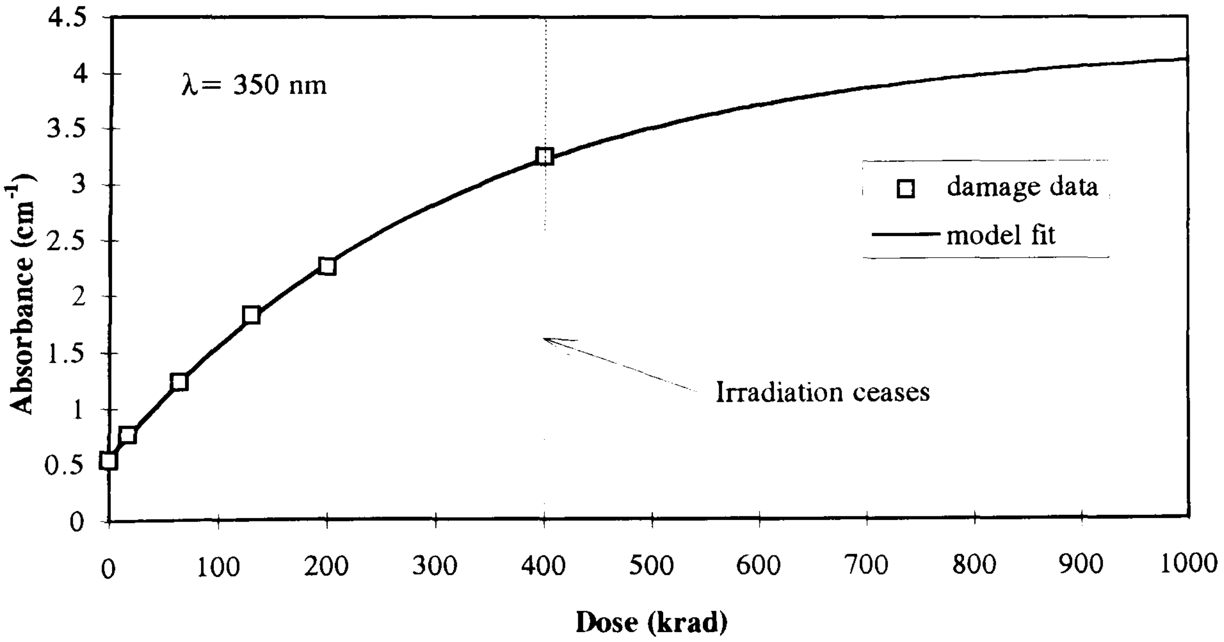

Figure 3.10 Radiation damage (top) and annealing (middle) data for HBALaSm glass (P51). The lower graph shows the exponential growth of absorbance at a fixed wavelength, the fit to a single expoenential is overlayed.

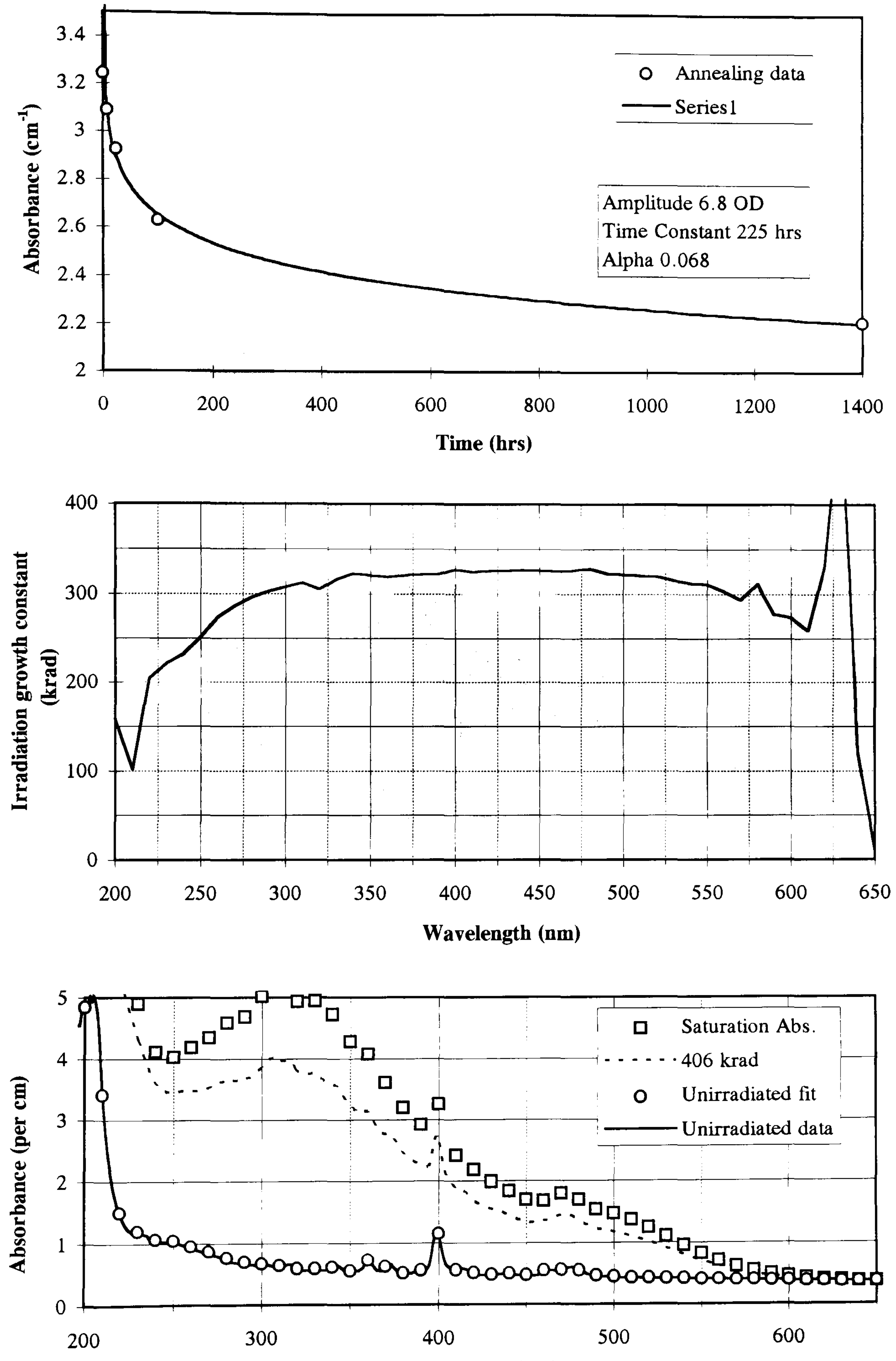

Figure 3.11 The annealing data for P51 (top) is described by a *stretched exponential*. The growth constant (middle) is reasonably flat in the region 250< λ <575 nm. The damage saturation (bottom) is calculated using the fitting routine.

3.3.4. Growth of individual defect centres

Radiation damage studies in crystals can give information about the structure of the material. The position of the peak energy of the F-band formed in alkali halides is a strong function of the lattice constant [13]. The Gaussian shape of the absorption band indicates how the F centre electron interacts with its neighbouring ions. Other colour centres can give an indication of the energy band diagram for the crystal. The Gaussian width of colour centre bands in crystals (FWHM≈ 0.3 eV) are narrower than those observed for glasses (0.5 to 1 eV) . This is explained by the wide variety of local environments in the glass matrix compared to a crystal in which the local environment of the defects are similar [13]. Appourchaux [11] gives a general expression for the macroscopic absorbance A_λ, which arises from Equation 3.10. At a given wavelength, the absorbance is the sum of several Gaussians.

$$A_\lambda = \sum_{i=1}^{n}\left[\sum_{k=1}^{p} f_{ik,\lambda}\left(t_{ik}\left[1-\exp\left(\frac{-D}{d}\right)\right]+a_{ik}D\right)\right] \qquad \text{Equation 3.14}$$

f is a function which is Gaussian when expressed in terms of photon energy, the sum with the subscript k indicates a sum over the absorbance bands for a particular colour centre. The sum over i considers different types of colour centres.

A relatively small proportion of our irradiated HMF glasses have discernible Gaussian structure in the spectrum of radiation induced absorbance. A multiple Gaussian fitting routine has been written to determine the positions, widths and heights of these radiation induced Gaussian features. A maximum of three Gaussians are fitted simultaneously by minimising a χ^2 function,

$$\chi^2 = \sum_{j=1}^{466} \frac{\left(A_E - \sum_{i=1}^{3} f_{iE}\right)^2}{(0.002)^2} \qquad \text{Equation 3.15}$$

f_{iE} again represents a Gaussian. The term, 0.002, in the denominator is the estimated error of the absorbance measurement. The fit to experimental data is displayed with the photon energy in the *x-axis* as the features are Gaussian in energy.

$$E = \frac{1240}{\lambda} \qquad \text{Equation 3.16}$$

Where E is in (eV) and λ is in (nm). Figure 3.10 shows irradiation measurements recorded at incremental radiation doses. At each incremental irradiation value, the data is fitted with three Gaussian functions.

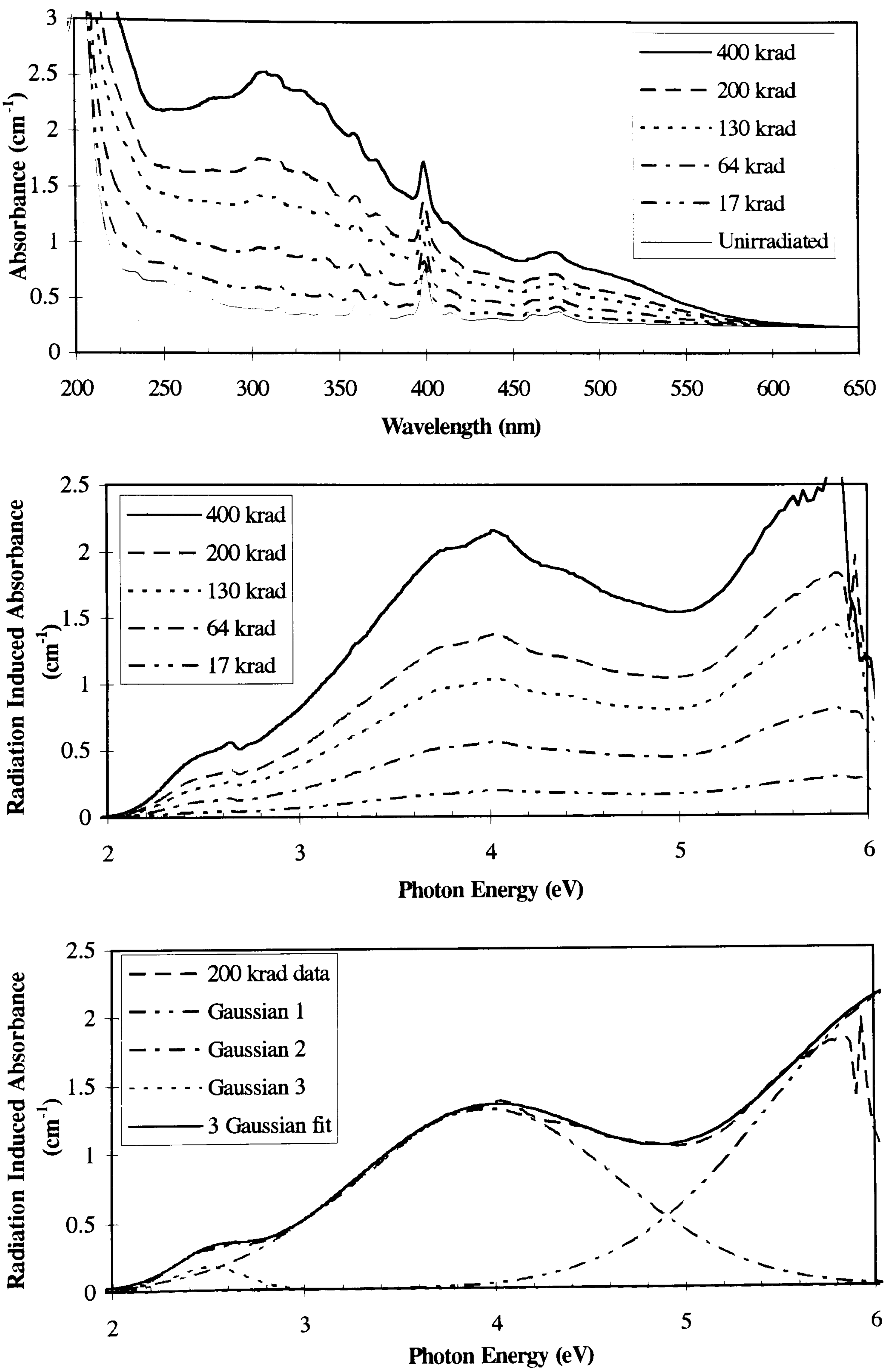

Figure 3.12 Radiation damage data for HBALaSm fluoride glass. The top graph shows absorbance data versus wavelength. The middle graph has the unirradiated absorbance subtracted from each curve and hence shows the radiation induced absorbance. The x-axis is expressed in terms of the photon energy (eV). The bottom graph shows how the experimental data for the 200 krad curve is composed of three Gaussian functions.

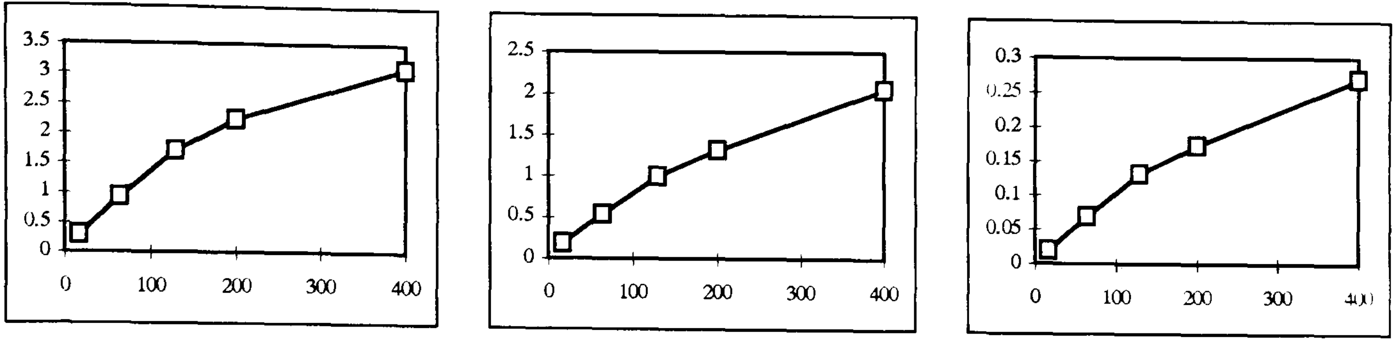

Gaussian Amplitude, $H_1(cm^{-1})$ versus dose (krad)

Gaussian Amplitude, $H_2(cm^{-1})$ versus dose (krad)

Gaussian Amplitude, $H_3(cm^{-1})$ versus dose (krad)

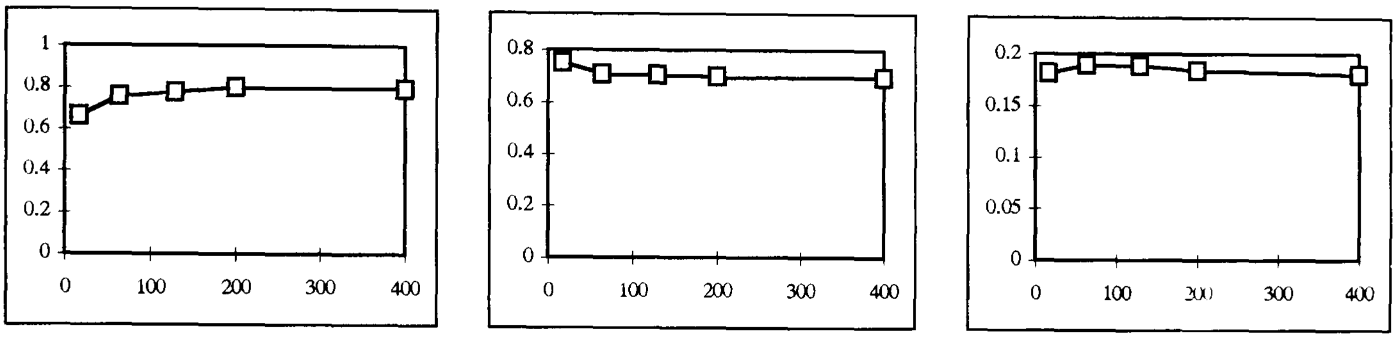

Gaussian width, σ_1 (eV) versus dose (krad)

Gaussian width, σ_2 (eV) versus dose (krad)

Gaussian width, σ_3 (eV) versus dose (krad)

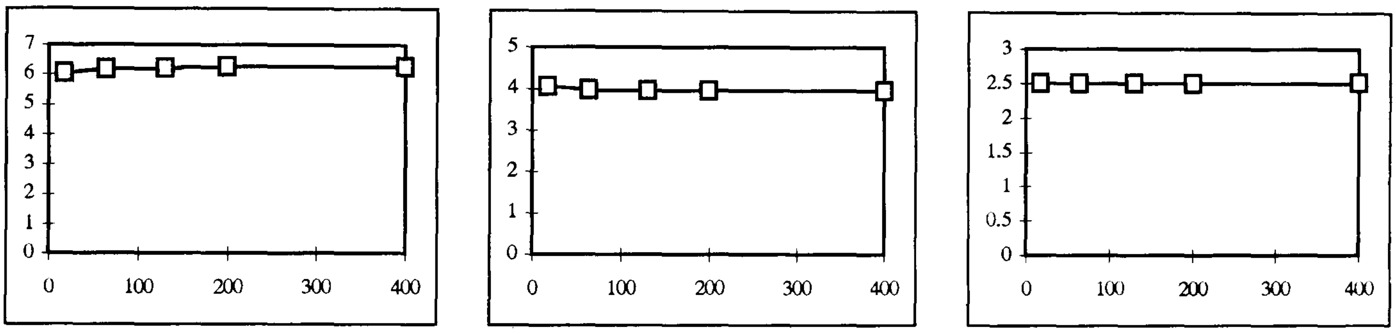

Gaussian Mean, μ_1 (eV) versus dose (krad)

Gaussian Mean, μ_2 (eV) versus dose (krad)

Gaussian Mean, μ_3 (eV) versus dose (krad)

Dose [krad]	Amplitude H_1 [cm^{-1}]	Mean μ_1 [eV]	Width σ_1 [eV]	Amplitude H_2 [cm^{-1}]	Mean μ_2 [eV]	Width σ_2 [eV]	Amplitude H_3 [cm^{-1}]	Mean μ_3 [eV]	Width σ_3 [eV]
17	0.29	6.05	0.66	0.19	4.05	0.75	0.02	2.50	0.18
64	0.93	6.19	0.76	0.54	3.97	0.71	0.07	2.50	0.19
130	1.71	6.22	0.77	1.00	3.96	0.71	0.13	2.50	0.19
200	2.24	6.26	0.80	1.31	3.95	0.70	0.17	2.51	0.18
400	3.09	6.24	0.80	2.05	3.95	0.69	0.27	2.51	0.18

Figure 3.13 The fitted amplitude, H_i (cm^{-1}), width, σ_i (eV) and mean, μ_i (eV) as a function of radiation dose (krad) for each of the three fitted Gaussians which describe the induced damage in HBALaSm (P51). The *means* and *widths* do not vary significantly as a function of radiation dose indicating a satisfactory analytical model has been used. The Gaussian *amplitudes* grow according to a saturating exponential as expected. The Gaussians grow similarly indicating that the absorbance bands probably arise from one colour centre.

Each Gaussian has three parameters, the mean (μ_i), the width, (σ_i) and the amplitude, (H_i). The fitting procedure has nine parameters to optimise, sometimes a satisfactory fit is obtained with just two Gaussian functions. The χ^2 for the fit and stability of the mean and the width of each fitted peak as a function of dose are indicative of the validity of the model. The amplitudes of the Gaussian absorbance bands increase with dose according to a saturating exponential. Figure 3.12 shows an example of the results from this fitting routine, the glass sample is a standard mix fluorohafnate glass which is doped with 1.5% samarium. The fit to absorbance data is shown for a dose of 200 krad. Figure 3.13 shows the values of fitted Gaussian parameters varying as a function of dose for the Samarium doped glass with the values tabulated in the same figure.

A full listing of the fitted absorbance bands for all glasses where this analysis was possible is given in Chapter 6. They are discussed and compared to absorbance bands identified in the literature.

3.3.5. Summary

The three methods discussed above for analysing radiation induced damage each have advantages and disadvantages. The single figure of merit has been used extensively despite its obvious inadequacies. It is ideal as a first level filter for identifying promising radiation hard CeF_3 based scintillators. It is easy to calculate and quick to comprehend.

Analysing the growth of radiation induced absorbance as a function of wavelength enables predictions of the induced damage spectrum at a given dose. This analysis corresponds only to a particular dose rate. To perform the fit to a single exponential at 10 nm intervals for the wavelength range $180 < \lambda < 650$ nm takes approximately one hour per sample. This includes importing the data, correcting, fitting, printing and storing the file. A similar procedure is required for analysis of the annealing data.

Fitting the induced damage in terms of growing Gaussian functions is of limited applicability because the majority of glasses do not possess distinct absorbance features. In cases where fitting is possible, the positions and widths of the Gaussian features when correlated with other studies, can give information on the underlying defects.

---

[1] A. Holmes-Siedle, private communication.

[2] *Photcoef*, AIC Software, P.O. Box 544, Grafton, Massachusetts 01519, USA.

[3] Perkin-Elmer Lambda 9 UV/Vis./NIR Technical Reference Manual.

[4] C. Woody et al, *Optical Bleaching in situ for Barium Fluoride Crystals*, CALT-68-1906 DOE Research and Development Report.

[5] S. Anderson et al, *Nucl. Instru. Meth.* **A332** (1993) 373.

[6] P. Lecoq, *Study of New Scintillators by the Crystal Clear Collaboration*.

[7] W. Zhou et al, *Preparation and Characterisation of CeF_3-Doped High Density Heavy Metal Fluoride Glasses: II, Doped Glasses*, presented at the 9th International Symposium on non-oxide glasses, Hangzhou, China, May 94.

[8] K. Tanimura et al, *J. Non-Cryst. Solids* **70** (1985) 397.

[9] L. Halliburton, et al, *Phys. Rev.* B **23** (1981) 6765.

[10] Y. Ohishi et al, *Elect. Lett.* **19** (1983) 830.

[11] T. Appourchaux, *Optical Engineering* **33** (1994) 1659.

[12] A.I. Gusarov et al, *Sov. Phys.* JETP **70 (2)** (1990) 289.

[13] J. Schulman and W. Compton, *Color Centers in Solid*, Pergamon Press, Oxford (1962).

CHAPTER FOUR

Determination of Scintillation Time Constants: Acquisition

4.1. Introduction

In Chapter 1 the Large Hadron Collider (LHC) and one of its experiments, the Compact Muon Solenoid (CMS) have been introduced. The operating parameters and environment of accelerators such as the proposed LHC necessitate improvements in many aspects of detector design if the ultimate Physics goals of the associated experiments are to be realised.

Commercially available scintillating materials which have been employed successfully in the ECAL of previous experiments (Crystal Ball, Crystal Barrel, CLEO, CUSB, and L3) are not suitable for the LHC. Radiation tolerance, density, scintillation output, cost or scintillation time constants preclude their use. Our research has pursued the development of HMF glasses for this application.

Determination of the temporal distribution of scintillation light is essential in assessing the suitability or otherwise of proposed scintillators. This chapter discusses the scintillation process and the experimental work carried out at Brunel University. Development of the apparatus and the measurement method has been a continual process of stepwise refinement over a period of two years. There are three main implementations discussed. The fundamental limitations and relative merits of each system are presented.

Fitting mathematical expressions which describe the time structure of scintillation light is deferred until Chapter 5.

4.2. Nature of Scintillation Light

The kinetic energy of charged particles, or the photon energy, is converted into UV/ visible light during the process known as scintillation. The interaction can be subdivided into three separate parts; excitation of the scintillating material, transport of excitation energy to luminescent centres and de-excitation resulting in the emission of photons. These are discussed below.

4.2.1. Excitation

Radiation interacts with the scintillator producing excitation and ionisation of lattice electrons by processes discussed in Chapter 2. The spatial distribution of excited charge depends on the energy of the incident radiation, its type, and the material with which it is interacting. Photons from typical radioactive sources can deposit all of their energy within a relatively small volume of material. All of the photon energy can be collected in a few cm^3 of Na(Tl)I, for example.

High energy electrons or photons *shower* in the absorbing material as described in Chapter 1. The shower develops along the path of the primary particle (or photon), the depth at which the maximum of the shower occurs increases with the logarithm of the beam energy. The energy of the impinging particle is transferred to the lattice causing electronic excitation in the vicinity of the shower. The mechanisms occurring during the excitation process are well understood [1].

4.2.2. Transfer

Excitation results in a large number of electrons becoming ionised to the conduction band of the material within a very short period ($<$ 1 ns). In Chapter 2, the various de-excitation pathways were considered. The main focus was defect formation by radiolysis, this involves de-excitation of high energy exciton states. For emission of scintillation light, electrons must become trapped at luminescent centres. This will involve migration through the material and then trapping at the active site. Recombination and trapping of electrons in optically inactive centres throughout the lattice interfere with the transfer. They can lead to formation of colour centres or cause slow scintillation components by acting as temporary traps. Naively, in the absence of any preferential transport mechanism to optically active sites, one would expect the number of electrons de-exciting optically to scale with the fraction of the active species.

4.2.3. De-excitation

The vast majority of excited electrons interact with lattice phonons as they move through the absorbing material until they are demoted to energy levels at the lower edge of the conduction band. The electrons become localised at a point in the lattice and recombination with hole states in the valence band can take place either directly or via further phonon exchange.

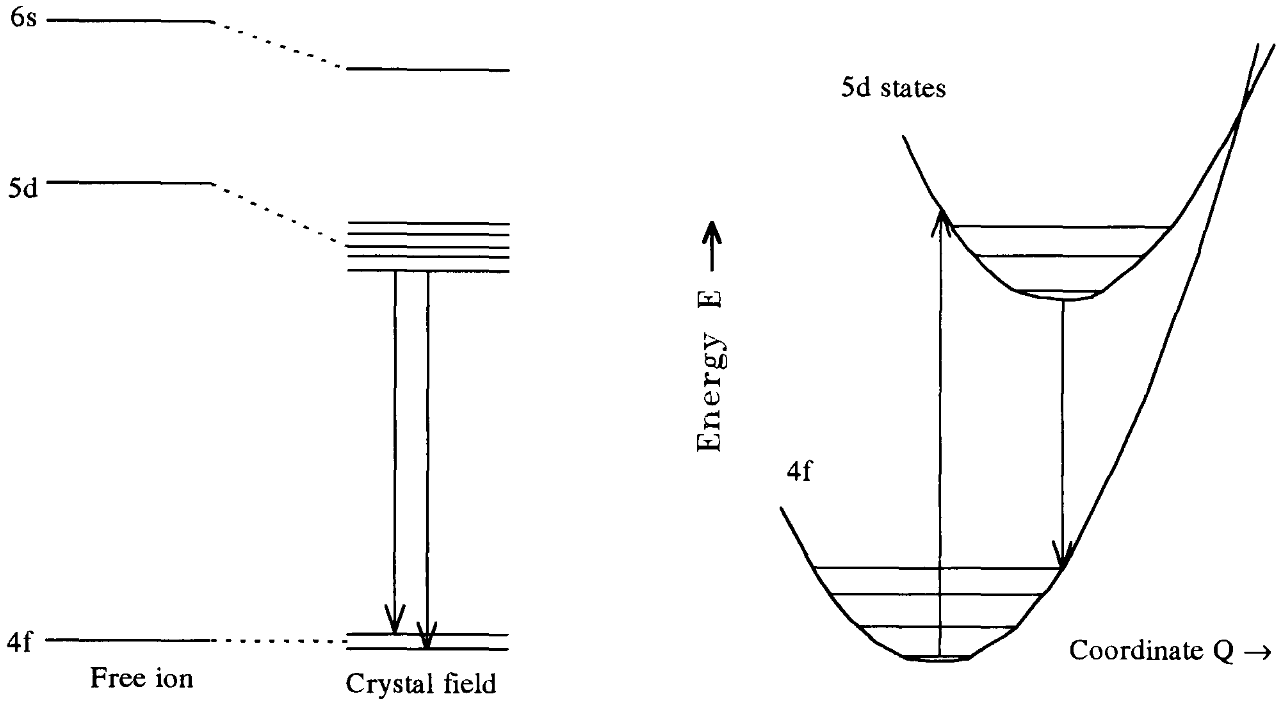

Figure 4.01. Energy levels of crystalline CeF_3. The optical transition is from the five times split 5d level to the 4f level which is twice split [2].

Electron de-excitation occurring from a luminescent centre via an optical pathway results in the emission of scintillation light. For high light yield, optical de-excitation must compete favourably with other relaxation mechanisms. The energy level diagram for a CeF_3 crystal is shown in Figure 4.01. Electrons are excited to the 5d level which is split five times by the crystal field. These electrons de-excite directly to the split 4f level, emitting a scintillation photon.

There is an additional process which affects the amount of scintillation light reaching the surface of a scintillator. Optical absorption of light when travelling from its emission point in the bulk of the scintillator to the external surface where it can be detected, can severely degrade the measured light yield. For efficient transport, the light must not be *self-absorbed*. This can be accomplished by the luminescent centre recoiling when the scintillation photon is produced. The photon is consequently emitted at a longer wavelength as the recoil atom takes some fraction of the available energy. When the photon energy is smaller than the band gap of the material re absorption is not possible.

4.2.4. Time structure of scintillation light

In small samples of scintillator, the excitation process occurs rapidly (< 100 ps). The development of a high energy shower takes ≈ 1 ns due to its longitudinal propagation (30 cm). Transfer to luminescent centres, in *most* materials occurs in a short time interval. Hence for all but the fastest scintillators ($\tau_d < 10$ ns), the promotion of excited electrons to upper energy levels is considered to be faster than the final emission of scintillation light. De-excitation of each optical site is independent. If the electrons are all trapped in identical sites within the lattice, then the probability, $P_{C\rightarrow V}$, of one electron de-exciting in a time period, *t*, is constant.

The number which de-excite in a particular time interval is proportional to the number in excited states occupied.

$$-dn \propto n_t dt \qquad \text{Equation 4.01}$$

Integration gives the number of photons emitted as a function of time,

$$n_t = n_o \exp(-t / \tau_d) \qquad \text{Equation 4.02}$$

This is a decaying exponential where n_o is the number of optically active sites populated initially. τ_d is the time constant for scintillation emission and is characteristic of the upper optical state de-excitation probability, $P_{C\rightarrow V}$.

This is a simple, idealised case. In reality, the local environment of trap sites may vary throughout the material due to local structural disorder. This will be the case for glasses, by definition. The variation means that there will be a distribution of optical decay probabilities which may lead to a deviation from the idealised exponential light emission.

Temporary trapping at non-optical sites followed by trapping at optical sites and subsequent optical emission will lead to slow scintillation components. This first-order corruption will introduce an additional component, $n_{t(trapped)}$ which is the convolution of non-optical and optical emission equations. $n_{trap(non-optical)}$ represents the number of non-optical trap sites which are populated initially, f represents the fraction of electrons which are trapped at optical sites after being emitted from non-optical sites. $\tau_{non-optical}$ and $\tau_{optical}$ are the decay constants for non-optical and optical trap sites respectively.

$$n_{t(trapped)} = n_{trap(non-optical)} \exp(-t / \tau_{non-optical}) \otimes f \exp(-t / \tau_{optical}) \qquad \text{Equation 4.03}$$

If $\tau_{non-optical} \gg \tau_{optical}$, the equation simplifies to a single exponential with a time constant equal to the non-optical term.

Additionally, the energy level diagram for the material may be such that there is more than one route by which optical de-excitation may proceed. Each pathway will have a different time constant and also different emission spectra. A decay time spectra will not have a single exponential but a number of superimposed exponentials each with different decay times and amplitudes. Despite the additional complications discussed here, the scintillation light emitted by most materials is adequately described by a number of super-imposed decaying exponentials.

4.3. Measurement of Time Constants

There are various methods which may be employed for the measurement of scintillation decay time. The scintillator under test and the required accuracy dictate the choice. A simple method which can quickly tell the ratio of fast scintillation to total light uses a gated charge sensitive amplifier and a PhotoMultiplier Tube (PMT) to measure the light output. The width of the gating pulse is varied to give the fraction of scintillation light which is given out promptly. This method can be used to identify those scintillators which have a slow scintillation component but cannot give the time constants accurately.

A second method which gives the decay times of the scintillation components uses a fast photomultiplier to view the scintillator. Individual pulses from the phototube are recorded using a digital oscilloscope. Many thousands of individual scintillation interactions are superimposed to obtain the time structure of scintillation light.

It is advantageous to use a separate source to trigger the oscilloscope because of timing jitter which results from variation in the shape and amplitude of the individual pulses form the test scintillator. The trigger is usually produced by a separate scintillator system which is excited synchronously with the test scintillator. Ringing in the phototube output and after-pulses can distort the measured timing spectrum. This particularly affects long time components. To form a trigger pulse and also deposit sufficient energy in the test scintillator, the interacting radiation must be energetic and penetrating. A typical implementation uses a high energy test beam as the excitation source.

The third alternative is called the *single-photon method*. A system which uses this method has been developed at Brunel University and used in the characterisation of over 100 different samples of glass. This method and its implementation is discussed in the following sections.

4.4. The Experimental Work Undertaken

Various implementations of the *single photon* apparatus have been studied extensively in this programme of work. Development has resulted in a system which can collect satisfactory timing data for materials with a wide variety of scintillation properties. Three different acquisition systems have been critically evaluated. Limitations which constrain the timing performance for each system are discussed.

4.5. Single Photon Method

4.5.1. Background Theory

Consider exciting a test scintillator at t=0, such that only one optical site becomes populated. The electron in the optical site will have a fixed probability of de-exciting in a time interval, *dt*. After some characteristic time, *t* the electron falls to the lower optical level and a scintillation photon is emitted. The time interval between excitation and optical emission is characteristic of the decay constant of the scintillator.

The single photon technique involves measuring the time delay corresponding to many thousands of individual scintillation events where only a single photon is detected. Recording events using this criterion ensures that timing data are selected randomly. Data are stored in a histogram whose x-axis corresponds to the time delay. The probability of detecting a scintillation photon within a time interval t→ t+dt after the sample is excited is proportional to the intensity of light emitted in that interval. The population of the histogram is representative of the time structure of the light emitted from the scintillator.

One must now consider what occurs when the single photon condition is not satisfied. In the classic arrangement [3], if two photons are detected, the acquisition system will only record the timing of the first photon to arrive. The second will be ignored, a fraction of the experimental data is biased as the photons are not selected at random. Instead, photons which arrive early are systematically favoured over photons which arrive late. The resulting time distribution contains too few events corresponding to longer decay times.

In the situation where two optical sites are populated and two scintillation photons are subsequently emitted, de-excitation of each site is independent. The probability of each site depopulating is the same as in the case of single optical excitation. However, since there are now two sites which can depopulate, the probability of detecting at least one in the time interval, t→ t+dt has doubled (compared to the case of single optical excitation).

$$-\frac{dn}{dt} \propto 2 \times n_t \qquad \text{Equation 4.04}$$

Always detecting the first of two photons instead of just one photon would give a timing spectrum whose decay constant, τ_d, was half of the correct value. Similarly detecting always the first of three photons per event would lead to a decay constant which is three times smaller than expected.

In reality, it is not possible to always detect three photons or two photons per scintillation event. Unless alternative measures are taken, the number detected will be governed by a Poisson distribution. The ratio of single : double : triple photon events will depend on the Poisson mean, μ. A timing distribution recorded using excitation where the number of photons detected per event is governed by Poisson statistics will have the functional form:

$$n_t = K \times \sum_{m=1}^{\infty} \frac{\exp(-\mu)\mu^m}{m!} \exp\left(\frac{-m \times t}{\tau_d}\right) \qquad \text{Equation 4.05}$$

For a scintillator which has a single decay constant, τ_d, the timing spectrum has a population, n_t which is the sum of all Poisson components. Their relative amplitudes are a function of the Poisson mean, μ. K is a scaling constant. Given the raw timing spectrum it would be extremely difficult to extract the correct decay time even if the Poisson mean was known accurately. Multiple photon data becomes even more complicated when the scintillator under investigation has more than one scintillation time constant. Excluding all events which result in the detection of multiple photons is the superior approach to determining τ_d.

4.6. Experimental Arrangement

4.6.1. Introduction

Measurement of scintillation decay time by the single photon method was first described in 1961 by Bollinger and Thomas [4]. The present apparatus employs a ^{22}Na source. This decays by emitting a positron which subsequently annihilates with an electron producing two photons which are emitted *back-to-back*. Conservation laws constrain the 511 keV annihilation photons to be emitted simultaneously at close to 180° to each other. In the experimental arrangement, one of the photons interacts in the trigger scintillator system, this accurately defines the start of the scintillation event, t=0. The other photon of the pair is constrained by geometry to intercept the test scintillator. Light produced in the test material is attenuated to ensure that the single photon condition is obeyed. The time difference between the start and stop signals is recorded.

4.6.2. Apparatus

The experimental arrangement shown in Figure 4.02 has been constructed for the measurement of scintillation time constants in the present work. The system incorporates two phototubes which have been optimised for fast timing, by P. Hobson and T. Price [5], a copy of this published work is presented in the Appendix 3.

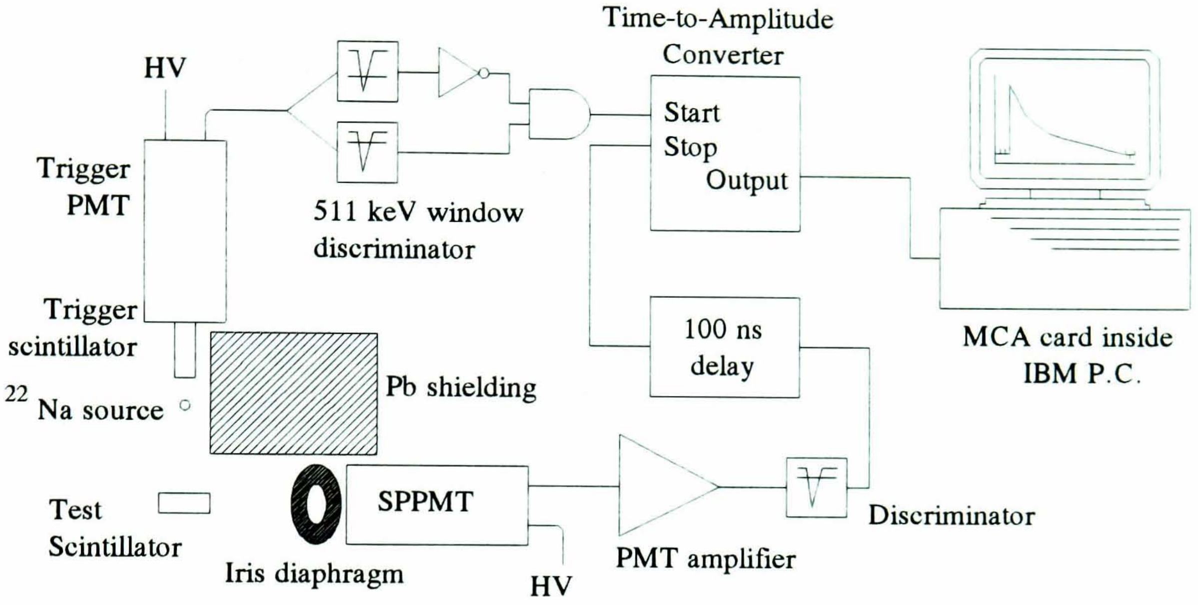

Figure 4.02. The *conventional* equipment used for recording timing data using the *Single Photon Method*. The Single Photon Photomultiplier Tube (SPPMT) detects light from the test scintillator.

Mechanical alignment of the various components of the system is important as it affects operational stability and repeatability. A system based on the Macrobench™ optical standard has been designed and constructed. Figure 4.03 shows the design. The various components which make up the system are discussed below.

4.6.3. The Trigger detector system

A 28 mm, quartz window Thorn EMI phototube model 9127Q is used for the trigger system. The voltage divider network has been optimised for fast timing applications in previous work [5] and is shown in Figure 4.04. Zener diodes are used to clamp the k-d_1 voltage to 300V. The tube is operated at 1800V. Barium Fluoride is used for the trigger scintillator. The end face of the $40\times 5\times 5$ mm^3 crystal is positioned centrally on the photocathode.

The scintillator is wrapped in three layers of PTFE tape for efficient light collection. Although superior timing performance can be achieved by coupling the scintillator to the phototube window by a suitable grease, none is used. Grease contamination would cause the reflectivity of the PTFE wrapping to deteriorate. Additionally, leaking of grease from the joint can also lead to variation in performance over time. As the timing performance of the whole system is not limited by the photon statistics associated with the trigger system, the scintillator is air coupled to maximise long term stability.

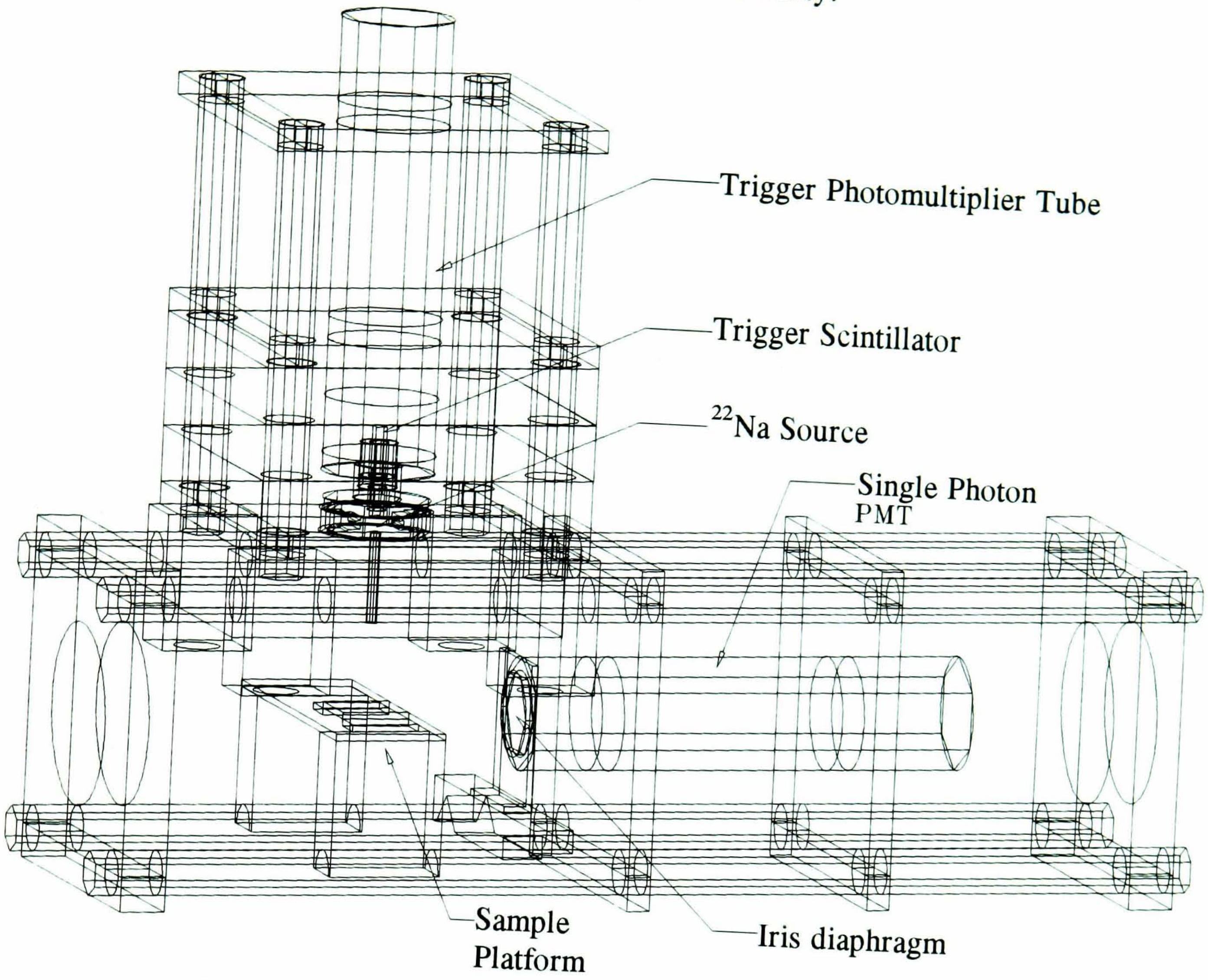

Figure 4.03. A wire-frame model of the single photon apparatus. The light intensity falling on the Single Photon PMT can be reduced by closing the iris diaphragm or retracting the SPPMT from the test scintillator. Lead shielding isolates the SPPMT from the source.

The photon attenuation coefficient of barium fluoride is 2.29 cm for 511 keV photons [6]. 83% of axial photons will interact in the 4 cm long trigger scintillator. Barium fluoride produces 10,000 photons per MeV. 20% are emitted in a 0.6 ns fast component at wavelengths of 190 and 220 nm. The remainder are emitted at 310 nm with a decay constant of 620 ns. The phototube has a quantum efficiency of 22% [7] for the 0.6 ns emission.

Timing is derived only from the fast component. Due to imperfect wrapping and mis-match of refractive index at the interface, one would expect to collect roughly 33% of the scintillation light. If the values above are correct then 150 prompt photoelectrons are produced at the photocathode. Our previous work [5] has shown that this number is sufficient for fast timing applications.

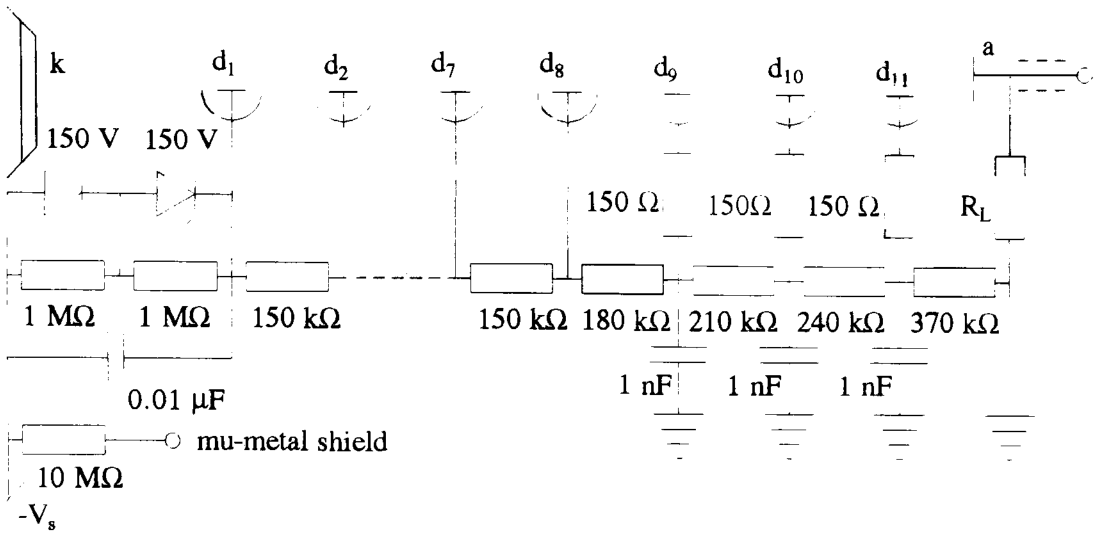

Figure 4.04. The divider network uses Zener diodes to maintain the voltage between photocathode and d_1 at 300V.

The output pulse from the PMT is divided using an impedance matched splitter. Both signals are used in a window discriminator. The discriminator is centred on the photopeak which corresponds to the 511 keV annihilation photons. ^{22}Na can also decay by emitting a 1275 keV photon which is not spatially correlated to any *back-to-back* photon. The energy spectrum for the trigger PMT is shown in Figure 4.05 with the discriminator levels indicated. The window discriminator acts as a veto for some 1275 keV events. Although erroneous triggers are still produced by those Compton events from the 1275 keV component which deposit approximately 500 keV in the barium fluoride. From Figure 4.05, the fraction of false start pulses is estimated to be 25%.

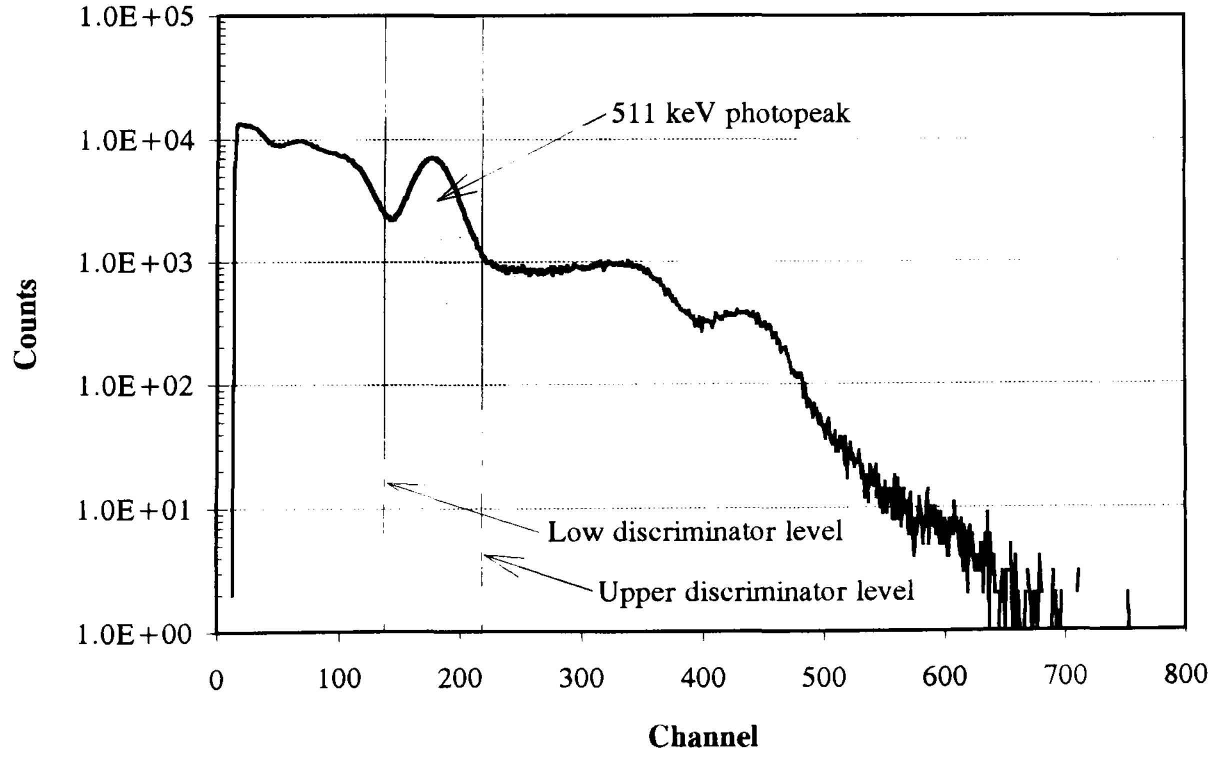

Figure 4.05. ^{22}Na energy spectrum measured using the 40× 5× 5mm^3 BaF_2 trigger phototube. The levels of the window discriminator which enclose the 511 keV photopeak are indicated.

4.6.4. Single photon tube

The second phototube detects single photon pulses from the test scintillator. It is configured differently to the trigger system. Every effort is made to attenuate scintillation light from the test material. The phototube is a 28 mm diameter Thorn EMI 9128Q. It has a quartz window and differs from the 9127Q in the respect that it has a curved photocathode. This minimises the variation in transit time between photoelectrons produced at different positions across the photocathode [5]. The quantum efficiency is shown in Figure 4.06 The PMT is oriented normally to the direction of the incident radiation to avoid detection of Cerenkov photons from relativistic electrons traversing the quartz window of the PMT.

To detect single photons, the phototube is operated at a voltage of 1800V. The output pulses are too small for the discriminator and require amplification by a PM amplifier. This boosts their amplitude by a factor of ×10 to approximately 40 mV.

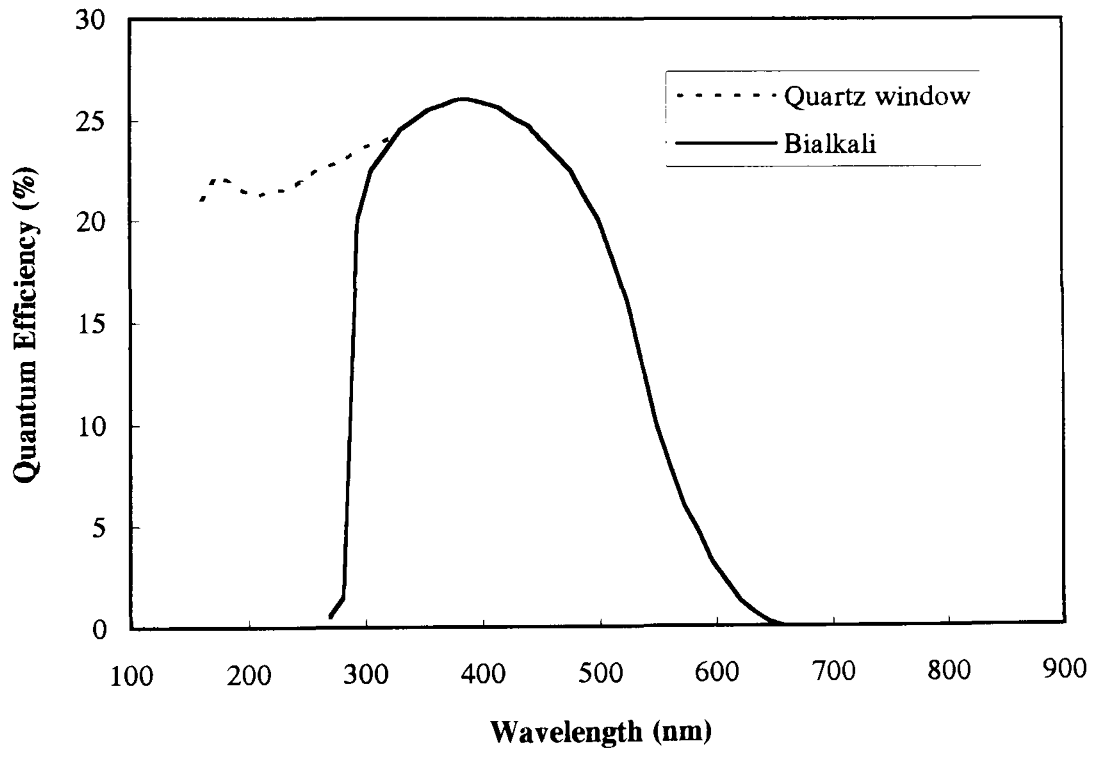

Figure 4.06. Typical quantum efficiency plot for the 9127Q and 9128Q photomultipliers. The PMTs used in this work had quatrz windows [7].

The gain of the phototube approximately doubles for an increase of 100V in its operating voltage. Without the PM amplifier, it would be necessary to operate the phototube at 2200V for 40 mV output pulses. At this voltage, the rate of noise counts from the tube is excessive. There is a compromise between the single photon pulse height and the rate of noise counts.

To reduce the amount of light incident on the window of the photomultiplier, the test scintillator is not wrapped and is not coupled to the phototube window. To control the amount of light incident, the phototube can be moved back from the scintillator. There is also an iris diaphragm to further attenuate the scintillation light. Using these two methods, the light level falling on the detector can be varied over three orders of magnitude. Single photon pulses from the phototube which exceed the discriminator threshold give a valid *stop* signal.

4.7. Conventional Method

This implementation is shown in Figure 4.02. An EG&G model 566 Time-to-Amplitude-Converter (TAC) is used to measure the timing of single photon stop pulses relative to the trigger pulse. Upon receipt of a start pulse, the TAC ramps a voltage from zero at a fixed rate. If no stop pulse is received in the time window of the TAC, it is reset and no output pulse is generated. If a stop pulse is received, the voltage ramp is stopped and a positive voltage pulse is seen at the output of the TAC. Its duration is set at 0.5 μs and its amplitude varies between 0 and 10 V. The voltage given out is directly proportional to the time difference between the start and stop pulses. Subsequent stop pulses are ignored. After producing the output pulse, the TAC is sensitive to further *start* pulses. For this program of work, the majority of measurements were recorded using a time window of 2000 ns.

The magnitude of output pulses from the TAC are measured by an 11-bit Analogue to Digital Converter (ADC) in the EG&G 916A Multi-Channel Analyser (MCA). Upon receipt of a TAC pulse, the ADC measures its maximum amplitude, this entry is placed in a histogram which is displayed on the computer screen. The MCA is then ready to receive the next event. The MCA has a dead time of 1 μs.

4.7.1. Set-up/ Calibration

4.7.1.1. Selecting the Poisson Mean

For a given test scintillator, the mean number of photons detected in the Single Photon Photo-Multiplier Tube (SPPMT) per radiation interaction is determined by the aperture of the iris diaphragm and the separation between the test scintillator and the SPPMT. Assuming isotropic light emission, the intensity falls off according to the inverse square of the separation.

As the actual number of photons incident on the photocathode is governed by a Poisson distribution, it is not possible to attenuate the light sufficiently to always have just one photon incident on the photocathode per radiation interaction. Attenuating the light merely adjusts the fraction of events which result in the detection of none, one, two, ... photons. By selecting a low value for the Poisson mean μ, the timing spectrum will contain predominantly events recorded where only a single photon was detected. However, the rate at which data is accumulated decreases rapidly with μ.

A good event is defined as one in which a single photon was detected, this has a probability

$$G = P(1, \mu) = \mu \exp(-\mu) \qquad \text{Equation 4.06}$$

Bad events are detected with more than one photon in the time window,

$$B = \sum_{n=1}^{\infty} P(n, \mu) \approx \frac{\mu^2 \exp(-\mu)}{2} \qquad \text{Equation 4.07}$$

In these equations it is assumed that, $\mu \ll 1$. The ratio of biased to unbiased events is

$$\frac{B}{G} \approx \frac{\mu}{2} \qquad \text{Equation 4.08}$$

If μ is set to 0.02 photons then 99% of detected events ($n_p > 0$) will correspond to single photons. Unfortunately, to obtain this level of purity it is necessary to attenuate the light to such a high degree, that 98% of all events are not detected at all ($n_p = 0$). There is an obvious reduction in acquisition rate if a high single photon purity is specified.

It is this factor which constrains the data acquisition rate for the *conventional* implementation of this method. The effects of Poisson statistics means that detection of multiple photons per event is inevitable. Consequently timing spectra will always contain a fraction of biased data.

4.7.1.2. Single Photon Calibration-setting discriminator thresholds

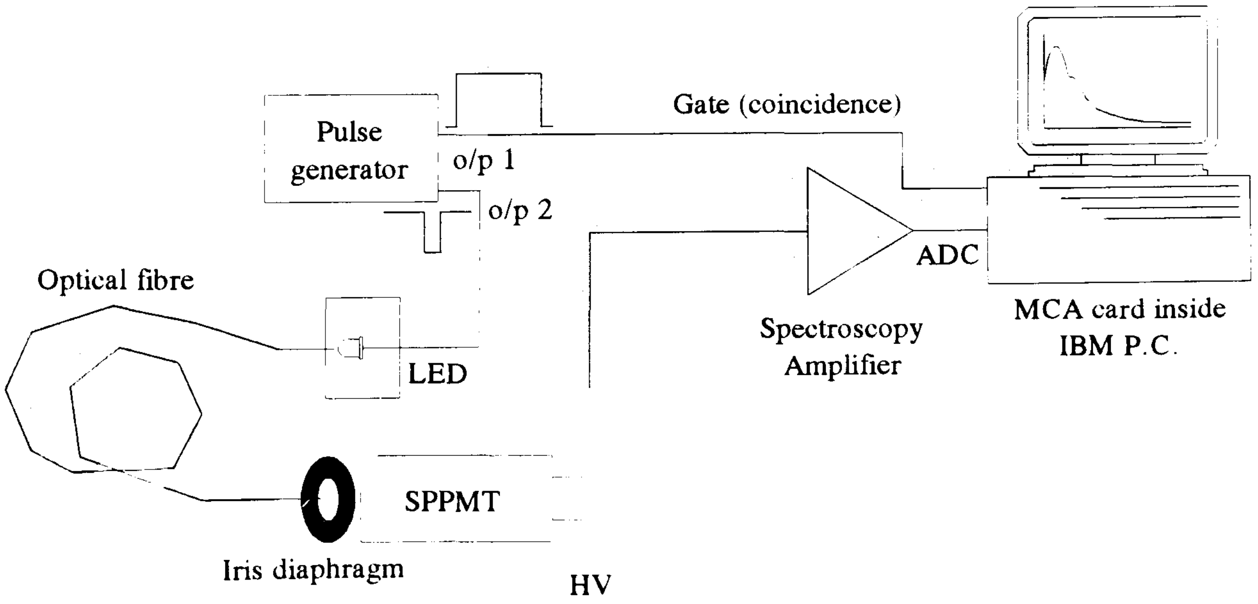

Figure 4.07. Apparatus used for the single photon calibration. The Single Photon Photomultiplier Tube (SPPMT) is isolated from any electronic pulse produced by the LED by an optical fibre. The MCA is gated in coincidence to reduce random pulses.

In order to estimate the mean number of scintillation photons detected by the SPPMT, it is necessary to measure the energy spectrum of pulses from this phototube. The energy scale was calibrated in terms of single photons. The experimental arrangement is shown in Figure 4.07.

A Lyons Instruments model PG73N dual output pulse generator is used to gate the MCA it also provides a driving pulse for the LED. Light from the LED enters an optical fibre whose other end is directed towards the phototube window. Coincident gating practically eliminates random counts from the energy spectrum of the phototube. A Canberra model 2021 spectroscopic amplifier is used to in conjunction with the MCA to measure the pulses.

Using a 1V, 20 ns driving pulse, the energy spectrum is approximately Gaussian in shape. As the pulse width is decreased, the mean of the Gaussian moves to a lower energy and its Full Width Half Maximum (FWHM) decreases. Eventually, reducing the LED drive pulse width does not produce a corresponding decrease in the mean of the distribution observed on the MCA. Instead the only effect is that the data accumulation becomes slower. In this situation, predominantly single photons are detected at the photocathode, see Figure 4.08, 'Low-level response'. Increasing the aperture of the iris diaphragm and keeping the same drive pulse width, results in a more pronounced shoulder on the high edge of the single photon response ('High-level response', Figure 4.08). This is due to detection of two photons. A high energy tail is observed which is due to detection of multiple photons, their larger Gaussian widths means that the tail has no discernible structure.

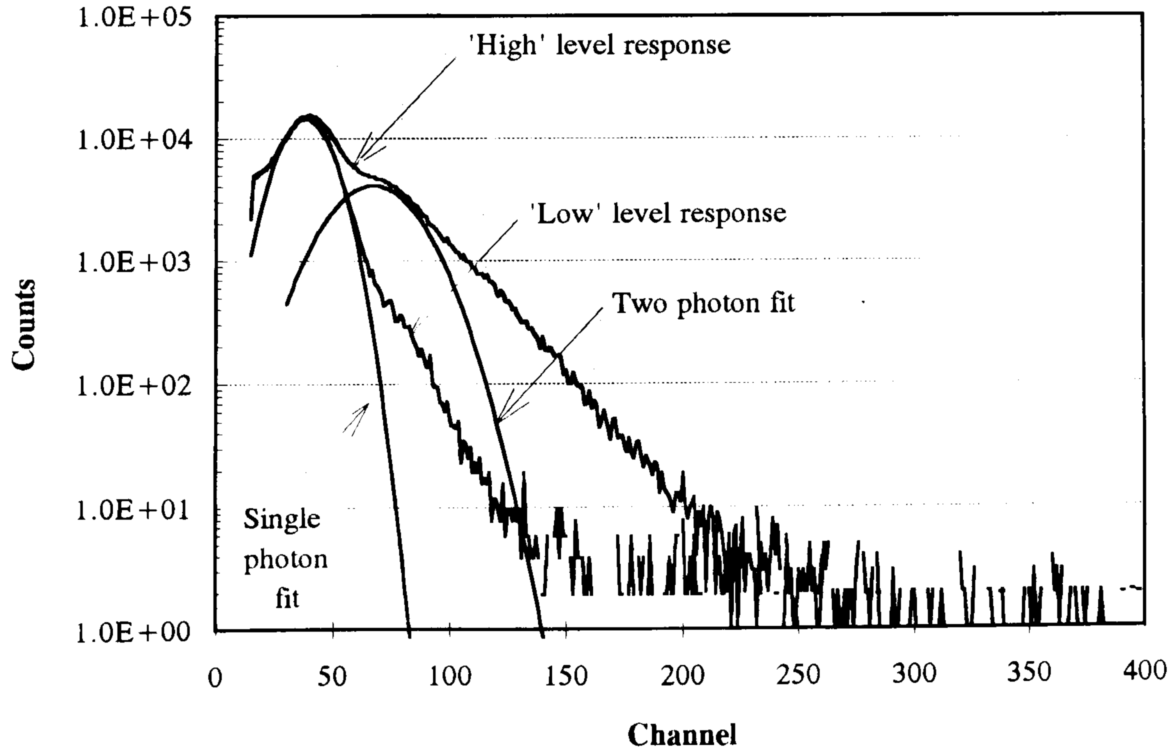

Figure 4.08. Single photon energy spectrum recorded using an LED as the optical source. Gaussian fits to the data are overlayed. Noise was partially suppressed by gating the acquisition system.

A fitting procedure has been used to estimate the parameters of the single photon Gaussian. This fit was then subtracted from the experimental data to leave only data corresponding to two or more photons. This data was now approximately Gaussian, with a high energy tail corresponding to events detected with >2 photons. The fitting procedure was again used to estimate the parameters of the *two photon* peak (labelled 'two photon fit'). The *means* of the single and double photon peaks are used as a calibration for the energy scale. It is only valid for small numbers of photons, but this is exactly where the SPPMT operates.

The LED system was also used for setting the level of the discriminator used for the SPPMT. An energy spectrum was recorded using the Canberra amplifier/ MCA combination viewing half of the SPPMT signal, Figure 4.09. The discriminator viewed the other half of the signal formed a veto for the MCA. This caused a cut-off in the energy spectrum which indicated the discriminator level in terms of single photons. The position of the cut-off was varied by adjusting the threshold of the discriminator until it was at the low edge of the single photon peak, above the electronic noise. A correction was applied to compensate as the discriminator was only viewing half of the PMT signal for the set up procedure. For all other work it viewed the entire signal.

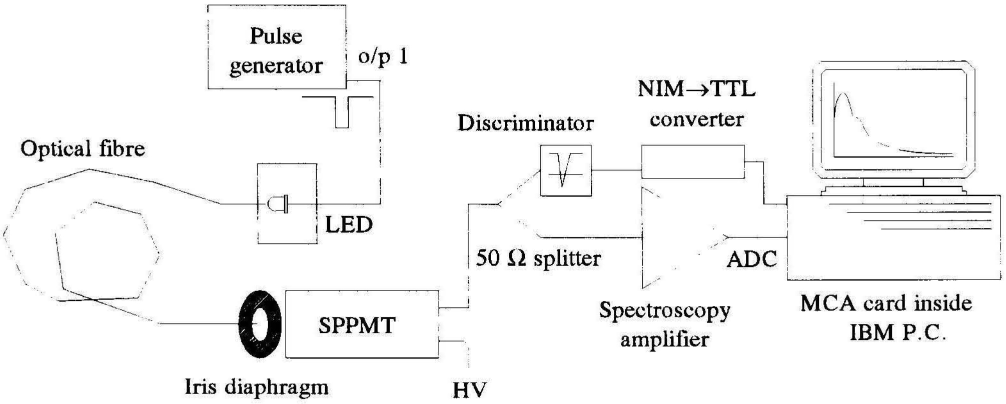

Figure 4.09. The LED was used to establish the level of the discriminator in terms of single photons by viewing the cut-off in the recorded energy spectrum.

Setting the levels of the trigger scintillator system was similar although it used events from the ^{22}Na source and the discriminators were set at the low and high edges of the 511 keV photopeak.

4.7.1.3. System Linearity / Time calibration

This was tested using a pulse generator at the input to the TAC. The signal was split, one branch entered the TAC *start* and the other branch entered the *stop* via a delay cable. A calibration was carried out by adjusting the delay and noting the MCA channel populated.

A least squares fit between the channel populated and the delay over the entire operating range at 100 ns intervals gave a correlation of 0.999991. Using 16 ns delay cables, the calibration was 0.9854 channels/ ns.

4.7.2. Operation

As the operating parameters of the single photon apparatus were kept constant, it was only necessary to recheck the discriminator thresholds periodically. In normal operation a scintillator was loaded onto the sample platform and its energy spectrum recorded. The optical signal reaching the SPPMT was reduced until the energy spectrum contains predominantly single photon events.

The time spectrum was then recorded. In addition to valid timing data arising from pairs of valid start-stop pulses, random pulses are seen in both phototubes.

4.7.2.1. Random events- causes

Random counts occur in both phototubes. In the case of the trigger system, 1275 keV events from the ^{22}Na source which deposit only a fraction of their energy can lead to start pulses from the discriminator network. In the case of the single photon tube, there are a number of sources of random pulses, in fact any processes which produce single photons will cause stop events. These include thermionic emission from the photocathode, direct interactions of the source with the phototube, radioactive decay of the materials from which the phototube is constructed, cosmic rays passing through the quartz window of the phototube, fluorescence of the phototube or the test scintillator or light leaks in the phototube enclosure. The majority of random counts are due to ^{22}Na interactions with the test scintillator which are not correlated with start pulses from the trigger system.

Great care has been taken to minimise all sources of non-correlated single photons where possible. The tube is operated at the lowest practical operating voltage to minimise counts arising from thermionic pulses. 5 cm thick lead shielding is used between the phototube and the ^{22}Na source to reduce direct interactions with the SPPMT. The light-tight enclosure where the experiment runs is only opened under very subdued light conditions and all samples are stored in the dark to minimise any effect due to long lived fluorescence. The light tight enclosure has been designed carefully to avoid leaks. It is tested periodically to confirm its integrity.

4.7.2.2. Random Events- effect

Random events in the two phototubes are, by definition, not correlated in time[§]. They lead to a background in the measured timing spectrum. If the random rates are low in both phototubes, the background is flat. If the rate of stop events is too high then the background has a negative linear slope due to the dead time of the TAC. With the exception of example figures presented in later sections of this chapter, all of the data in this thesis was recorded using sufficiently low random rates to give a flat background.

The start rate from the trigger scintillator system was approximately 1800 counts per second. The rates measured in the single photon phototube varied depending on the test scintillator and the experimental conditions. However a rate of 100 counts per second was typical. Using 1000 counts per second in the stop counter still resulted in perfectly flat backgrounds.

4.7.2.3. Cosmic Rays

At the surface of the Earth, the flux of cosmic rays is approximately 1 per cm^2 per min. Their zenith angle follows a $\cos^{2.1}\theta$ dependence. When the apparatus was designed, the interaction of cosmic rays was not explicitly considered. It was when the system was initially tested that cosmic rays provided the answer to what was observed.

With no test scintillator present, one naively expects no correlated events and hence a flat background from random events. Bin population is of course subject to statistical variations. When this was tested, in addition to the flat background, there was a low level of correlated start-stop events observed corresponding to zero delay in addition to the flat background. Removing the ^{22}Na source from the apparatus did not cause the correlated events to disappear or even diminish! After some thought, the only option which could explain the correlated phenomenon was cosmic rays.

A minimum ionising particle longitudinally traversing the barium fluoride trigger scintillator would deposit too much energy (6.6 $MeVcm^{-1}$) to be confused with a 511 keV photopeak. Cosmic rays showering near to the trigger scintillator could produce a similar size light pulse to the 511 keV photon response from the ^{22}Na. Also cosmic rays traversing the quartz window of the single photon phototube will exceed the Cerenkov threshold and

---

[§] Non-correlated events in the single photon PMT which have a certain degree of time structure are discussed in detail in section 4.9.5.

thus emit small numbers of prompt photons, typically a few. These fall upon the photocathode and hence the single photon condition is satisfied.

As a result of cosmic rays which pass through the BaF_2 trigger crystal and also the window of the SPPMT, pairs of prompt start and stop pulses are seen in the timing spectrum. To test this hypothesis, timing spectra were recorded as a function of the lateral displacement of the single photon phototube with no ^{22}Na source or test scintillator present. As expected, the rate of coincident events fell as the angle, θ was increased. When the tubes were laid side by side, ($\theta = 90°$) the timing spectrum contained no correlated events above the flat random background.

This is an amusing aside which does not affect the results particularly. It is useful as it provides an origin for the timing spectra. The level of cosmic events is usually significantly lower than events which arise from the ^{22}Na source except where the test material does not scintillate at all. These prompt events affect only the first few ns of the decay curve.

4.7.3. Concluding remarks

The ratio, *signal: background* depends on the value of the Poisson mean, μ. If the random background is large compared to the data which sits upon it, there will be a large statistical variation in the timing data which is due to the excessive background. This deteriorates the quality of the recorded data. There is a conflict of interests; the single photon condition must be satisfied above all else. But the data rate must not be allowed to become sufficiently low such that *signal: background* is compromised.

To obtain accurate timing data for a typical sample requires many thousands of events in the timing spectrum. The low detection efficiency dictated by the requirement for high single photon purity, means that acquisition times are necessarily large. A typical timing spectrum takes in excess of 24 hours to record and contains somewhere between 20,000 and 100,000 events.

Performance of the system is degraded by events which result in production of more than one photoelectron at the photocathode of the detector. These events are recorded in a biased way and systematically decrease the experimentally determined time constants. Minimising the fraction of multiple photon events gives the most accurate timing data. Although Poisson statistics make it inevitable that a finite fraction of events will always result in the detection of multiple photon events. Timing data recorded by a system which does not veto these events will not truly reflect the time structure of scintillation light.

The fundamental limitation of the single photon technique is the inherent inability to record timing information from second and subsequent photons to arrive at the SPPMT. Recently EG&G have produced a Multi Channel Scaler (MCS). This is capable of recording many stop events corresponding to a single start pulse. The evaluation of an MCS is discussed in the next section.

4.8. Evaluation of the Turbo-MCS

4.8.1. Introduction

An EG&G model 914 Turbo Muli-Channel Scaler (MCS) has been used for measuring the time structure of scintillation light. A PC interface card enables the MCS unit to be controlled and read out. This high-resolution multiple-stop time-spectrometer has selectable dwell time down to a minimum of 5 ns. The unit accepts either NIM or TTL inputs via front panel BNC connectors. The logic level is set by internal jumpers. Other front panel inputs enable the system to be monitored and controlled.

The scan length can be varied from 4 to 16,384 channels. Although there is claimed to be no dead time between channels, the maximum count rate on the 5 ns per channel range is 1 count per scan per channel. On the 20 ns to 70 ns per channel ranges this constraint is relaxed to 15 counts per scan per channel. In addition to the above, the maximum input rate is 150 MHz.

The conventional single photon apparatus which uses a Time to Amplitude Converter (TAC) has been discussed in detail. The system has two significant drawbacks. Experimental data produced by the apparatus are prone to error due to the inability of the system to detect photons in an unbiased way. Additionally, to satisfy the single photon condition, the acquisition rate has to be extremely low.

A Multi-Channel Scaler (MCS) has been incorporated into the delayed coincidence system, replacing the TAC and MCA of Figure 4.02. The potential advantage compared to a single-hit TAC is that the single photon condition no longer applies. The MCS is capable of detecting many *stop* photons for each event. The feasibility of increasing the data acquisition rate, whilst still maintaining acceptable data purity, has been investigated.

4.8.2. Operation

The MCS waits until a valid *start* signal is received. At the start of the next clock pulse, the MCS begins counting *stop* pulses for a predefined time, the *bin width*. This sum is stored and the scaler begins counting the number of *stop* pulses arriving in the next time bin. No counts are lost at the edges of adjacent bins. This procedure is repeated for adjacent time bins until the whole MCS time window has been scanned. The system is then sensitive to new *start* pulses. For decay time measurements it is necessary to sum the data for many thousands of scans across the time window.

The internal clock has a period of 10 ns. As the system waits for the beginning of the next clock pulse before starting to record data, there is an intrinsic timing jitter in the system. This arises from a variation in the delay when waiting for the next clock pulse after a *start* pulse has been received. By utilising start and stop pulses from a common source, the intrinsic system width has been measured. Theory predicts it to be rectangular in shape.

The minimum time bin width is 5 ns. Time bin granularity means that the measured intrinsic response is not 'square'. The width (10 ns) is significantly broader than that of the TAC based acquisition system (3.3 ns). This has implications for fitting equations to scintillation time constants which are very short. Measurements of these intrinsic widths and fitting equations to timing data is discussed in Chapter 5.

This system has true multi-photon capabilities. In contrast to the TAC based systems, the MCS is able to record the temporal properties of a large number of *stop* photons from each scintillation event. The system does however have a constraint. There is a dead time, *DT* associated with the detection of each stop event. If two stop pulses occur too closely to each other, the second pulse will be missed. Biasing of the timing data is evident. By sending the MCS two consecutive stop pulses which are separated in time by a variable delay, the system dead time has been measured. Minimising the width of input pulses results in a system dead time of 6 ns.

The following analysis is similar to Moses [8], it was developed independently. The probability of biased data when the system detects, n photons in the MCS time window, is the product of Equation 4.06 and the probability that any photon is detected in the next *DT* after the detection of any other photon.

$$P(n,\mu)P(any < DT) = \frac{\mu^n \exp(-\mu)}{n!}\left(1-\exp(-(n(n-1))\delta/2)\right) \qquad \text{Equation 4.09}$$

δ is defined as DT/τ_d. The probability of unbiased data is

$$P(n,\mu)P(none < DT) = \frac{\mu^n \exp(-\mu)}{n!}\left(\exp(-(n(n-1))\delta/2)\right) \qquad \text{Equation 4.10}$$

The ratio of biased events to unbiased events is,

$$\frac{B}{G} = \frac{\sum_{n=2}^{\infty} nP(n,\mu)P(any < DT)}{\sum_{n=1}^{\infty} nP(n,\mu)P(none < DT)} \qquad \text{Equation 4.11}$$

Figure 4.10 shows the variation of the fraction of biased events as a function of μ for various values of δ.

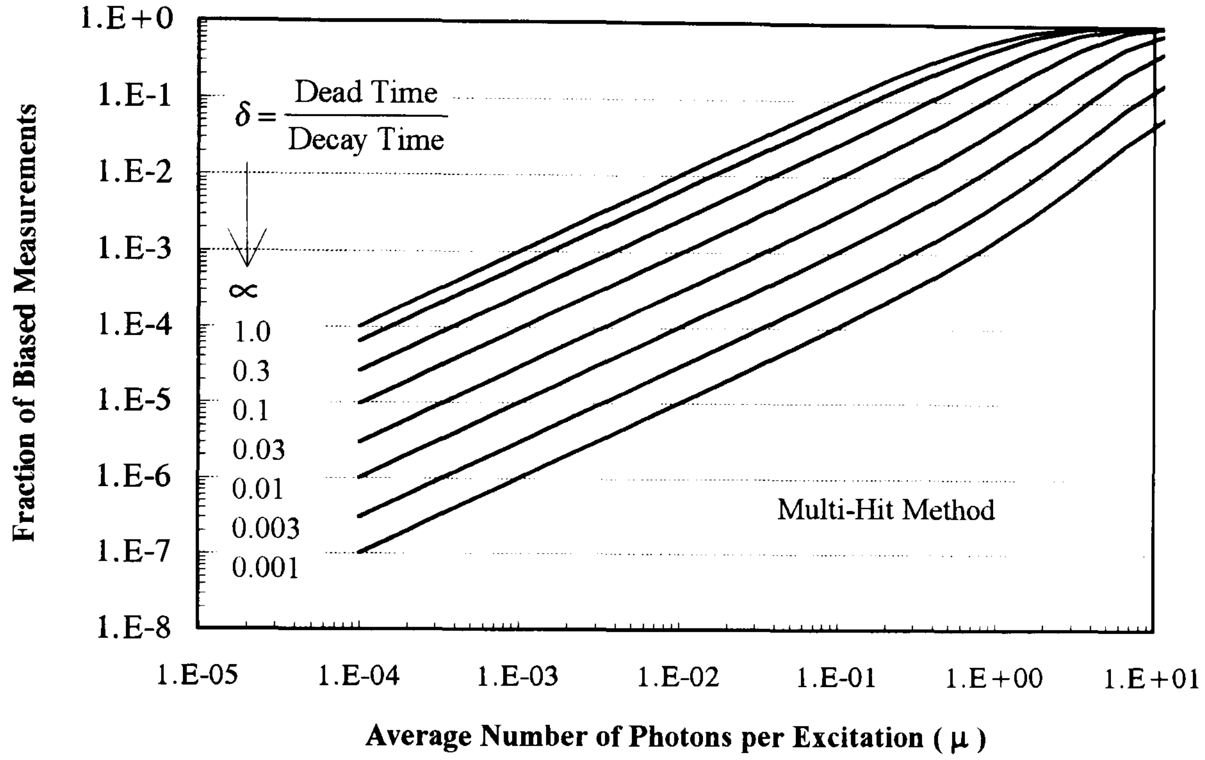

Figure 4.10. Fraction of biased photons detected per excitation verses the average number of photons per excitation (μ) for several values of δ when using the multi-hit method. In this case, biased events are due to pulse overlap [8].

For a given data purity, the acquisition rate limitation for the MCS is governed by the maximum light intensity reaching the photodetector. It should not detect two photons in any 6 ns time period otherwise events will not be recorded correctly. If events are lost due to this dead time effect, the events will be lost predominantly at the start of the scintillation event where the number of photons being detected per ns is highest.

For scintillators with decay constants which are large compared with the MCS dead time, there is a significant advantage to be obtained by using the MCS over the conventional system. Where the scintillation decay time is short, the advantage over the conventional TAC based system becomes more marginal.

4.9. One Hit Method- TAC system incorporating Veto

Despite improvements in acquisition rate and the relaxation of the single photon condition, the MCS still suffers data loss. This is large in scintillators which have fast scintillation decay constants. Also the intrinsic timing response of the MCS is relatively poor due to the jitter introduced by waiting for the beginning of the next clock pulse. In our research program the interest is to develop fast scintillators, so the MCS based acquisition system is of limited use. A modification to the *conventional* TAC based system which actively rejects multiple photon events is discussed below.

4.9.1 Veto Strategy

An abstracted description of the veto system is simple to understand. The system counts the number of stop pulses which fall within the TAC time window corresponding to each start event. If the number of photons counted is greater than one, the entire event is rejected by the acquisition system. The system checks explicitly for conformity to the single photon condition and rejects all multiple photon events. Since the system is capable of discriminating multiple photon events, it is no longer necessary to arrange for the fraction of multiple photon events to be minimised. Instead the number of events which correspond to detection of a single photon can be maximised. This offers the best possible single photon acquisition rate for this system.

4.9.2. New gating strategy- implementation

The gating logic is shown in Figure 4.11. A veto pulse is generated if there is more than one *stop* photon detected in the TAC time window. Timer 1 defines the 2μs TAC window, Timer 2 outputs 2μs NIM signal to indicate that the first single photon has been detected.

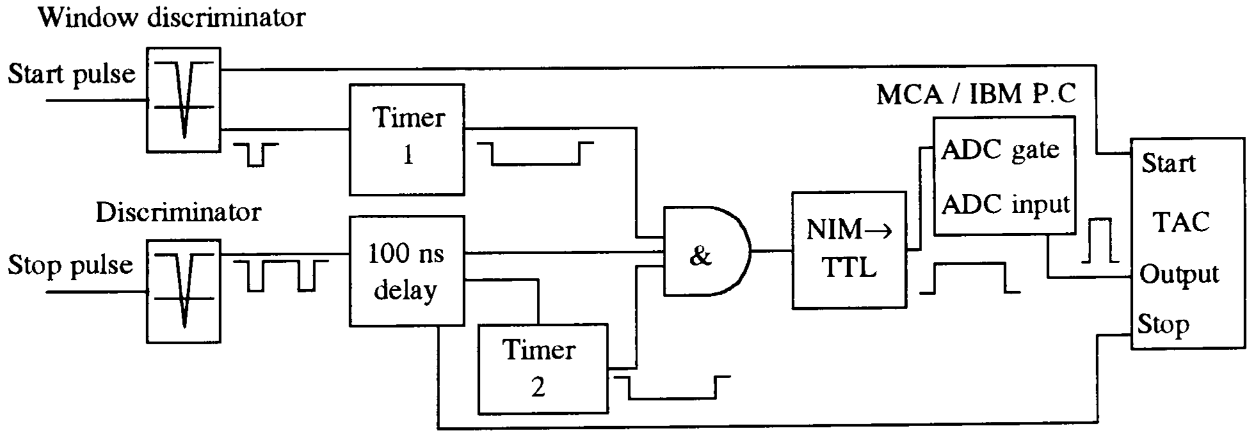

Figure 4.11. Gating arrangement for the *one-hit* single photon method. The timers, '&' gate and NIM→TTL units provide a > 1 photon veto.

The first input to the coincidence unit is simply the time window of the TAC. A veto signal is only required to reject invalid events which occur within the TAC window. The second input to the coincidence unit is *set* upon receipt of the first *stop* photon. This *arms* the veto system when the first photon is detected. The third input is an early version of the *stop* line. The timing of this input is set so that the first photon to be detected, which arms the veto system, arrives just too early at the coincidence unit to satisfy the 3-fold coincidence. Any subsequent *stop* pulses within the TAC window cause the armed unit to output a veto pulse. This veto pulse is converted to a stretched TTL pulse which overlaps the TAC output pulse and is used to gate the MCA acquisition system in anticoincidence.

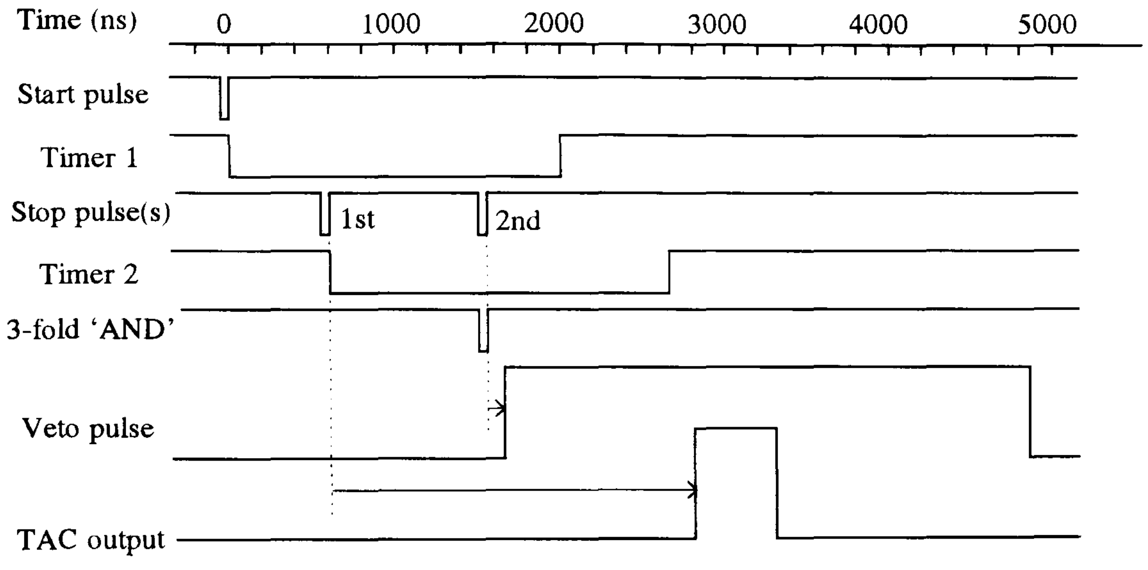

Figure 4.12. Timing diagram for the *one-hit* single photon method. The veto pulse is delayed ralative to the 2nd *stop* pulse whereas the TAC output has a fixed delay relative to the 1st stop photon. This introduces a jitter of 2000 ns.

The TAC output pulse is formed at a fixed delay relative to the first stop photon to be detected. In contrast, the veto pulse is formed relative to the second photon to be detected. There is inevitable jitter between the TAC output pulse and its corresponding veto pulse. The lower constraint approaches zero delay. The upper limit is 2000 ns. This corresponds to the first stop photon being detected in channel 1 of the TAC and the second pulse being detected at the other end of the TAC time window, channel 2000. The potential jitter between TAC output and the veto pulse is 2 µs.

In order that the veto system can cope with the extreme case of an early first photon and a late second stop photon, the TAC output pulse is formed after the end of the TAC event window as shown in the timing diagram, Figure 4.12. The 500 ns TAC output pulse is delayed relative to the start photon by 2200 ns. This allows sufficient time for a 'late' veto pulse to be generated and still envelope the TAC output pulse. To envelope this pulse and allow for a worst case jitter of 2 µs, the TTL veto pulse has to be at least 2.5 µs wide. It is set to 2.9 µs, this allows for a 200 ns safety margin. The acquisition rate of this system can be improved whilst still conforming to the single photon condition by increasing the flux of scintillation light onto the detector but gating out all events which correspond to more than one detected photon per event.

4.9.3. Selection of Poisson Mean

The number of photons which are detected by the single photon stop counter in any particular event is governed by a Poisson distribution as discussed earlier. This assumes mono-energetic photons interacting photoelectrically. As the system eliminates the 'two or more' photon events, and uses only single photon events, it is possible to increase the rate of data acquisition. The maximum rate of good events is obtained by differentiating Equation 4.06.

$$\frac{dG}{d\mu} = 0 = \exp(-\mu)(1-\mu) \qquad \text{Equation 4.12}$$

If the Poisson mean is increased to 1, the fraction of events which give rise to single photon events is maximised. 36% of all events are of the single photon type. An increase by a factor of ×18 in the data acquisition rate is possible over the *conventional* system operating with 99% single photon events.

4.9.4. Uncorrelated Events

There are two distinct classes of uncorrelated events, the first arises from genuine *single photon* sources and has been discussed earlier. These occur singly and have no predictable time structure. For moderate rates, they result in a flat background. The second type of event seen by the SPPMT is due to detection scintillation light from the test scintillator which has no corresponding start pulse. Unlike genuine single photon pulses, the uncorrelated scintillation light does have time structure ($\mu > 0.1$). This results in a background to the experimental data which is discussed in the next section.

4.9.5. Non-flat Background

4.9.5.1. Experimental data

Verification trials of the TAC based system incorporating > 1 photon veto over a variety of light levels produced data which was not self-consistent. BaF_2 was used as the test scintillator. The resulting timing distribution is shown in Figure 4.13. In addition to the fast and slow components of BaF_2, a non-flat background was observed. Even with the veto, genuine random single-photon pulses should still give a flat background.

The key to understanding this behaviour is to consider the time structure of uncorrelated scintillation 'packets'. For BaF_2, a scintillation pulse which consists of several individual photons, will have a time structure similar to that shown in Figure 4.14. This shows several cases where a random scintillation pulse occurs in the time window of the TAC.

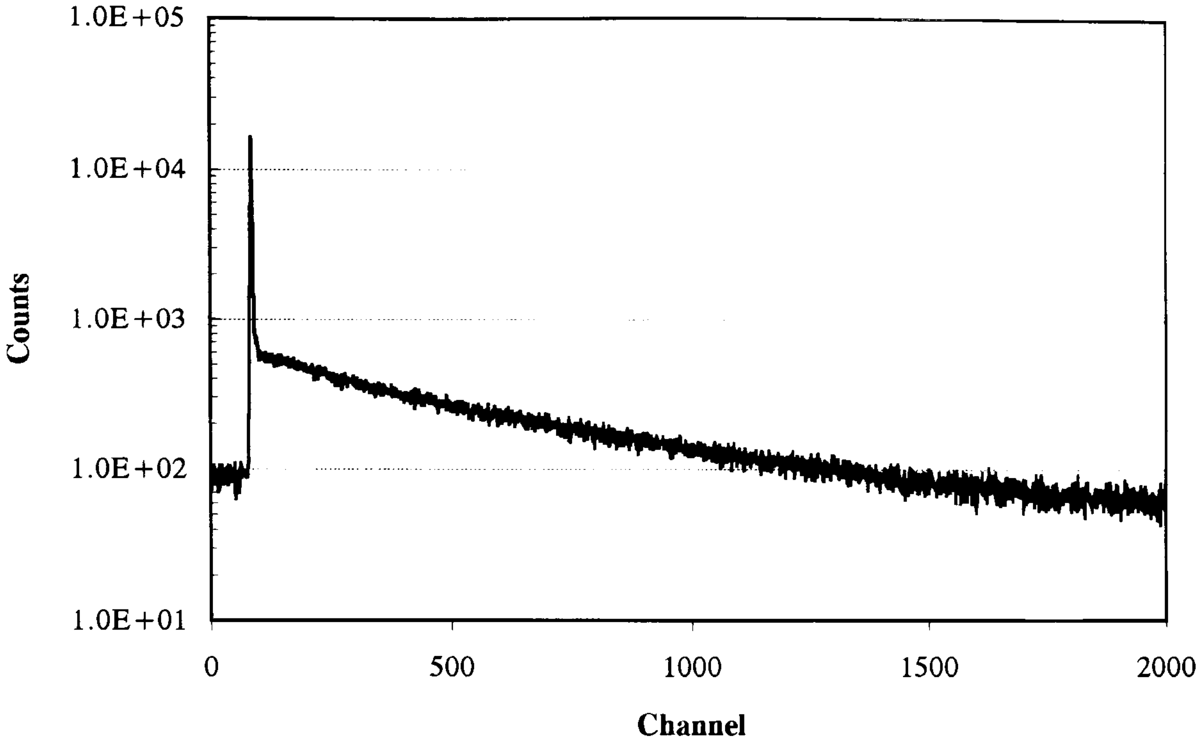

Figure 4.13. Timing data for BaF_2 recorded using the *one-hit* method which rejects all events where >1 photons are detected in the TAC window. The background is not flat indicating biased data.

In Case 1, the last photon from the scintillation pulse just falls within the TAC time window. Despite this being a *false* event, it is still accepted. Case 2 shows a higher degree of overlap. Three photons fall in the TAC window and the event is rejected in a similar manner to a correlated multiple photon event. Case 3 is similar to Case 2 and has an identical outcome. If the scintillation pulse is very late compared to the TAC it is likely that only the first photon will fall in the acceptance window of the TAC. These *false* events will also be accepted.

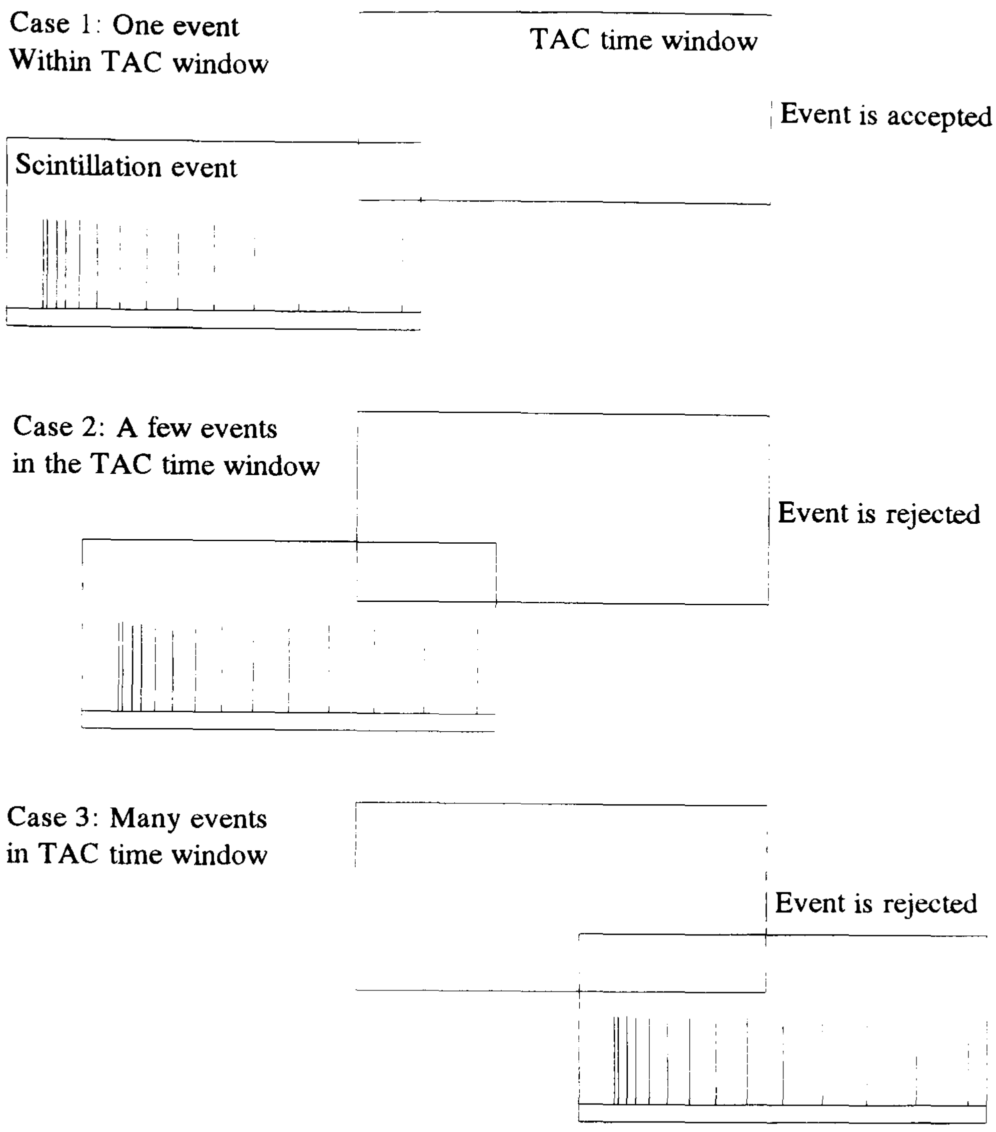

Figure 4.14. Examples of random scintillation events in the TAC time window. Case 1 is falsely accepted. Case 2 and Case 3 are correctly rejected by the >1 photon veto.

4.9.5.2. Simulation

It is intuitively possible to follow the argument presented above and conclude that extra events will occur predominantly in the early and late parts of the time spectrum. The exact distribution is not so easy to predict as it depends on the somewhat random arrival of scintillation photons. A computer program was written to simulate the detection of non-correlated events using a TAC system which was capable of rejecting multiple photon events.

The program prompts the user for the following parameters: the Poisson mean number of photons per event and also the scintillation characteristics of the test scintillator, A_1, τ_1, A_2, τ_2. A random overlap of the scintillation spectrum with the TAC window is generated. A subroutine produces a photon time profile based on a Poisson mean number of photons per pulse and the scintillation time properties of the scintillator.

The program calculates how many scintillation photons fall within the TAC time window. If the number is equal to 1, the position in the time window is stored. The program then generates a new overlap and a new photon profile and repeats the procedure. After a pre defined number of events, the histogram containing all accepted events is exported to a file and execution ceases.

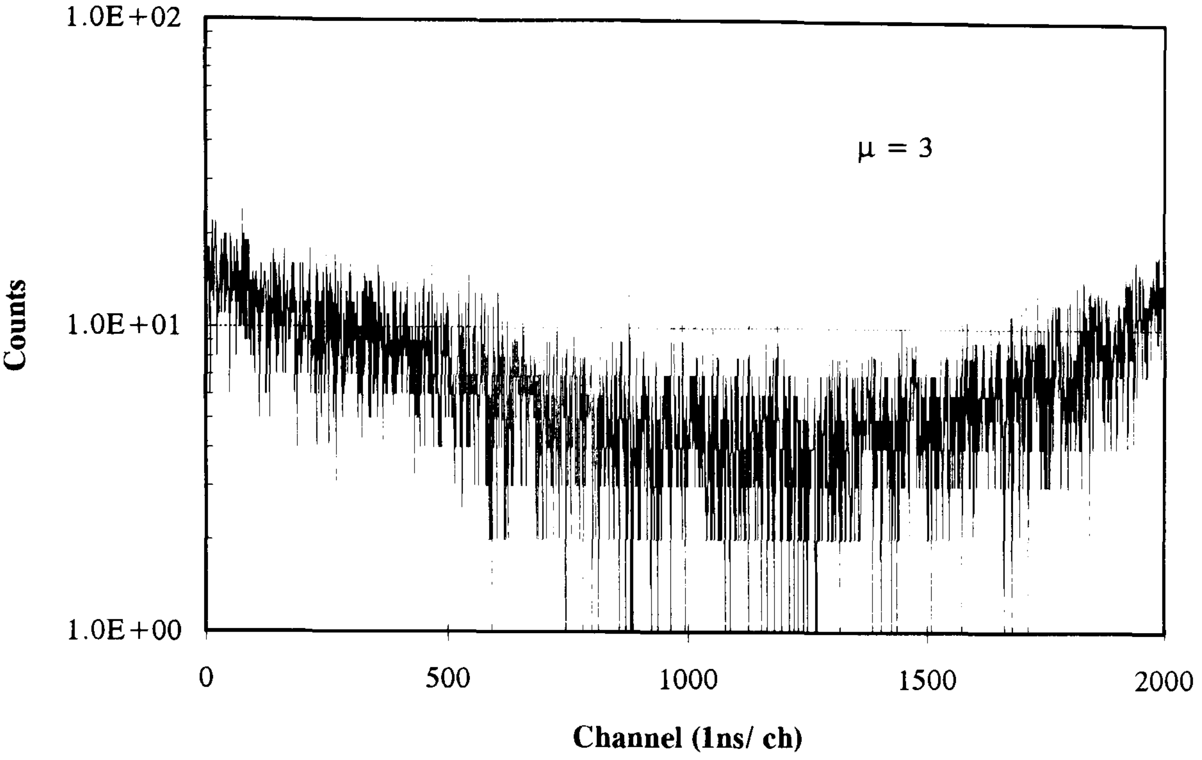

Figure 4.15. The data shows events accepted in the *one-hit* method due solely to random coincidences arising from scintillation events in the test scintillator. When >1 photons are detected, the distribution of accepted events is not flat. This simulation used BaF_2 and $\mu = 3$. Of all the *false* events which fall in the window, 24% are accepted.

A simulation for the scintillation light of BaF_2 is shown in Figure 4.15. For this the Poisson mean, $\mu = 3$. If the mean number of photons per event is increased further ($\mu = 10$), the mean time separation between the first two photons decreases and in the latter part of the time spectrum, only the very 'late' events are accepted (see case 3, Figure 4.14).

Data corresponding to late uncorrelated events, progressively occurs in the latter part of the time window as μ is increased. For $\mu = 10$, the late events occur between channels 1800 and 2000 and have a sharp, positive slope. This data has been compared to timing data recorded using BaF_2 triggered with a random start pulse, the experimental data was found to agree very well with the simulation.

This class of 'bad' events is only evident in simulated and experimental data when the Poisson mean, μ is large ($\mu > 1$). To eliminate these events entirely, the 3-fold coincidence condition was relaxed. An event in the relaxed configuration is rejected if any two photons arrive within 2000 ns of each other.

4.9.6. Additional Correlated Early Events

4.9.6.1. Experimental data

Despite relaxation of the veto-pulse gating logic to 2-fold coincidence, the data were still not perfect. Again BaF_2 was used as a test scintillator. Extra events were recorded in the early part of the scintillator time response. They accounted for ≈2% of all events and were described by an exponential decay from the origin of the scintillation event as shown in Figure 4.16. The fraction of bad events scaled with increasing μ. It was thought that veto inefficiency was the cause of additional events in the timing spectrum.

Events which result in the detection of two photons at the SPPMT should always be vetoed. When the time separation between the two stop photons is large the veto network is armed by the first photon and a veto pulse is generated by the second. The event is rejected. As the time separation becomes smaller, a point is reached where the veto is unable to distinguish the two photons as distinct entities and hence fails to veto the multiple photon event.

There is a higher probability of two photons being detected within the time resolution, *DT* of the veto generator soon after the start of the scintillation event because of the exponential nature of scintillation emission. This veto inefficiency will mainly lead to collection of events corresponding to two nearly coincident photons and not generally more.

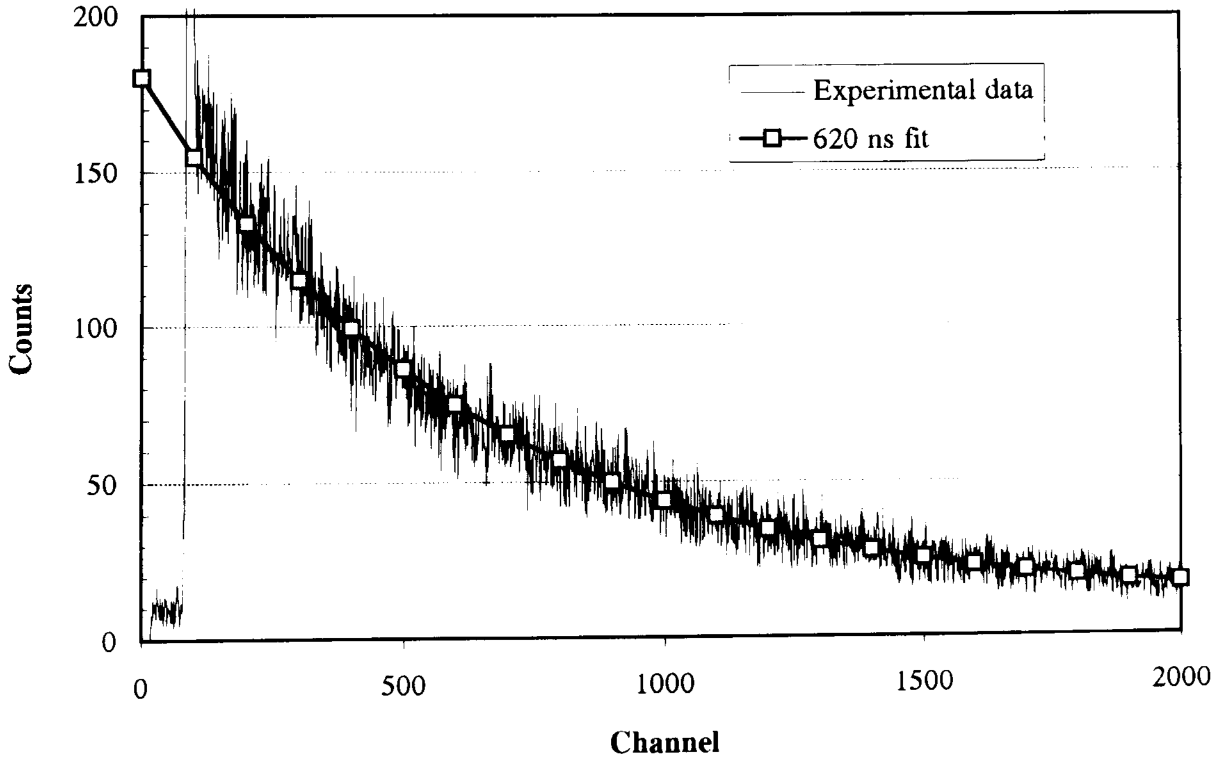

Figure 4.16. BaF_2 timing data produced using the *one-hit* implementation. The fit is to a 620 ns exponential. The additional component observed corresponds to 3% of events and is due to the dead time of the > 1 photon veto.

4.9.6.2. Simulation

A computer program was written to verify that the corruption of experimental data observed could be explained by the veto inefficiency. This considered only correlated events. The user specifies *DT*. A photon profile is generated for the scintillator specified by the user, based on the structure of its scintillation emission, A_1, τ_1, A_2, τ_2 and the Poisson mean, μ. The number of photons detected in the TAC time window are counted. If the sum equals one photon, the datum is stored in a histogram corresponding to only 'good' events.

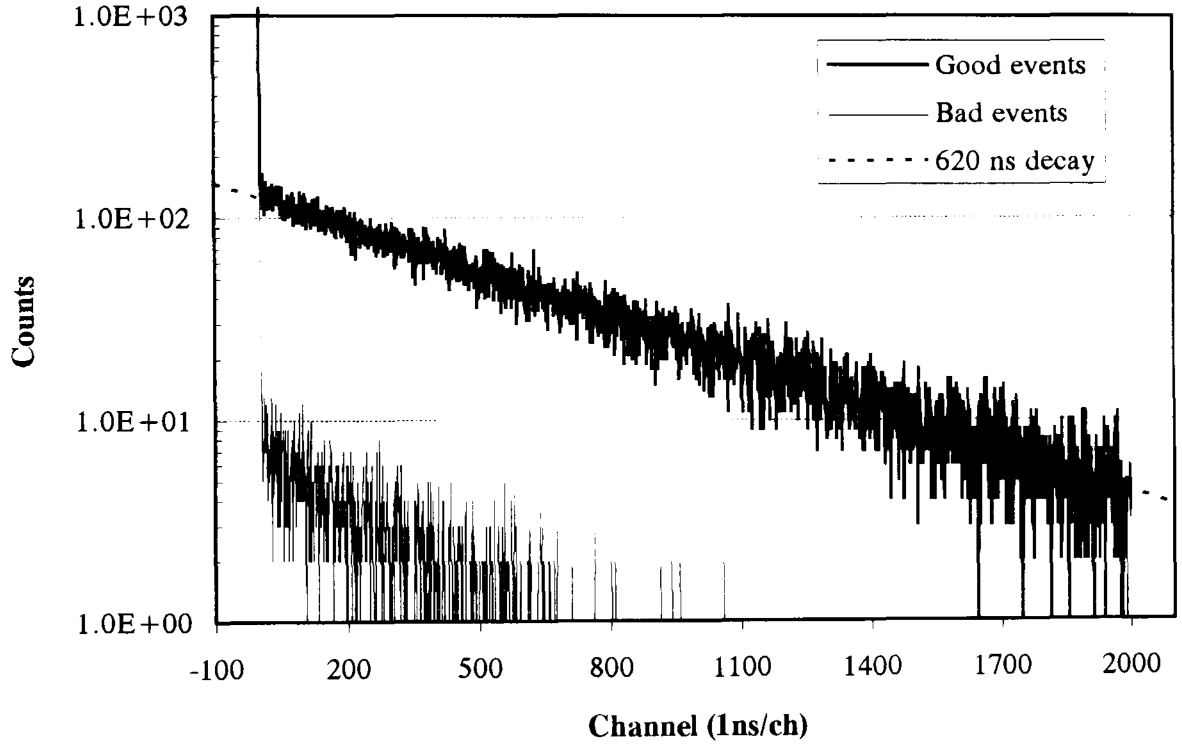

Figure 4.17. Dead time of the TAC >1 photon veto causes 'bad' events to be accepted. Results from a simulation show the accepted events separated into 'good' and 'bad' events. The 'good' events fit the correct decay time, 'bad' events do not fit a single exponential.

If the event corresponds to > 1 photon, but as a result of the finite two photon resolution of the veto, the event is not rejected, it is stored in a histogram which holds 'bad' events. Any 'bad' events which would have been rejected by the veto are ignored. The simulation determines the outcome from a specified number of events. The histogram data for both 'good' and 'bad' events are then output to a file. Figure 4.17 (μ = 5, dead-time= 10 ns) shows the results for BaF_2. The distribution of 'bad' events are similar to that observed experimentally. The fraction of bad events was calculated for different values of two photon resolution and values for the Poisson mean by executing the program several times. Table 4.01 shows the results of the simulation.

μ	Dead time, *DT* (ns)		
(photons)	10	26	42
2	3.1 %	4.49 %	7.75 %
5	3.52%	4.99 %	4.02 %
10	9.02%	9.05 %	9.13 %
20	9.13%	9.13 %	9.13 %

Table 4.01. Fraction of 'bad' events for various system dead-times and Poisson mean number of photons detected.

4.9.7. Summary

The following analysis is also similar to Moses [8], but was developed independently. The limiting constraint for the TAC based system incorporating the two photon veto is the dead time of the two photon veto circuit. The fraction of data in the timing spectrum which arises from 'bad' events that are not rejected depends on several parameters of the system and test scintillator. Namely the dead-time, *DT*, the Poisson mean, μ and the time structure of the scintillation light. For the veto to fail when *n* photons are collected in the time window of the TAC, the other (*n*-1) photons must all be collected within a time interval, *DT* after the first photon is detected.

$$P(n,\mu)P(all < DT) = \frac{\mu^n \exp(-\mu)}{n!}\left(1-\exp(-\delta)\right)^{n-1} \qquad \text{Equation 4.13}$$

The ratio of biased events to good events is,

$$\frac{B}{G} = \frac{\sum_{n=2}^{\infty} mP(n,\mu)P(all < DT)}{\mu \exp(-\mu)} \approx \frac{\mu}{2}\left(1-\exp(-\mu)\right) \qquad \text{Equation 4.14}$$

Figure 4.18 shows the fraction of biased events as a function of μ, for various values of δ. To maximise the number of single photon events, the Poisson mean should equal 1, but some events will inevitably be two photon events and a fraction of these two photon events will escape the veto. The biased fraction is considerably reduced by selecting a Poisson mean lower than one.

The One-Hit method can tolerate a higher μ than the Multi-Hit method because, in the single hit case, data is biased only when *all* photons overlap the first photon. Whereas in the multi-hit case, *any* photons which overlap bias the data.

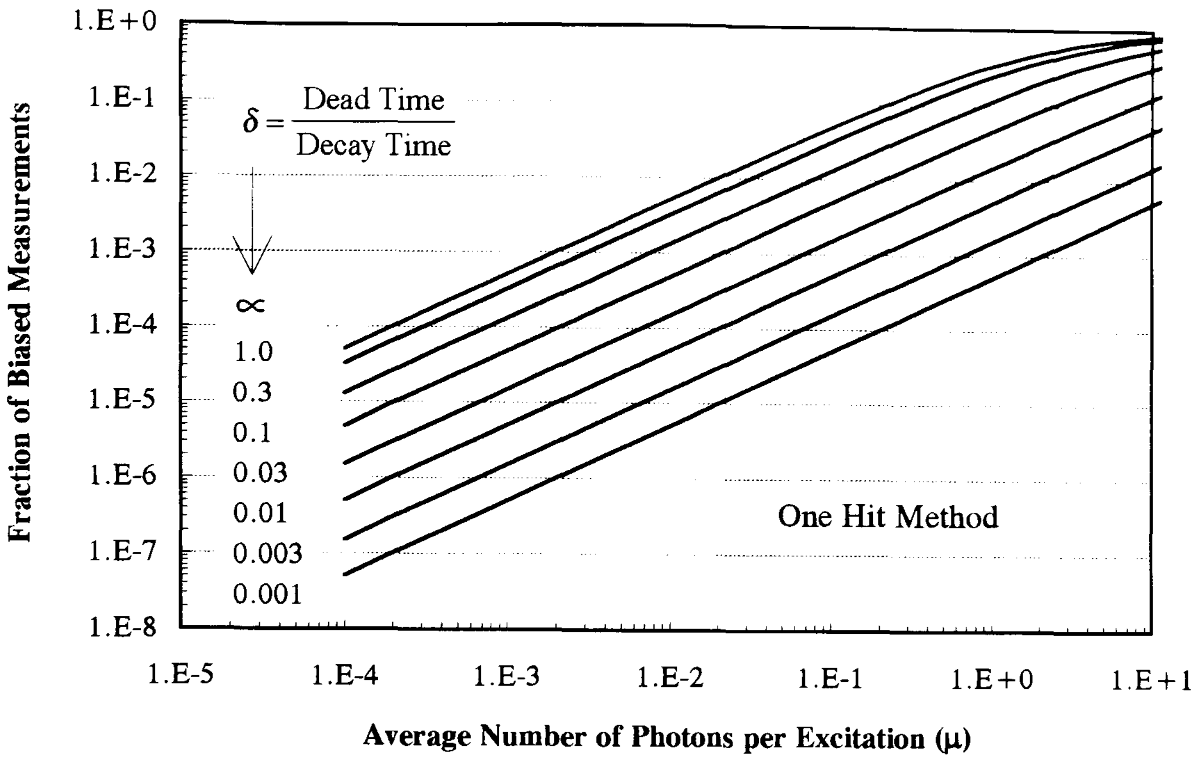

Figure 4.18. Fraction of biased photons detected per excitation versus the average number of photons per excitation (μ) for several values of δ when using the one-hit method. In this case, biased events are due to pulse overlap [8].

Efforts have been made to maximise the two photon resolution, it has been reduced to 10 ns. Scintillators with short decay constants are more likely to emit two photons in a short time period (Δt) and cause false events in the timing spectrum. This system has recorded satisfactory timing data for a range of slow commercial scintillators. Their relatively long decay constants (τ_d > 10 ns) mean that the constraint imposed by the two photon resolution is not critical and only a very small fraction of the timing data is biased.

In the case of HMF glasses, and other fast scintillators, care has to be exercised. In order to minimise the fraction of 'bad' events, the Poisson mean should be reduced significantly below 1. This increases the ratio of events which are detected with one photon over those which are detected with two photons. In practice, for HMF glasses in particular, their light output is sufficiently feeble that, in the current experimental configuration, the probability of detecting two photons in Δt = 10 ns is vanishingly small.

---

[1] G.F. Knoll, *Radiation Detection and Measurement*, John Wiley & Sons, New York, 1989.

[2] M.A. Schneegans, *Cerium Fluoride crystals for Calorimetry at LHC*, LAPP-EXP-93-07 (1993).

[3] M. Moszynski and B. Bengston, *Nucl. Instr. Meth.* **142** (1977) 417.

[4] L.M. Bollinger and G.E. Thomas, *The Rev. of Sci. Inst.* **32** (1961) 1044.

[5] P.R. Hobson and T.J. Price, *Nucl. Inst. Meth.* **A317** (1992) 315.

[6] S.E. Dorenzo and W.W. Moses, LBL-33295 UC-407 (1992).

[7] *Photomultipliers* (1986), Thorn EMI Electron Tubes Ltd.

[8] W.W. Moses, *Nucl. Instr. Meth.* **A336** (1993) 253.

CHAPTER FIVE

Determination of Scintillation Time Constants: Analysis

5.1. Introduction

The acquisition systems used for our timing measurements have been discussed in the previous chapter of this thesis. By analysing the deficiencies of each acquisition strategy, it has been concluded that all methods will contain some fraction of biased data. The 'one-hit' method offers the best combination of data purity and acquisition rate. An adequate timing spectrum can be recorded in 24 hours where the fraction of biased events is below 1%.

Analysis of the timing data is addressed in this chapter. The most fundamental description of the problem involves fitting the scintillation decay constant of a single exponential superimposed on a constant background. This problem can be solved analytically. Most of the timing data for HMF glasses are composed of typically three superimposed exponentials. Extracting the correct decay parameters for this type of data is significantly more complex. An iterative routine has been written for determining the values of the fitted parameters which minimise a multi-nomial χ^2 function.

To obtain a satisfactory understanding of the fitting procedure, an extensive program of verification trials were undertaken. Performance *envelopes* have been established for the fitting routine, the accuracy of the fitted parameters has been determined using test data. The fits to experimental timing data for several commercial scintillators are presented in the penultimate section of this chapter to indicate the level of accuracy which can realistically be obtained for the composite timing system.

5.2. Form of the Experimental Data

As a result of the finite timing response of the system, any measured timing distribution will be the convolution of the time decay of the scintillator and the intrinsic system response function. Random coincidences cause additional events in the timing spectrum, when the start and stop rates are low, the spectrum of random events is flat. The timing spectrum consists of discrete time bins, their population will be subject to statistical fluctuations. A 100 ns delay in the *stop* line artificially shifts the timing spectrum across the time window, giving a region prior to the scintillation event which is only populated by random coincidences.

Characterisation of the temporal distribution of a scintillator involves describing the structure of its scintillation light mathematically. It has been discussed in Section 2.2 that a decaying exponential or a number of decaying exponentials adequately describe the time structure of emitted light for the majority of scintillating materials. The aim is to measure the time constants and relative amplitudes of these exponentials. This is divided into two separate areas. Recording the timing data has been discussed in the previous chapter. Extracting the time constants and relative amplitudes which describe the data is the subject of the current chapter.

Software has been written to transfer data recorded using the TAC/ MCA. The program reads in an MCA file and translates the encrypted data into an ASCII text format containing the channel number and contents in a list from 1 to 2000. This data is stored to a new file using the ASCII format which can be read directly into other commercial programs. A similar program has been written for the MCS system.

5.3. Single exponential data on a flat background

Commercial scintillators were used in our research program for initially configuring the timing system and testing the hardware. A variety of scintillators were readily available and their properties well characterised [1 , and references cited within]. They also provided a range of scintillation decay constants from less than 1 ns to over 1 µs. To a first approximation, timing data from materials like BaF_2, NaI(Tl), CsI(Tl), and BGO is adequately described by a single decaying exponential superimposed on a flat background of random events, Z.

$$\langle h_i \rangle = Z \qquad 1 < i < 99 \qquad \text{Equation 5.01}$$

$$h_i = Z + A\exp\left(\frac{-(i-100)}{\tau_d}\right) \qquad 100 < i < 2000$$ Equation 5.02

For this problem the background can be estimated from the region of the time spectrum before the start of the scintillation response. Excluding the region below the Low Level Discriminator (LLD) of the MCA, and near to the leading edge of the scintillation response, gives approximately 60 channels which can be averaged to determine the mean background, $\hat{Z}$. The problem is then linearised as shown below and a least-squares approach can be used.

$$\ln\left(h_i - \hat{Z}\right) = \ln(A) - \left(\frac{i}{\tau_d}\right)$$ Equation 5.03

The x-axis, i contains no error, $\ln\left(h_i - \hat{Z}\right)$ is used as the y-ordinate. The simple least-squares estimate for the gradient, B and intercept, C, assumes that the measurement of y_i is governed by a Gaussian distribution centred on its true value, with a width parameter, σ_y.

$$B = \frac{N\left(\sum x_i y_i\right) - \sum(x_i)\sum(y_i)}{N\left(\sum x_i^2\right) - \left(\sum x_i\right)^2}$$ Equation 5.04

$$C = \frac{\left(\sum x_i^2\right)\left(\sum y_i\right) - \left(\sum x_i\right)\sum(x_i y_i)}{N\left(\sum x_i^2\right) - \left(\sum x_i\right)^2}$$ Equation 5.05

A simple least-squares minimisation is not strictly applicable because the uncertainty in $\ln\left(h_i - \hat{Z}\right)$ is not described by a single parameter, σ_y. The gradient, B and intercept, C must be calculated using the *weighted* least-squares estimates,

$$B = \frac{\left[\left(\sum w_i\right)\left(\sum w_i x_i y_i\right) - \left(\sum w_i x_i\right)\left(\sum w_i y_i\right)\right]}{\left(\sum w_i\right)\left(\sum w_i x_i^2\right) - \left(\sum w_i x_i\right)^2}$$ Equation 5.06

and

$$C = \frac{\left[\left(\sum w_i x_i^2\right)\left(\sum w_i y_i\right) - \left(\sum w_i x_i\right)\left(\sum w_i x_i y_i\right)\right]}{\left(\sum w_i\right)\left(\sum w_i x_i^2\right) - \left(\sum w_i x_i\right)^2}$$ Equation 5.07

w_i represents the weight of each point. For this type of counting experiment,

$$w_i = \frac{1}{\sigma_i^2} \equiv \left(h_m - \hat{Z}\right)$$ Equation 5.08

A computer program was written which solved for the parameters C and B. The decay constant, τ_d can be calculated from the estimate of the least-squares gradient, B,

$$\tau_d = \frac{-1}{B} \qquad \text{Equation 5.09}$$

This program, although mathematically correct, was relatively inflexible and relied on an accurate estimate of the background. It was soon realised that the majority of materials do not conform to a single exponential. With the increased level of complexity, it is not possible to find a non-iterative solution. Despite the rapid throughput of the non-iterative program, an alternative approach was required to fit parameters to complicated, multiple exponential data. The timing spectra for HMF glasses and some scintillators showed several time components. To parameterise these materials, a program which used an iterative search method was essential.

5.4. Intrinsic system response

The intrinsic timing response of a system is defined from the recorded spectrum of an impulse input. To obtain this measurement for the single photon apparatus, both the trigger scintillator and the stop system were excited synchronously. Quartz was used as the test material as it is known not to scintillate. Any excitation light given out by the quartz must originate from the Cerenkov effect and will therefore be prompt. The resulting time distribution for the TAC/ MCA system is shown in Figure 5.01. The distribution is expected to be Gaussian, its width is composed of several contributions added in quadrature. The two principal components are due to electronic noise and the Transit Time Variation (TTV) of the photoelectron produced in the single photon photomultiplier tube. The electronic contribution has been measured using a common pulse to *start* and *stop* the TAC apparatus. The fit to this distribution is also shown in Figure 5.01. A Gaussian fitting procedure has been used to estimate the Full Width at Half Maximum (FWHM) of the distributions. From this, σ has been estimated for the total response (σ_T= 1.40 ns). It is composed of electronic (σ_E= 0.33 ns) and TTV (σ_{TTV}= 1.36 ns) terms added in quadrature.

$$\sigma_T^2 = \sigma_E^2 + \sigma_{TTV}^2 + \ldots \qquad \text{Equation 5.10}$$

Similar measurements were recorded for the MCS system, the intrinsic width of its impulse response, σ_T= 4.26 ns. This value is dominated by the jitter introduced in the MCS by waiting for the beginning of the next clock pulse before recording a scan.

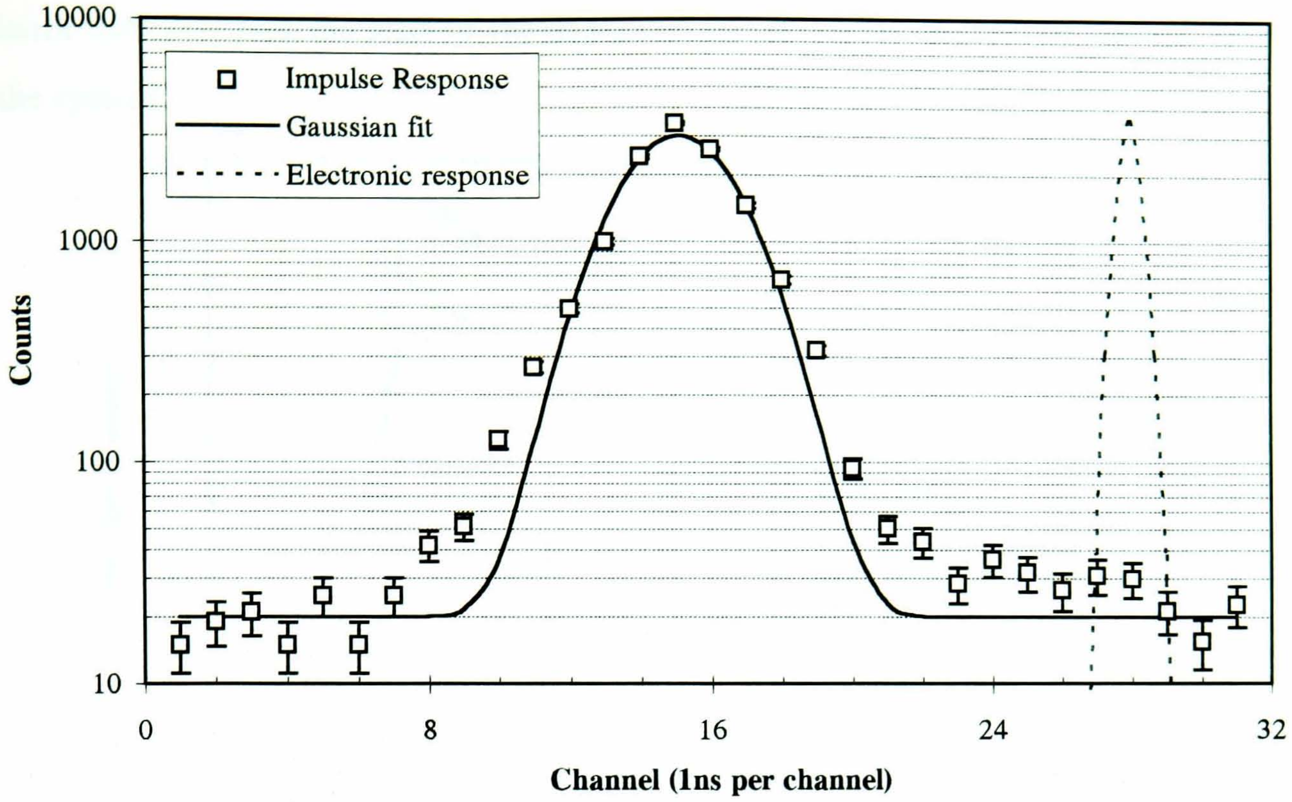

Figure 5.01 The measured impulse response for the TAC/ MCA system. It is approximated by a Gaussian with a $\sigma_T = 1.40$ ns (fit overlaid). A fit to the electronic contribution is also shown, this has a of $\sigma_E = 0.33$ ns.

When measuring a timing distribution which has the functional form *f(t)*, the TAC based system will record a distribution, *h(t)* which is the convolution of the underlying timing distribution with the intrinsic system response,

$$h(t) = f(t) \otimes g(t) \qquad \text{Equation 5.11}$$

g(t) represents the response function of the system. For the TAC/ MCA, it is approximated by a Gaussian of width, $\sigma_T = 1.40$ ns. There are two different methods for handling this corruption of the parent data; attempt to correct it, or exclude it from the fitting procedure.

5.4.1. Correcting using de-convolution

Ideally, the timing spectrum of a simple scintillator can be thought of as a single decaying exponential. For the first part of this section the definition is further constrained to have no background and also no statistical noise on the contents of each channel. The simplified functional form of the measured spectrum is,

$$h(t) = A_1 \exp\left(\frac{-t}{\tau_d}\right) \otimes \frac{1}{\sigma\sqrt{2\pi}} \exp\left(\frac{-t^2}{2\sigma^2}\right) \qquad \text{Equation 5.12}$$

Figure 5.02 shows visually the convolution of the ideal case described above. The effect is to '*round-off*' the peak of the exponential. The Gaussian function acts in a similar manner to a low pass filter in electronics. Our numerical simulations have shown that timing data more than $2\sigma_T$ past the start of the exponential is not affected by the intrinsic response of the system.

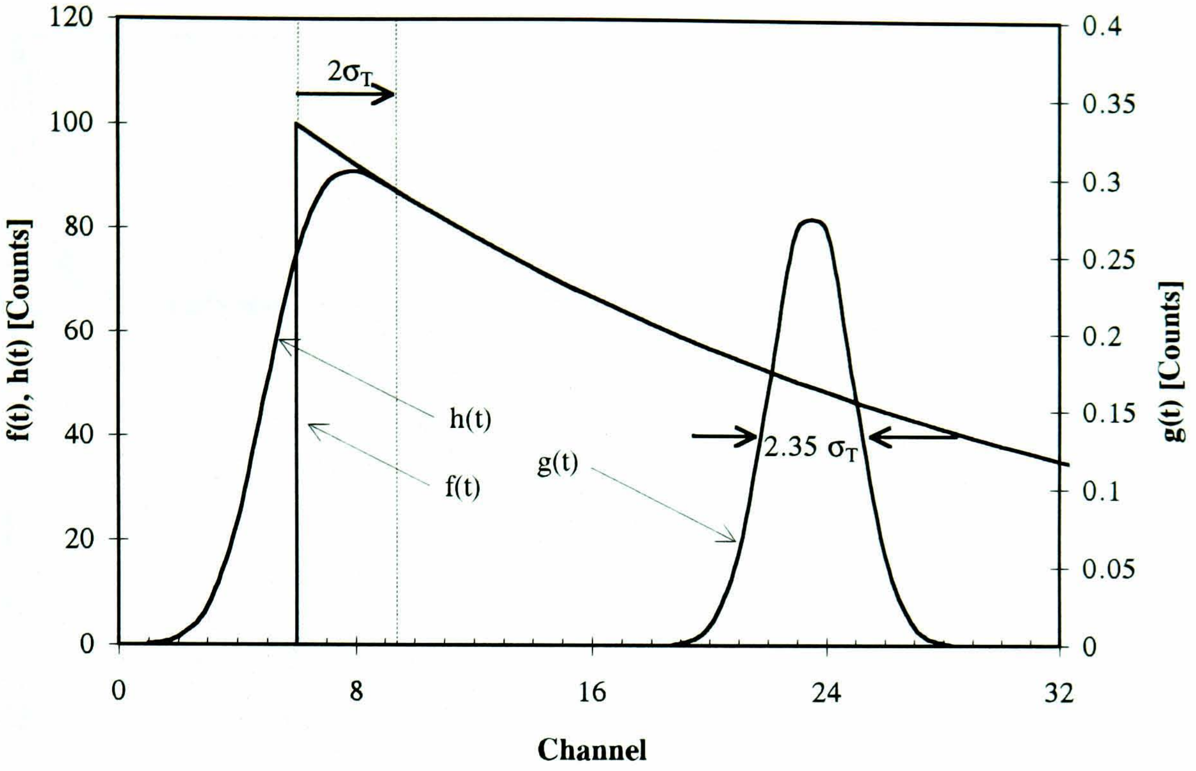

Figure 5.02 The convolution of an exponential with a Gaussian. The first $2\sigma_T$ ns of the leading edge is *rounded-off*.

Convolution is a reversible mathematical operation. In principle, it is possible to record a timing spectrum, *h(t)* and perform the de-convolution with the intrinsic system function, *g(t)* to obtain the original, *f(t)*.

$$f(t) = F^{-1}\left[F[h(t)] \Big/ F[g(t)] \right] \qquad \text{Equation 5.13}$$

Where $F[]$ and $F^{-1}[]$ represent the Fourier Transform (FT) and inverse FT functions respectively. In reality, the functional form of the timing spectrum *h(t)* is not known. Performing a de-convolution of the functional form, *h(t)* is therefore not possible. There are discrete observations of the function, h(1), h(2), .., h(2000) and also only discrete observations of the function *g(t)*, although it is assumed to be described well by a Gaussian of known width, σ_T. Discrete Fourier Transformations (DFTs) are required to convolve and de-convolve discrete functions. These are achieved using Fast Fourier Transforms (FFTs).

DFTs have a frequency cut-off imposed because of the discrete nature of the observations. The cut-off frequency corresponds to the inverse period of observations. i.e. (1/bin width). To perform the de-convolution, and recover the parent function, loosing no information, the functions, *g(t)* and *h(t)* must contain no components above the Nyquist sampling frequency. Realistic data recorded using the single photon apparatus also contains statistical noise on each data point. In the frequency domain, this noise appears as a component which is partially above the cut-off frequency of the FFT.

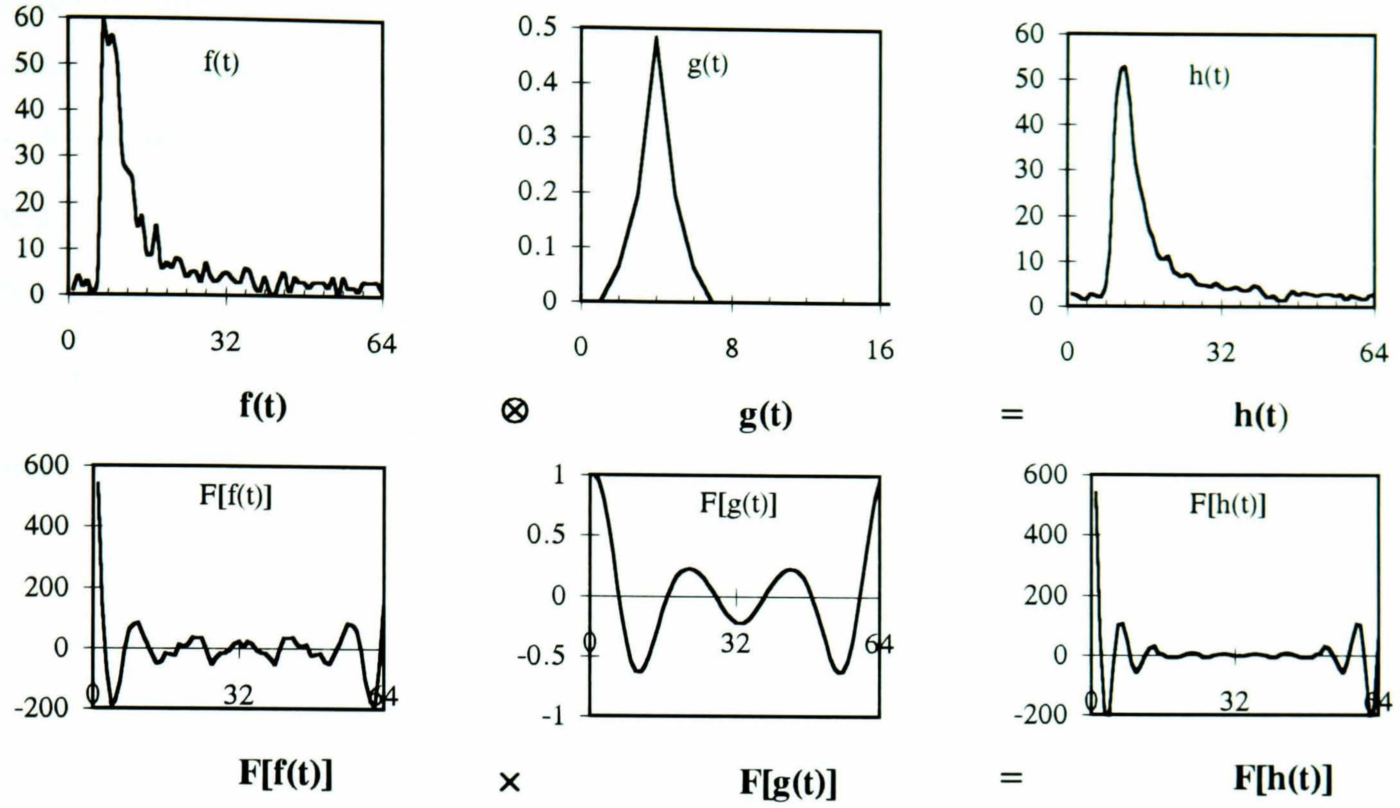

Figure 5.03 The convolution of a noisy decaying exponential with a Gaussian in time (above) and frequency (below) space. This data was calculated using 64 point FFTs. The resulting function is smoothed by the convolution with a Gaussian.

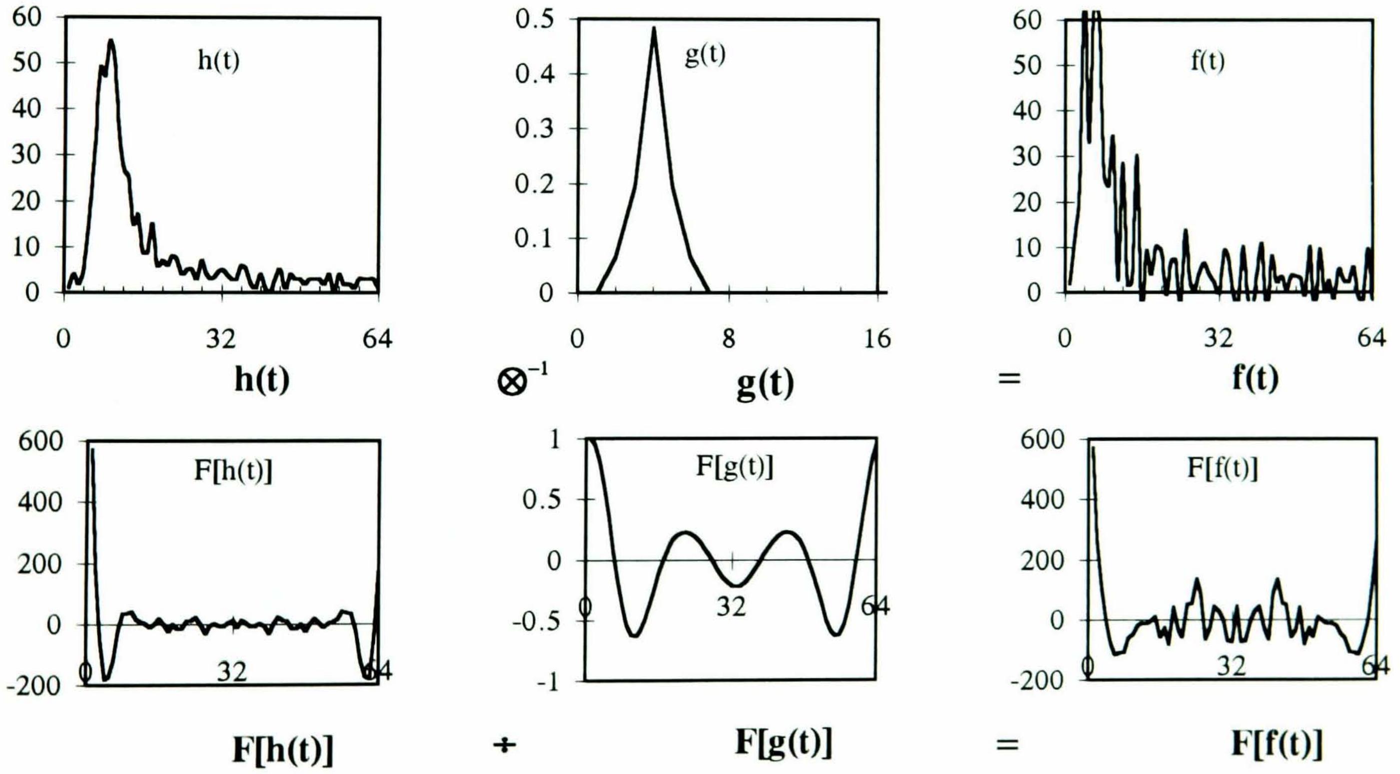

Figure 5.04 The deconvolution of a noisy exponential with a Gaussian sharpens the features of the resulting function. This data, in time (above) and frequency (below) space, was calculated using 64 point FFTs

Convolving $f(t)$ with a Gaussian (σ_T > 1/sampling frequency) results in suppression of high frequency noise in the resulting function, $h(t)$ due mainly to the filtering nature of the Gaussian. This is shown in Figure 5.03. Conversely, de-convolving $h(t)$, which contains statistical noise, with a Gaussian results in the function *f(t)* in which statistical noise is exaggerated. This is shown in Figure 5.04. The high frequency components of the input function, *h(t)* cause the apparent 'failure' of the de-convolution operation. During de-convolution this noise is exaggerated, this is similar to the leading edge of the timing distribution being 'sharpened' during the same operation.

Statistical noise is a supplementary distortion which occurs during data acquisition. The undistorted functions *g(t)* and *h(t)* are transformed by a statistical noise operator,

$$h(t) \rightarrow h_{noise}(t) \quad \text{Equation 5.14}$$

and

$$g(t) \rightarrow g_{noise}(t) \quad \text{Equation 5.15}$$

For de-convolution to be a viable option, $g_{noise}(t)$ and $h_{noise}(t)$ have to be artificially transformed back to *g(t)* and *h(t)* respectively before de-convolution. The function, *g(t)* has been assumed a Gaussian of known width, so this function can be modelled and transformed. The function $h_{noise}(t)$ is not known. Data smoothing would suppress the noise component of $h_{noise}(t)$ but would also distort the high frequency components of the underlying function *h(t)*.

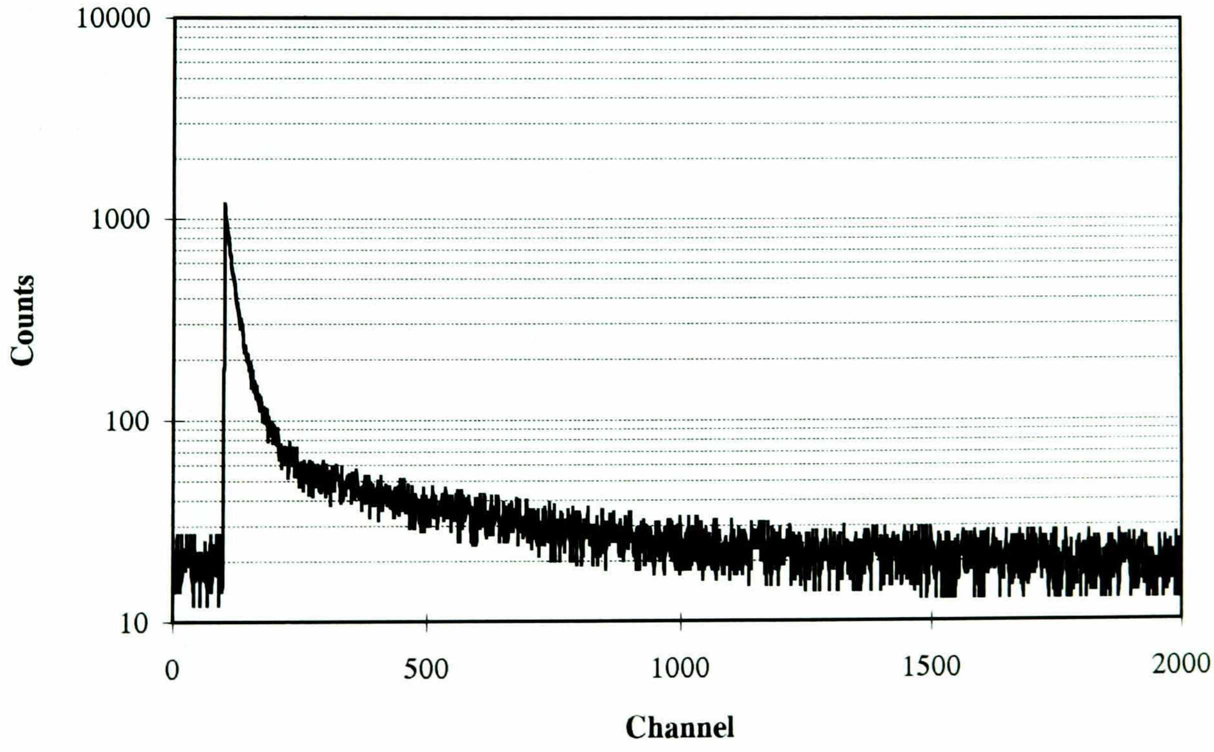

Figure 5.05 This test data represents the function $h(t)_{noise}$, it has been used as the input to the de-convolution routine.

For time spectra which contain statistical noise, the de-convolution procedure tends to distort the parent function unacceptably. Figure 5.05 shows the parent function, $h(t)_{noise}$, the underlying function *f(t)*, has been obtained by de-convolving $h(t)_{noise}$ (Figure 5.05) with a Gaussian, the result is shown in Figure 5.06. It is contaiminated with excess noise resulting from the procedure involving the inverse Fourier transform. Subsequent smoothing of Figure 5.06 is not viable since the underlying function *f(t)* also contains high frequency components.

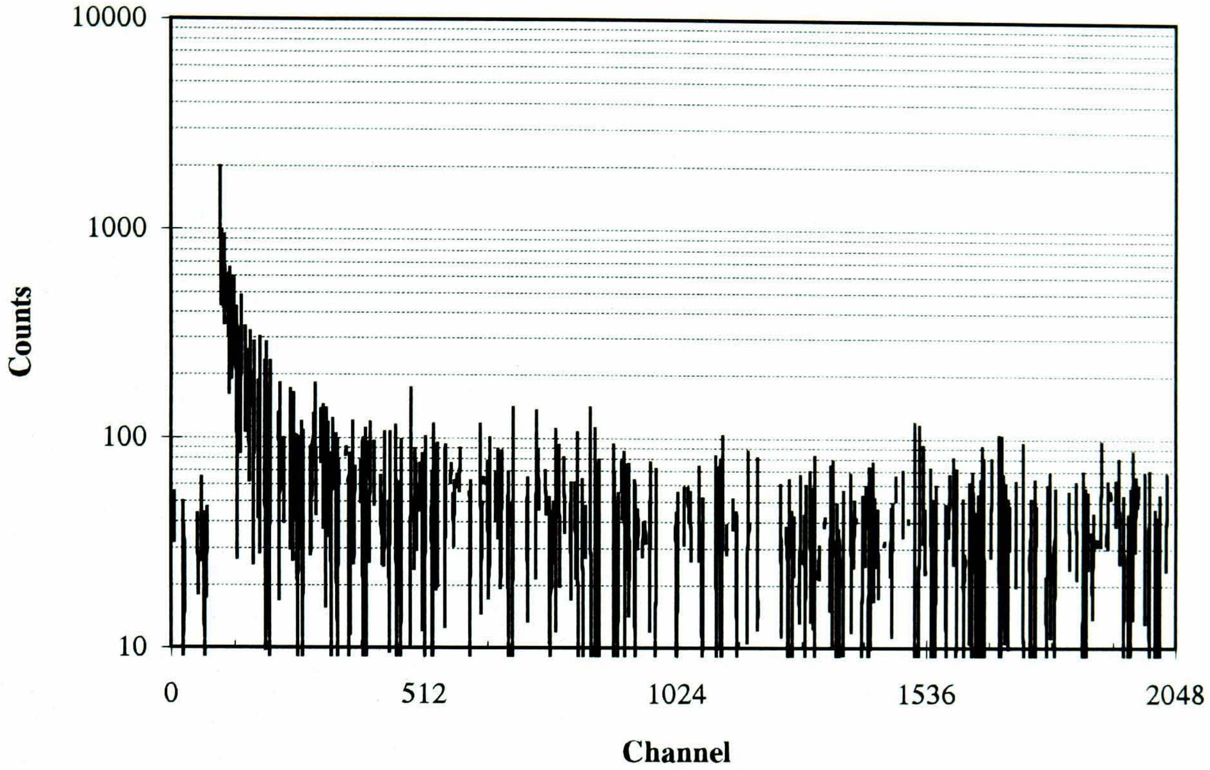

Figure 5.06 The data shown in Figure 5.05 has been deconvolved with a Gaussian whose $\sigma_T = 1$ ns. Even this unrealistically narrow Gaussian distorts the underlying function significantly.

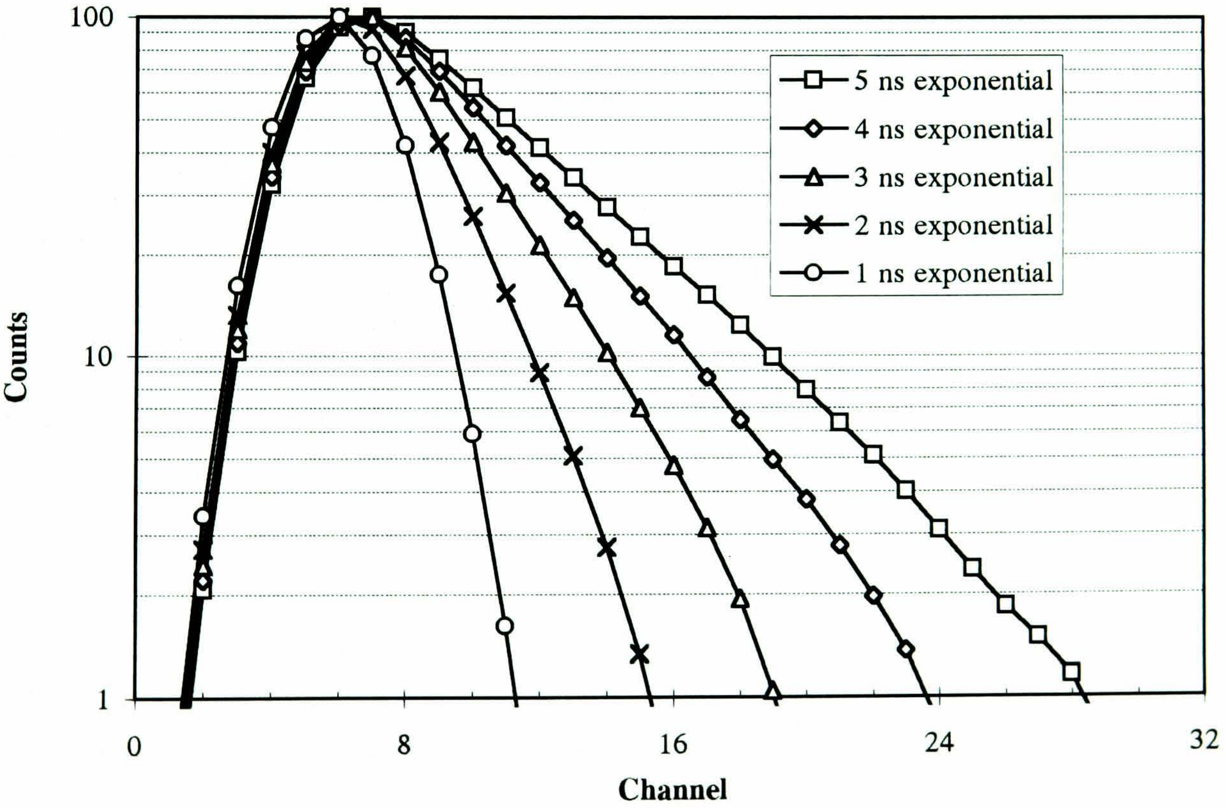

Figure 5.07 The curves are the convolution of a Gaussian, $\sigma_T = 1.4$ ns with various exponentials as indicated. Experimental data can be overlaid to determine the correct decay constant.

A procedure which eliminates the need for de-convolution is potentially suitable for the analysis of single exponential data with very short decay constants. It involves generating a family of curves which are the convolution of *g(t)* with various *f(t)* functions. Each curve has a different decay constant as shown in Figure 5.07.

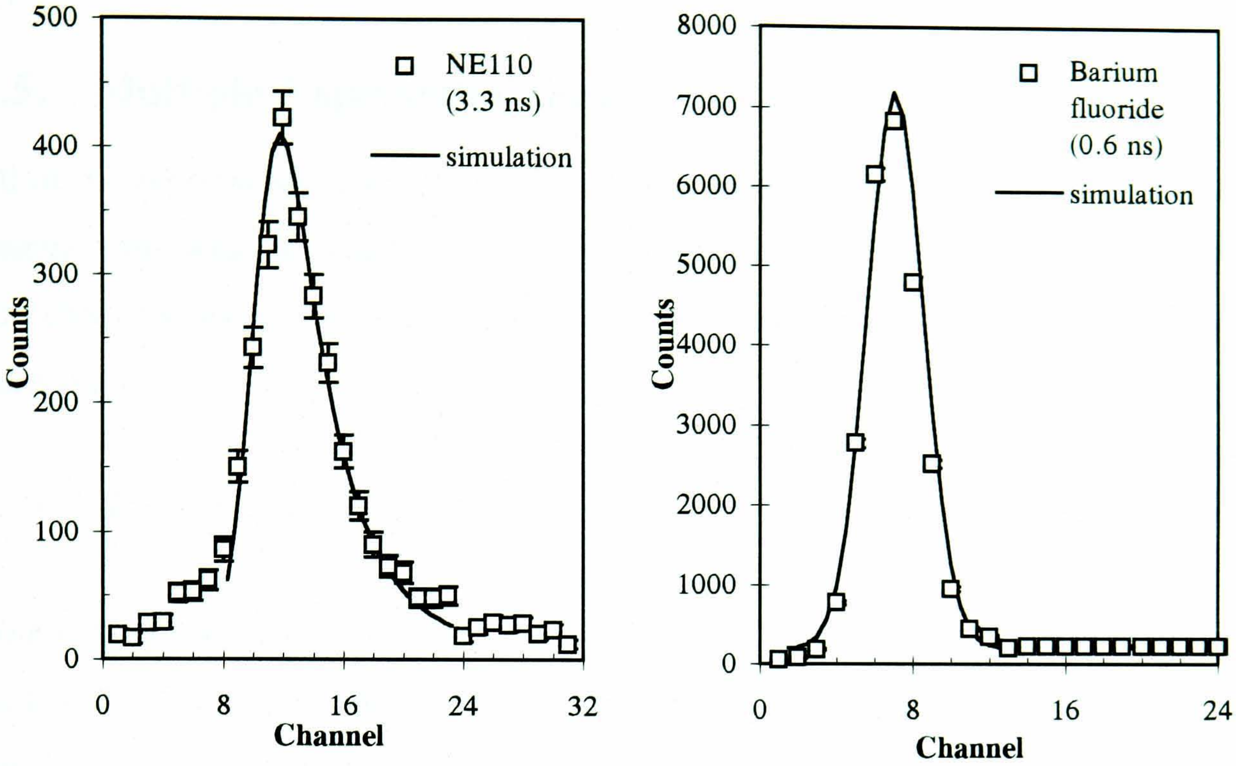

Figure 5.08 Examples where experimental data for NE110 and BaF_2 have been overlaid with their correct theoretical convolved exponentials.

Comparing the curves with experimental data can be used to estimate the decay constant of the fast exponential component. This is suitable for very short time components. i.e. $\tau_d <$ 3 ns. Examples of this are shown in Figure 5.08. The convolved functions have been visually overlaid although, if this procedure were used extensively, an automated fitting procedure would have been used.

5.4.2. Excluding the leading edge

This is by far the most simple option. The data which is used for the fitting procedure is truncated to exclude the first $2\sigma_T$ ns past the start of the exponential as shown in Figure 5.02. The drawback of this approach is that, to predict the initial amplitudes of the underlying exponentials, A_1, A_2, and A_3 it is necessary to *point-back* to the origin of the scintillation event. For scintillators with a short time constant, τ_1, uncertainty in the origin of the exponential leads to significant errors in the ratio A_1: A_2 associated with pointing back to the origin. It is beneficial when attempting to fit short decay constants to minimise the intrinsic width of the system response function *g(t)*.

Excluding the first $2\sigma_T$ ns of the leading edge was preferred over the de-convolution approach in this research programme due to the large number of timing spectra which required fitting, and the fact that none of the HMF glasses contain very fast (<3 ns) scintillation components. Additionally, solving FFTs which involve many data points require large computational resources. The drawback of truncation is that it is possible to completely miss short exponential time constants, this is discussed more fully in Section 5.7.

5.5. Multiple Exponential data

All of the experimental data recorded using the 'one-hit' single photon method used a 2000 channel time window which corresponds to approximately 2000 ns. The MCS data spans 400 channels, each 5 ns wide. The multi-exponential data should ideally be described by the equation,

$$n_i = Z + \sum_{k=1}^{N} A_k \exp\left(\frac{-i}{\tau_k}\right) \qquad \text{Equation 5.16}$$

Where n_i is the number of counts in channel, i. This equation assumes that there is no statistical noise or biasing present on the data. Z represents the level of the background which is due to random events. A_k and τ_k are the amplitudes and decay constants respectively of the exponentials which describe the scintillation emission. All of our work considers a maximum of three exponential components ($N= 3$), the notation used, assumes that $\tau_3 \geq \tau_2 \geq \tau_1$.

If biased events are assumed to make a negligible contribution to the spectrum, the equation above can be used as the basis for a fitting procedure. There are seven independent variables which define the governing equation. To obtain the best fit to experimental timing data, it is necessary to optimise the values of each parameter simultaneously. This is a multi-dimensional problem of considerable complexity. *Microsoft Excel 4.0a* was used for performing fits to experimental data.

Excel version 4.0a is a spreadsheet package which has an extensive library of functions available. There is a *Solver* routine which can minimise, maximise or set to a particular value, a cell in the worksheet by adjusting the contents of a range of other cells, subject to specified constraints. The routine terminates when a solution has been identified which is within a specified tolerance. Within this framework a spreadsheet was written which minimised the multi-nomial χ^2 [2],

$$\chi^2 = 2 \times \sum_{i=1}^{2000} h_i \ln\left(\frac{h_i}{n_i}\right) \qquad \text{Equation 5.17}$$

subject to the constraint that the number of data events and the number of fit events are equal,

$$\sum_{i=1}^{2000} h_i = \sum_{i=1}^{2000} n_i \qquad \text{Equation 5.18}$$

The *Solver* routine is extremely flexible, it is possible to alter the region over which the fit is performed, to fit over less than three exponentials or freeze certain variables and optimise others. The user can select the search method which the *Solver* routine will use. The search methods available are Newton or Conjugate, using either Tangential or Quadratic estimates which are calculated using either Forward Difference or the Central estimates.

Excel runs in the Microsoft Windows environment. It is possible to minimise χ^2 and graphically display the experimental data with the fit overlaid. All of these features combine to give a flexible package which can fit these complicated functions on an acceptable time scale. Due to the multi-dimensional nature of these fits and also the relatively large data sets, a significant advantage was observed by using an *Intel* 50 MHz 486 DX processor for this work. It takes approximately 20 minutes to export and fit parameters to one timing spectrum.

A point in the seven dimensional parameter space exists which corresponds to χ^2 having its *global* minimum value. However, there will also be a large number of other *local* minima which the solving routine may erroneously identify. This will lead to the non-optimal solutions being returned by the routine. Although all of the variables are independent it is known that there is a high degree of correlation between the values of various groups of parameters. Before the χ^2 minimisation routine was used on a large scale, the χ^2 minimisation template file and the *Solver* function generally were evaluated with this application in mind.

5.6. Verification of the Excel Solver routine

5.6.1. Evaluation procedure

After the template file had been tested for typing and simple coding errors, it was assessed using a range of input data. Initial tests used a single exponential plus a flat background with no statistical noise. The level of complexity was gradually increased to include multiple exponential data with statistical noise. Artificially generated test data was used for much of the evaluation work. Experimental timing data for commercial scintillators recorded using the TAC and MCS systems was then fitted using the χ^2 routine and compared to published data for these materials.

5.6.2. Input Data

From a study of published literature on this subject, and our own work, it is apparent that the accurate determination of scintillation decay times is not a trivial measurement. There is variability in the literature concerning the measured decay time constants of some 'standard' scintillators. An example is the slow decay constant of barium fluoride. Whilst the majority of the previous experimental work identifies a 620 or 630 ns slow component [3], Laval *et al* [4] have also observed a 430 ns emission.

The history of the sample, the manufacturer, impurity levels, surface contamination and the source of ionising radiation are all cited as possible reasons for variability in the quoted results. Additionally, since the object of this section is to evaluate the fitting procedure in isolation, it is a precondition that the test data must not be collected using our apparatus. Any uncertainty in the fitted parameters arising from the fitting procedure can be quantified separately by using artificially generated test data.

A computer program was written which could produce exponential data according to Equation 5.16. Statistical noise based on an underlying Gaussian distribution of width σ_i was added to the value of each data point. $\sigma_i = \sqrt{f_i}$ where f_i is the contents of a particular bin. An example of this artificially produced test data is shown Figure 5.05. It has decay constants of 12 ns, 32 ns and 400 ns. The initial amplitudes are 600, 500 and 50 respectively. The data is superimposed on a flat background of 20 events.

5.6.3. Programme of Trials

5.6.3.1. Single Exponential data

Data sets	Test Data			Fits			χ^2 /dof
	A	t	Z	A	t	Z	
1	20000	1000	20	20009	999.20	0	0.69
2	20000	10	20	19974	10.01	14.5	0.70
3	200	1000	20	201.1	994.23	19.06	0.70
4	200	10	20	197.9	10.07	17.08	0.70

Table 5.01 Results for single exponential data which contained statistical noise. The low χ^2 per degree of freedom indicates that the Gaussian noise function is an approximation.

To initially verify that the fitting procedure was operating correctly, it was tested with simulated data with no statistical noise. For a wide range of amplitudes, A_1, decay constants, τ_d and backgrounds, Z, the fitting procedure obtained the correct solutions. The solution was found more rapidly if the initial estimates of the parameters were close to their final values. Data which contained statistical noise was also tested, the agreement with the correct solution was also good but solving times were extended. Table 5.01 shows a subset of the test data and the corresponding observed fitted parameters for single exponential data with noise.

Changing the values of the fitted parameters at the few percent level, has no drastic effect on the χ^2 for the fit. An example is shown in Figure 5.09. The values for this figure were calculated using experimental data for BaF_2. This data indicates that the χ^2 is a well-behaved, slowly varying function.

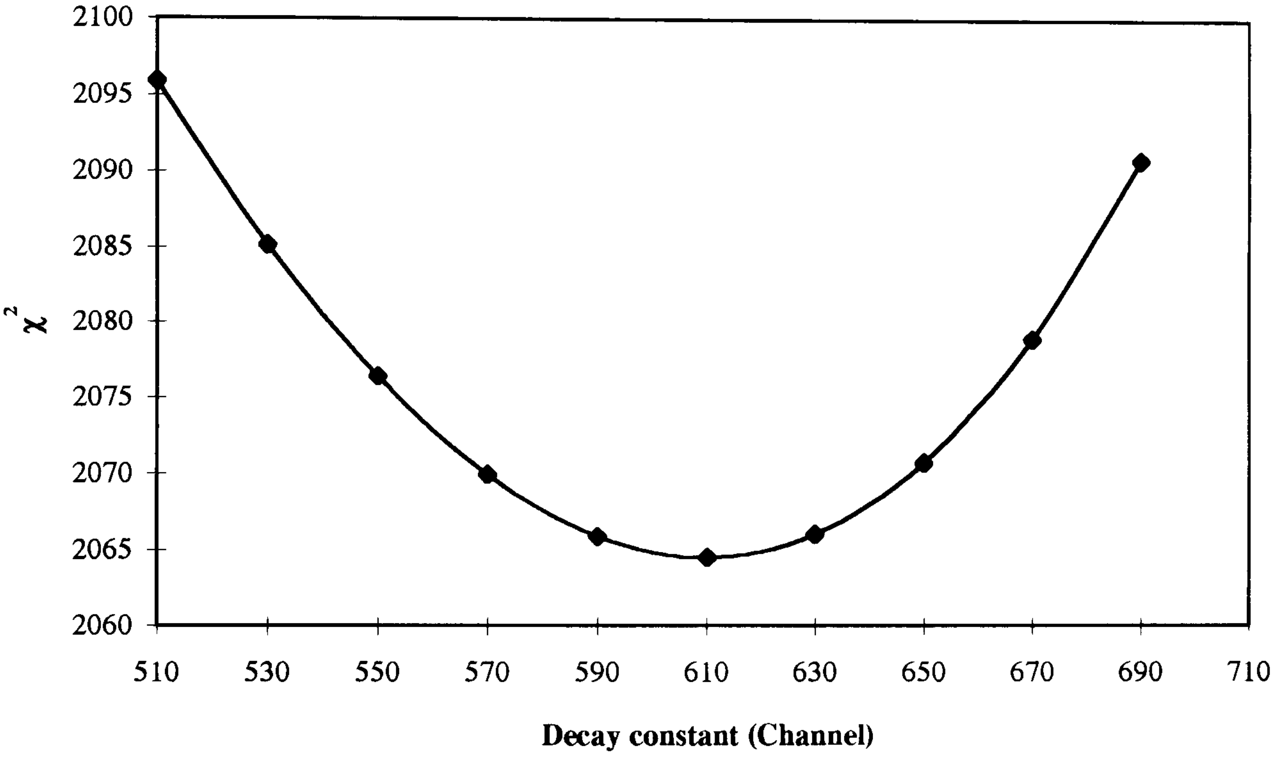

Figure 5.09 The minimum χ^2 is shown as a function of the decay constant, τ_1 for a single exponential. The minimisation is a smooth, well behaved function (2000 dof).

5.6.3.2. Residuals

Discrepancies between the fitted curve and the test data are difficult to distinguish due to statistical scatter in the latter. It is essential to also view the *residuals* (data- fit) or the *normalised residuals* (data-fit/ √data) when deciding if a fit is acceptable. Although a large amount of material is published reporting the time constants of scintillators and accompanying fits to experimental data [5 ,6 ,7], the residuals are only presented very rarely. If the published data is inspected closely, it is quite easy to see in several cases [5, 6], a significant deviation of the experimental data from the proposed fits.

5.6.3.3. Testing the fitting procedure with multiple exponential test data

There are obviously an infinite number of values which the input parameters A_1, A_2, A_3, τ_1, τ_2, τ_3 and Z can take. These could be used to establish the performance of the solving routine under any conditions. Generating the test data and fitting the parameters takes approximately 20 minutes for each data set. It is not feasible to test the procedure exhaustively. The aim of the evaluation is to demonstrate that the procedure works reliably for the subset of parameters which are encountered when fitting scintillation decay constants. It is also necessary to establish under what circumstances the fitting procedure fails, and why.

The *Solver* routine has been tested with many data sets that are typical of fast plastic scintillators, our HMF glasses, and also crystalline scintillators. In normal operation, the user enters initial estimates for each of the parameters. With sufficient practice, it is possible to start the fitting procedure very close to the optimal solution. However, it is sensible to ensure that the initial estimates of the parameters vary from the 'best-fit' parameters as the fitting procedure can *stick* with some of the initial estimates suggested by the user. This would bias the fit. Using typically a 5% deviation from the 'best-fit' values usually gives a final set of parameters which are independent of the initial estimates. Adopting this strategy significantly reduces the time required to obtain a solution and does not bias the final outcome.

If the *Solver* routine is called using estimates for the seven parameters which significantly disagree with the test data then the *Solver* routine often fails. It tends to force the values of the exponential parameters to the extremes of their defined range. Time constants are forced to 1 ns and amplitudes are forced extremely high or to zero. Alternatively the *Solver* returns the parameters for a local minimum which varies significantly from the global minimum solution.

Assuming sensible use, agreement between the parameters used to produce the test data and the fitted parameters is remarkably good. Estimates for the errors in the fitted parameters are given in Section 5.10. There are certain areas where the fitting procedure begins to encounter trouble. These are discussed under separate headings below.

5.6.3.4. *Similar decay times*

The *Solver* can fail to return the correct parameters for test data which have similar values for two of the decay constants. In the limit, $\tau_1 = \tau_2 \neq \tau_3$, the equation simplifies to a double exponential with amplitudes $(A_1 + A_2)$ and A_3. The *Solver* could not possibly be expected to differentiate between this data and the explicit definition in terms of three separate exponentials. When τ_1 and τ_2 are only slightly different, e.g. 10 ns and 12 ns, the *Solver* routine would fit a single exponential with a time constant of typically 11±1 ns. As the difference between the two times becomes larger, a single constant is fitted whose exact value is weighted by the relative amplitudes of the two similar components. i.e. the time constant will be numerically closer to the exponential component which has the larger amplitude, A.

If it is suspected that two time constants in a particular data set are similar, it is sometimes possible to separate the two components by forcing the initial estimate for the values of the time constants to lie on either side to the pair. e.g. if $\tau_1 = 12$ ns and $\tau_2 = 15$ ns, sensible initial guesses for τ_1 and τ_2 would be 9 ns and 17 ns. If the difference in the actual time constants is greater than 20% or 5 ns, whichever is the greater, the *Solver* routine would normally differentiate between the two components automatically. There is a degree of correlation between A_1, τ_2 and A_2, τ_1. If A_1 is too large and τ_2 is too small, τ_1 is forced to a larger value and A_2 becomes smaller to compensate. These non optimal solutions have non-flat residuals.

The user always has the ultimate power of *veto*, if the solution which the *Solver* generates is poor, the residuals will not be flat. This is immediately apparent to the user who can adjust the values of the initial estimates and re-call the solving routine until a solution which has residuals with negligible time structure is obtained.

5.6.3.5. *Long Time Component, τ_3*

If the time constant, τ_3 is large compared to the size of the data window (2000 ns), the exponential may not decay significantly over the data region. This is especially a problem when $Z/A_3 > 4$ and $\tau_3/window > 3$. Under these circumstances the correct fit is not obtained and the flat background is overestimated to include the long time component, $(Z + A_3)$. User intervention allows for correction of these non-optimal parameters returned by the *Solver* routine.

5.6.3.6. *Exponential components with different relative amplitudes*

When there are two scintillation components, and one contains significantly more events, the smaller component can be missed as it becomes lost in the statistical noise of the larger component. Residuals again indicate if this type of error has occurred. An example of this is the small fraction of biased data, typically 1% which can be missed altogether as the distribution of biased data contains so few events compared to the valid timing data.

5.7. Choice of the fit region

Section 5.4 discussed rounding of the leading edge of the measured timing spectrum due to the intrinsic system response. Simulations have shown that the effect significantly alters the first $2\sigma_T$ ns after the peak of the time distribution as shown in Figure 5.02. There are two strategies for coping with this corrupted data. Using DFTs it is possible to recover the underlying function, but statistical noise in the measured spectrum interferes with the Fourier Transformation. The other alternative is to exclude the first $2\sigma_T$ ns and fit the equation over the remainder of the time spectrum.

Excluding the first $2\sigma_T$ ns after the peak of the time distribution does present several problems. The fit to experimental or test data will estimate the values of the fitted amplitudes at $\Delta t = 2\sigma_T$ ns past the origin, $t=0$. The calculation to point back to the time origin is simple,

$$A_{k|t=0} = \frac{A_{k|t=2\sigma_T}}{\exp\left(\frac{-\Delta t}{\tau_k}\right)} \qquad k = 1...3 \qquad \text{Equation 5.19}$$

The subscript, k represents each of the three time components. The error in the predicted initial amplitude can be significant due to the uncertainty in the exact time delay of the fit window past the origin, Δt. The delay is the numerator of the exponential function in Equation 5.19, when $\Delta t/\tau_k \geq 1$, the error in $A_{k|t=0}$ becomes excessive. Figure 5.10 shows the uncertainty in the amplitudes at t= 0 for decay components with time constants of 15 and 4 ns where $\Delta t = 6 \pm 1$ ns.

For the TAC based system $\Delta t \cong 3 \pm 1$ ns, the uncertainty in the initial amplitude of a $\tau_d = 8$ ns component would be at worst, $^{+13\%}_{-12\%}$. The MCS has $\sigma_T = 4.25$ ns, the time bins are 5 ns wide. In this case $\Delta t = 10 \pm 2.5$ ns the error in an exponential component where $\tau_d = 8$ ns would be at worst, ±37%. This demonstrates one of the drawbacks of the MCS acquisition system.

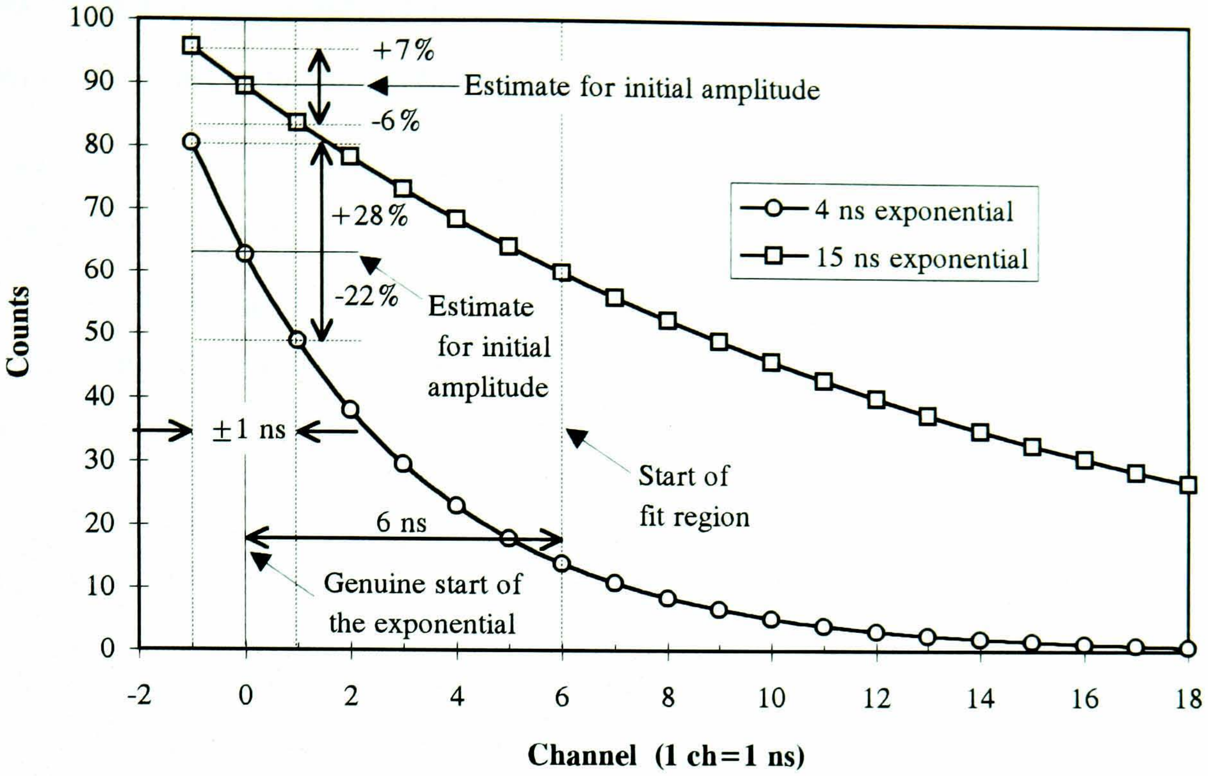

Figure 5.10 In this example, the fitting procedure obtains estimates for decay amplitudes at t ≅ 6 ns after the genuine start. For short decay components, *pointing-back* can give significant errors in the amplitudes at t= 0. The 15 ns and 4 ns components have worst case errors of $^{+7\%}_{-6\%}$ and $^{+28\%}_{-22\%}$ respectively.

By excluding the first portion of the timing spectrum, short time-scale components can be missed altogether by decaying before the start of the fitting window. The fitting procedure has a finite sensitivity to small amplitude time components which are superimposed on larger components with longer time constants. There is not a single '*amplitude sensitivity*' figure. Whether or not the fitting procedure can identify a component A_1, will depend on the values of all the other parameters which define the time spectrum. If it is assumed that the limit on A_1 being detected is $A_1 \geq \Pi$ counts, only time components which have an amplitude of $\geq \Pi$ at $2\sigma_T$ ns past the time origin will be identified by the *Solver* routine,

$$A_{1|t=0}\exp\left(\frac{-2\sigma_T}{\tau_d}\right)\geq \Pi$$

Equation 5.20

An example of the fitting procedure missing a fast time component is the 20%, 0.6 ns decay of BaF_2. This is superimposed on the larger 80% component that decays with a time constant of approximately 620 ns. The initial amplitudes are in the ratio fast: slow, 250: 1. Typically data is recorded until the slow component contains 1000 events per channel at ≈10 ns past the leading edge of the exponential. Using this figure the fast component will have an initial amplitude of 250,000. The exponential decay of the 0.6 ns component reduces its amplitude to only 10 counts by t= 6 ns. The fast component is not observed within the data fitting window. This short decay constant is an extreme example, time constants of fast plastic scintillators (t_d≈ 3 ns) can be measured. Determining the decay constants of very fast components has been discussed in Section 5.4.1.

Excluding the first portion of the timing spectrum should not affect the values of the fitted scintillation time constants. To prove this with test data, the same data set was fitted several times, excluding an increasing portion of the leading edge of the exponential. The fitted decay constants are stable within the limits of the fitting procedure and the amplitudes at the beginning of the fit region decrease with time as expected. This data is shown in Table 5.02.

Start Fit @	Background	Amplitudes [counts]			Decay Consts. [channels]			χ^2/dof
[channel]	Z [counts]	A_1	A_2	A_3	τ_1	τ_2	τ_3	
0	14.17	3000.3	2996.6	40.0	11.96	30.11	358	0.70
5	14.12	2168.5	2330.6	38.3	12.92	31.02	350	0.70
10	14.09	1657.5	1748.6	37.1	14.65	32.21	374	0.70
15	14.18	814.5	1870.5	38.8	11.50	29.78	356	0.69
20	14.18	525.1	1574.6	38.3	11.76	29.81	356	0.70
Test data	15.00	3000.0	3000.0	40.0	12.00	30.00	350	

Table 5.02 The position of the fit window does not affect the fitted time constants.

5.8. Selection of bin width

The TAC has a wide range of time windows which can be selected by the user. The choice of time window governs the calibration constant of the TAC/ MCA combination. It is possible to select any of the following 1, 5, 10, 50, ... ns per channel for the timing data.

If 1 ns per channel is used, the χ^2 routine will have many data points to fit over. The statistical noise on each data point will be large for a given number of events. If a larger bin width is used, the fitting procedure will have fewer data points to fit over but the statistical noise on each datum will be smaller. At the limit of an infinite bin width, all of the counts would fall in to one channel thus making a fit impossible. At the other extreme, infinitely narrow bins would never contain a statistically valid number of events.

From statistical theory, to fit an equation which has n degrees of freedom to data, one must have at least n+2 distinct observations of the data. As the apparatus must be capable of measuring short decay times (≈10 ns), all data was recorded with the finest bin width possible. For the TAC/MCA system this is 1 ns per channel. If it were required to convert the data to a 10 ns per channel format for the fitting procedure this could have been done.

On the other hand, retrospectively moving from a 10 ns bin width to a 1 ns bin width is impossible.

5.9. Results for standard scintillators

5.9.1. Introduction

In the previous sections of this chapter the fitting of parameters to test data has been discussed. The presented results indicate the level of uncertainty due to the fitting procedure in isolation. When used to fit experimental timing spectra, the fitted parameters will contain uncertainties due to the fitting procedure and also due to deficiencies in the measured experimental timing data.

Presented in this section is the timing data for a variety of commercial scintillators. The aim is to demonstrate that the system operates correctly, and to show the uncertainty in fitted parameters which are obtained using the composite timing system. The majority of the data shown below has been recorded using the TAC/ MCA combination in the 'one-hit' configuration. All of the fits for this data were calculated using 1 ns per channel granularity. However, for slow scintillators, the data has been re-binned to 10 ns per channel for display. The overlaid fits for the 10 ns per channel data are scaled from the 1 ns per channel fits.

Similar data has been recorded and analysed for the MCS timing system. For this data, the 5 ns per channel range was used for data acquisition, fitting and display. Table 5.03, summarises the published decay constants [1, and references cited within] and the experimentally determined parameters for both systems. The actual timing spectra for the MCS system is presented for only BaF_2 and BGO, as this system is inferior to the 'one-hit' method and was not used for the HMF glass results presented in Chapter 6. All data was recorded at room temperature which typically varied between 18 and 26°C.

In all cases, the data is plotted on a logarithmic scale with the *normalised residuals* (data-fit)/√data plotted above. The normalised residuals are scaled between -3σ and $+3\sigma$ throughout for consistency. Error bars are indicated on the timing data, these are calculated using, $\sigma=\sqrt{\text{datum}}$.

5.9.2. Cs I(Tl)

Thallium doped caesium iodide has a main decay constant of 1000 ns and an afterglow which corresponds to 0.5- 5% of the scintillation light after 6 ms [8]. The afterglow is too slow to be distinguished by the TAC/ MCA system and appears as an increased level in the flat background as shown in Figure 5.11. The peak emission wavelength is 550 nm but the spectrum extends down to 320 nm. Our experimental data shows a rounding of the leading edge of the timing response which has a 40 ns rise time in agreement with the literature [9]. This is due to the fact that all of the optically active sites are not populated simultaneously.

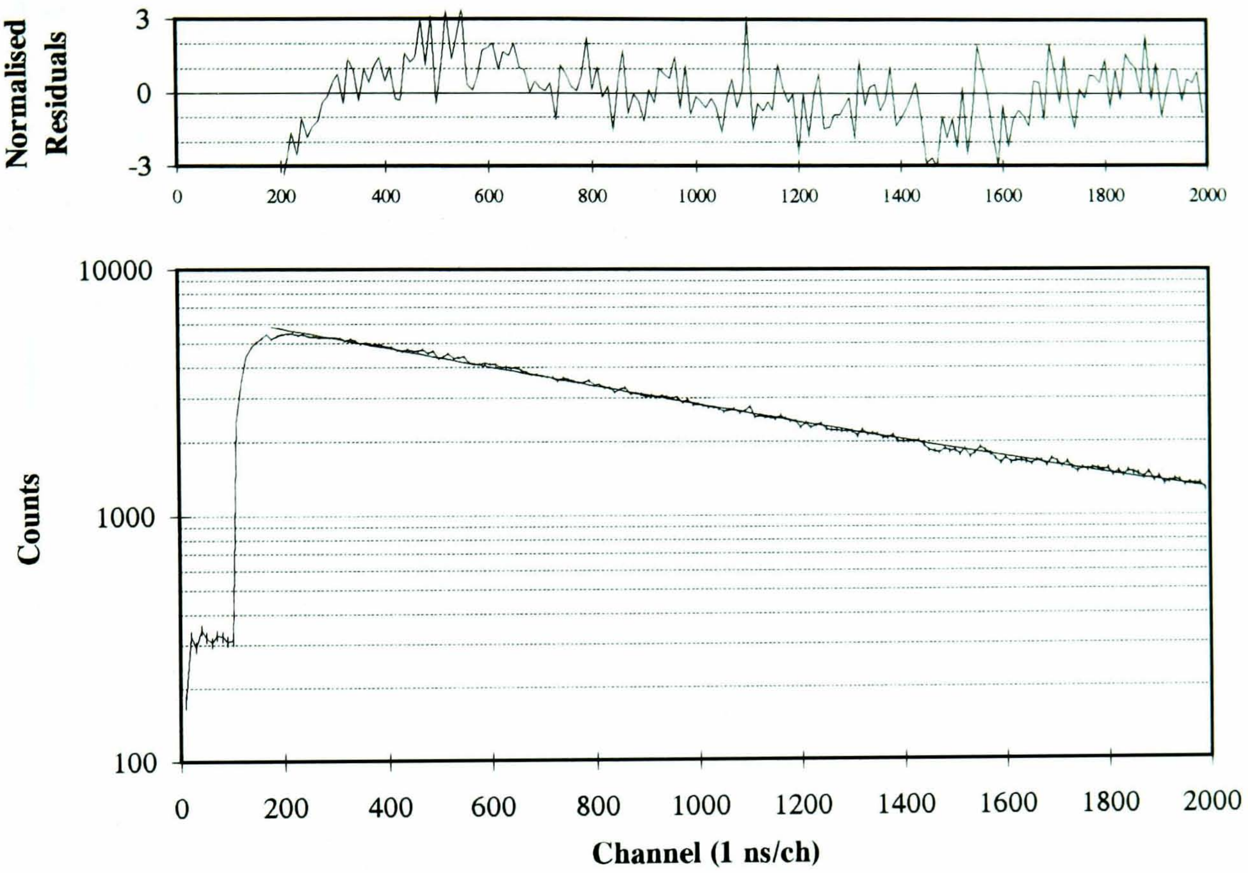

Figure 5.11 The TAC/MCA timing spectrum for CsI(Tl).

The fit to TAC/ MCA experimental data has reasonably flat residuals. The region of fit excluded the leading edge of the exponential, the fitted decay constant for this data is 1002 ns. The χ^2 is 1.18 per degree of freedom (1800 points).

5.9.3. BaF_2

Barium fluoride, BaF_2 has a 0.6 ns component emitted at a wavelength of 195, 220 nm, this corresponds to approximately 20% of the total emitted light. The main (80%) component is emitted at 310 nm with a decay constant of 620 ns. The experimental data in Figure 5.12 was recorded using the TAC/MCA, it clearly shows a fast spike which arises from the 0.6 ns emission, this falls outside the fitting window. The main component is fitted by a single decay constant of 583 ns. The relative proportions of each are 19.4% fast : 80.6% slow, the area of the 600 ps component was measured from the number of counts in the fast spike.

Allowing for the QE of the photocathode, at each emission wavelength, the ratio is revised to 21.5%:78.5%. The χ^2 for this data is 1.07 per degree of freedom. The fast spike has been qualitatively compared to a 0.6 ns exponential in Figure 5.02. The amplitude ratio agrees well with the literature indicating that dead time effects did not significantly interfere with data acquisition.

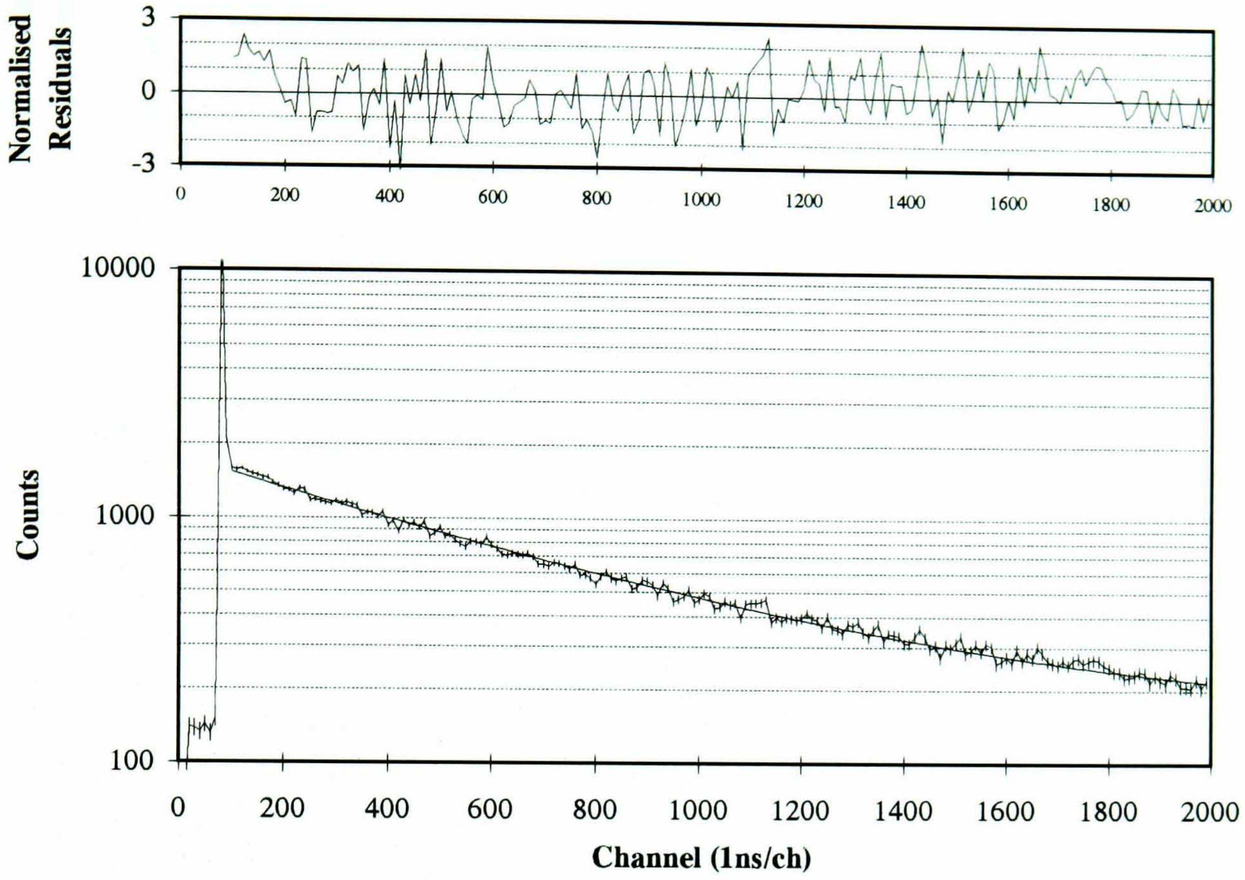

Figure 5.12 The timing spectrum for BaF_2 measured using the TAC/MCA system.

The MCS data is shown in Figure 5.13 , the fit to experimental data for the slow component is 615 ns, a 2%, 67 ns component is also observed.

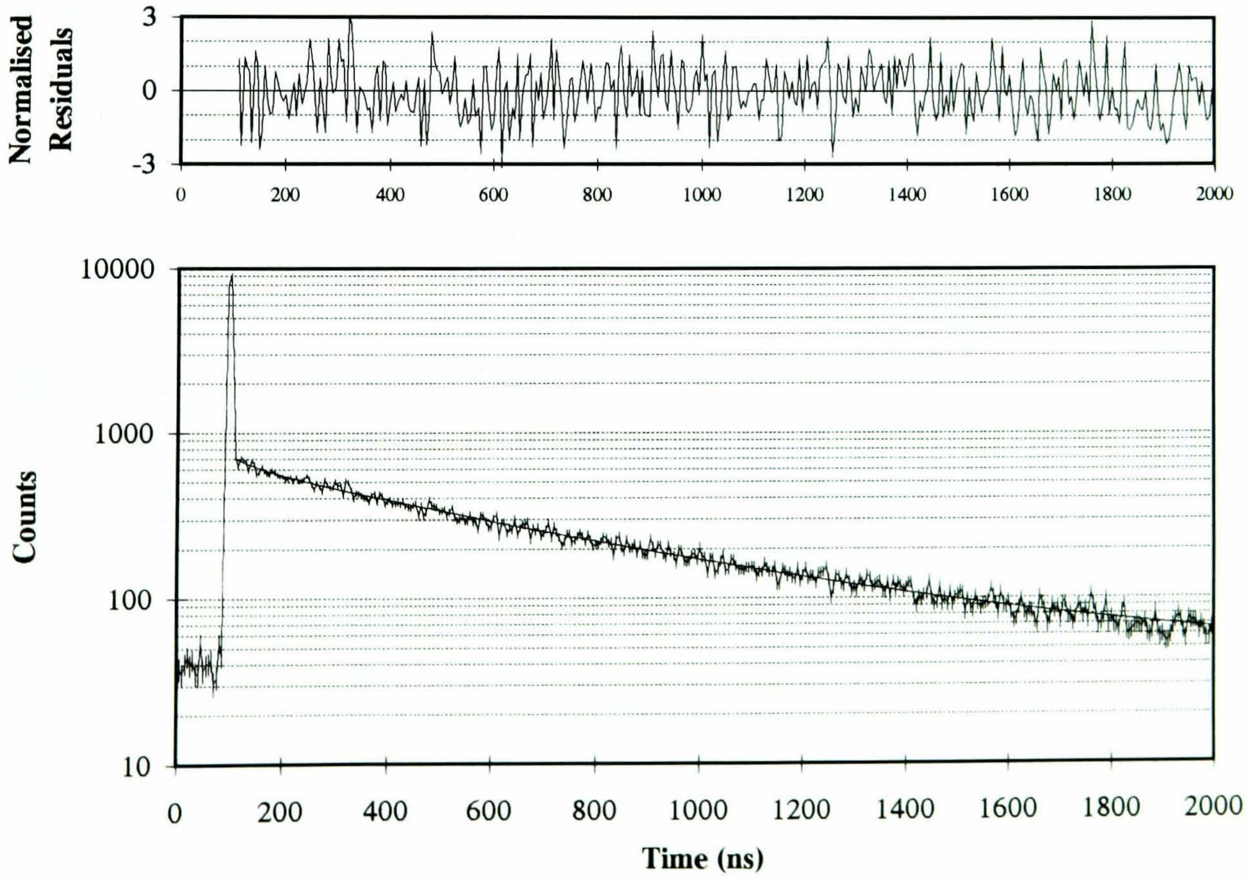

Figure 5.13 The timing spectrum for BaF_2 measured using the MCS system.

5.9.4. BGO

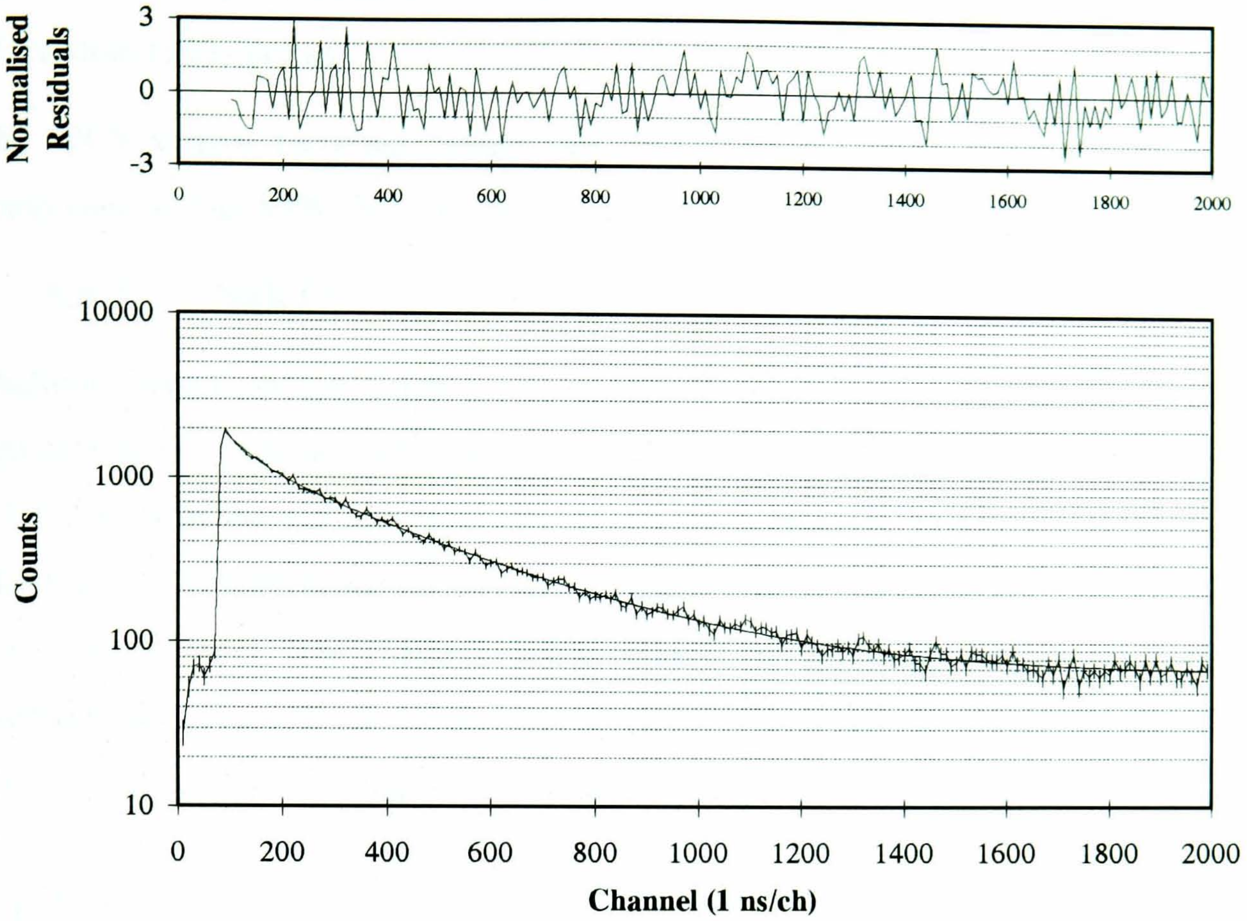

Figure 5.14 Timing spectrum for BGO measured using the TAC/MCA system.

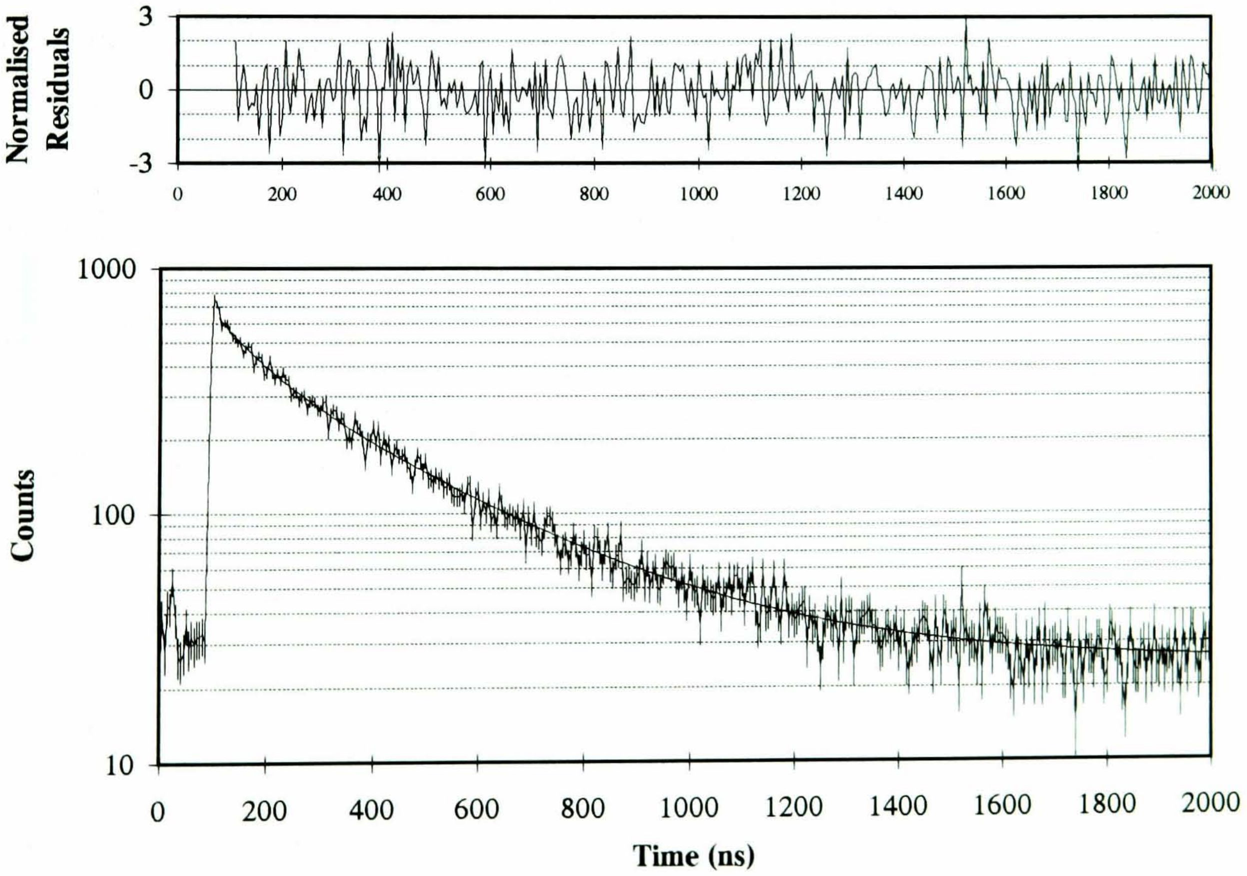

Figure 5.15 The timing spectrum for BGO measured using the MCS system.

The timing spectrum for BGO consists of two components. From the literature [10], these are quoted as a 10%, 60 ns component and a 90%, 300 ns component. The timing spectrum is presented in Figure 5.14. This was recorded using the 'one-hit' method. The residuals are completely flat indicating an excellent fit. The decay time constants are a 10%, 63 ns component and a 90%, 309 ns component. The χ^2 for the fit is 1.02 per degree of freedom (1900 points).

The MCS system recorded timing data for BGO, this data fitted to an 11%, 80 ns component and an 89%, 325 ns component. This is shown in Figure 5.15.

5.9.5. NaI(Tl)

Thallium doped sodium iodide is not described by a simple exponential decay. The optically active sites are populated by transfer from a level which has a lifetime of 60 ns [11]. Decay of the 415 nm optically active sites is characterised by a 230 ns exponential. The recorded timing spectrum shown in Figure 5.16 is distorted due to the nature of the population process. The fitting procedure could not be used for this data, the visually overlaid curve has a decay constant of 230 ns. As expected, the residuals are not flat and the χ^2 per degree of freedom is correspondingly high (3.54). This indicates a poor fit.

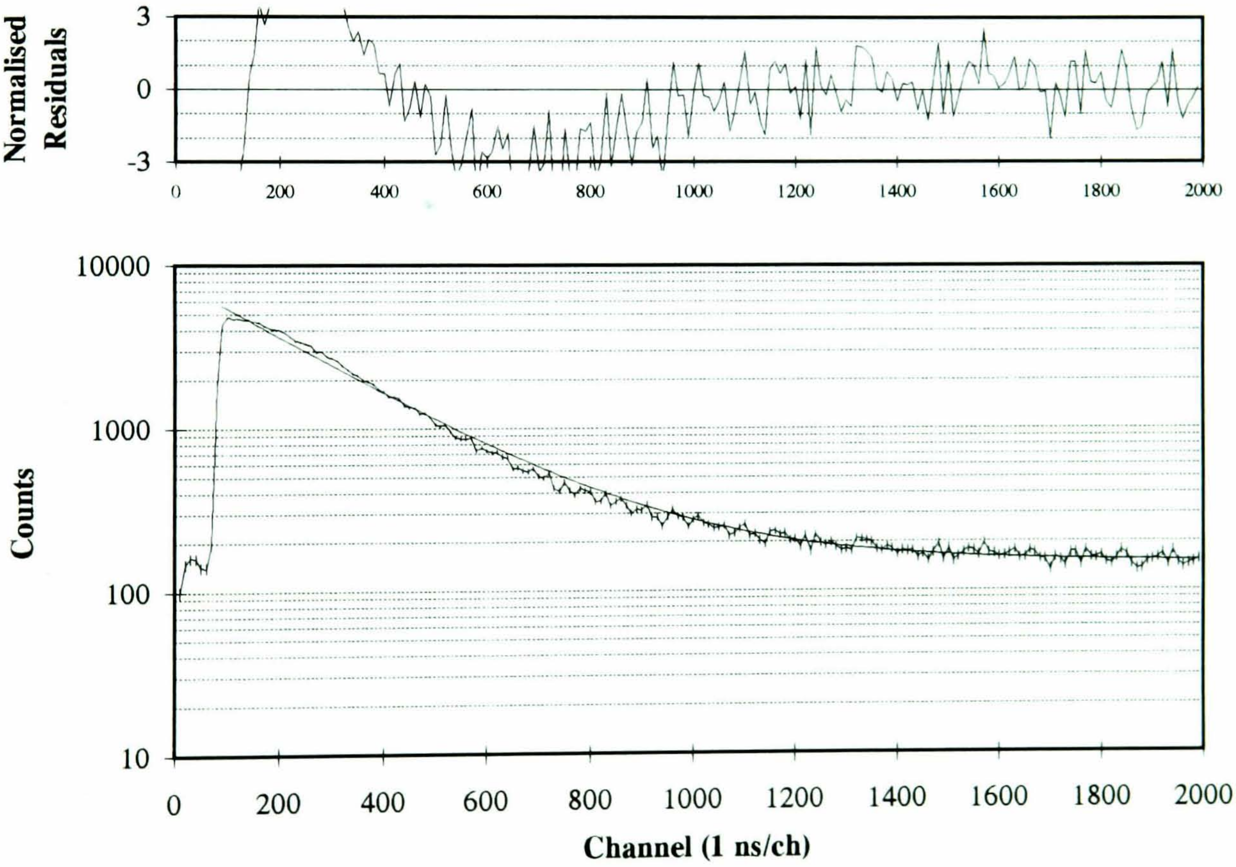

Figure 5.16 The timing spectrum for NaI(Tl) recorded using the TAC/MCA system.

5.9.6. CeF_3

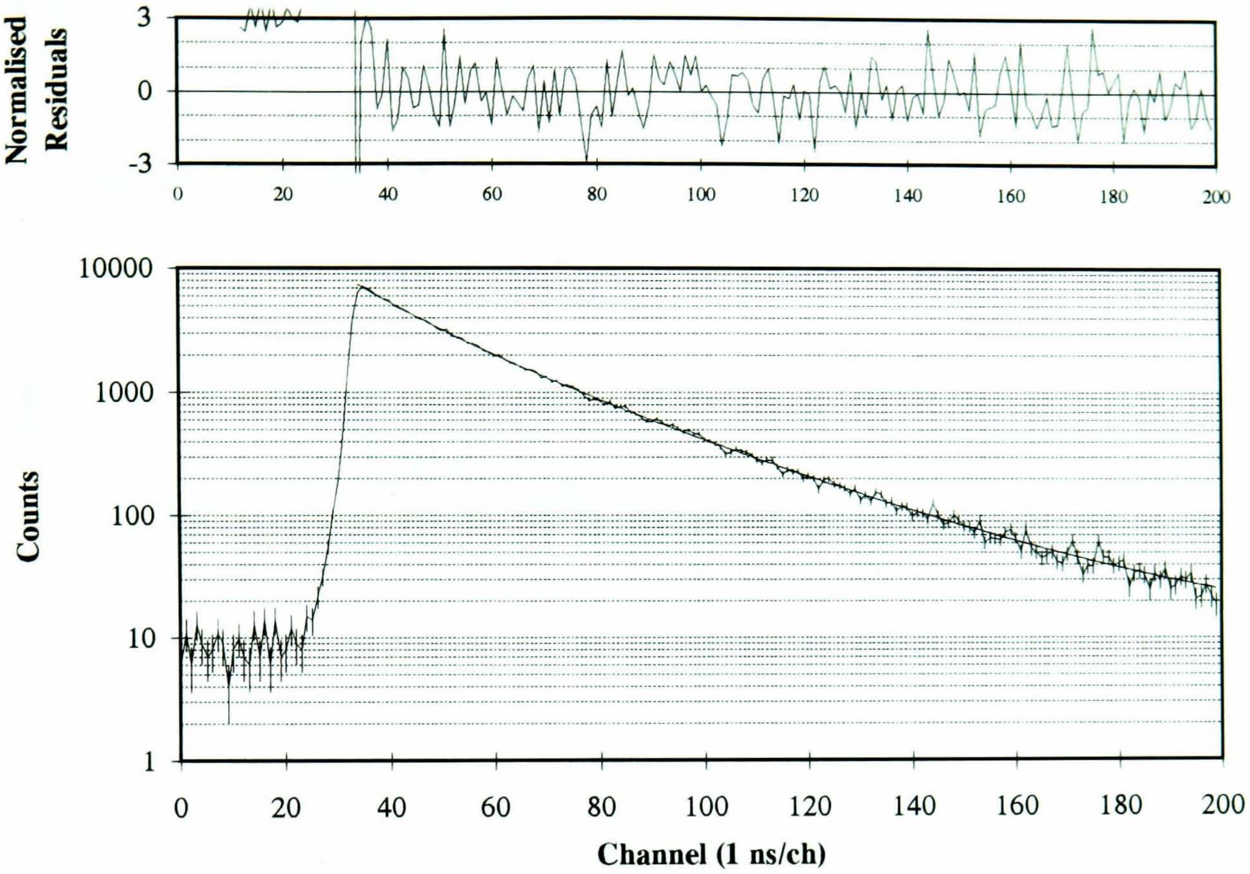

Figure 5.17 The TAC/MCA timing spectrum for CeF_3.

This crystal is an alternative to HMF glasses in the CMS experiment. The material has only relatively recently been identified as scintillator [12]. The decay constants and amplitudes are quoted as 8 ns and 25 ns by the Crystal Clear collaboration headed by P. Lecoq [13]. Our timing data for the sample shown in Figure 5.17 fits to a 25%, 12 ns component, a 73%, 28 ns component and a 1.6%, 361 ns component.

As it is a fast scintillator, the graph shown has not been re-binned to 10 ns per channel. Only 200 ns of the time spectrum is shown. χ^2 for this data over the whole time window is 1.09 per degree of freedom.

5.9.7. CsI (pure)

Pure Caesium Iodide has a main decay component of 16 ns. Our TAC/MCA experimental data fitted to 70% 7 ns, 19%, 34 ns and 11% 1.7 μs components. Only 500 ns of the time spectrum is shown, χ^2 for this data over the whole time window is 1.01 per degree of freedom. The MCS data (not shown) fitted to a 42% 14 ns and a 58% 45 ns components.

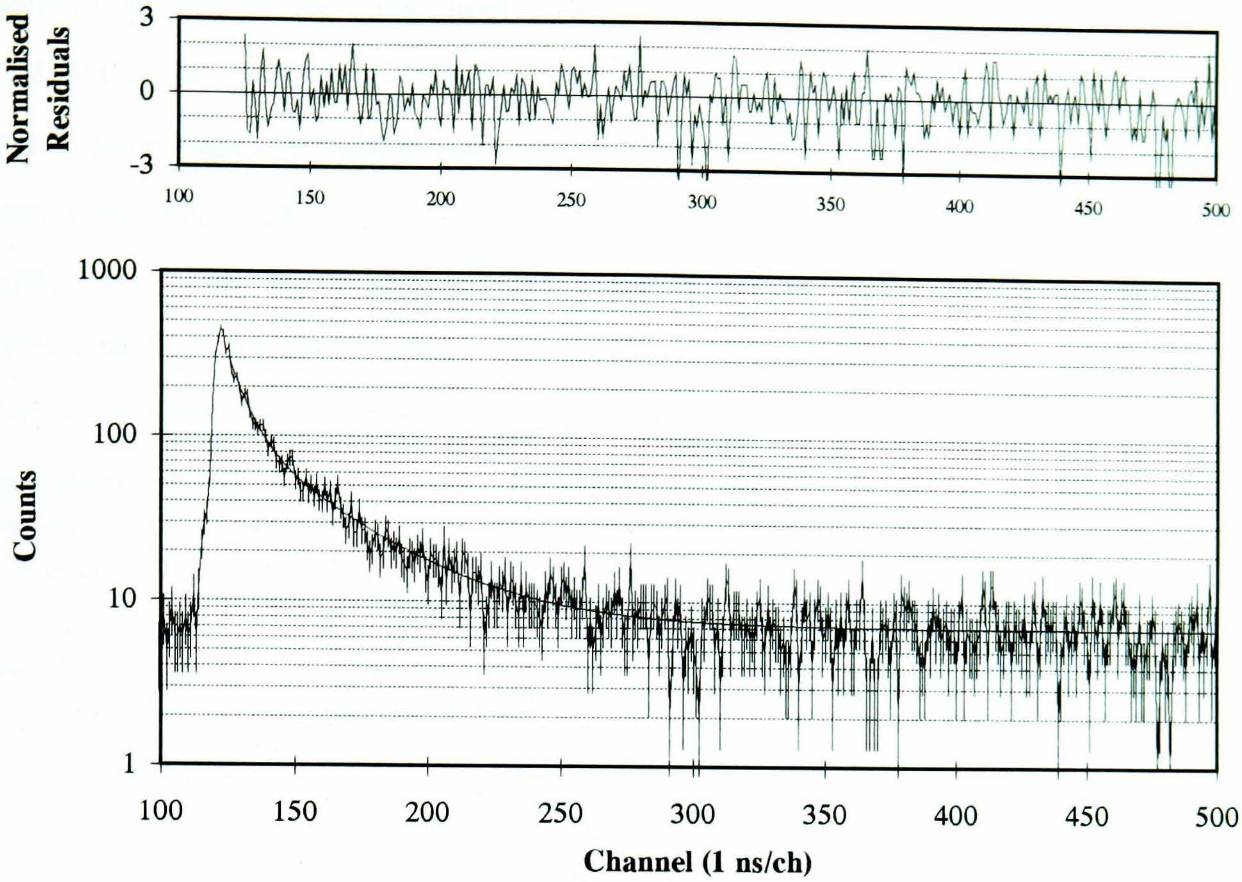

Figure 5.18 The TAC/MCA timing spectrum for pure CsI.

5.9.8. NE110

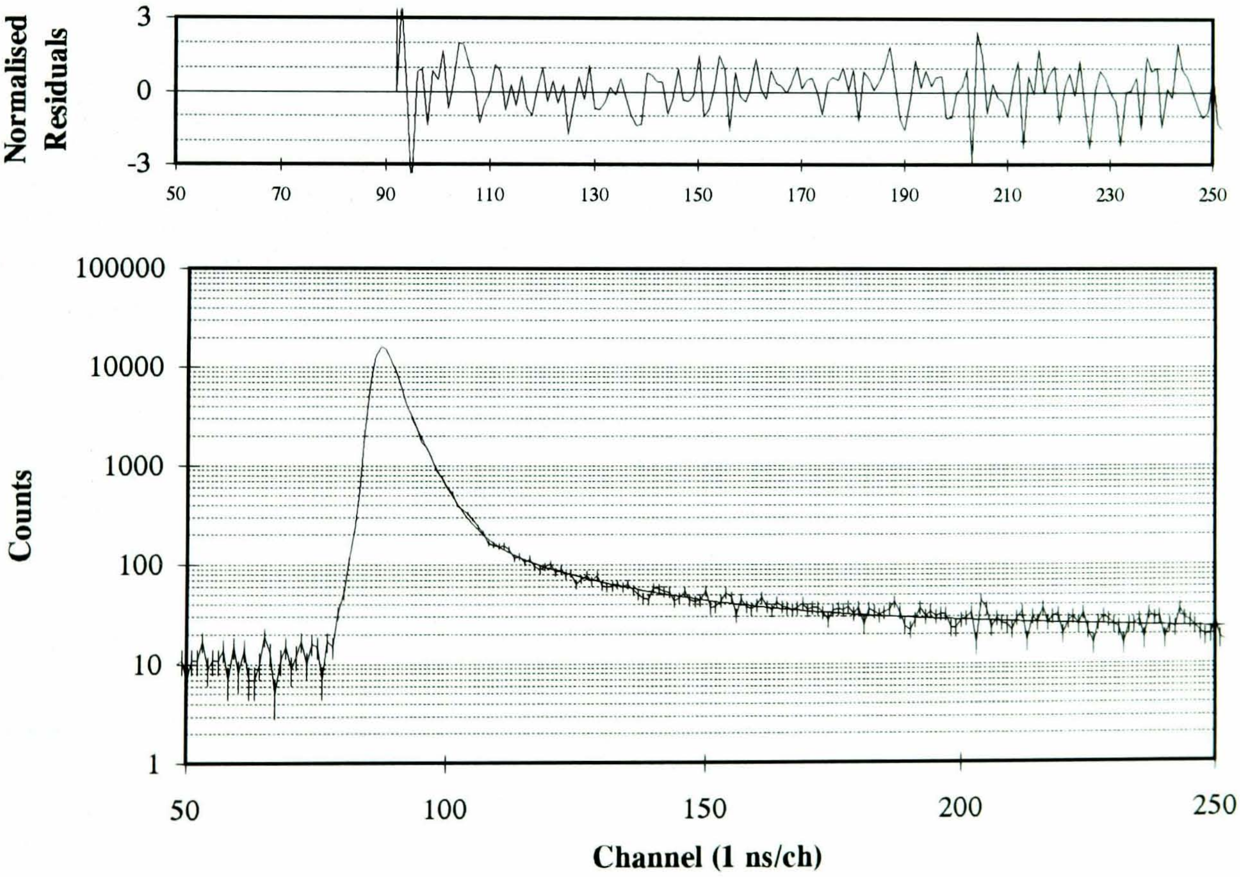

Figure 5.19 The timing spectrum for NE110 measured using the TAC/MCA system.

NE110 is a fast plastic scintillator, the manufacturer [14] states that the majority of scintillation light is emitted with a 3.3 ns time constant. But does not indicate the time constants of the other components. A qualitative fit to a 3.3 ns exponential is given in

Figure 5.08. The 3.3 ns component does extend in to the fitting window and has also been fitted using the multi-exponential χ^2 procedure. The timing spectrum was described by three exponentials, the fastest was a 3.6 ns component and the two slower components had decay constants of 28 and 389 ns. The ratio of their light yields is 31.8%: 31.0%: 37.2% respectively. The fit to experimental data is shown in Figure 5.19, the data points correspond to 1 ns per channel. The fit has flat residuals over the entire 2000 ns time window although only 250 ns is shown in the figure as this is a fast scintillator. The χ^2 for this data over the whole time window is 1.05 per degree of freedom (1920 points).

Sample	Quoted		TAC/ MCA system			MCS system		
	τ_d (ns)	rel.amp.	τ_d (ns)	rel.amp.	χ^2/dof	τ_d (ns)	rel.amp.	χ^2/dof
CsI(Tl)	1000 + afterglow	100%	1002	100%	1.18 (1800pts)	1063	100%	1.17 (380pts)
BaF_2	0.6 620	20% 80%	$0.6^{(a)}$ 583	20% 80%	1.07 (1900pts)	67 615	2% 98%	1.45 (380pts)
BGO	60 300	10% 90%	63 309	10% 90%	1.02 (1900pts)	80 325	11% 89%	1.16 (380pts)
NaI(Tl)	230 + growth	100%	-	-	-	-	-	-
CeF_3	8 25	- -	12 28 361	25% 73% 2%	1.09 (1900pts)	-	-	-
CsI	16	100%	7 34 1740	70% 19% 11%	1.01 (1900pts)	14 45	42% 58%	-
NE110	3.3	-	3.6 $3.3^{(a)}$ 28 389	32% - 31% 37%	1.05 (1920pts)	-	-	-

Table 5.03 Summary of the fits to experimental data obtained using the TAC/MCA and MCS systems. $^{(a)}$ indicates data fitted using the convolution procedure.

5.10. Summary

The procedure which has been written for fitting multiple exponentials to the scintillation decay time data is based on the minimisation of a multi-nomial χ^2 function. It has worked very well with artificial test data. Adding statistical noise to the test data does cause slight errors in the values of fitted parameters but these are typically very small:

10 ±1 ns 50±2 ns 300±10 ns

Due to the intrinsic width of the timing system response, the leading edge of the timing data is rounded off. To deal with this corruption, the first $2\sigma_T$ ns after the leading edge of the exponential is excluded from the fit, as it is only this region which is affected. σ_T is the intrinsic system width. To predict the ratio of the initial heights of the exponentials it is necessary to *point-back* to the time origin. For fast time components, uncertainty in the position of the time origin can cause errors in the estimated initial amplitudes. Using a restricted range of data for the fitting procedure does not affect the values of the fitted time constants. Exponential components which decay too fast are missed altogether by the fitting procedure, an example is the fast component of BaF_2.

Timing data will always contain a fraction of biased events due to dead time effects in the acquisition system. These additional events cause small amplitude components which are not perfectly exponential. They are fairly well described by an exponential term which has a time constant approximately half that of the true scintillation spectrum. This small number of events could be responsible for the low estimate obtained by the TAC/MCA system in the case of the 620 ns slow component of barium fluoride. Although, the MCS obtained a satisfactory fit for the same experimental configuration. (Data is recorded for both systems simultaneously in parallel).

The fitting procedure can fail to distinguish two genuine exponential components whose decay constants are within 20% or 5 ns of each other, which ever is the largest. Also small amplitude components are sometimes missed when the timing spectrum also contains larger components. It is essential to estimate initial values for all of the parameters of the fitting equation. This prevents the procedure attempting to optimise local minima or becoming lost. The minimisation function is well behaved in the vicinity of the global minimum.

Due to the complex nature of these problems, the fitting procedure has to be monitored. Sometimes it is necessary to adjust the parameters which are returned and re-call the *Solver* routine a second time. To qualitatively estimate the success of a particular fit, it is essential to inspect the residuals. i.e. a graph of *data-fit/√data* verses *channel*. For a satisfactory fit, the residuals should have no underlying structure. Except for statistical noise, the residuals should be flat. With care, the fitting procedure can return solutions for test data which are accurate at the few percent level. The agreement between experimental data and the published values for these materials also agrees at the few % level.

The fitting procedure has been used to fit data from both the TAC and MCS systems. The 5 ns bin width of the latter system and its large intrinsic system width detract from its ability to record fast timing data. These observations have been confirmed when attempting to fit MCS data. In contrast, the TAC system has a minimum bin width of approximately 1 ns and an intrinsic width (FWHM) of 3.3 ns. It is capable of recording time constants as low as 2 or 3 ns conventionally or below 1 ns using convolution.

---

[1] S.E. Dorenzo and W.W. Moses LBL-33295 UC-407(1992).

[2] S. Baker, R. Cousins, *Nucl. Instru. Meth.* **A221** (1984) 437.

[3] B.K. Sinha, R. Bhattacharya, *Nucl. Instru. Meth.* **A276** (1989) 237.

[4] M. Laval et al, *Nucl. Instru. Meth.* **206** (1983) 169.

[5] R. Zhu and Z. Wei, *Nucl. Instru. Meth.* **A332** (1993) 373.

[6] J. Webber, *Scintillation Mechanisms in Cerium Fluoride*, LBL-27609 (1993).

[7] S. Anderson et al, *Nucl. Instru. Meth.* **A332** (1993) 373.

[8] *Scintillation Detectors*, Harshaw, p19.

[9] H. Grasman et al, *Nucl. Instru. Meth.* **228** (1985) 323.

[10] M. Mozynski et al, *Nucl. Insrtu. Meth.* **188** (1981) 403.

[11] J.B. Birks, *The Theory and Practice of Scintillation Counting*, Pergamon Press, (1964) p452.

[12] D. Anderson, *IEEE Trans. Nucl. Sci.* **36** (1989) 137.

[13] P.Lecoq, *Crystal Clear Collaboration.*

[14] *Scintillation Materials*, NE Technology.

CHAPTER SIX

Experimental Results

6.1. Preliminary discussion

With the exception of the CERN beam tests which are presented in chapter seven, all experimental results from this research program are discussed in the current chapter. In addition to results concerning radiation damage and the determination of scintillation decay constants, the small sample light yield and density measurements for each glass are presented. The author has made no contribution to the small sample light yield measurements. This work was done at the Rutherford Appleton Laboratory by R.M. Brown *et al.*

Table 6.01 summarises the experimental data for each glass. The glass name is coded according to the site where it was produced. Indices prefixed with 'B' signify Brunel University (Physics Department); 'JHA', Brunel University (Materials Technology); 'HP', Paisley University; 'N', The Lebedev Institute, Moscow; and 'P', Sheffield University (Materials Department). HP are silicate glasses, for clarity these are separated from the fluoride glasses in Table 6.01. Compositional information is in mol% throughout the entire thesis. The columns labelled 'Balance' contains any elements of the glass which have not been specified separately in the preceding columns. 'Comments' contains information relevant to the production process. i.e. atmosphere, source of materials (M≡ Merck, JM≡ Johnson Matthey, R≡ The Lebedev Institute, Russia).

Name	Compositional Information (Fluorides mol %)										Production Information	Scintillation Decay Constants							Pile-up, Ω	Density	Light Yield	Dose const.	Sat.300	Sat.350	Sat.400	λ_{cut}	Resid. Abs.	%Anneal	Thickness	Name
	Hf	Ba	Li	Ce	Al	In	La	Yb	Balance	Balance	Comments	$A_2(t=0)$	$A_3(t=0)$	τ_1[ns]	τ_2[ns]		τ_3[ns]	χ^2/dof	frac(25/500)	ρ [gcm^{-3}]	Rel.CeF$_3$	[krad]	[OD cm^{-1}]	[OD cm^{-1}]	[OD cm^{-1}]	[nm]	[ODcm^{-1}]		[mm]	
B1	57	34	0	5	4	0	0	0				553	17	15	29		588	1.04	0.646	6.00		1000-370	8.47	3.26	1.95	299	1.37	57.9	3.07	B1
B4	57	34	0	5	4	0	0	0				1396	13	11	30		361	1.01	0.646											B4
JHA6	58	33	0	0	4	0	5	0				0	107	18	100		487	1.02	0.635	5.99		410	5.46	3.21	1.93	207	1.39	56.6	4.67	JHA6
JHA7	58	33	0	2	4	0	3	0				146	12	21	58		563	1.04	0.591	5.99		800-340	6.50	4.12	2.49	298	0.23	94.3	4.61	JHA7
JHA8												691	12	12	28		662	1.04	0.670			1000-630	7.63	3.92	2.50	301	2.03	48.2	4.59	JHA8
N1	54	20	0	0	2.5	2	3	0	Pr 1%	Na 18%		246	78	10	60		693	1.12	0.709	5.95		575	2.66	0.70	0.18	292	0.45	35.1	5.60	N1
N4	57	33	0	8	0	2	0	0	Zr 0.2%			754	5	9	25		818	1.04	0.692	6.01		520-400	-	0.55	0.18	304	0.43	22.5	4.00	N4
N5	57	33	0	8	0	2	0	0				610	4	10	27		456	1.05	0.693	6.04		480-400	3.00	0.45	0.10	301	0.26	42.2	5.33	N5
N6	57	33	0	8	0	2	0	0				948	6	8	24		255	1.04	0.684	6.05		500-200	3.00	0.43	0.10	301	0.24	42.5	5.04	N6
N7	57	33	0	8	0	2	0	0				451	4	9	25		840	1.03	0.705	6.04		550	-	0.80	0.30	303	0.46	42.7	4.77	N7
N11	55	15	20	5	2.5	1	0	0	Pb 2%	0.75%Wt	PTFE 0.25%	547	4	8	21		266	1.00	0.702	6.10		525	3.50	1.40	0.55	299	0.56	60.1	4.89	N11
	55	20	16	5	2.5	1.5	0	0			9 parts this mixture plus																			
N13	57	33	0	6	4	0	0	0			3 parts this,+ 1% wt Mn	170	8	6	24		383	1.02	0.696	5.60		460-300	2.80	0.55	0.23	299	0.08	86.0	5.07	N13
N14	54	17	20	5	2.5	0	0	0		TiO_2 0.5%	PTFE 0.25%Wt	497	9	11	29		518	1.00	0.686	6.09		550-425	2.00	0.30	0.08	303	0.20	31.8	5.21	N14
N16	55	20	17	5	2.5	0.5	0	0		Zn 1%Wt		653	19	11	30		416	1.02	0.678	6.48		525	18.40	2.76	0.61	295	0.48	82.7	1.63	N16
N17	57	33	0	8	0	2	0	0				758	5	9	26		414	1.09	0.691	6.27		525	5.52	0.83	0.18	300	0.41	50.1	5.43	N17
N26	54	20	17	5	3	1	0	0.5			Batch 2	319	49	10	30		598	1.04	0.704	5.89		520	3.30	0.80	0.19	298	0.64	20.3	3.19	N26
N27	54	20	17	5	3	1	0	0.8			Batch 3	174	63	12	34		650	1.01	0.699	5.89		500	-	2.80	0.40	298	0.42	85.1	2.72	N27
N28	54	20	17	5	3	1	0	0.5			Batch 2	560	47	9	26		653	1.02	0.697	5.80	2.70%	520	2.90	0.70	0.11	300	0.36	48.0	4.00	N28
N29	53	20	18	5	2.5	1.5	0	0			Batch 2	435	57	10	28		521	1.01	0.701	5.94	3.70%	480-400	3.30	0.37	0.09	296	0.22	40.3	2.02	N29
N30	55	17	20	5	2.5	1	0	1			PTFE 0.25	122	5	11	38		895	1.03	0.714			620-100	2.60	1.55	0.16	298	0.75	51.8	4.94	N30
N33	54	20	17	5	3	1	0	0.5			Batch 3	683	11	7	26		626	1.01	0.684	5.74		700	2.30	1.24	0.16	298	0.63	48.9	3.26	N33
N36	48	20	9	8	3	1	0	0.5				543	7	8	24		612	1.05	0.701			500	3.00	0.85	0.15	299	0.44	48.4	2.46	N36
P13	57	34	0	5	4	0	0	0			Pt 10% O_2									5.92		1000-700	4.52	2.70	2.26	300			5.74	P13
P14	57	32	0	5	4.1	0	0	0		Mn 1.5%	Pt 10% O_2	485	6	12	28		250	1.04	0.677	5.91		600-180	3.27	1.84	1.12	300	0.52	71.6	6.26	P14
P15	57	34	0	0	4	0	3.5	0		Gd 1.5%	Pt 10% O_2	202	52	10	47		435	1.03	0.714	5.98		500-265	3.45	2.16	1.36	282	1.04	51.9	6.24	P15
P16	57	34	0	0	4	0	3.6	0		Pr 1.37%	Pt 10% O_2									5.95		310	6.42	4.81	2.17	271	2.05	57.4	6.23	P16
P17	56	34	0	5	4	0	0	0	Zr 1%		Pt 10% O_2	1205	9	11	29		341	1.04	0.660	5.94		850-500	3.55	2.11	1.18	300	0.07	96.8	5.91	P17
P20	54	32	0	10	3.8	0	0	0			Pt 10% O_2	1283	4	9	26		233	1.05	0.672	5.93		800-500	2.56	1.36	0.80	305	0.23	83.1	6.24	P20
P21	0	34	0	5	4	0	0	0	Zr 57%		Pt 10% O_2	146	25	6	36		431	1.02	0.675	4.62		380-240	1.28	0.20	0.12	303	0.03	85.0	6.25	P21
P22	62	33	0	5	0	0	0	0			Pt 10% O_2									6.06		850-540	4.10	2.20	1.35	301	0.11	95.0	6.26	P22
P23	56	30	4	5	4	0	0	0			Pt 10% O_2	252	3	19	38		485	1.04	0.609	5.92		750-200	3.50	1.90	1.12	301	0.07	96.4	6.20	P23
P25B	57	34	0	5	0	4	0	0			Remelted Pt 10% O_2	166	10	11	33		850	1.06	0.708	6.02		520-700	3.77	0.58	0.15	300	0.21	64.1	3.16	P25B
P27	57	29	0	5	4	0	0	0		Pb 5%	Pt 10% O_2	424	6	8	22		544	1.00	0.704	6.08		800	7.20	2.27	1.71	302	0.55	76.0	6.18	P27
P28	58	27	7.2	1.4	3.3	0	2.7	0			Pt 10% O_2	52	6	21	116		1151	1.01	0.593	5.94		1000-600	6.32	3.42	2.10	295	1.09	68.3	3.26	P28
P31	0	20	0	0	3	0	4	0	Zr 53%	Na 20%	Pt 10% O_2	219	91	9	74		756	1.03	0.717	4.37		400	1.65	1.27	1.00	264	0.44	65.0	6.34	P31
P34	57	17	11	10	3	0	2	0			Pt 10% O_2	1130	6	8	25		381	1.07	0.679	5.90		800-200	2.66	1.41	0.94	301	0.42	70.2	3.19	P34
P35	58	35	0	5.1	2.3	2.4	0	0			Pt 10% O_2	315	6	12	31		802	1.06	0.694	5.98		450	3.97	0.48	0.09	301	0.16	67.3	6.30	P35
P40	29	34	0	5	4	0	0	0	Zr 28.5%		Pt 10% O_2	140	12	7	31		524	1.03	0.699	5.28		440-340	0.80	0.50	0.40	302	0.15	70.2	6.35	P40
P42	60	34	0	5	0	1	0	0			Pt 10% O_2	539	5	12	29		616	1.10	0.675	6.04		430	1.82	0.16	0.00	303	0.03	84.3	6.31	P42
P43	57	34	0	0	4	0	3.5	0		Eu 1.5%	Pt 10% O_2	114	41	7	55		765	1.06	0.700	5.95		400	5.15	1.20	0.00	213	0.40	67.0	6.31	P43
P46	57	34	0	0	4	0	3.5	0		Er 1.5%	Pt 10% O_2	189	74	8	50		477	1.08	0.710	5.93		225	5.70	2.45	1.15	244	0.93	62.0	6.35	P46
P47	57	34	0	0	4	0	3.5	0		Nd 1.5%	Pt 10% O_2	135	53	8	83		723	1.07	0.721	6.23		250-120	3.90	2.45	1.05	258	0.49	80.0	6.31	P47
P48	0	0	0	0	17	17	4	0	Zn 19%	Pb 43%	Pt 10% O_2	64	33	8	66		621	1.07	0.723	6.17		420-150	3.92	1.25	0.78	294	0.50	60.2	3.19	P48
P49	57	34	0	5	0	0	0	0		Ga 4%	Pt 10% O_2	956	8	12	29		477	1.09	0.660	6.00	6.31%	425-300	2.06	0.63	0.16	303	0.29	54.1	6.31	P49
P51	57	34	0	0	4	0	3.5	0		Sm 1.5%	Pt 10% O_2	176	41	9	89		800	1.07	0.721	5.93		320	5.00	4.30	3.25	269	1.70	60.5	6.33	P51
P57	57	34	0	5	3	1	0	0			Pt 10% O_2	481	4	13	30		741	1.09	0.673	6.07		460-360	2.06	0.16	0.05	302	0.07	55.6	6.31	P57
P58B	57	34	0	5	4	0	0	0			Remelted Pt 10% O_2											600-350	3.20	1.90	1.26	300	1.09	42.5	5.00	P58B
P59	57	34	0	0	4	0	3.5	0		Lu 1.5%	Pt 10% O_2	225	46	12	56		647	1.05	0.698	5.97		340-190	5.00	3.20	2.20	288	1.45	54.6	6.33	P59
P60	57	34	0	3.5	4	0	0	0		Gd 1.5%	Pt 10% O_2	446	15	14	36		550	1.12	0.650	5.96	5.80%	Damaged sample				302			6.28	P60
P80	57	34	0	5	3.5	0.5	0	0			(M) Pt 10% O_2	354	7	16	34		467	1.09	0.634	5.98	6.19%	480-100	2.64	0.19	0.08	301	0.05	72.4	6.24	P80
P81	57	34	0	5	0	0.5	0	0		Gd 3.5%	(M) Pt 10% O_2	966	9	9	27		331	1.08	0.680	6.01	5.23%	440-100	2.52	0.27	0.10	303	0.13	51.2	6.23	P81
P82B	57	30	0	8	0	0	0	0			(M) Pt 10% O_2	860	6	13	28		527	1.04	0.651	6.06	8.54%	980-600	1.89	0.97	0.63	302	0.25	74.7	3.16	P82B
P83	62	30	0	8	0	0.5	0	0			(M) Pt 10% O_2	606	4	12	27		617	1.10	0.680	6.05	6.49%	480	1.42	0.14	0.03	301	0.05	64.4	3.13	P83
P85	54	19	17	5	4	1	0	0.7			(R) Pt 10% O_2	166	5	17	44		900	1.10	0.644		4.61%	300-200	2.10	0.20	0.07	299	0.09	57.3	6.20	P85
P86	57	34	0	5	4	0	0	0			(R) Pt 10% O_2	739	19	12	30		281	1.03	0.661		3.80%	310-160	4.00	2.90	2.20	325	1.19	59.0	6.17	P86
P87	65	22	0	8	4	1	0	1.1			(R) Pt 10% O_2	746	5	10	24		683	1.16	0.690		5.65%	300-150	2.00	0.20	0.10	302	0.10	52.4	6.25	P87
P90	57	34	0	5	3	0	0	1			(R) Pt 10% O_2	900	10	8	23		234	1.01	0.689		4.81%	700-0	1.70	1.85	0.10	303	0.49	73.6	6.20	P90
P91	62	30	0	8	0	0.3	0	0			(R) Pt 10% O_2	900	5	9	25		583	1.04	0.687	6.07	6.89%	500-300	1.30	0.13	0.07	302	0.04	71.9	3.18	P91
P92	55	19	18	5.1	2.5	0	0	0			(JM) Pt 10% O_2	1025	14	12	29		375	1.00	0.657	5.86	7.92%	850-450	3.60	3.10	2.30	300	1.29	58.5	4.92	P92
P93	62	30	0	8	0	0.7	0	0			(R) Pt 10% O_2	656	5	10	26		822	1.06	0.693	6.07	6.37%	440	1.10	0.10	0.01	301	0.02	77.6	3.10	P93
P94B	54	19	18	5	4	0	0	0			(JM) Pt 10% O_2	74	7	21	64		555	1.09	0.590	5.83	8.56%	660-360	4.75	2.90	2.00	300	1.38	52.3	5.01	P94B
P96B	65	22	0	8	4	1	0	1.6			(R) Pt 10% O_2	395	10	6	20		638	1.08	0.691		1.24%	460	0.40	0.50	0.04	319	0.22	56.4	6.22	P96B
P100	56	20	15	5.2	4.2	0.5	0	0			(JM)	368	10	15	34		512	1.05	0.653	5.87	7.93%	460	0.40	0.50	0.04	302	0.21	57.6	6.23	P100
P127	54	19	18	5	3.5	0.5	0	0			(JM)											260-50	2.47	0.31	0.12	301			4.98	P127
P136	54	19	18	5	3.5	0.5	0	0			(JM) Pt cruc. N_2 atmos.											400-240	3.62	0.39	0.07	299			4.97	P136
P136	54	19	18	5	3.5	0.5	0	0			(JM) Pt cruc. N_2 atmos.											350-180	3.50	0.45	0.19	299			4.99	P136
P136	54	19	18	5	3.5	0.5	0	0			(JM) Pt cruc. N_2 atmos.											400-250	3.45	0.38	0.06	299			4.98	P136
P138	54	19	18	5	3.5	0.5	0	0			(JM) Pt cruc. N_2 atmos.											200-400	2.80	0.72	0.60				4.97	P138
P155	54	19	18	5	3.5	0.5	0	0			(JM) Pt cruc. N_2 atmos.											320-110	3.37	0.58	0.29	299			4.99	P155
P155	54	19	18	5	3.5	0.5	0	0			(JM) Pt cruc. N_2 atmos.											420-300	3.40	0.37	0.05	299			4.98	P155
P143	54	19	18	5	3.5	0.5	0	0			(JM) Pt cruc. N_2 atmos.											420-200	3.50	0.40	0.07	299			4.98	P143
P143	54	19	18	5	3.5	0.5	0	0			(JM) Pt cruc. N_2 atmos.											320-120	3.20	0.40	0.15	299			4.97	P143
P179	54	19	18	5	3.5	0.5	0	0			Pt 10% O_2,(JM) 4×2×2cm^3	3225	77	13	30		178	1.25	0.578			Analysis not possible							20.00	P179
P180	54	19	18	5	3.5	0.5	0	0		Gd 1.5%	Pt 10% O_2 (JM)											340-240	2.10	0.24	0.05	302			6.19	P180
P200	54	19	18	5	3.5	0.5	0	0			(R) Pt cruc. N_2 atmos.											200	1.65	0.22	0.08				6.17	P200
P202	62	30	0	8	0	0.7	0	0			(JM) Pt cruc. N_2 atmos.											200-150	3.17	0.38	0.08				3.14	P202
ZBLAN	0	21	0	0	3.4	0	4.5	0	Zr 52%	Na 20%																208			2.78	ZBLAN

Name	Compositional Information (Oxides mol %)										Production Information	Scintillation Decay Constants							Pile-up, Ω	Density	Light Yield	Dose const.	Sat.300	Sat.350	Sat.400	λ_{cut}	Resid. Abs.	%Anneal	Thickness	Name
	Si	Ba	K	Ca	Na				Balance	Balance	Comments	$A_2(t=0)$	$A_3(t=0)$	τ_1[ns]	τ_2[ns]		τ_3[ns]	χ^2/dof	frac(25/500)	ρ [gcm^{-3}]	Rel.CeF$_3$	[krad]	[OD cm^{-1}]	[OD cm^{-1}]	[OD cm^{-1}]	[nm]	[ODcm^{-1}]		[mm]	
HP24	70	10	20	0	0															2.99		300	-	3.15	2.10	329	2.61	17.1	5.73	HP24
HP42	80	0	0	8	12						Annealed SLS tridymite									2.53		420	2.05	1.75	2.05	312			4.71	HP42

Table 6.01 Glass Results (see text for details)

In Table 6.01, the scintillation decay amplitudes have been normalised to $A_1 = 1000$ counts. 'Frac25/500' indicates the ratio of scintillation light collected in the first 25 ns compared to that collected in the first 500 ns. The Archimedian up-thrust has been used to measure the 'Density' of each glass, the experimental uncertainty is sensitive to the volume of the sample. The error analysis for this measurement is presented in Appendix 4. The relative light yields have been measured by R.M. Brown *et al* at the Rutherford Appleton Laboratory, the experimental arrangement is described in Appendix 2. A 1 cm^3 CeF_3 crystal from Optovac was used as the reference sample.

The 'Dose const.' [krad] characterises the exponential which describes the development of radiation induced absorbance with dose. Values of absorbance for which damage would saturate are given at wavelengths of 300, 350 and 400 nm, and are in units of Optical Density (OD). These measurements correspond to a path length of 1 cm in the table and throughout the chapter. The 'λ_{cut}' column gives the wavelength for which the unirradiated UV edge corresponds to an internal transmission loss of 50%.

In some glasses the dose constant does not vary as a function of wavelength throughout the spectral region in which radiation induced damage is observed. In other glasses the induced damage develops more slowly in the vicinity of the UV edge, the growth constant gradually falls to a constant level at longer wavelengths.

In Table 6.01, the damage mode which a particular glass conforms to is indicated in the 'Dose Const' column. A single figure indicates a growth constant which is flat as a function of wavelength. Two numbers separated by a hyphen denote a growth constant which falls into the second category. The number immediately before the hyphen is the growth constant at the UV edge, the number after the hyphen gives the flat level which the growth constant falls to at longer wavelengths. Examples of the two types of behaviour are shown in Figure 6.01. There is no evidence to suggest that the variation of the growth constant as a function of wavelength is correlated with any compositional property of the glass.

The fractional recovery of optical absorbance at room temperature is given ('%Anneal') as well as the residual damage which is present after 1 year of annealing, 'Residual'. The residual absorbance corresponds to a path length of 1 cm. The transmission thickness, is also included for information, it is stated in millimetres.

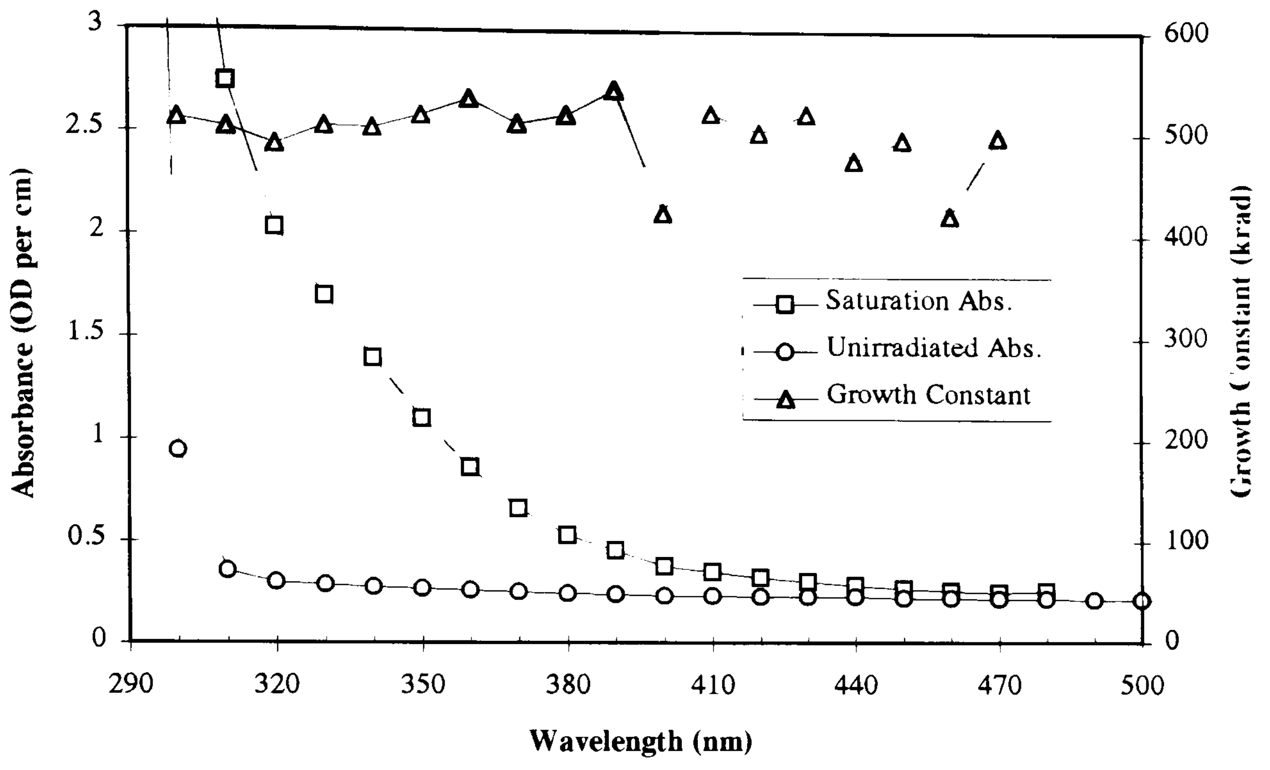

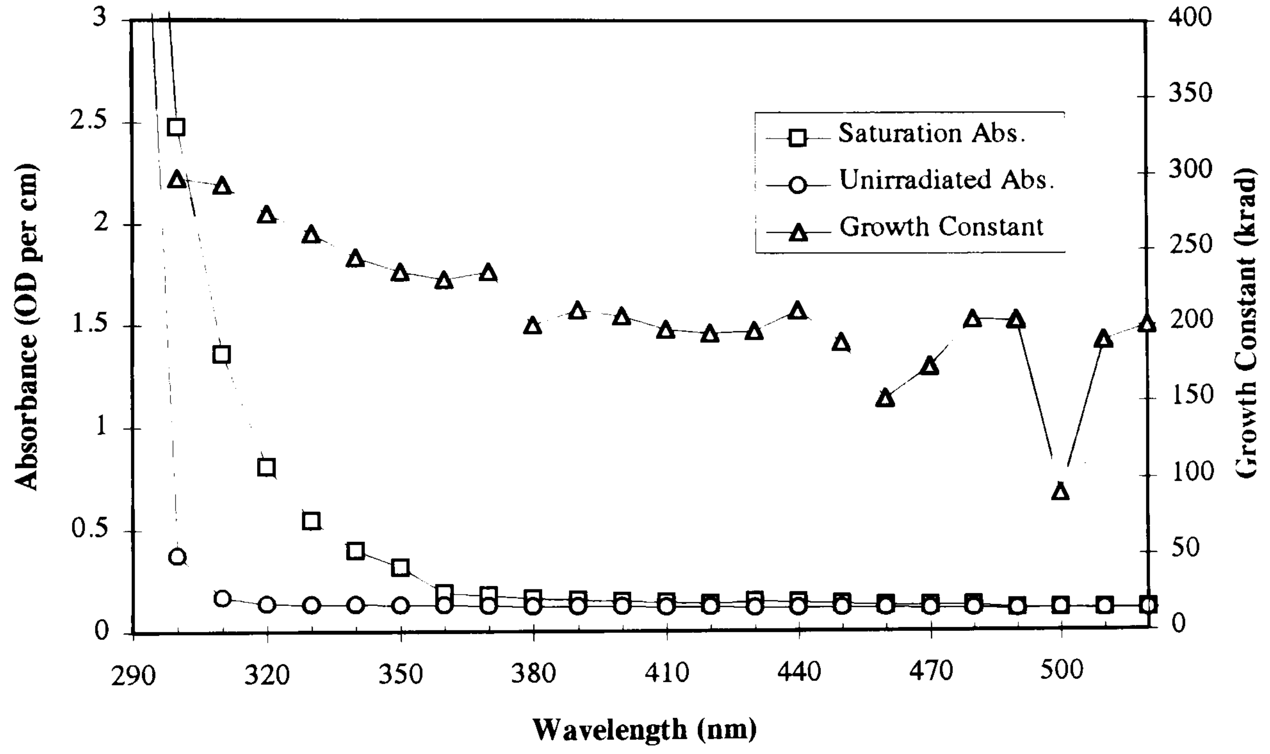

Figure 6.01 The growth constant for N36 (top) does not vary as a function of wavelength. The growth constant for P85 (bottom) in not flat and varies as described in the text. Included in the two graphs are the unirradiated and saturation absorbance curves.

6.2. Radiation Damage

6.2.1. Production Sites

Although the majority of the fluoride glasses were produced by P. Flower at Sheffield University, a significant fraction were made at the Lebedev Institute, Moscow and a few at Brunel University. Each site employed different production regimes. At Brunel University, the samples were heated in a furnace which was continually purged with N_2. The melt was then removed and cast in air, subsequent annealing was also in air. Platinum crucibles were used at Brunel University and also at Sheffield University. Sheffield glasses were melted, cast and annealed in a controlled atmosphere. Two different gas mixtures were used. Glasses P1 to P130 and 178 to 189 were made in an *oxidising* 10% O_2, 90% N_2 atmosphere, 'P' glasses with indices 131 to 177 and 190 to 205 used pure N_2. The Lebedev Institute exclusively used a *neutral* atmosphere (pure N_2), their materials were heated in vitreous carbon crucibles.

Glasses produced under a neutral atmosphere had lower intrinsic absorbance than those produced using an oxidising mixture. For a similar composition, the poorer (oxidising atmosphere) glasses suffered less radiation induced absorbance than those produced under a neutral atmosphere. Caution must be exercised when comparing similar glass compositions which have been produced under different conditions.

6.2.2. Starting Compositions

One fundamental ternary matrix which forms a stable fluoride glass is composed of ZrF_4, BaF_2 and LaF_3, this is known by the acronym ZBL [1]. It contains divalent Ba^{2+}, trivalent La^{3+} and Zr^{4+} which has a valency of four. To produce a stable glass, the proportions of each component have to be controlled quite closely. Feasible compositions are usually displayed in the form of a stability diagram [2]. For ZBL the most stable composition corresponds to Z:B:L= 62:33:5 mol%. Variations of ±2% can be tolerated in this ZBL glass. Additional additives tend to extend the region of glass stability. Zr can be substitutionally replaced with Hf [3], similarly Al can replace La. The present work has investigated deviations from this basic composition, observing the effects of incorporating relatively small amounts of additional dopants.

6.2.2.1. Hafnium Fluoride

Most of the published research into HMF glasses over the last 10 years has concentrated on the Zr matrix. These glasses have insufficient densities to be of use in CMS. Replacing Zr with Hf improves the density from ~4.5 gcm^{-3} to ~6 gcm^{-3}. In this work a series of three glasses have been used to characterise the effect of the Zr/Hf substitution on radiation tolerance. The control was based on the ZBCeA matrix (P21) and contained no Hf. In one sample, the Zr was replaced with Hf (P13), the other glass contained equal proportions of Hf and Zr (P40).

Induced absorbance in the Zr glass developed most rapidly (with dose) but this saturated at a lower level than was observed for the glasses containing Hf. Of the three, the HfBCeA glass experienced the most induced absorbance. Damage in the mixed Hf/ Zr glass was between that of the Zr and Hf glasses. The induced damage scales uniformly with the proportion of Hf rather than Zr constraining the induced damage to that observed in the ZBCeA glass. The superior performance of Zr has been previously reported by Tanimura [4]. It is attributed to Hf^{3+} acting as a deeper electron trap than Zr^{3+}. The CMS application imposes a density constraint, $\rho > 6$ gcm^{-3} making it essential to use Hf despite its inferior radiation tolerance. In addition, Zr glasses do not scintillate for Ce doping between 0 and 10%.

6.2.2.2. *Barium Fluoride*

Although in other work [5] substituting Ba with Sr has resulted in stable glasses, none of the present glasses completely eliminated Ba. For reasons of glass stability, the fraction of Ba only varied between 17 and 34% in all of the present fluoride glasses. It is assumed that any variation in radiation tolerance was dominated by the additional components rather than the relatively small variation in the fraction of Ba.

6.2.2.3. *Cerium Fluoride*

There is considerably more scope for substitution of trivalent components within these glasses. The relatively small proportion of trivalent elements ensures that large changes in the composition of this component have little effect on the density of the glass. Small amounts of additional dopants can however have a drastic effect on the radiation tolerance.

Cerium has been used to improve the radiation tolerance in silicate glasses for many years [6]. Similar effects have been observed in the fluoride glass matrix [7]. The incorporation of CeF_3 is essential for the CMS application as this ion is responsible for the observed scintillation light. In the current work, several different compositional groups which incorporate Ce have been produced. In all cases, the radiation tolerance of the glass has improved by increasing the fraction of Ce. The level at which the damage saturates at 350 nm is shown below for three different groups of glass, the fraction of Ce is indicated in square brackets. Indium drastically improves the radiation tolerance of these glasses.

Glass Type	Name, Induced damage (OD), [%Ce]	Name, Induced damage (OD), [%Ce]
HBCeIn	P93, 0.10, [8%]	P42, 0.16, [5%]
HBCe	P82B, 0.97, [8%]	P22. 2.20, [5%]
HBCeA	P20, 1.36, [10%]	P13, 2.70, [5%]

Table 6.02 Examples of glasses in which the fraction of Ce was varied. A lower level of radiation induced damage is observed as the proportion of Ce is increased.

6.2.2.4. Other Lanthanide Elements

Encouraged by the improvement observed by doping with Ce, a series of HBALa glasses were evaluated. Small quantities of the rare-earth elements, Gd (P15), Pr (P16), Eu (P43), Er (P46), Nd (P47), Sm (P51), Lu (P59), and Yb (P90) were each added to samples of the base glass. In addition, a control sample (JHA6) was produced. The Gd doped glass showed strong intrinsic absorbance below 270 nm. It suffered radiation induced damage that was predominantly located in the UV, but extended into the visible. Radiation damage at 350 nm saturated at an absorbance of 2.16 OD. The Pr doped glass was initially a pale green colour due to intrinsic absorbance bands at 441, 465, 478 and 587 nm. These bands were narrow (< 0.07 eV) and did not encroach on the $300 < \lambda < 350$ nm region. Irradiation caused significant damage throughout the spectrum but was particularly severe in the UV, the induced damage at 325 nm saturated at 4.81 OD.

Europium completely eliminated any radiation induced absorbance above a wavelength of 390 nm. At shorter wavelengths the performance of this glass was poor. Radiation damage at 350 nm saturated at an absorbance of 1.20 OD. The properties of Eu in the fluoride glass matrix have previously been reported by France *et al* [8]. This dense, non-scintillating radiation-hard glass could be suited to applications including 'hot-cell' windows and as a transparent showering medium for an inhomogeneous 'sandwich' calorimeter.

The Erbium doped sample contained many absorbance bands prior to irradiation. The main features were narrow Gaussians centred at 244, 377, 486 and 519 nm, these resulted in its initial pale pink colour. The bands had similar widths to those observed in the Pr doped glass. The wavelength range, $300 < \lambda < 350$ nm was free from any significant intrinsic absorbance features. Irradiation produced absorbance bands in the UV, these had tails that extended in to the visible. At 350 nm radiation damage saturated at an absorbance of 2.45 OD.

Radiation induced damage in the Nd doped glass was similar to that observed for the Er glass. Intrinsic absorbance features at 327, 350, 509, 520 and 576 nm were present. The 327 nm band had a FWHM of 0.1 eV and a peak absorbance of 0.14 OD, this precludes the use of this Nd doped glass in CMS as its attenuation length it too high even before irradiation has started.

The absorbance graph for the Sm doped glass has been shown in Chapter 3. Upon irradiation, this glass showed broad absorbance features at 6.19, 3.98 and 2.50 eV which were approximately Gaussian. These had widths of $\sigma = 0.76$, 0.71 and 0.18 eV respectively. The damage at 350 nm saturated at 4.30 OD. In contrast to the Pr, Gd, Eu, Er, Nd and Sm doped glasses, the Lu doped glass showed no intrinsic absorbance features in the optical transmission window. This probably results from its full outer electron shell. The sample had a steep UV edge which occurred at 288 nm. Damage in this sample is typical of all glasses doped with Lanthanide elements, showing induced absorbance in the UV which extended into the visible region above 400 nm. An example of this behaviour is shown in Figure 6.02.

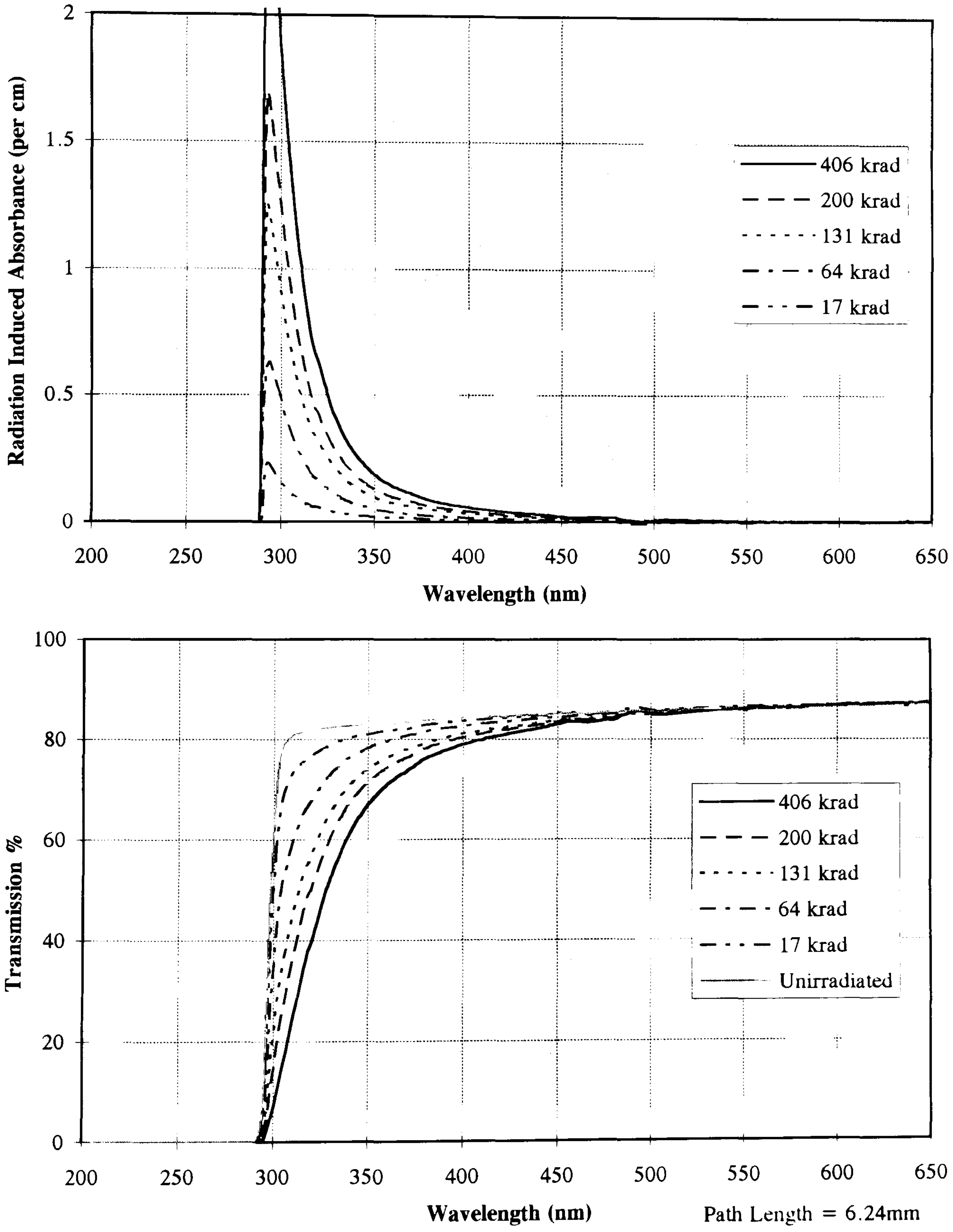

Path Length = 6.24mm

Figure 6.02 Radiation induced absorbance and external transmission data for P85. Damage is predominantly located in the UV but absorbance tails extend in to the visible.

P90 which contained 1% Yb, developed a Gaussian absorbance feature at 330 nm during irradiation, it had a width, $\sigma = 0.3$ eV. The induced absorbance in this glass was relatively small above 400 nm, but as a result of the 330 nm band, it was 1.85 OD at 350 nm. The appearance of this Gaussian absorbance band in Yb doped glasses is discussed in Section 6.2.4.

6.2.2.5. *Non-Lanthanide Additives*

Compositional optimisation started from a glass based on HBCe (P22). The radiation tolerance of this glass was improved by adding 4% Al (P58B) at the expense of Hf. This improved the induced damage marginally although it was clear that Al was not a crucial component. Substituting Ga (P49) for Al showed a more marked effect especially above 350 nm. Indium (P83) plays a key role in determining the overall radiation resistance of these glasses. In the Indium doped glass, the radiation tolerance was not improved by the presence of Al (P80).

Glass Type	Sat. Induced damage (OD) @350 nm
HBCe	P22, 2.20 [-]
HBCeAl	P58B, 1.90 [Al= 4%]
HBCeGa	P49, 0.63 [Ga= 4%]
HBCeIn	P83, 0.14 [In= 0.52%]
HBCeAlIn	P80, 0.19 [Al=3.5%, In= 0.5%]

Table 6.03 Summarises the radiation induced absorbance observed for different glasses based on the HBCe matrix. All glasses were produced under an oxidising atmosphere.

Indium and Cerium have been identified as the principal components which improve the observed radiation tolerance in the glasses that have been tested. Adding Indium to HBCeAl (P57/P58), HBCe (P42/P22), and HBLiCeAl (P100/P92) significantly improves the tolerance in all of these glasses. To determine the optimum fraction of Indium versus Ce, a series a series of eight glasses were produced, these are shown in Table 6.04. Increasing the fraction of Indium decreases the measured small sample light yield of these glasses. Since performance in this respect is marginal, the fraction of Indium should be maintained at the lowest tolerable level consistent with acceptable radiation induced damage.

Name, Sat. Induced damage (OD), [% In] HBCeIn [8%Ce]	Name, Sat. Induced damage (OD), [% In] HBCeAlIn [5%Ce]
P82B, 0.97, [In=0%]	P86, 2.9, [In= 0%]
P91, 0.13, [In= 0.3%]	P80, 0.19, [In= 0.5%]
P83, 0.14, [In= 0.5%]	P57, 0.16, [In= 1.0%]
P93, 0.10, [In= 0.7%]	P35, 0.48, [In= 2.4%]

Table 6.04 Radiation induced absorbance for which damage would saturate. The values are calculated at 350 nm for various proportions of Ce and Indium [mol %]. In the case of 5%Ce, the damage is minimised for 1% Indium.

6.2.3. Lithium Doped Glasses

Small test samples were produced reliably for a range of glasses provided that the mixture corresponded to a stable composition and the melt was cast using the correct temperature regime. Compositions which were on the verge of stability contained a layer of crystallites along the central plane of the sample. For glass formation (as opposed to crystal growth) the solidifying front must propagate faster through the melt than the rate of crystal growth in the sample. Any crystallites are seen at the centre of the glass because the cooling rate is lowest in this region. This is due to the poor thermal diffusivity of the solidifying material. When the cooling rate is fast enough, the melt has insufficient time to arrange atoms appropriately for crystal growth and hence a pseudo-random *glass* network is created.

Incorporation of LiF in the melt enabled the thickness of samples to be increased above 5 or 6 mm. Presumably due to the small Li atoms packing into the Hf-Ba *matrix* and stabilising it. Although Li has an Atomic number of three, the density of glasses containing Lithium tends to be greater than the corresponding non-Li glasses. It is thought that Li atoms can be accommodated in between the larger Hf and Ba ions without significantly disturbing the geometry of the glass matrix. The effect of LiF on the radiation induced absorbance was evaluated using the glass, HBLiCeAl. A series of three glasses were produced, these included 0, 4 and 18% Li which replaced Ba in all glasses. The Ce content was 5% and Al, 4%. The sample which contained no Li developed radiation induced absorbance most slowly, the 4% Li glass was most radiation resistant, and the 18% Li glass damaged most severely. The results are shown in Table 6.05.

A high Li content (18%) is required to produce glass samples thicker than 6 mm. Attempts were made to counterbalance the detrimental effects of this amount of Li by incorporating various combinations of elements which had proved fruitful in non-Li glasses. Two

HBLiCeALa glasses (P28 and P34) which contained respectively 1.4 and 10% Ce demonstrated that increased amounts of Ce in improved the radiation tolerance Li doped glasses. The induced damage at 350 nm was 3.42 OD (P28) and 1.41 OD in P34.

Glass	Li[%]	DoseConst [krad]	Sat 300 nm [OD]	Sat 350 nm [OD]	Sat 400 nm [OD]
P13	0	1000-700	4.52	2.70	2.26
P23	4	750-200	3.50	1.90	1.10
P94B	18	660-360	4.75	2.90	2.00

Table 6.05 This series of three glasses demonstrates that Li detracts from the radiation tolerance of HBCeAl glass.

Using the HBLiCeAlIn matrix, 0% Indium (P92), 0.5% (P100) and 1.5% (N29) glasses were evaluated. The 0% Indium glass was clearly the poorest suffering a radiation induced absorbance of 3.10 OD at 350 nm. The 1.5% Indium glass appeared the most radiation resistant. It should be noted that the 1.5% Indium glass was produced in a neutral atmosphere whereas the 1% Indium glass was produced using and oxidising atmosphere. This fact alone could account for the difference in radiation hardness. Clearly, Indium improved radiation tolerance although a more extensive investigation would be required to determine exactly what amount of Indium minimises radiation induced absorbance in Li doped glasses. Small sample light yield estimates indicate that increasing the fraction of Indium reduced the scintillation light yield in both Li and non-Li glasses.

A series of Lithium doped HBLiCeAlInYb glasses; N28 (0.5% Yb), P85 (0.7% Yb), N27 (0.8% Yb) and N30 (1.0%Yb) were irradiated after Ytterbium had shown promising radiation resistance in non-Li glasses. A similar pattern of induced damage was observed in both Li and non-Li (P90) glasses. Both types proved to be reasonably radiation hard above 400 nm but a Gaussian feature was observed at 330 nm.

N26, N27, N28, N30, N33 and N36 were all produced at the Lebedev Institute under neutral conditions. With the exception of N27 in which the band was not resolved, these (HBLiCeAlInYb) glasses all showed Gaussian absorbance bands centred at 330 nm. The features had FWHM of 0.30±0.03 eV. This induced Gaussian was not observed in any glass which did not contain Yb.

No Gaussian band was observed in the Li doped glass (P85) which was produced under an oxidising atmosphere and contained 0.7% Yb and 1% Indium. P96B (oxidising atmosphere) which contained 1.6% Yb did show a characteristic absorbance band at 330 nm despite containing 1% In. This was possibly due to the higher level of Yb compared to the other samples which all contained 1% or less. There is considerable evidence to suggest that the intrinsic band at 330 nm is related to the presence of Yb, the band is partially suppressed in glasses produced under an oxidising atmosphere; for low (< 1%) levels of Yb, the Gaussian band can be practically eliminated by the incorporation of 1% Indium.

6.2.4. Gaussian Data

A small fraction of the glasses developed radiation induced damage that was described by a number of superimposed Gaussians. Table 6.06 gives the parameters of the Gaussians, the glass composition and also candidate defects identified from the literature. The uncertainty in the *means* have been estimated from the spread in the fitted values as each was determined at several different doses. In the fitting procedure, all of the parameters were free to vary. The silicate glasses HP24 and HP42 were included to contrast with the results for fluoride glasses. It has been possible to correlate the absorbance bands in the silicate glasses with specific defects identified from the literature. The close agreement verifies that this method of analysis is appropriate and that the values of returned parameters are correct within the limits of experimental uncertainty.

Evidence has already been presented which correlates the 3.78 eV (330 nm) band with Yb in the Hf fluoride glass matrix. The results also suggest that the UV edge is characterised by a defect at 4.24~4.52 eV with a σ of 0.13~0.31 eV. It has not been possible to definitively identify the defect associated with any absorbance band observed in the Hf based glasses. Details of the optical absorbance bands resulting from specific radiation induced defects is restricted in the main to Zr based glasses or the Cl related defects in Hf based glasses [2]. The Er (P43) and Sm (P51) glasses show unique absorbance bands, it is reasonable to assume that the defects arise from the Er and Sm respectively. Although it is not shown explicitly in the table, the amplitudes of the individual Gaussian absorbance bands for each glass increased in a similar manner. The accepted conclusion is that, for a given glass, the radiation induced bands all arise from one type of defect centre.

Glass [Ref#]	Parameters	Gaussian1	Gaussian2	Gaussian3	**Composition**, Comments, identified bands.
HP24	A[OD]	1.44	4.12	0.66	**70 SiO_2, 10 BaO, 20 K_2O**: 2.0 and 2.7 eV bands [trapped holes, ref. 9] identified
[21]	μ [eV]	2.69±0.00	4.22±0.02	1.93±0.00	
	σ [eV]	0.43	0.59	0.24	
HP42	A[OD]	1.39	1.06	0.39	**80 SiO_2, 8 CaO, 12 Na_2O**: 4.0 eV [trapped electron, ref. 10] , 2.0 and 2.7~2.9 eV bands [trapped holes, ref. 9]
[29]	μ [eV]	2.90±0.05	4.06±0.02	1.96±0.00	
	σ [eV]	0.56	0.42	0.21	
JHA6	A[OD]	0.44	3.54	0.56	**58 Hf, 33 Ba, 4 Al, 5 La**:
[39]	μ [eV]	3.20±0.12	4.79±0.23	6.03±0.17	
	σ [eV]	0.55	0.79	0.77	
P31	A[OD]	0.39	0.47	1.54	**ZBLAN** compared with ZBLALi [7] where, μ= 2.69 eV, σ=0.62 eV is Zr^{3+}. μ= 4.27 eV, σ= 0.53 eV is V centre. μ= 6.12 eV, σ= 0.60 eV is unidentified
[86]	μ [eV]	2.88±0.02	4.29±0.03	6.00±0.02	
	σ [eV]	0.66	0.63	0.78	
P43	A[OD]	0.62	3.93	1.31	**57 Hf, 34 Ba, 4 Al, 4 La, 1.5 Eu**: This is the only Eu doped glass
[90]	μ [eV]	4.04±0.02	5.12±0.01	6.10±0.02	
	σ [eV]	0.29	0.56	0.23	
P51	A[OD]	0.27	2.05	3.09	**57 Hf, 34 Ba, 4 Al, 3.5 La, 1.5 Sm**: This is the only Sm doped glass
[93]	μ [eV]	2.50±0.00	3.98±0.04	6.19±0.01	
	σ [eV]	0.18	0.71	0.76	
N28	A[OD]	0.25	1.22	0.08	**54 Hf, 20 Ba, 17 Li, 5 Ce, 3 Al, 1 In, 0.5 Yb**:
[98]	μ [eV]	3.79±0.05	4.52±0.18	5.66±1.45	
	σ [eV]	0.24	0.28	1.61	
P80	A[OD]	0.05	38.0		**57 Hf, 34 Ba, 5 Ce, 3.5 Al, 0.5 In**:
[100]	μ [eV]	3.72±0.08	5.87±0.13	-	
	σ [eV]	0.68	0.59		
P90	A[OD]	0.64	0.36		**57 Hf, 34 Ba, 5 Ce, 3 Al, 1 Yb**:
[107]	μ [eV]	3.79±0.01	4.22±0.04	-	
	σ [eV]	0.30	0.13		
N30	A[OD]	0.64	0.97		**54.5 Hf, 17 Ba, 20 Li, 5 Ce, 2.5 Al, 1 In, 1 Yb (0.25PTFE)**:
[110]	μ [eV]	3.83±0.05	4.25±0.04	-	
	σ [eV]	0.35	0.15		
N33	A[OD]	0.36	0.52		**54 Hf, 20 Ba, 17 Li, 5 Ce, 3 Al, 1 In, 0.5 Yb**:
[111]	μ [eV]	3.82±0.03	4.27±0.02	-	
	σ [eV]	0.30	0.16		
n36	A[OD]	0.07	0.18	0.75	**48 Hf, 20 Ba, 9 Li, 8 Ce, 3 Al, 1 In, 0.5 Yb**:
[112]	μ [eV]	3.61±0.23	3.85±0.05	4.33±0.03	
	σ [eV]	0.46	0.27	0.21	
P96B	A[OD]	0.34	0.18		**65 Hf, 22 Ba, 8 Ce, 4 Al, 1 In, 1.56 Yb**:
[116]	μ [eV]	3.84±0.01	4.22±0.06	-	
	σ [eV]	0.34	0.10		
N26	A[OD]	0.27	0.16	0.91	**54 Hf, 20 Ba, 17 Li, 5 Ce, 3 Al, 1 In, 1.5 Yb**:
[96]	μ [eV]	3.75±0.07	3.86±0.92	4.50±0.19	
	σ [eV]	0.22	0.46	0.32	

Table 6.06 the glasses which developed radiation induced damage that was described by a number of super imposed Gaussian absorbance bands are included above. The fitted parameters, glass compositions and identified defects are given.

6.2.5. Material Purity

In addition to the density, radiation tolerance and scintillation criteria on which these glasses are judged, the finished glasses have to fall within very strict financial constraints if the project is to be feasible. The principal component in these fluoride glasses is HfF_4. Excluding the HMF glass market, HfF_4 is only used in very small quantities as a spectroscopic reference. Commercial suppliers routinely sell ultra-high purity, gram quantities. The new HMF glass market has created demand for kilogram quantities of these materials.

Even with the substantial bulk discounts offered by Johnson Matthey after negotiations spanning twelve months, the cost of pure HfF_4 was still too high for the material budget of the CMS electromagnetic calorimeter. This cost was dominated by a final purification process that removed principally Zr. Purchasing HfF_4 which had not undergone the final purification process offered a substantial cost benefit. Johnson Matthey supplied 5 kg of 'impure' HfF_4 which was used to produce most of the glasses for this work. In addition to 0.2% Zr, their broad spectral analysis, recorded by Johnson Matthey, showed the following impurity levels (ppm):

Al	200	Cu	< 10	Ni	10	Nd	< 1
Ca	< 10	Fe	< 25	Ti	30	V	< 5
Co	< 5	Mg	< 10	W	< 10	Na	6
Cr	< 10	Mn	< 10	Zn	< 50	Er	< 1

Bulk discounts combined with purchasing 'impure' HfF_4 reduced the cost by nearly a factor of ten over spectroscopy grade HfF_4 purchased in small quantities. Although it is known as 'impure', this description is misleading as the material contains $>99\%$ HfF_4. The effect of impure HfF_4 on radiation hardness was of considerable interest. Duplicate glasses were produced with 'pure' HfF_4 (from the Lebedev Institute, Russia) and 'impure' HfF_4 from Johnson Matthey. These are identified by the subscripts $_R$ and $_{JM}$ respectively. $P200_R$ and $P138_{JM}$ were HBLiCeAlIn glasses, their composition and radiation damage parameters are given in Table 6.07. This table also includes details of a second pair of glasses, $P93_R$ and $P202_{JM}$. This HBCeAlIn glass corresponded to one of the most radiation resistant compositions.

From the table, it is clear that the radiation induced absorbance in the glasses made using 'impure HfF_4' is significantly worse than in equivalent high-purity glasses. Additional impurities in the cheaper Johnson Matthey HfF_4 significantly deteriorate the induced absorbance. Incorporation of Indium which has been shown to alleviate damage in a wide variety of HMF glasses fails to significantly offset the additional induced damage in the cheaper HfF_4. The key to solving this problem is to identify which impurities are responsible and to eliminate them or devise new strategies for minimising their effect. This may involve further compositional optimisation.

Name	Hf	Ba	Li	Ce	Al	In	Dose Const	Sat300	Sat350	Sat400	Cut-off	Comment
P138	54_{JM}	19	18	5	3.5	0.5	200-400	2.8	0.72	0.6	295	slope
P200	54_{R}	19	18	5	3.5	0.5	200	1.65	0.22	0.08	295	flat
P202	62_{JM}	30	0	8	0	0.7	200-150	3.17	0.38	0.08	302	slope
P93	62_{R}	30	0	8	0	0.7	440	1.1	0.1	0.01	301	flat

Table 6.07 Two sets of identical glasses made with 'impure' and high-purity HfF_4 to investigate the effect of impurities on radiation hardness.

6.2.6. Overall Rating

The discussions concerning radiation induced absorbance have concentrated on the effects of adding various dopants to specific glass matrices. The aim has been to identify trends that establish which elements improve and which are deleterious to radiation induced absorbance. Below is a chart which gives a more *global* comparison of the radiation tolerance of the main compositional groups. This summary chart agrees with all of the observations which have already been discussed individually. The bar chart represents the mean optical absorbance (OD), at 350 nm, for which radiation induced absorbance would saturate at the dose rate used in all of the irradiations (1.2 rads^{-1}). It relates to a 1 cm path length. The high and low points show the extreme values which have been measured. Large deviations from the average behaviour result from the compositional variations of the key constituents. For example the two data points for HBLiCeAlLa glass correspond to 1.4 and 10% Ce. Despite the two glasses belonging to the same compositional group, there is a significant difference in radiation induced absorbance which is related to the amount of Ce. Where possible, the compositional groups have been further separated into glasses produced under oxidising and neutral atmospheres. In all cases, the glasses in the former category suffer less damage than the neutral atmosphere glasses. P86 and N27 are excluded from the data sets used for Figure 6.03, they differ widely from the average behaviour for similar glasses. The compositional information gives no indication why damage in these glasses should vary from (P13, B1, P58B) and (N26, N28, N30, N33) respectively. Irradiations were carried out in a systematic manner, possible reasons for the difference may be contamination of the melt or variation in the production procedure.

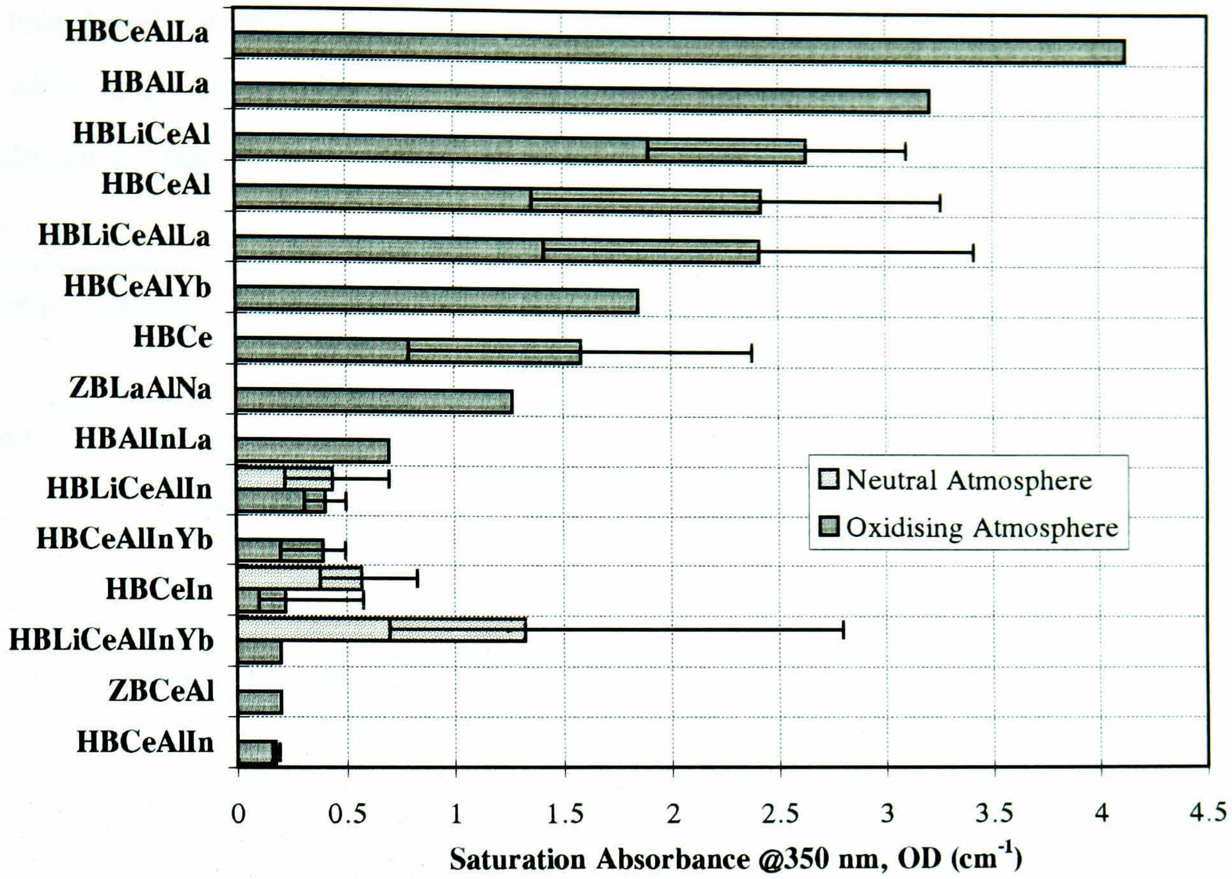

Figure 6.03 Global rating of the radiation tolerance of various types of glass. They are separated according to compositional group and where possible according to the oxidising or neutral atmosphere under which they were produced. The *max* and *min* bars are representative of the compositional variation within a particular group.

6.3. Recovery of Radiation Damage

In addition to monitoring the development of radiation induced damage, absorbance measurements were recorded for each glass after the ^{60}Co irradiations had ceased. The samples were stored in the dark at room temperature (22± 2°C) in an atmosphere which was kept dry with silica gel. The recovery of induced absorbance was initially rapid but slowed at longer delays. As shown in section 3.30, the data is described by a stretched exponential which has been suggested by Griscom [11].

$$A_t = A_0 \exp\left[-\left(\left(\frac{t}{\tau}\right)^{\alpha}\right)\right] \qquad \text{Equation 6.01}$$

where $0 < \alpha < 1$. The absorbance eventually attained a stable value which was in between that corresponding to the maximum dose and the unirradiated absorbance curve. The fractional recovery at 350 nm is given for each glass in Table 6.01.

$$\text{fractional recovery} = \frac{\text{Saturation Abs.-Residual Abs.}}{\text{Saturation Abs.}-\text{Unirradiated Abs}} \qquad \text{Equation 6.02}$$

There is no compositional trend which can be used to predict the fractional recovery in induced absorbance. Excluding the glasses produced at the Lebedev Institute which were only monitored for seven days after irradiations had ceased, the fraction recovery varies from 48% in JHA8 to 97% in P17. When room temperature annealing is also taken into consideration, the glasses which develop the least induced damage are as shown in Table 6.08.

Name, Residual Absorbance OD		Name, Residual Absorbance OD	
P93	0.022	P80	0.052
P42	0.025	P17	0.067
P21	0.030	P23	0.069
P91	0.037	P57	0.070
P83	0.050	N13	0.077

Table 6.08 Residual absorbance of the most radiation resistant glasses after room temperature annealing for 1 year. The six glasses which show the lowest radiation induced absorbance immediately after irradiation (P93, P91, P83, P57, P42, P80) also feature in the ten most radiation tolerant glasses after room temperature annealing.

6.4. Position of the UV edge

The values presented in Table 6.01 were measured using a definition of the UV cut-off in terms of the wavelength at which the internal transmission curve for the unirradiated sample falls to 50% of its value in the transmission window. The UV edge in Ce doped glasses falls in the vicinity of 300 nm due to a strong absorbance band in the UV. Evidence from the literature [12] suggests that the exact position of the edge varies with the fraction of CeF_3.

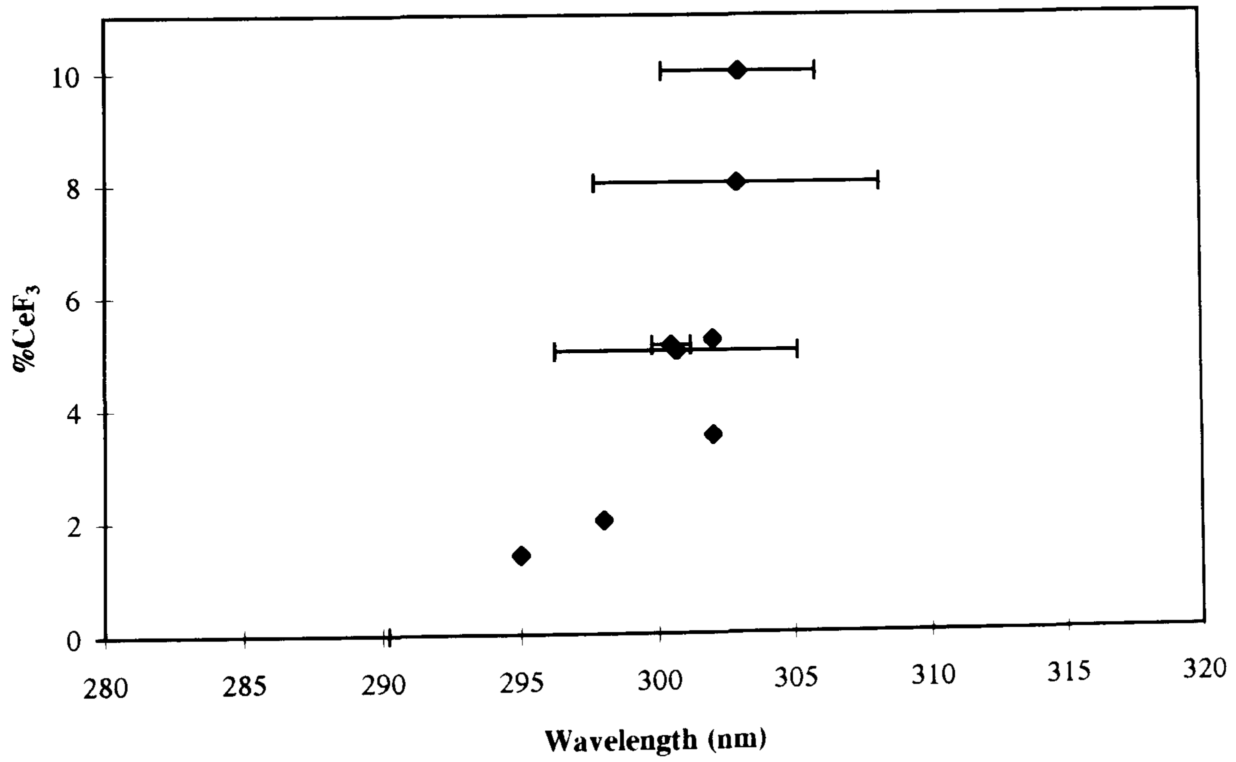

Figure 6.04 The position of the UV edge as a function of CeF_3 concentration. The High / Low bars indicate the range of measurements, the level of scatter is due to the large degree of compositional variation in the data set.

Figure 6.04 shows the *mean* position of the UV edge for various CeF_3 concentrations, this data comes from the glasses of Table 6.01.

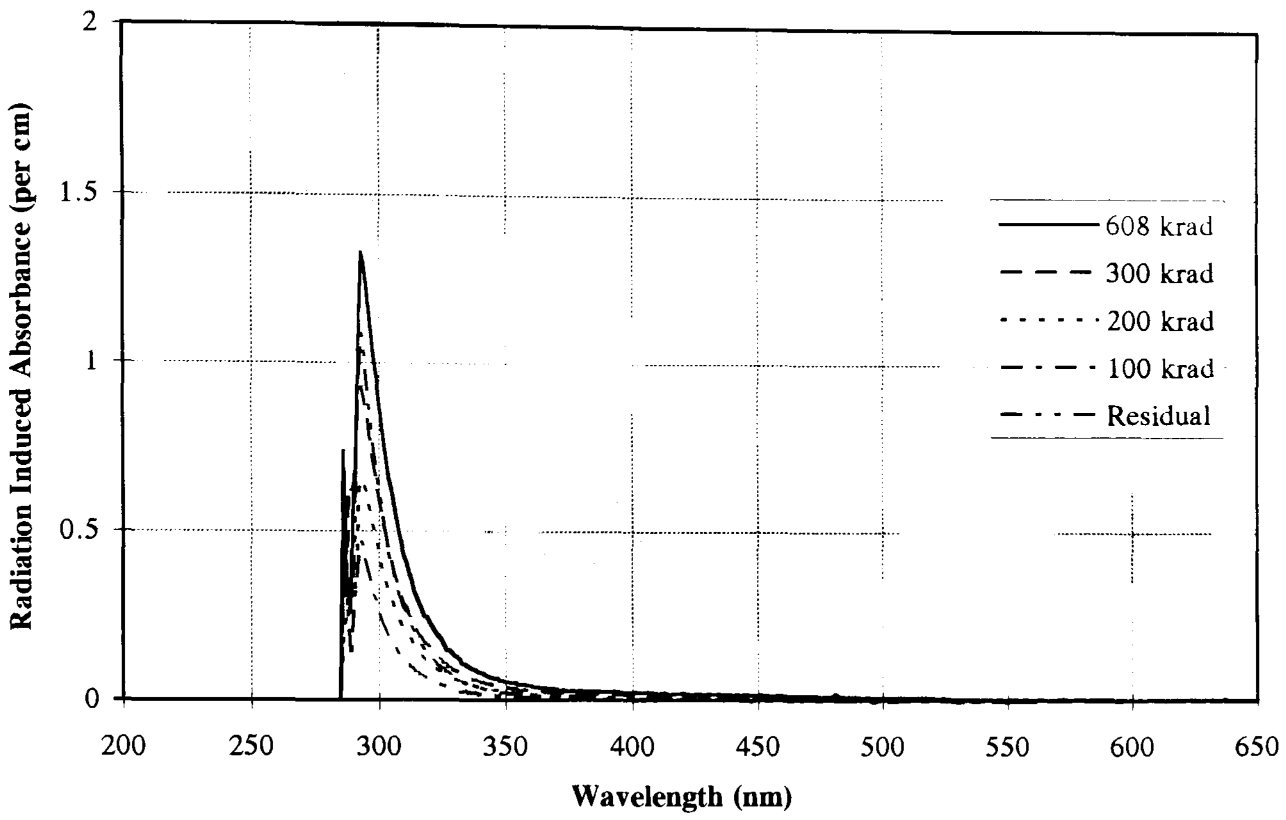

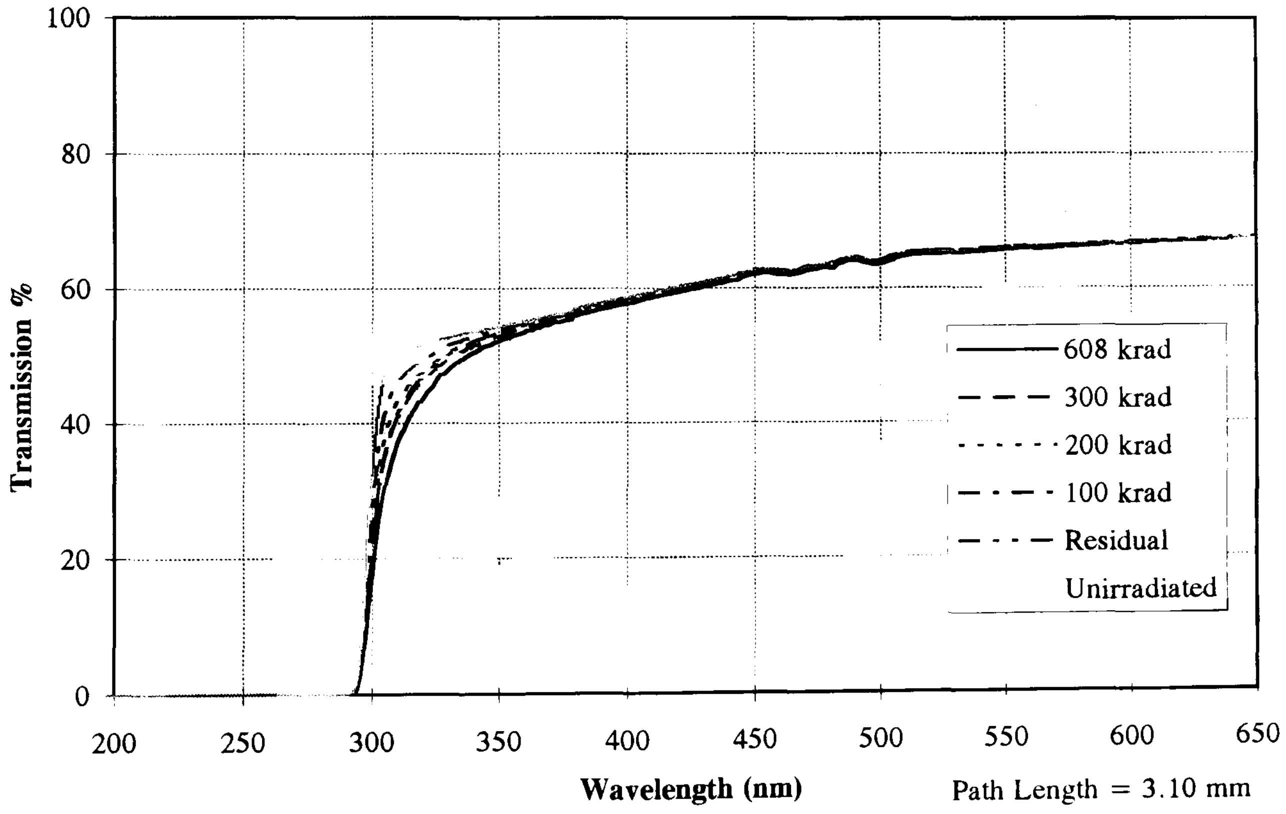

Figure 6.05 Radiation induced absorbance and annealing data for P93, which was the most radiation resistant glass identified in this work. The curve labelled 'residual' indicates the radiation induced absorbance which was observed after 1 year of annealing under the conditions specified in the text. Absorbance values for $\lambda < 290$ nm have been suppressed as they are dominated by noise.

6.5. Scintillation Time Structure

There are seven parameters in the summary spreadsheet which describe the time structure of scintillation light for each glass. The timing spectra were fitted with three decaying exponentials, the initial amplitudes, A and decay constants, τ account for five of the parameters. The amplitudes A_1, A_2 and A_3 are normalised so that A_1 equals 1000 events. As A_1 is the same for each glass, it is not included explicitly in each row. The goodness of fit, χ^2 is given per degree of freedom, the fits were performed over typically ~1870 data points with seven variables A_1, A_2, A_3, τ_1, τ_2, τ_3, and Z. Z described the flat background upon which the data was superimposed.

One parameter of principal interest is the fraction of scintillation light which is collected within 25 ns of an event compared to that collected within 500 ns. This rather bizarre parameter arises from the CMS application, 25 ns corresponds to the interval between consecutive bunch crossings. This figure indicates the susceptibility of a scintillation detector to pulse *pile-up*. When the value is close to unity, most of the scintillation light is emitted within 25 ns and consequently, the detector is resistant to problems associated with pulse pile-up.

$$\text{pile-up parameter, } \Omega = \frac{\sum_{i=0}^{25}\sum_{j=1}^{3} A_j \times \exp\left(-i/\tau_j\right)}{\sum_{i=0}^{500}\sum_{j=1}^{3} A_j \times \exp\left(-i/\tau_j\right)} \qquad \text{Equation 6.03}$$

Identifying correlations between composition and the individual exponential parameters is difficult. Uncertainty in individual time constants and amplitudes can lead to inconsistencies in potential trends. The majority of the following discussion concerning time constants has been based principally on this final pile-up parameter, Ω. The error in Ω is considerably smaller than the error in any of the individual exponential parameters. In addition to calculating Ω from the fitted equation, the pile-up parameter has also be measured directly from the timing data, the two values were consistent (±3%) provided that the start of the exponential is identified correctly (see section 5.7).

Global correlations of, for example, $\%CeF_3$ versus Ω were inconclusive due to large variations in the composition of the glasses. When they are separated into the different compositional categories, trends with Ω are more easily identified. In the following sections, compositional groups are discussed individually, finally conclusions which are globally applicable (within this data set) are gathered together in a summary section of this chapter.

6.5.1 Time structure within similar compositional groups

6.5.1.1. HBAlLa

In the collection that consisted of HBAlLa glasses doped with various Lanthanides, all dopants considerably enhanced the pile-up parameter compared to the control sample (JHA6). It is plausible that trapping sites introduced by additional lanthanides cause quenching of the scintillation light resulting in a faster emission. The timing spectrum for the Pr doped glass (P16) showed an abnormally high flat background. This can be explained by a fluorescent component that has a time constant which is significantly longer than the time window used for this measurement.

Name, Dopant, Pile-up parameter	Name, Dopant, Pile-up parameter
JHA6, control, 0.635	P47, Nd 1.5%, 0.721
P59, Lu 1.5%, 0.698	P46, Er 1.5%, 0.710
P15, Gd 1.5%, 0.714	P43, Eu 1.5%, 0.700

Table 6.09 Lanthanide dopants increase the Ω in HBAlLa glasses.

6.5.1.2. HBCeIn

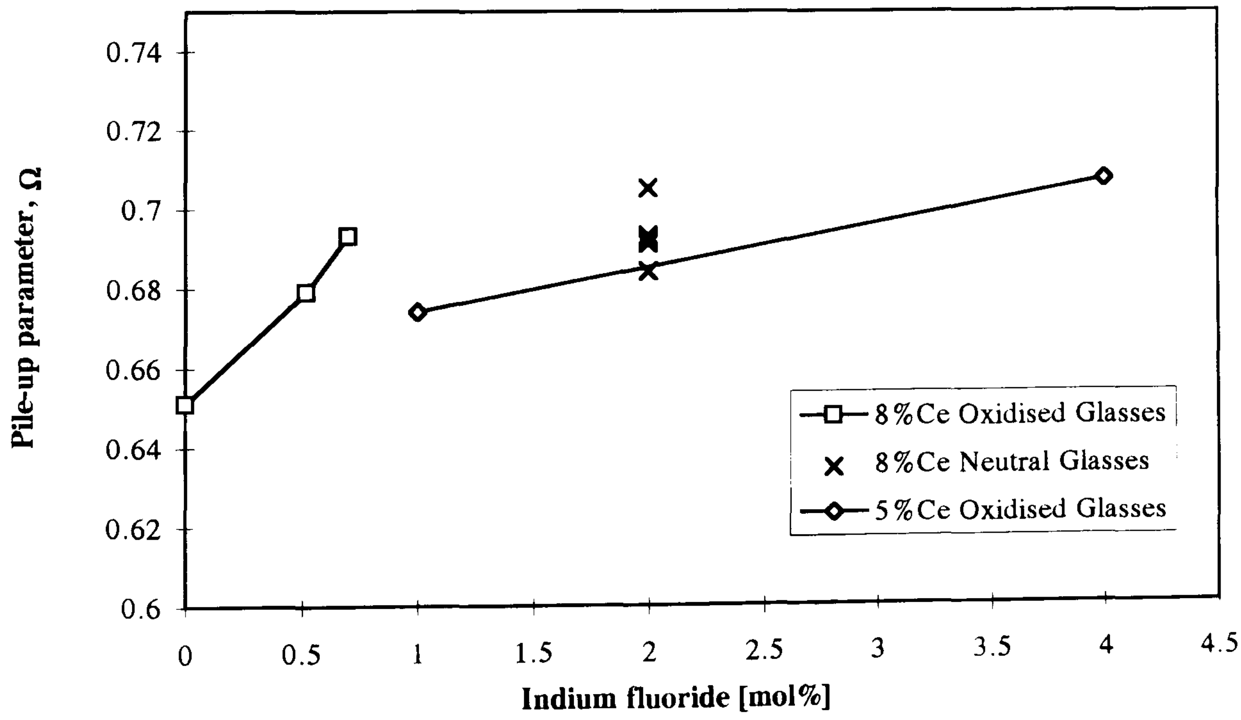

Figure 6.06 In the HBCeIn glass matrix, there is evidence to suggest that Ω increases with the fraction of Indium present in the sample.

The HBCeIn set consisted of fourteen glasses, approximately half were produced under an oxidising atmosphere and half under neutral conditions. Excluding those glasses containing additional dopants, it was clear that the 8% Ce glasses produced under neutral conditions (N4, N5, N6, N7 and N17) were systematically faster (0.693± 0.007) than P93, P91, P83, and P82B which were produced under an oxidising atmosphere (0.678± 0.016). The neutral glasses contained 2% Indium whereas in the oxidised glasses, the amount varied between 0 and 1%. There was one 4% Indium (oxidised) glass which was as fast as the neutral glasses. There is some indication of Ω increasing with the Indium content, the graphical form of the relationship is shown in Figure 6.06. It can be seen from the five neutral atmosphere glasses that the intrinsic spread is approximately $\sigma = 0.007$. These glasses all had identical compositions and are represented with crosses.

6.5.1.3. HBCeAl

This set of nine consisted of mainly 5% Ce glasses, doped at the 1.5% level with various fluorides. In agreement with the HBAlLa glasses, the doped samples predominantly had larger values of Ω than the control samples. The order in which the pile-up parameter increased is shown in Table 6.10. In this series, the 10% Ce doped glass (P20) had an Ω of 0.672 whereas the values for the similar 5% glasses, B1 and P86 were 0.646 and 0.661. It appears that Ω increases with the fraction of Ce. This entire set of glasses was produced under oxidising conditions.

Name, Dopant, Ω	Name, Dopant, Ω	Name, Dopant, Ω
B1, control, 0.646	P17, Zr 1.0%, 0.660	P27, Pb 5.0%, 0.704
P60, Gd 1.5%, 0.650	P14, Mn 1.5%, 0.677	P40 Hf/Zr 0.699
P86 control 0.661	P20 10%Ce 0.672	

Table 6.10 The pile-up parameter is lower for the undoped control sample than the doped samples.

6.5.1.4. HBCeAlIn

The series B1, P57 and P35 were doped with an increasing fraction of Indium. In agreement with the HBCeIn glasses, Ω increased with the Indium content. For 0, 1 and 2.4% Indium, the pile-up parameters were 0.646, 0.672 and 0.694. The Yb doped HBCeAlIn glasses, P96B (1.6% Yb) and P87 (1% Yb) had similar Ωs (0.691 and 0.690).

6.5.1.5. HBLiCeAl

Production of large single glass blocks can only be realised by the incorporation of approximately 18% Li in these glasses. It has been shown in the earlier sections of this chapter that a high Li content generally detracts from the radiation tolerance observed in fluoride glasses. Comparing B1, P23 and P94B which contain 0, 4 and 18% Li, shows that the pile-up parameter, decreases as the Li content is increased. Ω=0.646, 0.609 and 0.590 respectively.

The 4% Al glass (P94B) and the 2.5% Al glass (P92), had pile-up parameters of 0.590 and 0.657. This set also contained one glass (N14) produced under neutral conditions, it had the highest Ω of this set (0.686). It is not possible to deduce any conclusions concerning oxidising versus neutral production atmospheres as this sample also contained 0.5% TiO_2.

P34 and P28 are HBLiCeAlLa glasses which contain 10 and 1.4% Ce respectively. These glasses were both produced under oxidising conditions. The 10% Ce glass has an Ω of 0.679 whereas for the 1.4% Ce glass, the figure is only 0.593. A higher fraction of Ce is consistent with a large pile-up parameter.

6.5.1.6. HBLiCeAlIn

Two glasses (P179, P100) produced under oxidising conditions are compared with four glasses produced using a neutral atmosphere (N16, N29, N11 and N13). All of the neutral glasses are faster than the oxidised samples. Direct comparisons are not possible because no pair of neutral and oxidised glasses are compositionally identical. In the neutral glasses, the Ω improves with the incorporation of Zr and Indium. P179 varies from all of the other fluoride glasses tested as its dimensions were 40× 20× 20 mm^3. The other samples were typically 20× 10× 5 mm^3 or smaller. It should be noted that this glass is the slowest of the entire set.

Name, Dopant, Pile-up parameter	Name, Dopant, Pile-up parameter
P179, Oxidising,40×20×20mm^3, 0.578	N29, 1.5%In, 0.701
P100, Oxidising,20×10×5mm^3, 0.653	N11, 1%In, 2%PbO, 75%Mn, 0.702
N16, 0.5%Indium 1%Zn, 0.678	N13, Mixed Hf/Zr, 0.696

Table 6.11 The pile-up parameter improves when Indium or Zr are included in the glass. P179 has the poorest Ω of the entire set.

6.5.1.7. HBLiCeAlInYb

P85 was the only glass in the HBLiCeAlInYb set that was produced under oxidising conditions, its Ω was 0.644. This is contrasted with the six neutral glasses (N27, N26, N28, N30, N36 and N33) which had pile-up parameters varying between 0.684 and 0.714. The compositions of all of these glasses were very similar, this set offers the most conclusive proof that the neutral glasses have systematically faster decay constants than oxidised glasses.

Name	Hf	Ba	Li	Ce	Al	In	Yb	Ω
P85	54	19	17	5	4	1	0.7	0.644
N27	54	20	17	5	3	1	0.8	0.699
N26	54	20	17	5	3	1	0.5	0.704
N28	54	20	17	5	3	1	0.5	0.697
N30	54.5	17	20	5	2.5	1	1	0.714
N36	48	20	9	8	3	1	0.5	0.701
N33	54	20	17	5	3	1	0.5	0.684

Table 6.12 The pile-up parameter and compositional information for the HBLiCeAlInYb glasses.

6.5.2. Ω, the top and bottom 10%

If the glasses are arranged in order of increasing pile-up parameter, the highest and lowest are as shown in Table 6.13. P179 was physically larger than the rest of the glasses. P94B, JHA7, P28, P23 and JHA6 all contain no Indium and small amounts (<5%) of Ce. Additionally, most of these glasses contain Li which deteriorates radiation tolerance, none of these glasses were radiation resistant. The majority of the fastest glasses in Table 6.13, contain no Ce. As a result, these glasses have practically zero light yield. The time structure of 'scintillation' light is fast because the small number of photons which are detected, are predominantly due to prompt Cerenkov light.

Lowest pile-up parameter			Highest pile-up parameter		
Name,	Pile-up parameter,	Comment	Name,	Pile-up parameter,	Comment
P179,	0.578,	40×20×20 mm^3	P48,	0.723,	PbZnAlInLa
P94B,	0.590,	18%Li no In,Ce	P47,	0.721,	HfBaAlLaNd
JHA7,	0.591,	no Indium	P51,	0.721,	HfBaLaAlSm
P28,	0.593,	7%Li no Indium	P31,	0.717,	ZrBaLaAlNa
P23,	0.609,	4%Li no Indium	N30,	0.714,	HfBaLiCeAlInYb
JHA6,	0.635,	no Indium, no Ce	P15,	0.713,	HfBaAlLaGd
			P46,	0.710,	HfBaAlLaEr

Table 6.13 The glasses with the fastest and slowest pile-up parameters.

The only glass in the list which contained Cerium was N30. In contrast to the Sheffield glasses (prefix P), the time constants for the Russian glasses (prefix N) were measured prior to irradiation. It is apparent that the N glasses are generally faster. If the list of the fastest glasses is continued beyond P46, the overwhelming majority of the subsequent glasses are unirradiated Russian samples; N1, P25B, N7, P27, N26, N11, N29, N36, P43, P40, N27, P59 and lastly, N28.

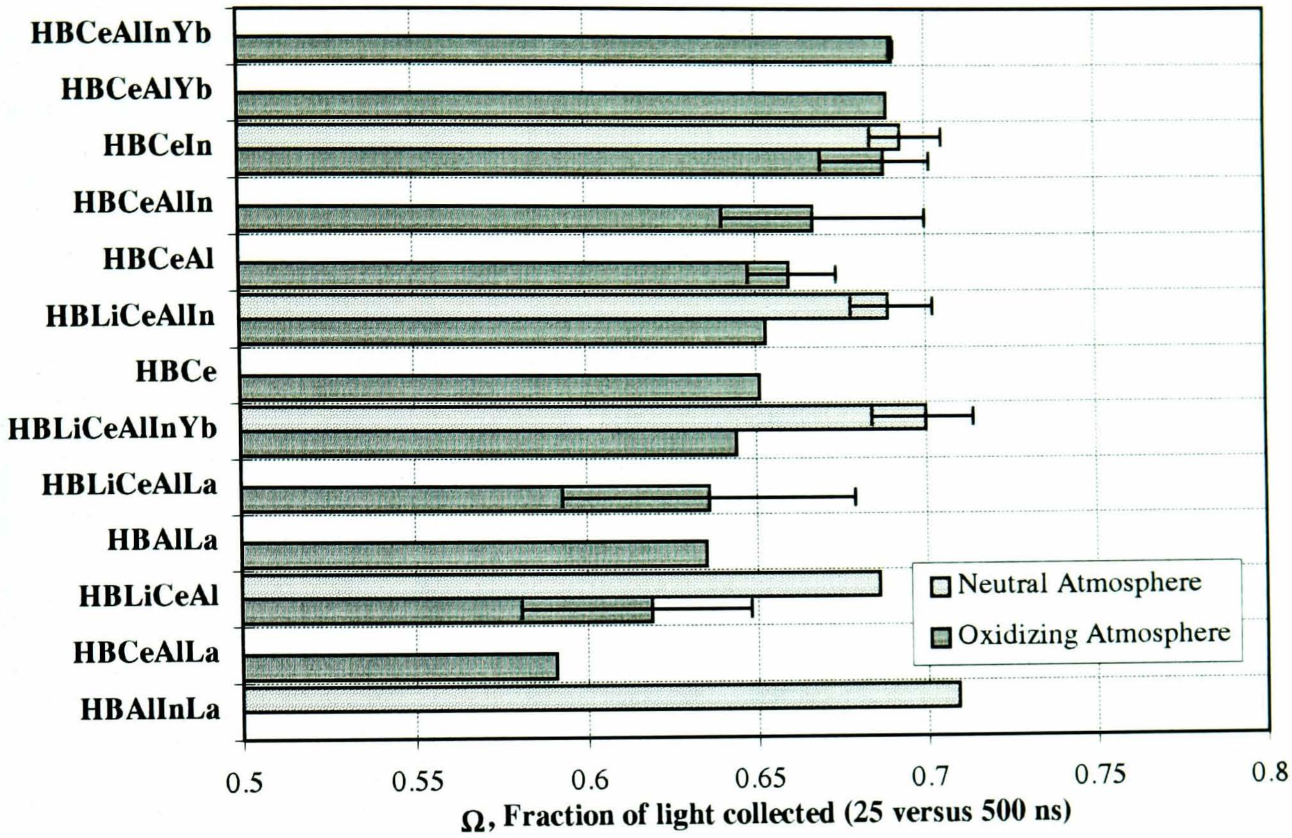

Figure 6.07 The mean pile-up parameter, Ω is shown for various glass compositions evaluated in this work. The results are separated where similar glasses have been produced using oxidising and neutral conditions. The glasses have been sorted in order of the fastest oxidising atmosphere groups.

In a similar manner to the results presented in Figure 6.03, the glasses in Figure 6.07 have been separated into compositional groups and placed in order of increasing pile-up parameter. In some of the groups it was possible to further divide the glasses into those produced under oxidising and those produced under neutral conditions. All Zirconium glasses, have been excluded from this figure as they emit practically no scintillation light. Also, glasses that contain additional dopants (e.g. TiO_2, Pb, Zn, Ga, Lu, ... etc.) have not been included.

There is a correlation between the radiation tolerant glasses of Figure 6.03 and those which emit their scintillation light with the shortest decay constants. The three slowest oxidising atmosphere groups were also the three least radiation resistant Hf based glasses in Figure 6.03.

6.5.3. Ω versus τ_1, τ_2, τ_3, A_1, A_2, A_3

Variations of Ω with composition have been successfully identified. Ω is a rather abstract variable, to complete the discussion, the dependence of Ω with the individual scintillation decay parameters is considered below. Using the data from Table 6.01, there was no relationship between any of the exponential amplitudes and the pile-up parameter. The longest decay constant (τ_3) was not correlated with Ω either. The two shortest time constants both decrease as Ω improves towards unity. These observations are consistent with the definition of Ω. The graphical relation ship of τ_1 and τ_2 versus Ω is shown in Figure 6.08.

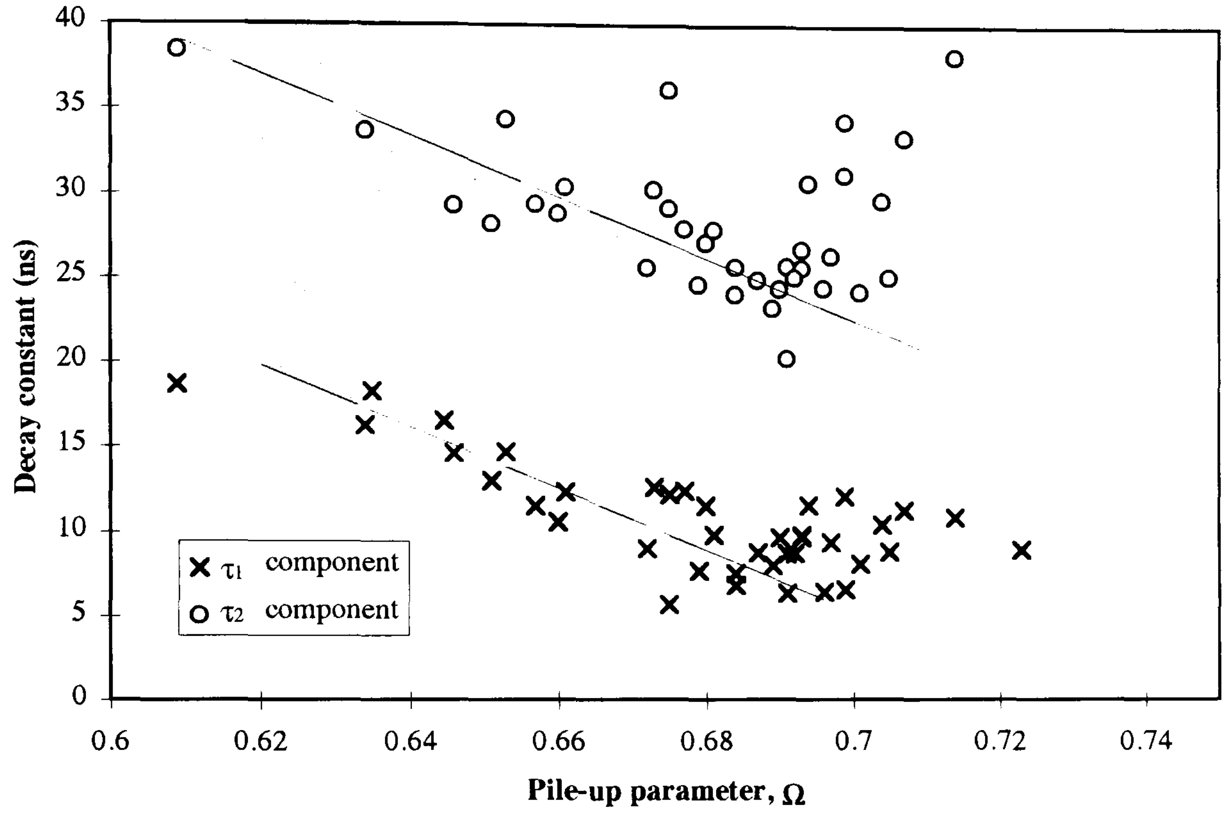

Figure 6.08 The two shortest scintillation decay constants are shown as a function of Ω for HBCeAl glass. There is a loose anti-correlation between Ω and the two shortest time components.

The individual time constants and amplitudes have all been compared with each other. The only parameters which show any degree of correlation are the time constants of the two fastest scintillation components. In Figure 6.09, τ_2 has been plotted against τ_1. The majority of CeF_3 doped glasses fall between the two lines overlaid on the graph. The lines have been visually overlaid to guide the eye but they also indicate an approximate functional relationship,

$$\tau_2 = \frac{5}{4}\tau_1 + 16 \qquad \text{Equation 6.04}$$

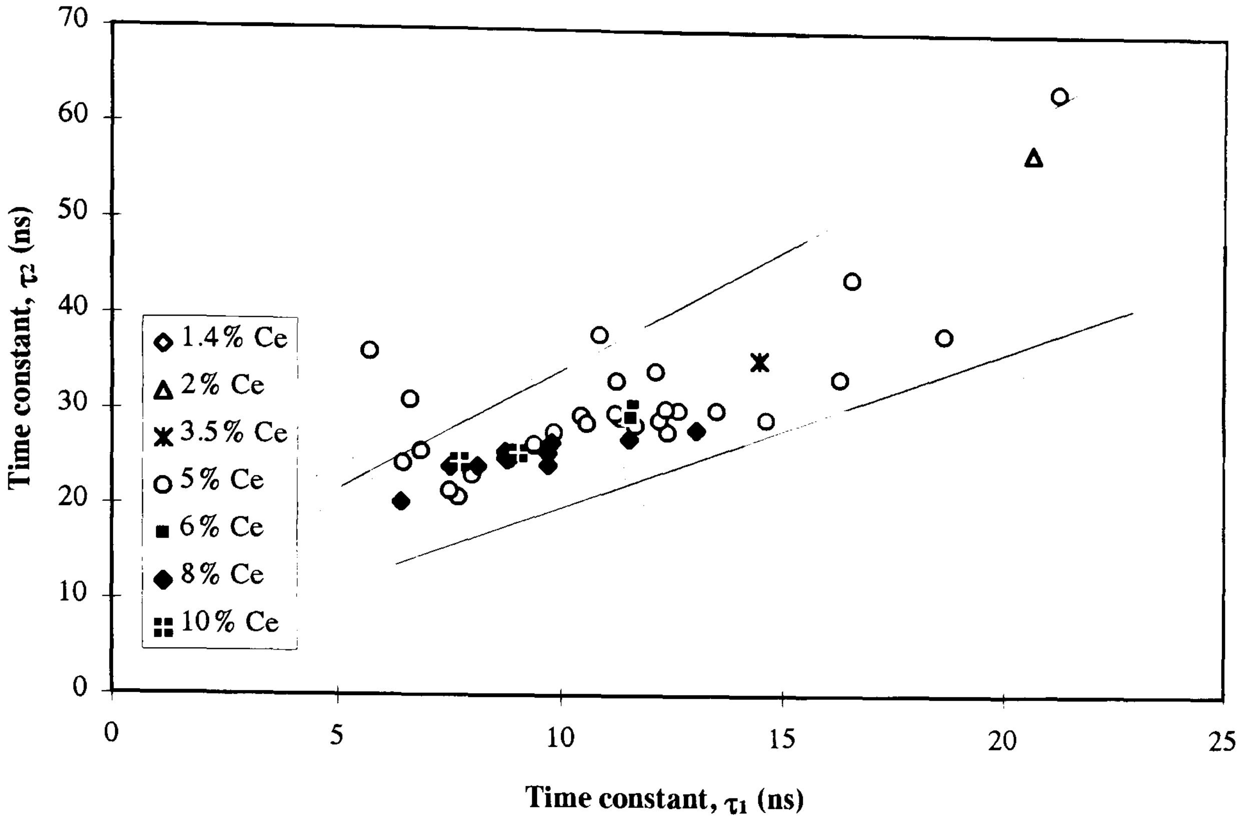

Figure 6.09 The time constant τ_1 versus τ_2, the glasses are separated according to the CeF_3 content.

6.6. Summary

In this chapter a saturating exponential has been used to describe the development of radiation induced damage with dose. This model is consistent with defect production due to the radiation field and annihilation of defects by recombination. The amplitude and growth constants for each glass are given in Table 6.01. This approach has been useful for comparing different glasses and identifying trends with composition.

Several elements which enhance the radiation resistance of fluoride glasses have been identified. Indium has caused a significant improvement throughout the entire spectral region, Yb doping has a similar effect for wavelengths above 400 nm. Eu doping causes the fluoride glass, HBAlLaEu to be completely radiation resistant above 400 nm. Ce is responsible for the scintillation light observed in these glasses, it has also improved the radiation resistance of several Hf based glasses. Other lanthanide elements have proved detrimental to radiation resistance in the 300- 350 nm region. The effects of radiation resistant components in these glasses is not cumulative.

Using cheaper HfF_4 resulted in glasses which were inferior to their ultra-pure equivalents, additional impurities were thought to be responsible for the observed degradation. Glasses produced under an oxidising atmosphere suffered less radiation induced absorbance but their intrinsic optical transmission was inferior to the neutral glasses prior to irradiation.

The most radiation resistant glass (P93) is shown in Figure 6.05, this glass produced in an oxidising atmosphere has a poor unirradiated transmission curve.

From the application point of view the classification in terms of saturation absorbance and growth constants is less than ideal. A calculation in required to predict the damage at any intermediate dose. The anticipated radiation environment at the LHC is equivalent to an accumulated dose of 1 Mrad in the barrel region over the 10 year operational lifetime of the experiment. Immediately after a 1 Mrad dose, the most radiation resistant glass is P93. At 325 nm, the radiation induced absorbance is 0.1 OD for a 10 mm path.

Detailed *Monte Carlo* simulations of the effects of induced absorbance on the energy resolution of calorimeter modules due to exposure to the LHC radiation environment are currently under investigation. The work which involves ray tracing is being carried out by S. Salih (Brunel University) and B. Kennedy (RAL). A naive model of the tolerable induced absorbance assumes that the loss in transmission along the entire length (40 cm) of the calorimeter module must not exceed 5%. This rather arbitrary definition corresponds to a loss of 0.004 OD for a 1 cm path. Even the Hafnate glass which develops the least radiation induced absorbance (P93) falls outside this limit by a factor of twenty five. The challenge of radiation tolerance in these glasses has not yet been solved despite considerable progress in this direction. The duration of the CMS experiment provides considerable scope for the spontaneous recovery of optical absorbance at room temperature. Allowing for this recovery, the most radiation resistant glass has an absorbance of 0.022 OD, this is merely a factor of five too poor. Unfortunately this composition can not be produced in the large blocks which are necessary for the electromagnetic calorimeter of CMS.

During the preceding discussions concerning scintillation decay constants, it has been suggested that there is a connection between the radiation tolerance and the scintillation pile-up parameter, Ω for these fluoride glasses. Increasing the fraction of Ce and Indium tends to increase Ω, these elements also tend to improve radiation tolerance. In almost every case where compositional trends with radiation tolerance have been identified, the same trend has been observed for the pile-up parameter.

Lithium has been shown to detract from the radiation resistance of a range of fluoride glasses. The Li doped glasses also show poor scintillation decay characteristics compared to non-Li glasses.

One notable exception is the classification which separates the glasses into those produced under oxidising and those produced under neutral conditions. Paradoxically radiation tolerance in oxidised glasses was found to be superior compared to neutral glasses. In contrast, the neutral glasses have systematically higher pile-up parameters compared to similar oxidised samples. This observation is contrary to the general conclusion which links radiation resistance and short scintillation decay constants.

This inconsistency may be resolved if the transmission spectra of the glass samples are considered. The majority of timing measurements presented in Table 6.01 were recorded using samples which had already been irradiated. In corresponding measurements recorded for glasses which were not irradiated, the fraction of light collected in the first 25 ns was systematically higher than in the irradiated glasses. An example of this is the set of Russian Glasses (prefix, N).

These results are consistent with the time components of the scintillation emission having a wavelength dependence. Residual absorbance in the irradiated glasses alters the spectrum of scintillation light and hence its time structure. Since residual damage is predominantly located around 300 nm in Ce doped glasses and reduces with increasing wavelength, the results imply that the slower time component occurs at a longer wavelength. The faster component that is attenuated in damaged glasses must occur in the region which shows relatively high induced damage. The fraction of light collected in the first 25 ns (compared to the first 500 ns) merely reflects the suppression of the faster emission in glasses which show significant residual induced damage.

Further evidence which suggests that the fast emission is in the vicinity of the UV edge is that the largest sample tested (pre-irradiation), P179, had the lowest Ω of the entire series. The faster emission was more strongly attenuated than in smaller samples because of the additional path length required to escape from the glass, thus giving a lower Ω.

This explanation involving the spectral emission of light in HMF glasses is consistent with the description of scintillation light in CeF_3 by D. Anderson [13] and more recent work by P. Lecoq [14]. In crystalline CeF_3, P. Lecoq has measured a 300 nm, 8 ns component and a 340 nm emission with a time constant of 25 ns.

---

[1] A. Lecoq and Ma. Poulin, *J. Non-Cryst. Solids* **34** (1979) 333.

[2] I. Aggerwal and G. Lu, *Fluoride Glass Fibre Optics*, Academic Press Inc, ISBN 0-12-044505-0.

[3] Ma. Poulin and J. Lucas, *Verres Refract.* **32** (1978) 505.

[4] K. Tanimura, et al., *J. Non-Cryst. Solids* **70** (1985) 397.

---

[5] M. Saad and Ma. Poulin, *Mat. Sci. Forum* **5** (1985) 105.

[6] J. Stroud, *J. of Chem. Phys.* **37** (1962) 836.

[7] E. Friebele and D. Tran, *J. Non-Cryst. Solids* **72** (1985) 221.

[8] P.W. France et al., *Fluoride Glass Optical Fibres*, Blackie, CRC Press, Inc.

[9] A. Bishay, in: *Intern. Conf. on Silicate Industry*, Budapest, 1963.

[10] J.H. Mackey, et al., *J. Phys.Chem Solids* **27** (1966) 1773.

[11] D.L.Griscom, et al., *IEEE Trans. Nucl. Sci.* **41** (1994) 523.

[12] W.W.Moses, et al., LBL-27609 (1993).

[13] D.F. Anderson, *IEEE Trans. Nucl. Sci.* **36** (1989) 137.

[14] P. Lecoq, *Study of New Scintillators bt the "Crystal Clear Collaboration"*.

CHAPTER SEVEN

CERN Beam Tests

7.1. Introduction / preliminary discussion

Light yield measurements are routinely carried out on all small test samples ($20\times 10\times 5$ mm^3) by our colleagues at the Rutherford Appleton Laboratory (Appendix 2). These measurements involve exciting the glass sample with a minimum ionising proton beam, of momentum 750 MeV/c. The scintillation light is detected using a Thorn EMI 9814Q photomultiplier tube and recorded using a Lecroy 7200 digital oscilloscope. All measurements are relative to an Optovac CeF_3 sample ($10\times 10\times 10$ mm^3).

The proposed application of these HMF glasses is as the EM calorimeter material for the CMS experiment. In this application the configuration would comprise many individual calorimeter modules. Each module would consist of a 400 mm, tapered block laterally segmented so that the largest piece is 280 mm long, and has end dimensions of $\approx 30\times 30$ mm^2. The anticipated read out will employ photodiodes or APDs due to their compactness, unit cost and relative immunity to the 4T analysing magnetic field. The detector will be mounted on the rear surface of each module.

Extrapolating the light yield measured using small test samples to the predicted light yield for full size calorimeter blocks is a difficult task. It requires a multi-stage calculation, there are many variables which have to be estimated and several simplifying assumptions inherent to the procedure. Propagating errors result in an estimated yield which has a high degree of uncertainty, potentially ±50% or worse. To compare experimental results in the wider academic community it is essential to obtain accurate light yield measurements for a realistic calorimeter configuration. This is achieved by performing tests in high energy particle beams, using calorimeter modules which simulate the realistic detector closely.

7.1.1. Glasses used for the beam tests

This work has identified glasses with densities in excess of 6 gcm^{-3}, this is sufficient for the CMS application and corresponds to a radiation length, X_0 of 1.57 cm. By August '93, developments in the production process had resulted in tiles of dimensions, 40× 40× 5 mm^3. This geometry was constrained by two parameters. One dimension had to be small (5 mm) to enable the melt to cool rapidly enough to form a glass. The second constraint was merely logistical, the crucible used to heat the melt had a capacity of 30 cm^3. This amount of the various HMF powders melts down to approximately 10 cm^3 of glass. The glass composition with one of the highest *small sample light yields* was produced in tiles for the beam test evaluations.

Tiles produced for the beam tests fell into two main groups. All samples had the same nominal composition, HfF_4, 54; BaF_2, 19; LiF_3, 18; CeF_3, 5; AlF_3, 3.5; InF_3, 0.5 mol%. However, approximately half of the tiles were produced under an atmosphere of pure N_2, the other half were produced under 90% N_2, 10% O_2. The two types of glasses are known as *nitrogen tiles* and the *oxygen tiles* respectively. Typical transmission spectra for these glasses are shown in Figure 7.01. The spectrum for the *oxygen tile* shows a clear rounding of the UV edge compared to the *nitrogen tile*. This is precisely in the region of Ce^{3+} emission [1] which peaks at 300 and 340 nm.

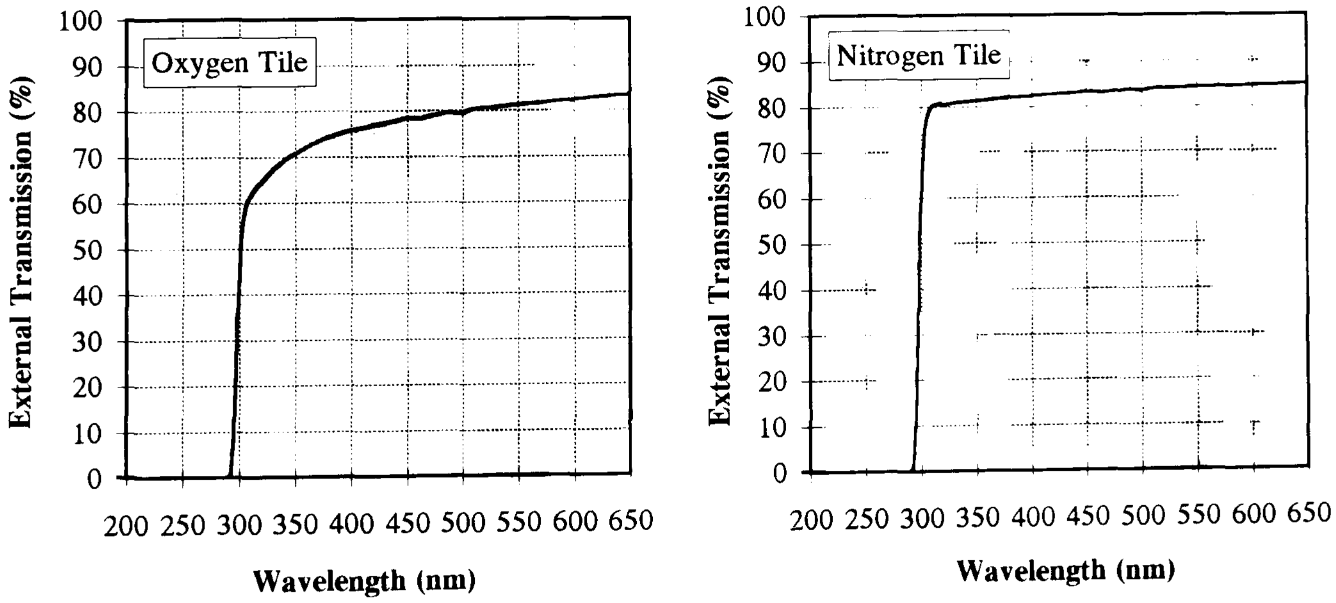

Figure 7.01 Transmisson spectra for Nitrogen and Oxygen tiles.

The link between an oxidising atmosphere and a rounding of the UV edge was only identified after twenty of the inferior *oxygen tiles* had been produced for the beam tests. It is possible to re-melt an *oxygen tile* under pure N_2 and recast the melt producing a *nitrogen* *tile*. This procedure takes 6 hours per tile. Time constraints were such that re-melting twenty tiles was not feasible. Production switched to *nitrogen tiles* for the remainder of the set.

A total of forty tiles were produced for the May '94 beam tests, twenty of each type. Prior to shipping to CERN, the transmission spectrum of each tile was measured through the 5 mm dimension. The tiles were then rated on a four point scale which referred to the loss in transmission, κ at 325 nm. This was measured through the 5 mm thickness. 'A' $\equiv 0 < \kappa < 1\%$, 'B' $\equiv 1 < \kappa < 2\%$, 'C' $\equiv 2 < \kappa < 5\%$, and 'D' $\equiv 5 < \kappa < 10\%$. The tiles were stacked as shown in Figure 7.02.

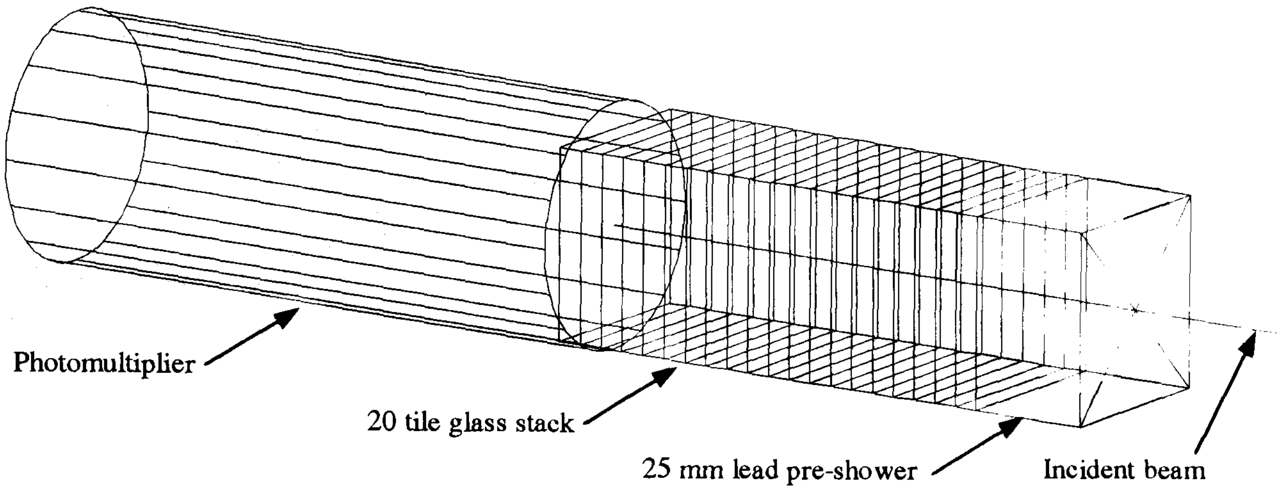

Figure 7.02 Arrangement of glass tiles in the composite stack showing the photodetector and the direction of the incident beam. In the illustration a 20 mm thick lead block which acts as a preshower is positioned at the front of the stack.

7.1.2. Stack construction

Following earlier work carried out by P. Hobson and T. Price [2], DC200 grease was used to optically couple the tiles. This material has excellent transparency in the UV down to a wavelength of 200 nm [3]. For each stack configuration, the tiles were arranged in order of optical quality (A> B> C> D) and then greased together. Great care was taken to ensure that all air bubbles were excluded from each interface, excess grease was removed from the exposed surfaces. The ensemble was wrapped in Aluminised Mylar on all sides except the 40×40 mm^2 end face which was used for optical readout. A comprehensive survey of various scintillator wrapping media was carried out by our colleagues at the Rutherford Appleton Laboratory. In tests using a CeF_3 crystal and a ^{137}Cs source, they identified *Millipore HAWP04700* [4] as having the highest light collection. Unfortunately, this paper has an adverse reaction with the optical coupling grease. After a short contact period, the paper becomes translucent. This is similar to the effect observed with PTFE [5]. For mechanical support, the stack was wrapped in black tape before finally being coupled to the photodetector using DC200 grease.

]

7.2. Interaction

The beam test evaluations involved high energy electrons and muons passing axially along the glass stack as indicated in Figure 7.02. Electrons with energies in the range 8 GeV< E< 50 GeV were used. At least 25 X_0 of material are required to *contain* these high energy electron showers [6]. For HMF glasses, this corresponds to a stack height of 40 cm. By the beginning of the beam tests only 20 cm (12.7 X_0) were available. A shortfall in the number of tiles results in leakage from the rear of the stack. Consequently, the non-containing glass block will only sample the shower. Lateral spread of the shower gives rise to further leakage from the sides of the stack.

It is preferential to test an array of calorimeter modules instead of just one in isolation. The amount of beam leakage into adjacent towers can be measured by summing the signals from the eight adjacent towers. A higher yield is recorded in the central module as those adjacent compensate lateral beam loss to a certain extent.

7.3. Detector choice

The choice of detector is restricted as the glass stack does not contain the entire shower. Some high energy charged particles will pass into the photodetector which is placed on the rear surface of the stack. Direct detection of any shower leakage significantly enhances the observed signal causing deterioration of the energy resolution because of fluctuations in the amount of leakage. Large area silicon detectors are most susceptible to this effect. The problem of direct detection can be solved using two photodiodes. One views the scintillation light from the block (and inevitably any shower leakage) the other is 'blind' and only detects shower leakage. The calorimeter signal is derived from the difference between each photodiode signal. Photomultipliers are relatively 'blind' to shower leakage and offer a convenient detector system.

For the beam tests a Thorn EMI 9814B 2", 11-stage photomultiplier with a bialkali photocathode and a Quartz window was used. The typical QE plot for this tube is shown in Figure 4.06. The QE (23% at 325 nm) is well matched to the emission spectrum of Cerium emission [1].

7.4. Preliminary light yield estimates

Standard dynode chains provide an overall gain of approximately 10^6 (10-stage)-10^7 (12-stage) [7]. A routine application involves measuring the scintillation light from standard radioactive sources using a commercial scintillator. Typically less than 10,000 photoelectrons are produced per MeV. Detection of a 1 MeV photon results in a voltage pulse developed across the anode which would peak at less than 10V.

High energy electron beams showering in the HMF glass block deposit a significant fraction of their energy even though the modules are non-containing. The electron energies used were 8, 20, 35, and 50 GeV. If 50% of the beam energy is deposited in the glass block, and the light yield of the glass is 100 photoelectrons per MeV, the signal will exceed that measured using fixed sources by a factor of two hundred. To avoid saturation of the photomultiplier output, the divider network was redesigned.

A new network was constructed and tested at Brunel University, it had a design gain of ×8000 (at 1500 V) instead of 10^6. To supply the output current pulses produced by electron showers whilst maintaining the dynode voltages, large capacitors were required on the last few dynodes. High inter-dynode voltages were used to ensure efficient collection of photoelectrons in the first two amplification stages. Zener dynodes fixed the k-d_1 voltage at 300 V. To avoid build-up of space-charge, the inter-dynode voltage of the last few stages was progressively increased. The divider network is shown in Figure 7.03.

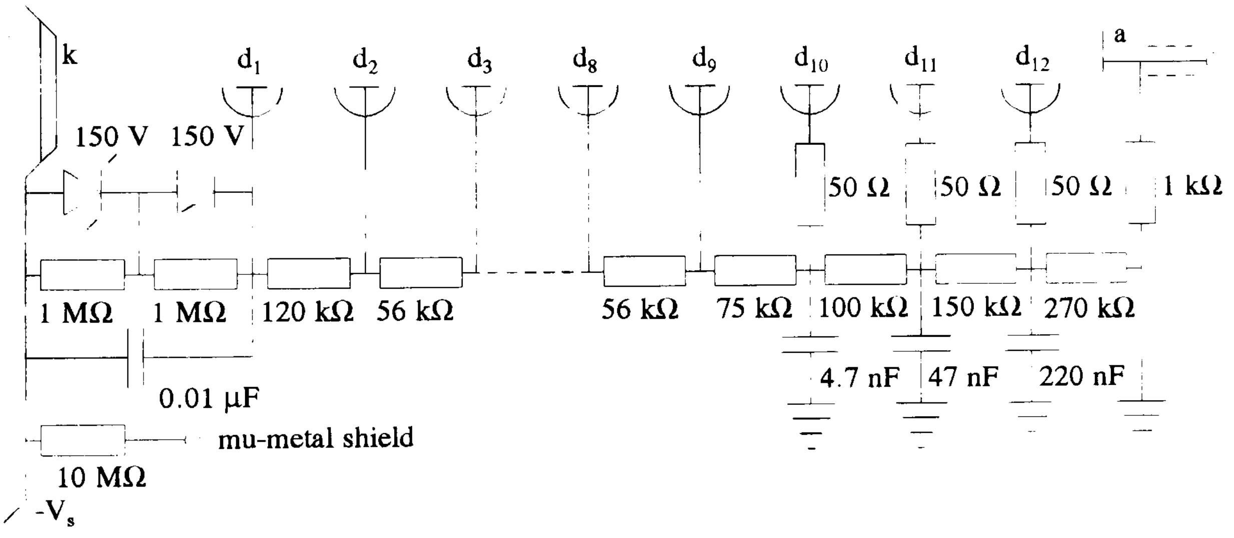

Figure 7.03 The divider network for the photomultiplier used in the beam tests. Despite their large size, the capacitors were soldered directly onto the PMT base to minimise inductance of the circuit.

Prior to exporting the photomultiplier for use in the beam tests, the system linearity was measured at Brunel University using a pulsed LED as the excitation source. The driving pulse was kept constant (10V, 30 ns) throughout the calibration, the light level falling on the PMT was varied using a set of neutral density filters. To relate the measured response to an absolute light level in terms of photoelectrons, a Harshaw Type 8D8 NaI(Tl) crystal (cylindrical ϕ50 mm × 50 mm) was grease coupled to the photomultiplier and used to measure the energy spectrum of ^{137}Cs. Allowing for the 23% photocathode QE at 415 nm, this light level corresponds to approximately 5800 photoelectrons at the photocathode.

A single LED and a standard pulse generator can not produce a light flux equivalent to that anticipated from a multi-GeV electron showering in the glass block. To deliver an integrated light pulse which was equivalent to scintillation from an electron shower, the width of the driving pulse had to be increased to 30 ns. This was one limitation of the linearity measurement using an LED.

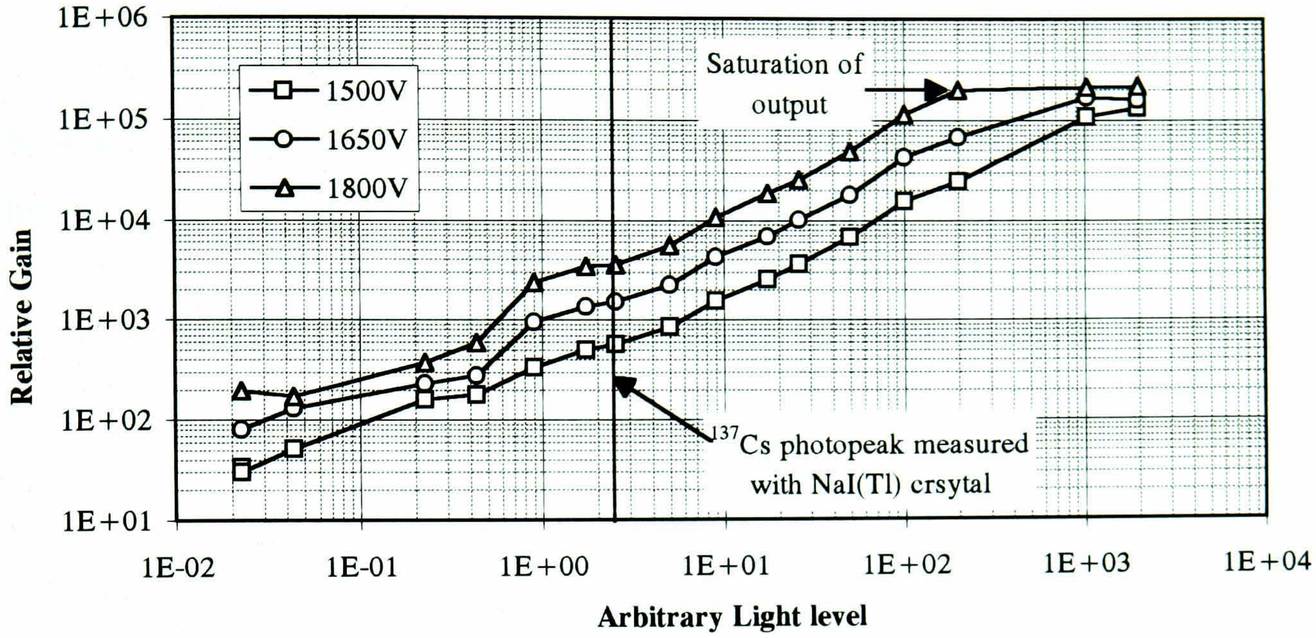

Figure 7.04 The relative gain of the photomultiplier versus an arbitrary light level, the position of the 662 keV photopeak measured using NaI(Tl) crystal is indicated. This photopeak corresponds to approximately 5800 photoelectrons.

7.5. Experimental configuration

The tests were allocated 4 days of beam time in the H4 beam which is located in the Northern Area, Prevesin, CERN. The beam line was served with an traversable platform which moved in x, θ, and φ under stepper motor control. The calorimeter module and calibration LED were placed inside a light-tight box on the platform. Leads which were approximately 100 m long ran from the beam-line to the control room. A series of beam defining counters intercepted the beam upstream from the experimental platform as shown in Figure 7.05. These provided *wide* beam (20×20 mm^2) and *narrow* beam (2×2 mm^2) triggers. MWPCs which enabled inspection of the beam profile were also positioned upstream.

The test beam consisted of a burst of electrons which lasted for approximately 2 seconds every 14 seconds. In between beam bursts, calibration pulses were recorded using the LED which was excited by an appropriately triggered pulse generator. A pedestal measurement was also recorded out of beam.

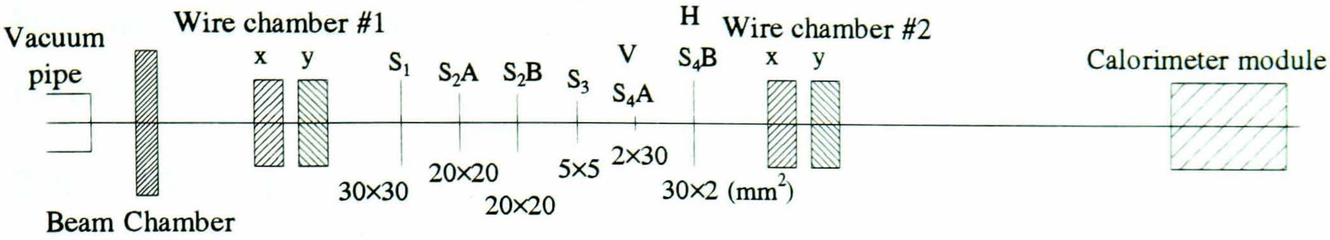

Figure 7.05 The trigger counters at the H4 beam site. Wide-beam and narrow beam counters were available. Wire chambers for inspecting the beam profile are shown, these are resolved in x and y directions.

There were two data acquisition systems available. A single channel of the CAMAC multi-channel acquisition system was used and the data saved successfully to tape. This exercise was merely to practice using the CAMAC system for later beam tests involving arrays of calorimeter modules. For the majority of the beam test work, a LeCroy qVt was used to record energy spectra from the calorimeter module. The gating arrangement is shown in Figure 7.06

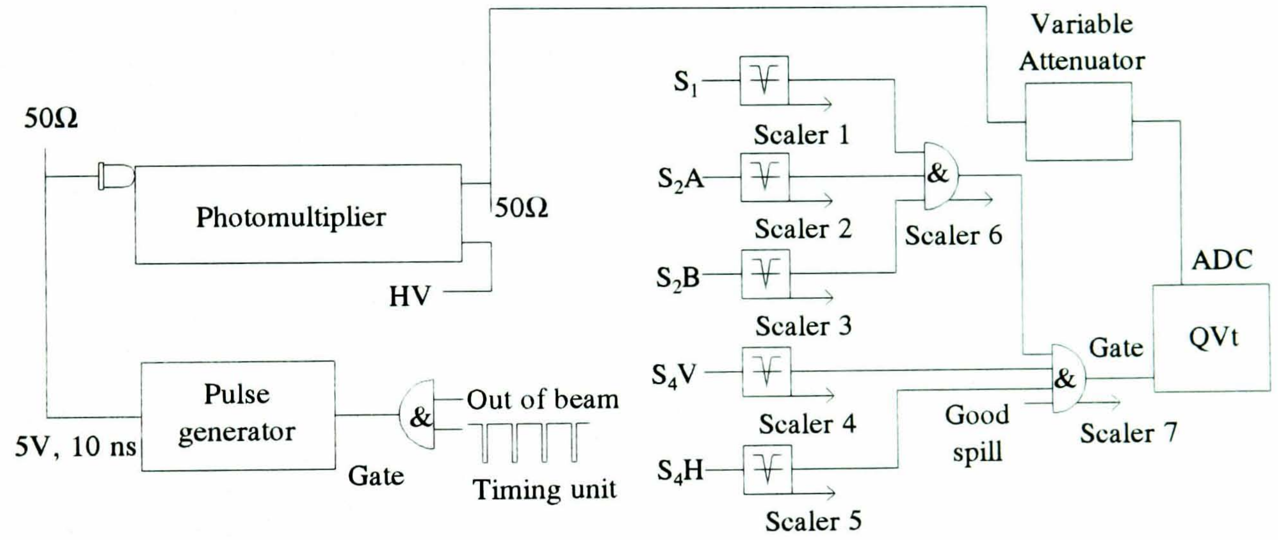

Figure 7.06 Gating arrangement for beam tests.

The photomultiplier was operated at 1500V. All experimental data collected used the *narrow* beam trigger for data acquisition. This used the logic,

$$S_1 \bullet S_2A \bullet S_2B \bullet S_4V \bullet S_4H \bullet (\text{good spill})$$

The coincident rate varied for different beam energies. The highest rate was observed with 35 GeV electrons (280 Hz). The qVt used a 500 ns gate which occurred 20 ns before the start of the output pulse from the photomultiplier. The full scale of the qVt corresponded to a charge of 256 pC. An impedance matched variable attenuator ensured that the charge seen at the qVt input did not exceed this value.

In addition to a range of electron beam momenta, the bending and collimating magnets upstream of the experimental area were tuned to produce 225 GeV muons. In contrast to high energy electrons, the minimum ionising muons deposited considerably less energy in the glass block.

7.6. Photon calibration

During all beam tests, light from a pulsed LED was incident on the photomultiplier. The LED served three purposes; to verify that the system was working, to provide a constant excitation level for cross-calibration of energy spectra and to provide the absolute calibration for the energy scale in terms of photoelectrons produced at the photocathode. The first two items were used during acquisition of beam data, calibration of the energy scale occurred out of beam. The energy scale calibration was the primary responsibility of the author, it relied on the statistical variation in the number of photoelectrons produced at the photocathode.

Consider the LED excited so that N photons are incident on the photocathode per pulse. On average, N_p photoelectrons are liberated form the photocathode. The actual number of photoelectrons varies on an event by event basis with an underlying Gaussian distribution which has a width parameter, $\sigma \propto \sqrt{N_p}$. Measuring the energy spectrum resulting from a constant excitation source gives a single Gaussian peak with a mean, μ, and a width, σ. The resolution of the peak is related to the mean number of photoelectrons, N_p by the equation,

$$R = \frac{\sigma}{\mu} = \frac{k \times \sqrt{N_p}}{k \times N_p} = \frac{1}{\sqrt{N_p}} \qquad \text{Equation 7.01}$$

The calibration involves recording energy spectra corresponding to different mean positions, μ and fitting the width, σ of each Gaussian response. The corresponding number of photoelectrons can be calculated for each Gaussian. Populating several positions uniformly across the range of the acquisition system provides a calibration of the energy scale in terms of the number photoelectrons produced at the photocathode.

In a real system, the intrinsic response broadens the width, σ_T of any measured Gaussian response. If it is assumed that the intrinsic response is dominated by random electronic noise, its distribution will be Gaussian with a width, σ_i. The intrinsic response was measured by recording an energy spectrum with no driving pulse to the LED. Subtracting in quadrature the additional width contribution, σ_i from the measured, σ_T gave the width due entirely to statistical variations in the number of primary photoelectrons, N_p.

$$\left(\sigma_{N_p}\right)^2 = \left(\sigma_M\right)^2 - \left(\sigma_i\right)^2 \qquad \text{Equation 7.02}$$

This corrected σ_{N_p} was used for the calibration. The argument presented above assumes that the width σ_{N_p} is entirely due to variation in the number of photoelectrons produced at the photocathode. This is the point in the detection process where the number of electrons which represents the size of the detected light pulse is the smallest. Therefore statistical processes will have the largest effect at the photocathode. However, statistical variations also influence the multiplication of charge at d_1 and subsequent dynodes along the photomultiplier chain. To calculate the effect of statistical variation at subsequent dynodes consider N photoelectrons produced at the photocathode. The variation in this number is equal to $\sqrt{N}$.

$$N \pm \sqrt{N} \qquad \text{Equation 7.3}$$

At the first dynode, d_1 the inter-dynode gain is δ. Therefore the number of electrons at the first dynode is

$$\delta N \pm \sqrt{\delta N} \qquad \text{Equation 7.4}$$

and at an the m^{th} dynode, the number of electrons is,

$$\delta^m N \pm \sqrt{\delta^m N} \qquad \text{Equation 7.5}$$

The statistical contributions from each amplification stage add in quadrature,

$$\left(\frac{\sigma_T}{N_T}\right)^2 = \left(\frac{\sigma_1}{N_1}\right)^2 + \left(\frac{\sigma_2}{N_2}\right)^2 + \ldots + \left(\frac{\sigma_m}{N_m}\right)^2 \qquad \text{Equation 7.6}$$

Where N_T is the number of electrons at the anode. To simplify this equation, the relation $\sigma_m = \sqrt{\delta}\,\sigma_{m-1}$ is used.

$$\left(\frac{\sigma_T}{N_T}\right)^2 = \left(\frac{\sigma_1}{N_1}\right)^2 + \left(\frac{\sqrt{\delta}\,\sigma_1}{\delta N_1}\right)^2 + \ldots + \left(\frac{\sqrt{\delta}^{\,m}\sigma_1}{\delta^m N_1}\right)^2 \qquad \text{Equation 7.7}$$

$$\left(\frac{\sigma_T}{N_T}\right)^2 = \left(\frac{\sigma_1}{N_1}\right)^2 \left[1 + \frac{1}{\delta} + \frac{1}{\delta^2} + \ldots + \frac{1}{\delta^m}\right] \qquad \text{Equation 7.8}$$

If $\delta > 1$, the expression simplifies,

$$\left(\frac{\sigma_T}{N_T}\right)^2 = \left(\frac{\sigma_1}{N_1}\right)^2 \left(\frac{\delta}{\delta - 1}\right) \qquad \text{Equation 7.9}$$

The correction factor in the equation above involving the inter-dynode gain, δ accounts for statistical variation at subsequent dynodes.

$$N_p = N_{p_{simple}} \times \left(\frac{\delta}{\delta - 1} \right)$$ Equation 7.10

This analysis assumes a constant inter-dynode gain. The dynode chain designed for use in the beam tests employed high inter-stage voltages for the first two and last three multiplication stages. Equation 7.10 could not be used because the interdynode gain was not constant. An effective correction factor was calculated for the overall operating voltage using the inter-dynode gain for each stage. The relationship between the inter-dynode gain and voltage was provided by the manufacturer [7]. The correction factor was 1.262 at 1500 V. Using a high gain first stage ($g_1 = 6$) drastically reduced the statistical contribution from the subsequent dynodes.

7.7. Beam Tests- Experimental Results

7.7.1. Calibration

Showering electrons deposit typically ×1000 as much energy in the glass block as muons. The photomultiplier was required to remain linear in its response to both electrons and muons. Figure 7.05 shows the linearity measured at three different operating voltages. For the beam tests, the operating voltage was set at 1500V to ensure that the system was linear over the required range. The attenuator was set at 16 dB for electrons and 0 dB for muons to match the output from the PMT to the qVt. These two settings required separate energy scale calibrations in terms of photoelectrons.

The 0 dB calibration obtained 145 photons per qVt channel (1024 channel scale), the 16 dB calibration recorded 850, this is equivalent to 135 photons per channel at 0 dB. These two separate calibrations are mutually consistent. Correction for the statistical variation at subsequent dynodes has been applied. The calibration graphs are shown in Figure 7.07, the calculation used to estimate the error bars is presented in Appendix 5.

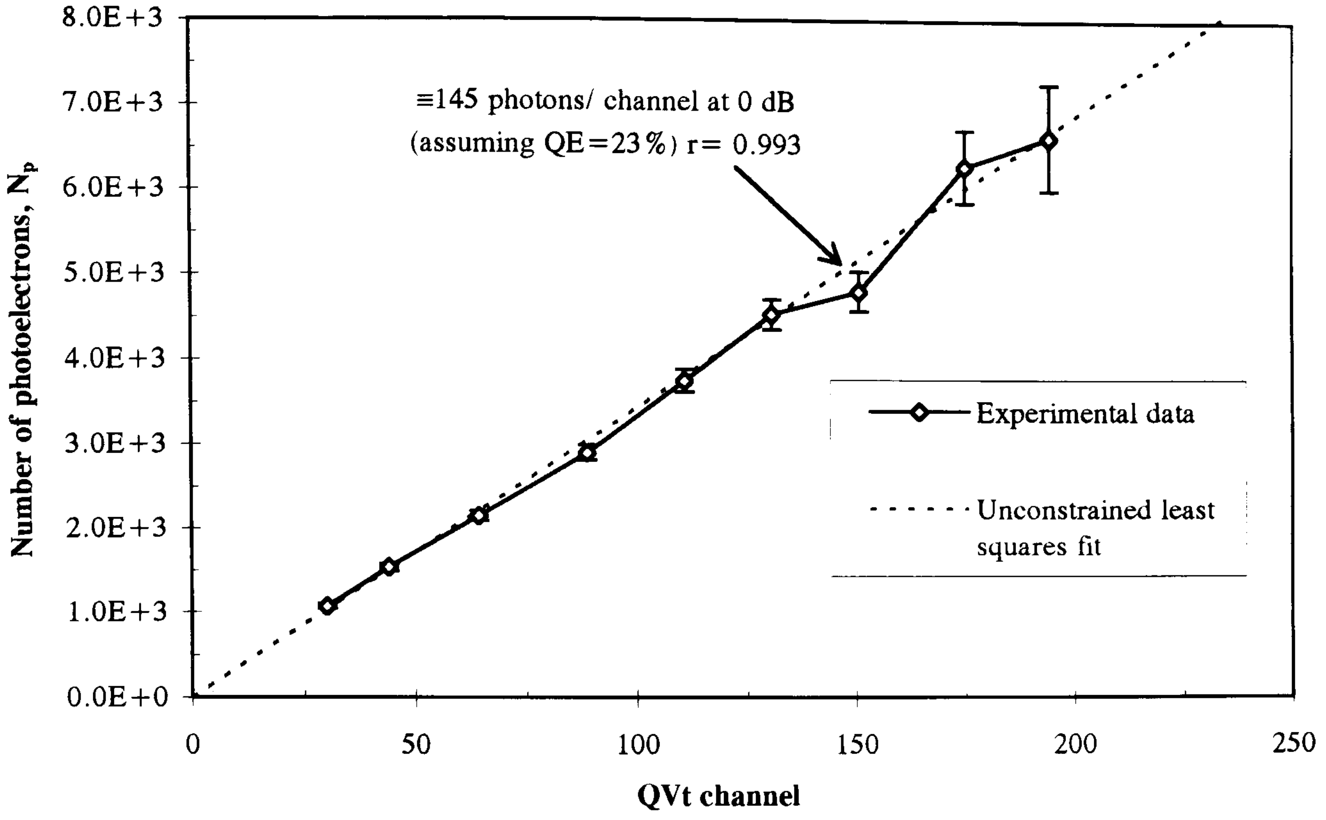

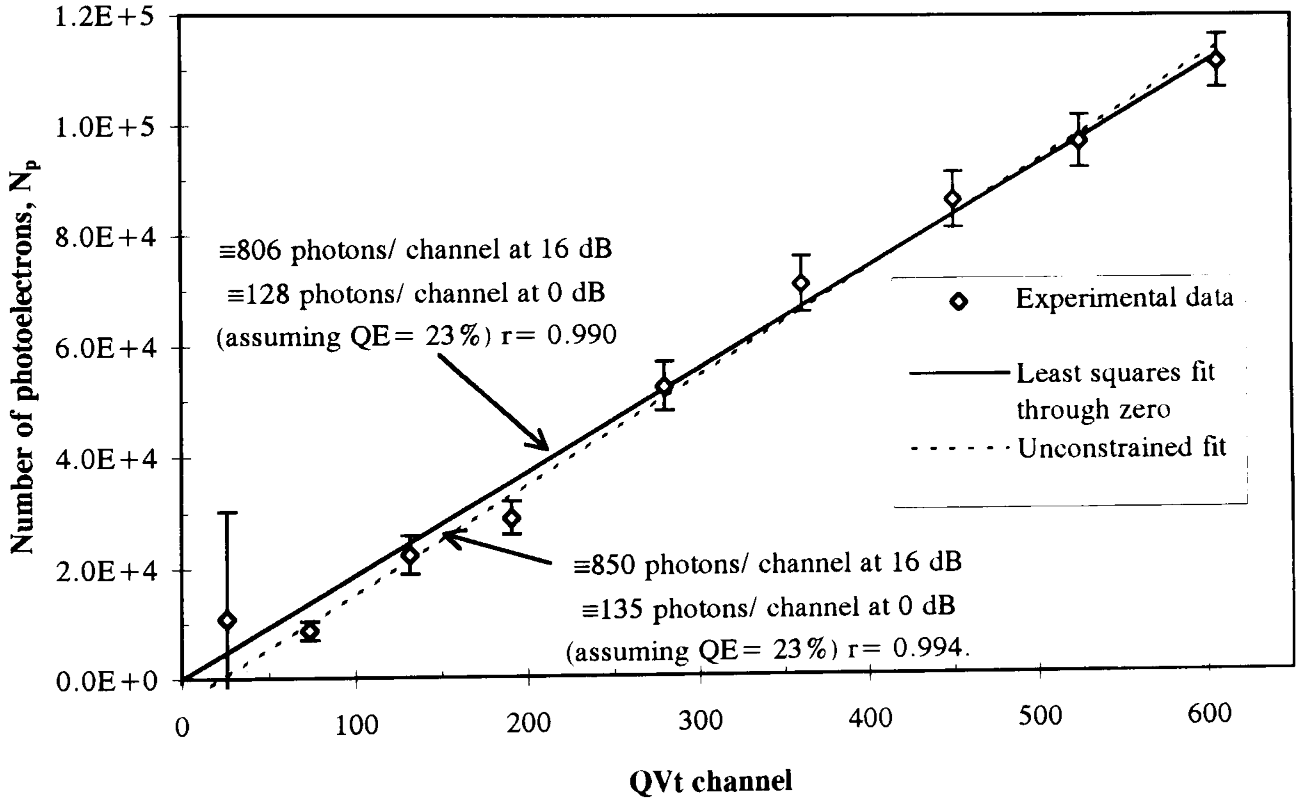

Figure 7.07 Gaussian calibration data for muons (top) and electrons (bottom). In the graphs, the gradients of the best fit lines line have been used to calculate the number photoelectrons per qVt channel).

7.7.2. Monte Carlo Simulations

During the beam tests, various different configurations were used; different lengths of glass stack, different amounts of Pb pre-shower and different beam energies. S. Potashov and P. Hobson independently simulated the various experimental situations. The data which is shown here was calculated using *GEANT 3.14 Monte Carlo*. The work assumed a monoenergetic electron (or muon) beam incident normally on the centre of the stack as indicated in Figure 7.02. Electrons were tracked through the material as were all resulting secondary electrons, photons and positrons. An electron and photon cut-off energy of 100 keV was applied in the glass and 1000 keV in the Pb.

The mean deposited energies extracted from the Monte Carlo simulations have been used for calculating the light output of the glass stack. These simulations have also been used for ensuring that the system is linear and that particles were interacting as expected.

Three different stack configurations were tested. The first was a 10 cm (6.4 X_0) stack constructed from tiles produced under oxygen. The second was also 6.4 X_0 long but was made from the optically superior *nitrogen tiles*. A 12.7 X_0 (20 cm) stack which used all of the tiles was also tested. Typical energy spectra and their corresponding Monte Carlo simulations are shown in the figures below.

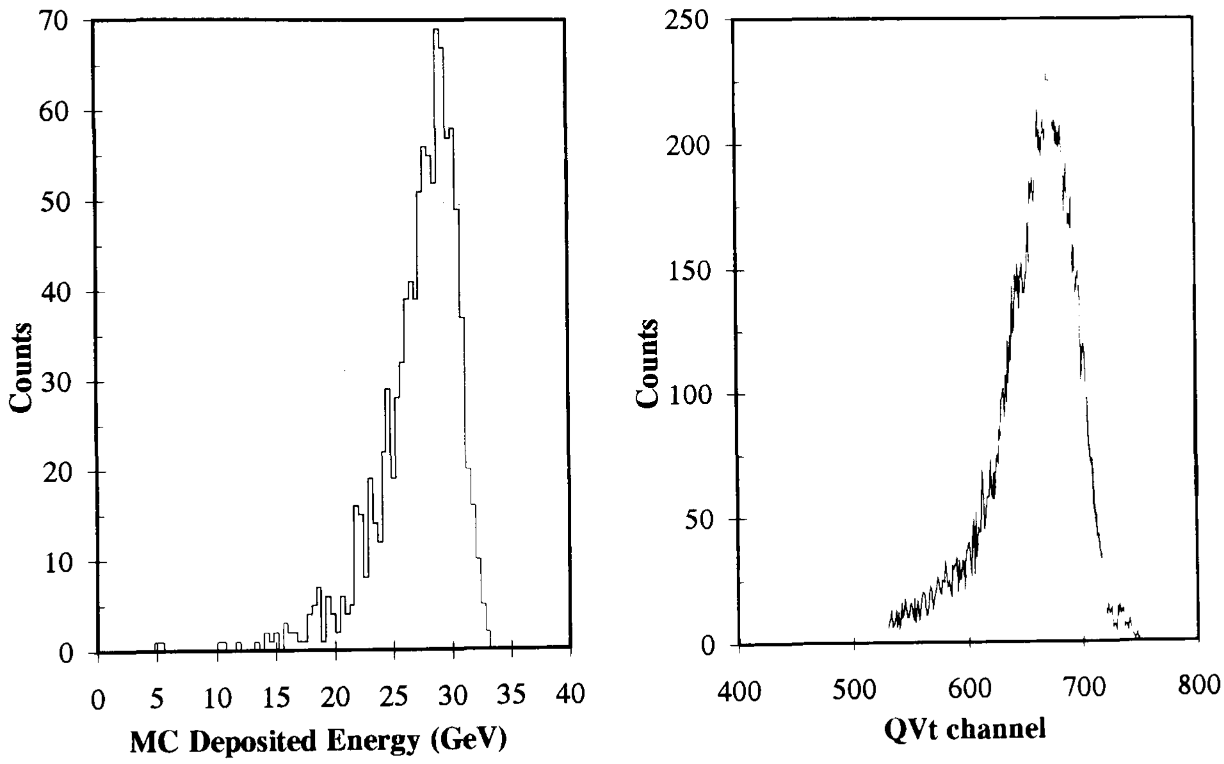

Figure 7.08 20 GeV electrons recorded using the 20 tile 6.4 X_0 nitrogen glass stack with no pre-shower. The Monte Carlo simulation is shown for comparison (left).

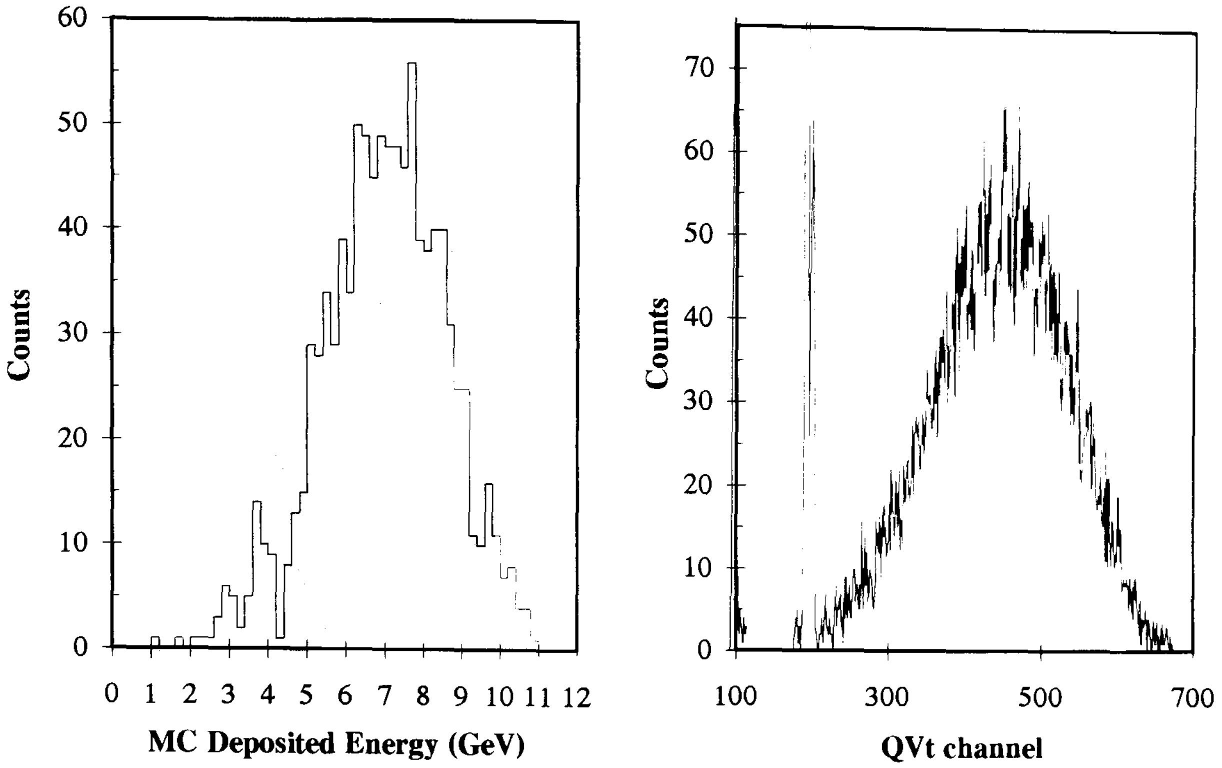

Figure 7.09 50 GeV electrons recorded using the 20 tile 6.4 X_0 nitrogen glass stack with 20.4 mm Pb pre-shower. The Monte Carlo simulation is shown (left) for comparison.

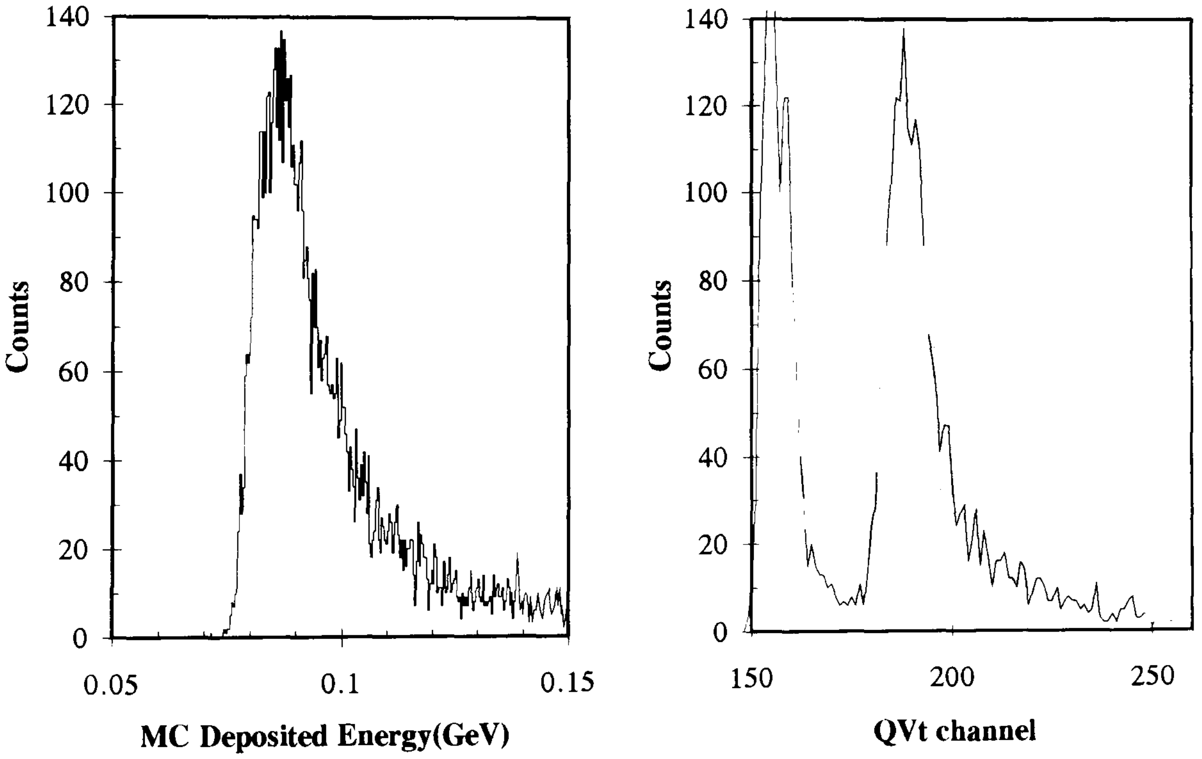

Figure 7. 10 225 GeV muon data recorded using the 40 tile 12.7 X_0 nitrogen glass stack. Monte Carlo simulation is also shown (left).

These distributions are representative of the level of agreement between the Monte Carlo simulations and the beam data. The peak positions of the distribution for the various configurations are shown in the tables below.

Beam Energy	Monte Carlo energy [GeV]	Nitrogen 6.4 X_0 glass stack [photons]	12.7 X_0 stack glass [photons]
225 GeV muons	0.086	3045	4495
8 GeV electrons	3.50	140900	119900
20 GeV electron	6.97	254400	309200
35 GeV electrons	10.37	546200	566300
50 GeV electrons	13.58	-	753300

Table 7.01 Monte Carlo and test beam data (no pre-shower).

Beam Energy	Monte Carlo energy [GeV]	Oxygen 6.4 X_0 glass stack [photons]	Nitrogen 6.4 X_0 glass stack [photons]	12.7 X_0 glass stack [photons]
225 GeV μ^-	0.086	-	-	5220
8 GeV e^-	4.80	-	146400	59500
20 GeV e^-	11.59	155900	379700	172900
35 GeV e^-	19.65	305100	645000	346100
50 GeV e^-	27.22	386600	857000	513300

Table 7.02 Monte Carlo and test beam data (20.4 mm pre-shower).

Beam Energy	No pre shower		20.4 mm pre shower		40.8 mm pre shower	
	N_p [photons]	MC [GeV]	N_p [photons]	MC [GeV]	N_p [photons]	MC [GeV]
225 GeV muons	4495		5220		-	
8 GeV electrons	119900	6.402	59500	5.30	-	2.09
20 GeV electron	309200	15.45	172900	14.30	54000	6.62
35 GeV electrons	566300	26.44	346100	25.65	122600	13.09
50 GeV electrons	753300	37.13	513300	37.10	210400	20.03

Table 7.03 Monte Carlo and test beam data for the 40 tile stack.

Figure 7.11 demonstrates clearly that the mean deposited energy of the experimental distributions are linearly related to those predicted by the Monte Carlo simulations to within experimental limits (±5%). This figure also shows that the *oxygen tiles* have a lower yield than the equivalent stacks which were made from only *nitrogen tiles*. This is due to the inferior optical transmission of the *oxygen* glass as shown in Figure 7.01. The stack which was 12.7 X_0 long had the poorest yield of the three. The inclusion of many tiles with extremely poor transmission, and the large number of interfaces, appears to attenuate the scintillation light significantly.

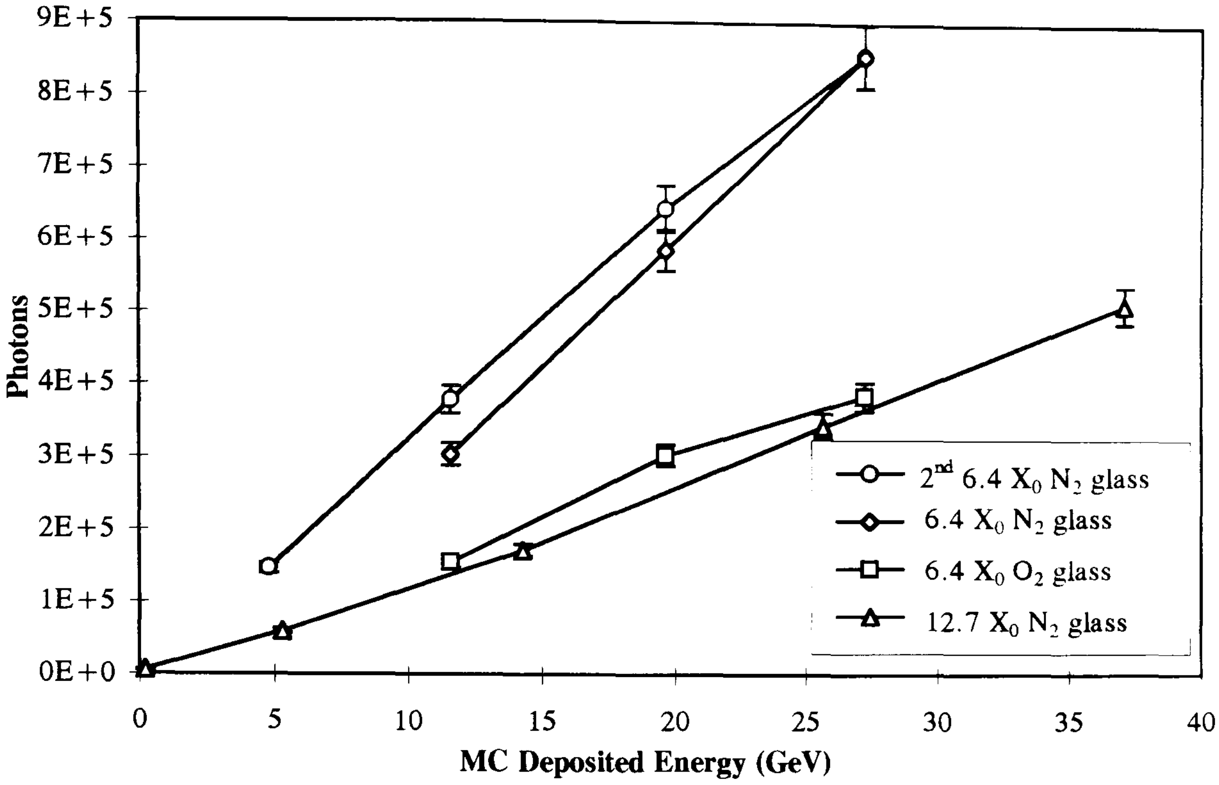

Figure 7.11 Photon yield of the various glass stack configurations versus MC deposited energy. The 20 tile *nitrogen stacks* had a higher yield than the 20 tile *oxygen stack* which in turn has better yield than the 40 tile stack.

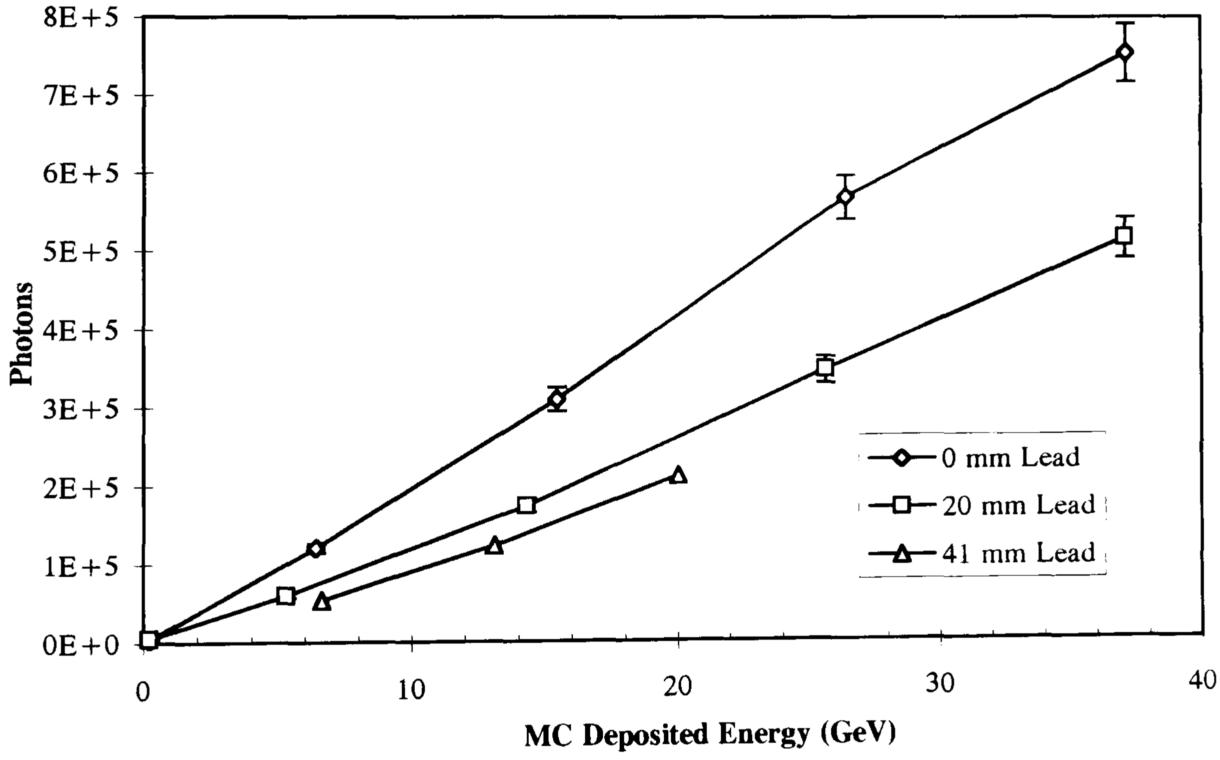

Figure 7.12 Photon yield for the 12.7 X_0, 40 tile stack for various depths of pre-shower. The data are consistent with the tiles having poor transmission drastically attenuating the scintillation light.

Further confirmation of this conclusion is neatly demonstrated in Figure 7.12. For the 12.7 X_0 stack, the apparent yield measured for different amounts of Pb pre-shower decreased in the order, 0 mm >20.4 mm> 40.8 mm. This can be explained by considering the energy deposited as a function of penetration depth in to the structure.

Firstly, with no pre-shower, the shower maximum occurs at a relatively large depth into the 40 tile stack. The maximum amount of light is produced near to the photomultiplier in the region which contains tiles with the highest transmission. The highest light yield is recorded as forward scattered scintillation light is collected efficiently.

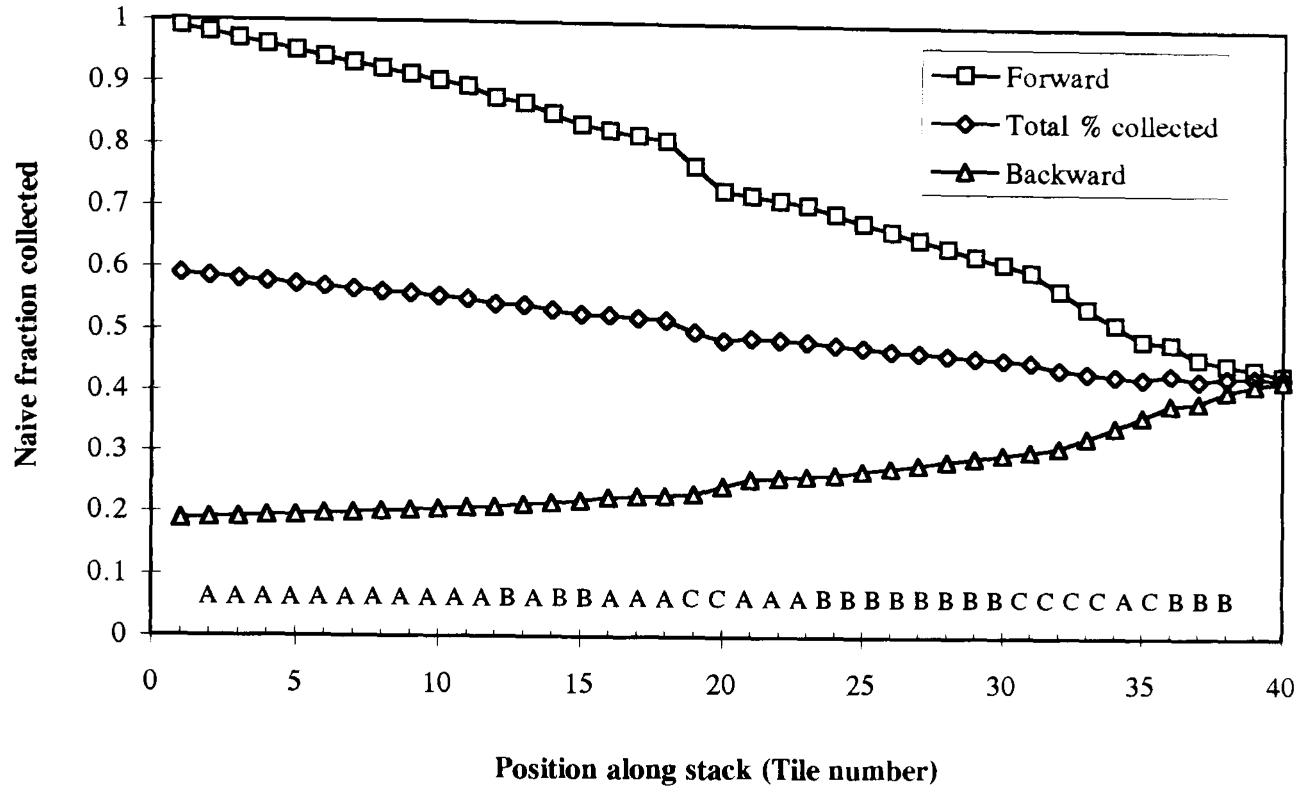

Figure 7.13 The transmission ratings for the tiles are shown in their position in the 40 tile stack. These ratings were used for the light collection calculation. The graph shows the naieve % of light collected as a function of interaction point in the stack. The average is composed of forward and backward emission directions which are also shown individually.

In contrast, when the 40 tile stack has 20.4 mm of Pb pre-shower, the shower maximum occurs further from the photomultiplier. The forward scattered scintillation light has to pass through a further 57 mm of glass. This additional path results in a further reduction of the measured light yield.

Scintillation light emitted directly away from the PMT window will be heavily attenuated. An extremely simple model has been written to obtain some feeling for the collection efficiency of scintillation light as a function of position in the 40 tile glass stack. The model assumed that all scintillation light was deposited in a single tile, half of the light was directed towards the photomultiplier. The other half was emitted in the opposite direction. In traversing each tile, the scintillation light was attenuated according to the simple transmission rating of that tile. Scintillation light emitted in the forward direction in tile *n* would pass through tiles *n*+1, *n*+2, ..., 40. Backward emitted light would pass through n-1, n-2, ...,1,1,2,...,n, n+1, ...,40. The return trip which backward emitted scintillation light experiences is equivalent to an extra passage along the entire length of the block. An end reflection of 100% was assumed. Results from this over-simplistic calculation are shown in Figure 7.13.

7.7.3. Best Yield Estimates

The largest light yield was measured for the 20 tile nitrogen stack which suffers least from the intrinsic transmission of poor tiles. Even by selecting the 20 tiles which had the best transmission, it was still necessary to use 4 tiles which suffered a 2% loss in transmission over a 5 mm path. These add up to a total attenuation of 8%. Figure 7.13 gives some feeling for the effect that these bad tiles have on the measured light yield. The actual best yield from these beam tests corresponded to 37 photons per MeV.

The 2" photomultiplier did not match the exit window of the glass block (40× 40 mm^2) perfectly. If the scintillator is placed centrally on the photomultiplier, 10% of the glass block (the corners) overhang the PMT window. This inevitably leads to further loss of light, possibly 10%.

7.8. Summary

A yield of 37 photons per MeV may initially sound somewhat disappointing. This is less than half of the yield measured for small test samples of this glass at the Rutherford Appleton Laboratory. However, there were several factors which reduced the yield in the experimental arrangement,

1) The tiles were optically coupled with a viscous (300,000 cSt) grease. Despite great care, air bubbles were inevitably incorporated at some interfaces. These bubbles acted as scattering centres for scintillation light.

2) The poor intrinsic transmission of some tiles used for this work caused a significant reduction of the measured light yields. Their effect is minimised by placing the poor tiles at the front end of the stack furthest from the PMT. However, the simple light transport model demonstrates that they still have a profound effect on light collection. It is recommended that future beam tests exclude any glass which is as poor as those falling in the groups 'C' or 'D' of the present classification.

3) The tiles were cast in a rectangular mould, contraction at the top surface during cooling resulted in a distorted top edge. This irregular portion was cut off each tile using a diamond impregnated cutting disk. The trimmed tiles were 40× 40× 5 mm^3. Five of the sides were reasonably flat due to the surface of the mould. The machined edge was also flat but severely scratched due to the cutting marks left by the abrasive disk. No additional polishing of the tiles used for the beam test was undertaken. All of the tiles were aligned so

that the rough edge of each tile was presented to a single face of the composite glass block. This poorly reflecting surface inevitably caused a further reduction in the measured yield.

4) Mis-match of the PMT to the output face of the glass block could be responsible for up to 10% reduction in yield, the diameter of the photocathode was only 43 mm.

5) The glass had a refractive index of 1.505, the corresponding figure for the optical coupling grease was 1.405. This mismatch would have caused significant multiple reflection of scintillation light in the current stack configuration due to the large number of interfaces.

The deficiencies summarised above are not impossible to rectify. Using only good tiles, glued together with a 'bubble-free', index matched adhesive would improve the mechanical stability. It would then be possible to grind and polish the exterior surfaces flat and wrap the block in *Millipore* [4] paper which is currently excluded due to the adverse reaction with DC200 grease. A physically matched detector system can be envisaged.

Since the beam tests, further research into the production process has increased the maximum block size of a single ingot. The 'minimum dimension' is currently 20 mm. 130× 30× 10 mm^3 rods and 50× 30× 20 mm^3 blocks can be produced with an acceptable success rate. Beam tests using glass blocks of these dimensions were carried out in September '94 (the author made no contribution). The yield using single blocks increased to 90 photons per MeV [8].

---

[1] P. Lecoq, *ECAL Homogeneous Media*, May 18, 1994.

[2] P.R. Hobson and T.J. Price, *Nucl. Instru. Meth.* **A317** (1992) 315.

[3] W. Klamra et al, *Nucl. Instru. Meth.* **A254** (1987) 25.

[4] Millipore UK Ltd., Boulevard Blackmore Lane, Watford, WD1 8YW.

[5] P. Sperr, *Nucl. Instru. Meth.* **A254** (1987) 635.

[6] R. Fernow, *Introduction to Experimental Particle Physics*, Cambridge University Press (1986) p263.

[7] *Photomultipliers and Accessiories*, Thorn EMI Electron Tubes Ltd., 1993.

[8] D. Cockerill, private communication.

CHAPTER EIGHT

Conclusions

8.1. Introduction

This thesis describes work which has been carried out principally by the author. The results form part of a larger research program whose aims were to characterise the suitability of HMF glasses for the ECAL of CMS. Determining of the time structure of scintillation light and the development of radiation induced damage in these glasses have been discussed in particular detail as these studies were performed by the author. The CERN beam tests required a collaborative effort, in addition to generally assisting with the beam tests, the author was solely responsible for the LED calibrations which have been discussed in Chapter 7.

To maintain some degree of focus, no significant discussion has been allocated for the work carried out by the wider collaboration although some of their results are quoted in Chapter 6. Other additional characterisation (X_o, R_m, neutron irradiations,...) which, whilst not strictly essential to the authors work, have addressed the wider aims more fully.

8.2. Time Structure of Scintillation Light

An extension to the *single photon* method has been employed to characterise the scintillation emission of these glasses. The specific implementation has resulted from developments spanning a two year period. One photon from the positron annihilation that results from ^{22}Na decay, is detected in a trigger scintillator. The second photon excites the material under test. This scheme is especially suitable for the characterisation of materials with relatively low light yields. Detection of more than one photon is the curse of the *single photon* method as it biases all data and, in the simple implementation, is unavoidable. The system used in this work overcomes the problem by explicitly checking for conformity to the single photon condition, actively vetoing all events which result in the detection of > 1 photon.

The active veto relaxes the single photon condition and improves the data rate potentially by ×18. Whilst the active veto is better able to cope with biased data than the simple single photon system, it does cause two alternative types of low-level corruption to the parent data. The first arises from the biased detection of random scintillation events due to their underlying time structure. The second is caused by the finite two photon resolution of the veto circuit. These two separate sources of corrupted data have been satisfactorily explained and modelled in terms of adjustable parameters of the system (Poisson mean number of detected scintillation photons, μ, rate of uncorrelated events, R_{un}, and the Dead Time of the veto circuit, *DT*). Biased data can be suppressed to a significant degree by careful selection of the relevant parameters.

It is advantageous to minimise the detection of uncorrelated events by good experimental design, and to maximise the interaction probability of correlated 511 keV photons in the trigger and test scintillators. The best possible two pulse discrimination should be used, in the present work this is limited to ≈ 8 ns due to the width of (and the timing jitter in) the pulse from the single-photon PMT which detects scintillation light from the test material. The timing data presented in this thesis is not significantly affected by these two potential sources of bias.

The experimental timing data is described satisfactorily by a maximum of three superimposed decaying exponentials. Fitting parameters to the mathematical equation that describes the timing data is a precarious procedure which has a potentially large scope for error. Due to the complexity of the underlying data, no analytical solution has been identified. An iterative procedure that minimises a multi-nomial χ^2 function has been successfully employed. Careful monitoring of the results, comparison of the fit with the parent data, and considering the χ^2 are all essential in assessing the accuracy (or otherwise) of the equation which describes the data. Using sensible initial estimates for the parameters, the optimal solution can be identified on an acceptable time scale. Poor initial estimates can result in non-optimal solutions being pursued, ultimately the routine becomes 'lost' in the variable space and returns an inappropriate solution corresponding to a local minimum. The procedure can fail to distinguish two exponential components that have time constants which are very similar (2 ns or equal within 10%, which ever is the greater). These potential weaknesses mean that it is unwise to accept a solution without first inspecting the residuals.

The experimentally determined time constants and amplitudes from a range of commercial scintillators have been presented, with the accompanying fits. No significant deviation has been observed from the expected results. Timing studies have shown that the results for Cerium doped fluoride glasses are similar to the scintillation emission from crystalline CeF_3. The glasses have two principal time components, the shorter has a time constant of $6 \leq \tau \leq 15$ ns, the longer component has a time constant of $20 \leq \tau \leq 35$ ns. For a given glass, a small value for τ_1 is accompanied by a small τ_2 and vice versa. This is genuine feature of the glasses and is not intrinsic to the acquisition or the fitting procedure as in non-Ce doped glasses, the time constants show no degree of correlation. The emission spectrum of a Ce doped HMF glass has been recorded as described in Appendix 1. The X-ray excited emission spectrum was observed between $300 \leq \lambda \leq 350$ nm.

Results presented in Chapter 6, concerning the time structure of scintillation light in fluoride glasses, is consistent with the scintillation emission having two components. Is has been concluded that the faster emission is in the vicinity of the UV edge (≈300 nm) because this component is suppressed in radiation damaged glasses and large samples. The slower component is less strongly attenuated in radiation damaged glasses as it is emitted at longer wavelengths (< 350 nm). The upper limit on the wavelength of the slow emission comes from the measurement of the emission spectrum.

In addition to the spectral dependence which has been inferred from experimental data, it has also been noticed that additional dopants tend to enhance the ratio of the fast: slow emission. A plausible explanation for this behaviour is that the additional dopants act a quenching centres, reducing the time constants of the emission at the expense of the light yield. No evidence was observed that definitively correlated the time structure with the amount of Ce present in the glasses There is some suggestion that glasses containing higher concentration of Cerium exhibited faster scintillation emission.

8.3. Radiation Damage Studies

A ^{60}Co facility at Brunel University was used for all of the gamma radiation damage studies. A reasonably constant irradiation rate (1.2 rads^{-1}) was used for all glasses, although depletion of the source with time over the period of measurements (2 years) accounted for a worst-case 10% variation. The lower density (silicate and zirconate) glasses attained dose rates of 1 and 1.1 rads^{-1} respectively. These exceed the anticipated dose rate at the LHC by approximately ×1000.

Optical absorbance measurements were recorded as a function of dose although it was not possible to maintain an identical schedule for every glass. Measurements were also recorded as a function of time after the irradiation had ceased. An analytical approach that enabled the different glasses to be compared on an equal basis was undertaken. The radiation induced absorbance at a given wavelength was adequately described with a single growing exponential which eventually saturated. The parameters of the exponential (saturation level, and growth constant) were fitted using measurements at five or more dose levels. The uncertainty in the absorbance measurements (±0.002 OD) detracted from the fit, especially in particularly radiation resistant glasses.

Optical absorbance measurements were not consolidated with more definitive ESR work as the primary motivation was to survey the radiation damage in a wide variety of different glasses. ESR studies are normally used to identify the cause of radiation damage in a specific composition.

The optical characterisation identified specific elements which improved the radiation tolerance of these glasses. Indium has the most pronounced effect which extends to a lower wavelength of 300 nm, Ce, Ga, Gd and Eu also improve radiation hardness above 400 nm although their effects are not cumulative. Elements which lead to additional damage have also been identified, these include most lanthanides and Li. Variations in production atmosphere and material purity have both caused changes in radiation hardness of these glasses. The most radiation resistant glass currently identified, HBCeIn, was produced under an oxidising atmosphere using ultra-pure materials. It suffered radiation induced absorbance immediately after irradiation which was a factor ×20 too high for the LHC application. This result was initially disappointing. The subsequent annealing of these glasses at room temperature displayed a stretched exponential behaviour. After a period of 1 year the induced absorbance in the most radiation resistant sample was only a factor of five too high for the LHC.

In addition to further compositional optimisation, the feasibility of optical annealing is being investigated. Practically 100% recovery of optical absorbance has been observed in some non-Indium doped glasses illuminated directly with a Hg arc lamp. This 'annealing' experiment has demonstrated the procedure, however direct annealing is not feasible for the LHC. A more realistic scenario is optical annealing down ≈ 3 m of quartz optical fibre. Investigations to demonstrate optical annealing of a large glass block by light via a 30 m fibre is currently being pursued. Raising the temperature of a damaged HMF glass to 450 K causes relaxation of all defect centres which result in optical damage. This method has not been investigated in the current work because it is not a realistic option for a detector at the LHC.

It seems likely that recovery at room temperature coupled with periodic annealing using UV light via an optical fibre, could provide glasses with sufficient radiation tolerance for the LHC. The CERN winter shut-down which lasts for ≈ 4 months from December to early April would provide an ideal window in which to counteract the induced damage resulting from the previous eight months high-luminosity running.

A comprehensive study of a wide range of HMF glasses has resulted from collating information from the wider collaboration. The research is continuing despite the contribution of the author coming to an end, whilst the glasses presented here fail the stringent list of CMS criteria, there is no evidence to suggest why a suitable composition will not be identified as a result of further work. The measured properties are summarised in the table below,

Property	CeF_3	$PbWO_4$	HfF_4 Glass	Pb/ Scint
Radiation length cm	1.7	0.9	1.6	1.7
Molière radius cm	2.6	2.0	2.8	3.4
Density g/cm^3	6.2	8.3	6.0	4.5
Photon Yield γ/MeV	1500	70	100	13
τ (short) ns	9	≤10	8-13	≤10
(long) ns	32	36	20-33	-
% Light in 25 ns	50	90	60-70	≈ 100
Peak wavelength nm	325	440,530	325	500
Temp.dependence of light yield %/°C	0.15	-1.9	-0.39	-
Index of refraction	1.6	2.2	1.5	-
Radiation Hardness Mrad	≈10	≥ 2	< 0.05	1
Vol. for 25 X_o, $\lvert\eta\rvert \leq 2.5$ m^3	26.3	12.5	24.5	26.3

Table 8.01 Properties of the potential CMS ECAL materials.

Further optimisation is continuing directly from these studies. A three month programme of work with Johnson Matthey has recently commenced, the aim is to identify the acceptable levels of the various impurities in the hafnium fluoride. This will definitively answer whether or not the less expensive HfF_4 can be used for the glasses. The problem of large sample size is being studied by a collaboration involving RAL, Sheffield University and

Merck. 2 cm thick samples can now be produced reliably, this coincides with a revised segmentation of the CMS ECAL from 4 cm at the end face to 3 cm. A scintillation light yield of approximately 10% CeF_3 has been observed for HMF glasses doped with 8 to 10% CeF_3, the yield scales approximately with the proportion of Ce. The fraction of light collected in 25 ns is acceptable for CMS, as are the Radiation length, X_o, the Molière radius, R_m and the density, ρ. Cost is an essential parameter of paramount importance in a detector which is under tight financial constraints. The predicted cost of the finished HMF glasses may marginally exceed $1-00 cc^{-1}.

The CMS Technical board have recently (Oct '94) decided to choose $PbWO_4$ as the material for the ECAL of CMS. Specific research into the other options (CeF_3 and HMF glasses) as candidate materials for CMS will diminish over the next 12 months. It is worth noting a point made recently in the light of this choice, the next generation of detectors designed for higher energy accelerators beyond the LHC (if they are built) will not be able to use crystals for their homogeneous calorimeters. The large number of radiation lengths required to contain showers will exclude the use of single crystals. It is inevitable that glasses will have to be given a higher profile when the potential candidates are evaluated. It is possible that glasses will be the only material from which a homogeneous calorimeter could be produced.

Appendix 1

Measurement of X-ray excited Emission Spectra

A Philips X-ray set model, PW1720, operating at 40 kV, 35 mA was used excite small samples of test material. For all of this work a Cu target was used, the diameter of the X-ray collimator was widened to 5 mm to maximise the number X-rays incident on the sample. A typical emission spectrum from a Copper X-ray tube is shown in Figure A1.01. Scintillation light would be emitted from only the irradiated surface as the low energy X-rays are not strongly penetrating.

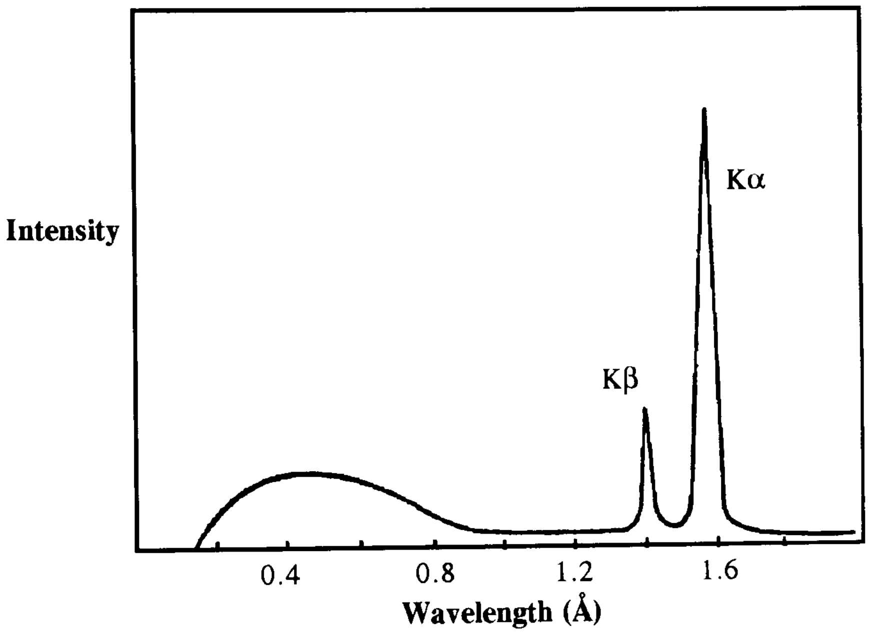

Figure A1.01 A typical emission spectrum from a Copper X-ray tube showing characteristic emission of Cu K lines superimposed on a continuous spectrum [1].

To collect a large fraction of the scintillation light, the sample was placed at one focus of an ellipsoidal mirror which was surface coated with Rhodium, the entrance slit of a Chromex monochromator was at the other focus as shown in Figure A1.02. An Alton Instruments Lamda LS2000 PCCD photodiode array incorporating an internal Peltier Cooler was used to record the emission spectra. The linear array which consisted of 2000 closely spaced photodiodes was placed in the focal plane of the monochromator.

The software package that interfaced with the photodiode array enabled adjustment of the exposure, and provided features to manipulate the parent data, these included rebinning, averaging several frames, summing several frames and a moving average function. Cooling the array by 10°C reduces thermally generated dark counts by a factor of ×2 [2]. Operation at 0°C reduced the noise by ×4 compared to operation at room temperature (20°C).

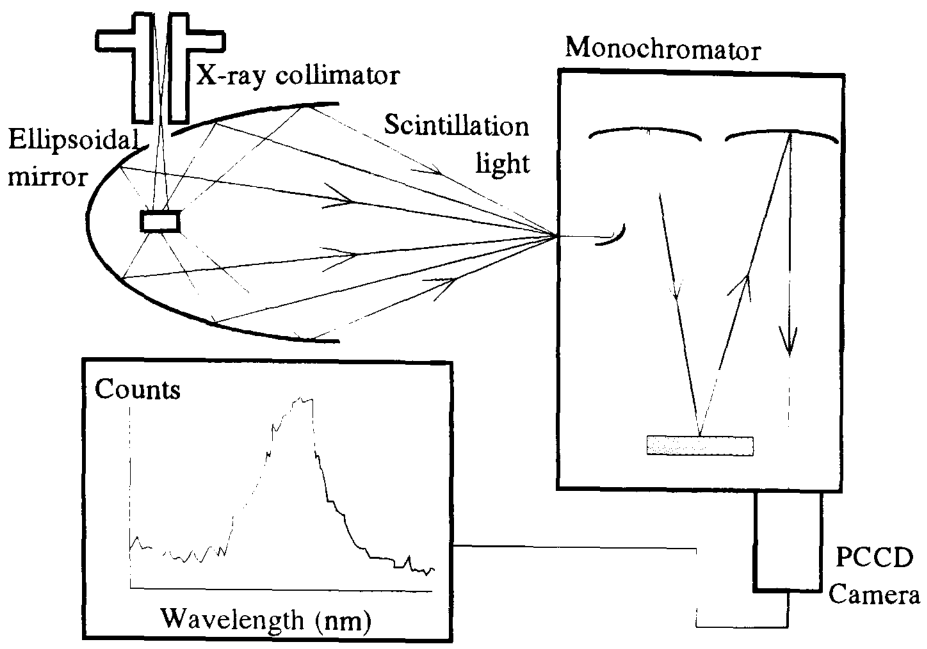

Figure A1.02 The experimental apparatus used for measuring emission spectra.

The system was calibrated using the characteristic lines from a Hg discharge lamp. The emission spectra for a range of commercial scintillators were then recorded. The widest Chromex aperture setting (2000 µm) was used. Care was taken to optimise optical collection but even using the most coarse grating (3 nm/ pixel), the *signal: background* was extremely poor. The results for BaF_2, CsI(Tl), and NE110 are shown in Figure A1.03.

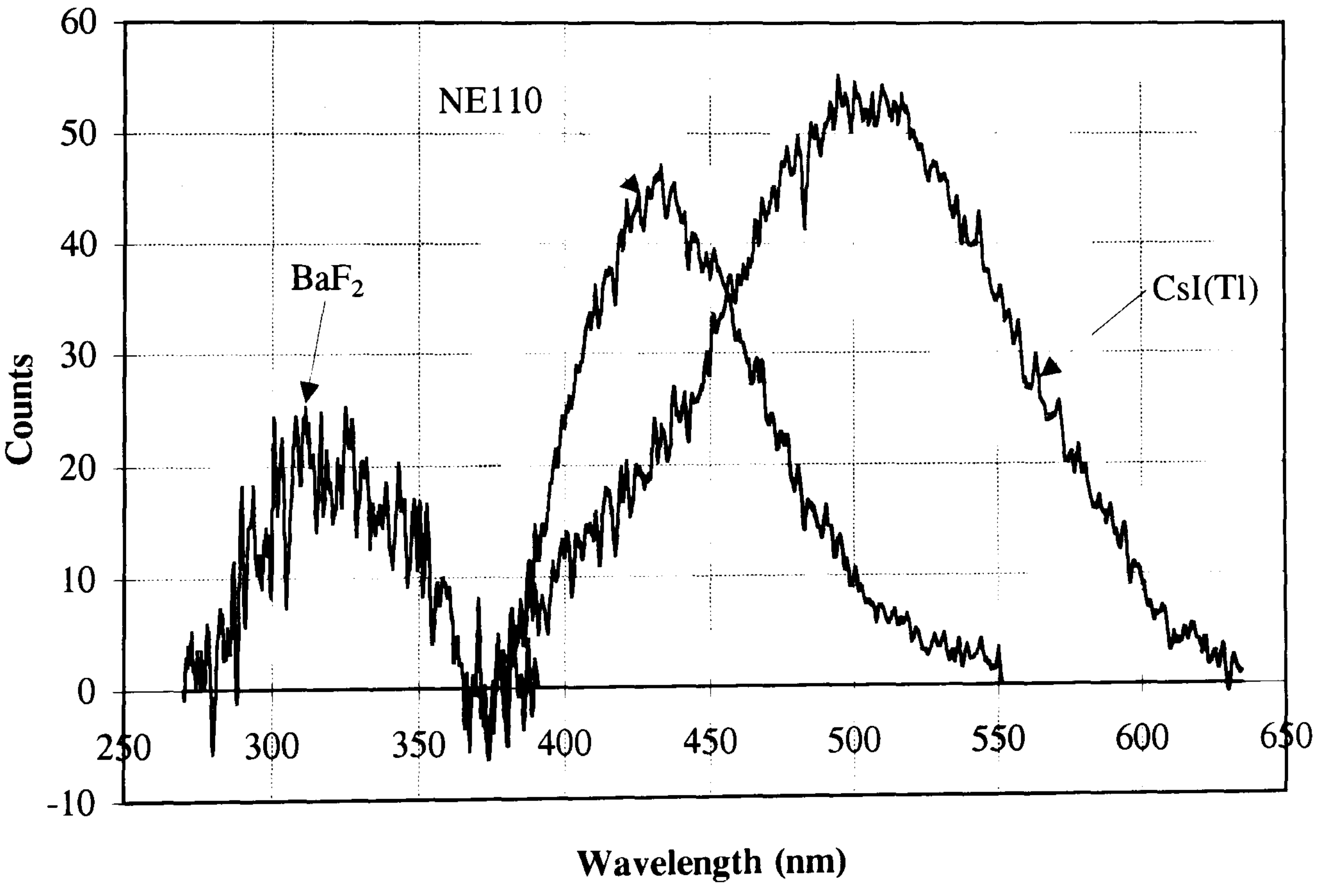

Figure A1.03 The X-ray excited emission spectra measured for several commercial scintillators.

The background noise has been subtracted in each case and a correction for the variation of photodiode QE as a function of wavelength has been applied [2]. These graphs were recorded using the average of 100, five second exposures, a moving average of five channels was used to smooth the data. Despite significant statistical fluctuations which result from the small signal superimposed upon a large background, the emission spectra for the commercial scintillators, BaF_2 [3], CsI(Tl) [3], and NE110 [4], were as expected.

A factor which complicated the data acquisition was a variation in the background level as a function of time. This made automatic background subtraction inaccurate. The variation was consistent with thermally generated noise which resulted from the temperature of the photodiode array ramping up and down. The temperature is controlled by a thermostat which maintains the externally set target temperature (0°C).

The quoted light yields for the commercial scintillators tested are typically $\approx 10^4$ γs/MeV. In contrast the fluoride glasses have yields of $\approx 10^2$ γs/MeV. Many attempts were made to record the emission spectrum of a fluoride glass containing Cerium. Only one spectrum which contained a signal above the background was successfully recorded. This is displayed in Figure A1.04, although because it could not be readily repeated, there is scope for questioning its authenticity. There are three factors which link the feature with the emission spectrum of Cerium in the glass:

- The spectrum was not observed in any spectra which contained no fluoride glass.
- The feature is in the spectral region, $300 < \lambda < 350$ nm which is similar to crystalline CeF_3, the similarity between scintillation light in Ce doped fluoride glasses and crystalline CeF_3 has been consistently stated in this thesis.
- The ratio of the integrated areas, Fluoride glass: NE110 is consistent with their relative light yields.

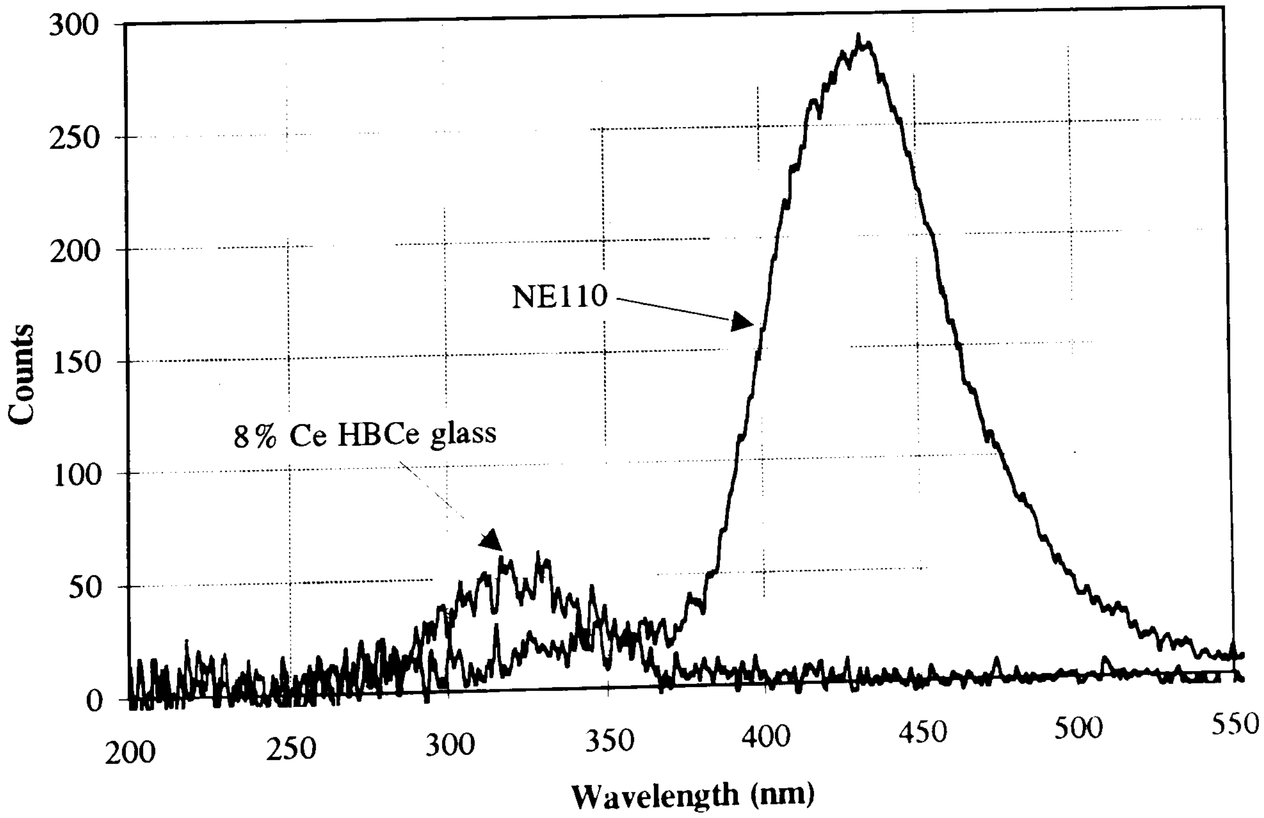

Figure A1.04 The emission spectrum of NE110 and a Ce doped fluoride glass.

[1] I. Adler, *X-ray Emission Spectrography in Geology*, Elesevier Publishing Co. (1966) p10.

[2] Lamda LS-2000 Series Technical User Manual, Alton Instruments AI Corporation Cal. 92714, USA.

[3] *Scintillation Detectors*, Harshaw (1992).

[4] *Scintillation Materials*, NE Technology.

Appendix 2

Small Sample Light Yield: Rutherford Appleton Laboratory

The light yields presented in Table 6.01 were measured by R.M. Brown *et al* at the Rutherford Appleton Laboratory using minimum ionising protons to excite the glass samples. A charged-particle test beam facility at RAL uses a parasitic internal target in the proton synchrotron accelerator of the ISIS neutron spallation source. This beam line was tuned to a momentum of 750 MeV/c, determined by examining the time-of-flight difference between protons and deuterons.

A schematic diagram of the experimental arrangement is shown in Figure A2.01. Two small counters immediately before and after the sample define the beam. They are larger than the sample hence a pedestal arises from events which intercept the counters and not the glass. To prevent spurious signals from particles passing through the body of the counter system, a large veto counter shadowed the whole sampling system except the hole chosen to match the defining counters. Scintillation light is collected using a Thorn EMI 9814QKB photomultiplier. The PMT is not directly coupled to the glass sample to prevent protons intercepting the PMT. An Aluminised Mylar cylinder is used as a light pipe to ensure adequate collection efficiency.

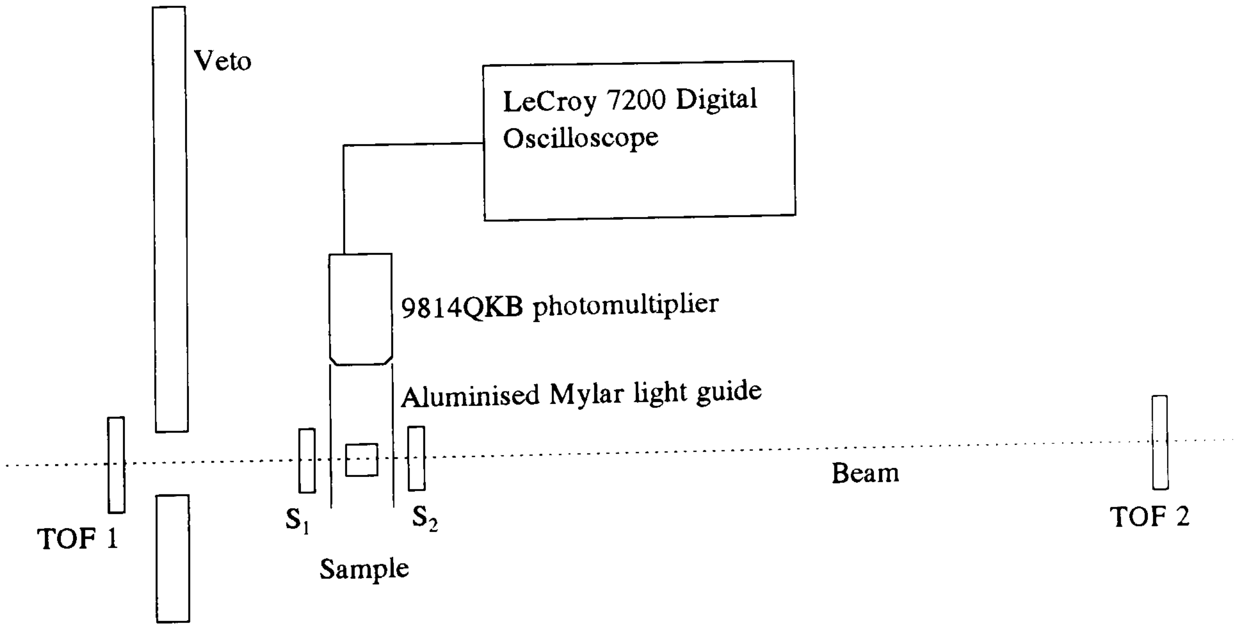

Figure A2.01 Apparatus used for measuring the relative light yield of scintillators.

The PMT signal is recorded using a LeCroy 7200 digital oscilloscope which achieves a 1Gs/sec sampling rate by interleaving two 500 Ms/sec ADCs. The oscilloscope is triggered by a signal derived from the veto, the two small counters and the TOF counters,

$$\text{Trigger} = \overline{Veto} \bullet S_1 \bullet S_2 \bullet (TOF = p^+)$$

The oscilloscope is configured to average 50,000 triggered events, due to the rate of beam hits in the glass, the data takes several hours to record. By using a Peltier cooler, this apparatus has also been used to record the temperature dependence of light output. The average of 50,000 events can be used to determine the time structure of scintillation light and also the relative light yield.

Relative light Yield

The mean integrated pulse height is calculated from the distribution of the 50000 events. To measure the relative yield, several reference were samples used, an Optovac 1 cm^3 crystal of Cerium Fluoride, a Thallium doped Sodium Iodide crystal and a 1 cm^3 cube of NE110 plastic scintillator. Some of their properties are collected together in Table A2.01.

Material	Light yield (γ/MeV)	spectral region, (QE of tube)	$(1/\rho)dE/dx$ (MeV/(gcm^{-2}))	density (gcm^{-3})	Thickness (mm)
NaI(Tl)	38,000	415, (23%)		3.67	-
CeF_3	1,600	320, (20%)	1.41	6.19	10
NE110	10,000	434, (23%)	1.95	1.032	10

Table A2.01 Physical properties of the reference samples used for light yield measurements.

To normalise the yield of one sample relative to another it is necessary to consider their relative pulse heights, the energy deposited by the proton in each sample and to account for the QE of the PM tube for the spectral emission of each. The following equation is used,

$$\frac{LY_{Glass}}{LY_{Ref}} = \frac{p.h._{Glass}}{p.h._{Ref}} \times \frac{\rho_{Ref}}{\rho_{Glass}} \times \frac{\left(dE/dx\right)_{Ref}}{\left(dE/dx\right)_{Glass}} \times \frac{QE.factor_{Ref}}{QE.factor_{Glass}} \times \frac{thickness_{Ref}}{thickness_{Glass}} [\%]$$

Equation A2.01

The physical parameters for a typical HMF glass are calculated from the composition, for example, the glass HBCeAl has the composition,

	HfF_4 (57%)	BaF_2 (34%)	CeF_3 (5%)	AlF_3 (4%)
Molecular weight (g)	254.49	175.33	197.11	83.98

Table A2.02 The molecular weights of the fluorides used to make P13, HBCeAl.

Mean Molecular weight = 217.89 g

Density

Density = $(0.57\times6.74)+(0.34\times4.89)+(0.05\times6.16)+(0.04\times2.88)$

= 5.93 gcm^{-3} (compared to 5.92 gcm^{-3} measured)

Composition by weight

Element	Amount	(1/ρ)dE/dx	Reference
72 Hf	46.69%	1.16	(74 W)
56 Ba	21.43%	1.24	(54 Xe)
58 Ce	3.22%	1.24	(54 Xe)
13 Al	0.50%	1.62	
9 F	28.17%	1.78	(0.5 (8 O + 10 Ne))

Table A2.03 The radiation length of the various components which make up P13, a HBCeAl, fluoride glass.

Mean (1/ρ)dE/dx= 1.36 $\mathrm{MeVg^{-1}cm^{-2}}$

Radiation length

$$X_o = \frac{1}{5.93}\left(\frac{0.005}{24.01}+\frac{0.2143}{8.45}+\frac{0.2817}{33.16}+\frac{0.4669}{6.91}+\frac{0.0322}{8.08}\right)^{-1}$$

$$= 1.60 \text{ cm}$$

Results

R.M. Brown *el al* have measured the relative light yield for a range of HMF glasses, the values (relative to CeF_3) are presented in Table 6.01. The graph below summarises the results. It shows that the light yield scales approximately with the mol% of CeF_3. The lines connect glasses which have similar compositions.

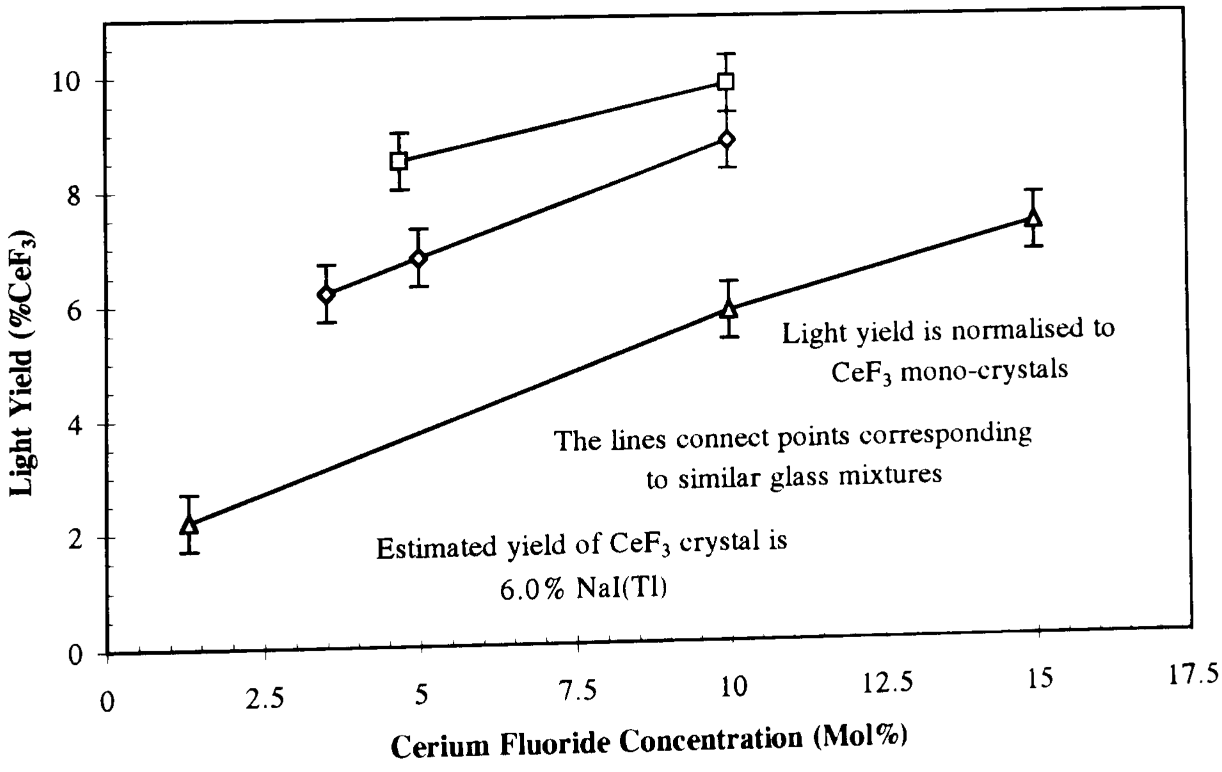

Figure A2.02 The light yield versus mol% CeF_3 for a selection of HMF glasses (courtesy R.M.Brown et al).

Appendix 4

Glass density measurement: Error Analysis

The Archimedian up-thrust experienced when a sample is immersed in a liquid is proportional to the volume of liquid displaced and can be used to infer the volume of the sample. Combining this with the mass of the sample in air, gives the density, ρ_g. All masses were measured using a pan balance which has a random error characterised by a $\sigma_r = 0.0002$ g. As fluoride glasses undergo a chemical reaction when exposed to water and similar ionic liquids, the choice of floatation medium is restricted to covalent liquids. In practice covalent liquids are normally used for this measurement due to their low viscosity and surface tension. Kerosene was used for this work, it has a density of 0.895 gcm^{-3} at STP. A pan was used to support the glass when its mass in kerosene was measured, the mass of the empty pan in kerosene was also recorded. In the subsequent analysis, the following notation is used:

M_g	Mass of glass in air	[g]
$M_{(g+p)k}$	Mass of glass and pan in kerosene	[g]
$M_{(p)k}$	Mass of empty pan in kerosene	[g]
$M_{(g)k}$	Mass of glass in kerosene	[g]
ρ_k	Density of kerosene	[gcm^{-3}]
ρ_g	Density of glass	[gcm^{-3}]

The density of the glass is given by

$$\rho_g = \frac{M_g}{Vol} \qquad \text{Equation A4.01}$$

Archimedian up-thrust = $M_g - M_{(g)k}$, but $M_{(g)k} = M_{(g+p)k} - M_{(p)k}$

$$Vol = \frac{upthrust}{\rho_k} \qquad \text{Equation A4.02}$$

$$\rho_g = \rho_k \times \frac{1}{\left(M_g - \left(M_{(g+p)k} - M_{(p)k}\right)\right)} \times M_g \qquad \text{Equation A4.03}$$

$$= \rho_k \times \frac{1}{\left(1 - \left(\frac{M_{(g+p)k} - M_{(p)k}}{M_g}\right)\right)} \qquad \text{Equation A4.04}$$

To calculate the error in the glass density, let $A = M_{(g+p)k} - M_{(p)k}$,

$$\delta A = \sqrt{\left(\delta M_{(g+p)k}\right)^2 + \left(\delta M_{(p)k}\right)^2} \qquad \text{Equation A4.05}$$

Let $B = A/M_g$,

$$\left(\frac{\delta B}{B}\right)^2 = \left(\frac{\delta A}{A}\right)^2 + \left(\frac{\delta M_g}{M_g}\right)^2 \qquad \text{Equation A4.06}$$

Let $C = 1 - B$,

$$\delta C = \sqrt{(\delta 1)^2 + (\delta B)^2} = \delta B \qquad \text{Equation A4.07}$$

Let $D = 1/C$,

$$\left(\frac{\delta D}{D}\right)^2 = \left(\frac{\delta 1}{1}\right)^2 + \left(\frac{\delta C}{C}\right)^2 = \left(\frac{\delta C}{C}\right)^2 \rightarrow \frac{\delta C}{C} = \frac{\delta D}{D} \qquad \text{Equation A4.08}$$

Let E= $\rho_k \times D$,

$$\left(\frac{\delta E}{E}\right)^2 = \left(\frac{\delta \rho_k}{\rho_k}\right)^2 + \left(\frac{\delta D}{D}\right)^2 = \left(\frac{\delta \rho_k}{\rho_k}\right)^2 + \left(\frac{\delta C}{C}\right)^2 = \left(\frac{\delta \rho_k}{\rho_k}\right)^2 + \left(\frac{\delta B}{1-B}\right)^2 \qquad \text{Equation A4.09}$$

$$\left(\frac{\delta E}{E}\right)^2 = \left(\frac{\delta \rho_k}{\rho_k}\right)^2 + \frac{B^2}{(1-B)^2}\left(\left(\frac{\delta A}{A}\right)^2 + \left(\frac{\delta M_g}{M_g}\right)^2\right) \qquad \text{Equation A4.10}$$

Substitute E≡ ρ_g,

$$\frac{\delta \rho_g}{\rho_g} = \sqrt{\left(\frac{\delta \rho_k}{\rho_k}\right)^2 + \frac{B^2}{(1-B)^2}\left(\frac{\left((\delta M_{(g+p)k})^2 + (\delta M_{(p)k})^2\right)}{\left(M_{(g+p)k} - M_{(p)k}\right)^2} + \left(\frac{\delta M_g}{M_g}\right)^2\right)} \qquad \text{Equation A4.11}$$

where,

$$B = \frac{M_{(g+p)k} - M_{(p)k}}{M_g} = \frac{M_{(g)k}}{M_g} \qquad \text{Equation A4.12}$$

This functional form of the error in the glass density measurement has been modelled using *Microsoft Excel*, realistic estimates have been used for the errors in the various parameters,

$\rho_k \pm \delta\rho_k = 0.4812 \pm 0.0001$ gcm^{-3} at STP

$\delta M_g = \delta M_{(g+p)k} = \delta M_{(p)k} = 0.0002$ g

The majority of the glass samples had dimensions ≈ 20× 10× 5 mm^3, the error in the density of these samples was ≈1%. The smallest sample was a polished Russian sample N8, which was only ≈ 5× 5× 5 mm^3, the uncertainty in the density of this sample, was 8%.

The balance was checked with standard weights and also compared with two similar balances. There was no significant systematic error associated with the mass measurements. Any systematic error (glass-to-glass) due to the variation of the density of kerosene as a function of temperature, was removed by measuring the mass of all samples in one afternoon. The temperature of the kerosene was stable at 22±0.5°C for the duration of these measurements.

Appendix 5

Photon Yield Calibration (Figure 7.07): Error Analysis

Figure 7.07 consists of two calibration graphs, the data sets for these were recorded during the CERN beam tests. One corresponds to the electron and the other to the muon energy range. The graphs consist of pairs of (X-Y) data points, the Y-ordinate is the number of photoelectrons calculated from the equation,

$$N_p = \left(\frac{\mu_s}{\sigma_s}\right)^2 \qquad \text{Equation A5.01}$$

In the equation above, neither σ or μ are measured directly. There is a pedestal associated with the acquisition system, which corresponds to no photoelectrons being detected. In this analysis, the pedestal occurs at μ_p and is characterised by a Gaussian distribution of width, σ_p. The width arises mainly from electronic noise. The distribution that is measured corresponding to a finite light level falling on the photomultiplier, at μ_T (total) is also approximately a Gaussian, of width, σ_T. This distribution is the sum in quadrature of the intrinsic pedestal width and the statistical term resulting from fluctuations in the number of photoelectrons detected, σ_s.

$$\sigma_T^2 = \sigma_p^2 + \sigma_s^2 \qquad \text{Equation A5.02}$$

The mean position is the sum of the pedestal and the signal due to light falling on the PMT,

$$\mu_T = \mu_p + \mu_s \qquad \text{Equation A5.03}$$

The expression for the propagated error in N_p resulting from uncertainty in μ and σ is,

$$\left(\frac{\delta N_p}{N_p}\right)^2 = \left(\frac{\delta(\mu_s^2)}{\mu_s^2}\right)^2 + \left(\frac{\delta(\sigma_s^2)}{\sigma_s^2}\right)^2 \qquad \text{Equation A5.04}$$

$$\sigma_s^2 = \sigma_T^2 - \sigma_p^2 \qquad \text{Equation A5.05}$$

hence the error in σ_s^2 is,

$$\delta(\sigma_s^2)^2 = \delta(\sigma_T^2)^2 + \delta(\sigma_p^2)^2 \qquad \text{Equation A5.06}$$

and

$$\mu_s = \mu_T - \mu_p \qquad \text{Equation A5.07}$$

the error in the mean, μ_s is,

$$(\delta\mu_s)^2 = (\delta\mu_T)^2 + (\delta\mu_p)^2 \qquad \text{Equation A5.08}$$

$$\left(\frac{\delta N_p}{N_p}\right)^2 = \left(\frac{(\delta\mu_T)^2 + (\delta\mu_p)^2}{(\mu_T - \mu_p)^2}\right)^2 + \left(\frac{\sqrt{\delta(\sigma_T^2)^2 + \delta(\sigma_p^2)^2}}{\sigma_T^2 - \sigma_p^2}\right)^2 \qquad \text{Equation A5.09}$$

$$\frac{\delta N_p}{N_p} = \sqrt{\left(\frac{(\delta\mu_T)^2 + (\delta\mu_p)^2}{(\mu_T - \mu_p)^2}\right)^2 + \left(\frac{\delta(\sigma_T^2)^2 + \delta(\sigma_p^2)^2}{(\sigma_T^2 - \sigma_p^2)^2}\right)} \qquad \text{Equation A5.10}$$

Typically, the uncertainty in the mean position of the measured Gaussians is small compared to the difference, μ_T-μ_p. Hence the first term in the square-root is approximately zero.

$$\frac{\delta N_p}{N_p} = \sqrt{\cancelto{0}{\left(\frac{\delta(\mu_T)^2 + \delta(\mu_p)^2}{(\mu_T - \mu_p)^2}\right)^2} + \left(\frac{\delta(\sigma_T^2)^2 + \delta(\sigma_p^2)^2}{(\sigma_T^2 - \sigma_p^2)^2}\right)} \qquad \text{Equation A5.11}$$

$$\frac{\delta N_p}{N_p} \approx \sqrt{\left(\frac{\delta(\sigma_T^2)^2 + \delta(\sigma_p^2)^2}{(\sigma_T^2 - \sigma_p^2)^2}\right)} \qquad \text{Equation A5.12}$$

σ_T and σ_p are measured,

$$\partial(\sigma^2) = 2\sigma\partial\sigma \qquad \text{Equation A5.13}$$

$$\frac{\delta N_p}{N_p} \approx \sqrt{\left(\frac{(2\sigma_T\delta\sigma_T)^2 + (2\sigma_p\delta\sigma_p)^2}{(\sigma_T^2 - \sigma_p^2)^2}\right)} \qquad \text{Equation A5.14}$$

From the equation above it is apparent that, as the difference between the width of the signal Gaussian and the width of the pedestal becomes small, the fractional error in the estimated number of photoelectrons, increases. This conclusion is borne out in the observed spread in experimental points in the calibration graphs of Figure 7.07. The error bars in the figure are calculated assuming $\delta\sigma = 0.025$, this was measured from the spread in experimental data.